

FORCE-GRADIENT DETECTED NUCLEAR MAGNETIC RESONANCE AND  
THE ORIGINS OF NONCONTACT FRICTION

A Dissertation

Presented to the Faculty of the Graduate School

of Cornell University

in Partial Fulfillment of the Requirements for the Degree of

Doctor of Philosophy

by

Seppe Kuehn

August 2007

© 2007 Seppe Kuehn  
ALL RIGHTS RESERVED

# FORCE-GRADIENT DETECTED NUCLEAR MAGNETIC RESONANCE AND THE ORIGINS OF NONCONTACT FRICTION

Seppe Kuehn, Ph.D.  
Cornell University 2007

Magnetic resonance is a ubiquitous technique for the interrogation of chemical and biological systems. Despite this prominence, the intrinsic low sensitivity of inductive detection has prohibited the application of magnetic resonance to individual cells and molecules. Magnetic resonance force microscopy (MRFM) has been proposed as a route to magnetic resonance imaging with single nucleus sensitivity. MRFM brings the possibility of subsurface, non-destructive, chemically specific imaging, to the atomic length scale.

We have demonstrated a new MRFM measurement protocol: detecting the presence of nuclear magnetic moments as a frequency shift in a micromechanical oscillator. Our method obviates the need for long, coherent manipulation of spin magnetization at the oscillator frequency. In doing so, we lift the restriction that samples studied by MRFM exhibit long spin-lock lifetimes and reduce the radio frequency irradiation duty cycle. Using this technique we have demonstrated a sensitivity of  $\sim 10^5$  proton magnetic moment equivalents by detecting magnetic resonance from  $^{108}$   $^{71}\text{Ga}$  nuclear magnetic moments at 4.4K and 7T using a custom fabricated single crystal silicon cantilever. At the time of publication this represented the most sensitive NMR measurement by a general method.

The dominant source of noise in all high sensitivity MRFM measurements to date has been noncontact friction between the tip of the cantilever and the sample. Prior to our work, no physical mechanism of noncontact friction had been experimentally validated. We have shown that noncontact friction can arise from dielectric fluctuations within the sample. Using high sensitivity, custom fabricated, single crystal silicon cantilevers we have measured energy losses over poly(methyl methacrylate), poly(vinyl acetate), and polystyrene thin films at room temperature. A new theoretical analysis relating noncontact friction to the dielectric response of the film was consistent with our experimental observations. This work constituted the first direct, mechanical detection of friction due to dielectric fluctuations.

## BIOGRAPHICAL SKETCH

Seppe Kuehn was born on May 11<sup>th</sup>, 1978 in Athens, Ohio to Jack Kuehn and Ellie Kaastra. Until age nine he lived in a solar powered house on Sunflower farm, in southeastern Ohio, built and maintained by his parents. His interest in experiments was piqued early by observing his father's sometimes adventurous, and periodically successful, experimentation with the house's electrical, heating and water systems. His childhood was marked by much time spent outdoors. His father was a self employed bee keeper and his mother a social worker. His sister, Erika, was born in 1982 and the family spent many summers in The Netherlands visiting his grandparents and extended family.

Seppe's education began at River Valley Elementary School in Athens, Ohio. He moved to Champaign, Illinois in 1990 so his father could take a job keeping bees at the University of Illinois. He attended Champaign Central High School. In 1996 he began studies at Beloit College in Beloit, Wisconsin. While studying physics, the liberal arts experience allowed him to pursue other interests such as: philosophy, mathematics, history, english literature and chemistry. He spent half of his third year at Beloit studying at the Eötvös Kollégium in Budapest, Hungary. On returning to Beloit he received a B.S. in 2000.

After deferring his admission to Cornell University Seppe spent a year living in Portland, Oregon working as a carpenter's apprentice. In Oregon he spent most of his free time mountaineering and climbing snow, rock and ice in the Cascades. In the summer of 2001 he arrived in Ithaca and began graduate studies at Cornell University, where, working with Dr. John Marohn he produced this thesis. As a post doctoral researcher Seppe will study microbial population dynamics in closed ecosystems with Dr. Stanislas Leibler at The Rockefeller University.

Science is not about control. It is about cultivating a perpetual condition of wonder in the face of something that forever grows one step richer and subtler than our latest theory about it. It is about reverence, not mastery.

- Richard Powers

Personal density is directly proportional to temporal bandwidth. Temporal bandwidth, is the width of your present, your now. It is the familiar  $\Delta t$  considered as a dependent variable. The more you dwell in the past and in the future, the thicker your bandwidth, the more solid your persona. But the narrower your sense of Now.

- Thomas Pynchon

## ACKNOWLEDGEMENTS

### Colleagues

The work presented here was only possible because of the truly remarkable guidance I received from my advisor, Dr. John Marohn. From the beginning John treated me as a colleague, gently establishing high expectations and by fulfilling those expectations as a team. John has always implicitly and selflessly demanded that his graduate students become their own scientists, their own thinkers. He made graduate school a safe testing ground for my own scientific ideas, successful and unsuccessful alike. Where the pressures of academia, especially the tenure process, often placed more importance on rapid publication than education John never wavered from his role as a mentor and educator.

It has been refreshing and inspiring to work with an advisor who maintains such a strong stake in the quality of the work, independent of the rewards it might bring. John attacks scientific problems with a vigor and excitement that is ruthlessly faithful to, and motivated by, the data. I aspire to do the same.

John's attitude towards science cultivated an exceptional group of graduate students. I would especially like to thank Sean Garner and Bill Silveira for their guidance in the early days. They created a supportive, collaborative environment while pushing all of us to higher standards. What resulted was a dedicated group of hardworking graduate students who were heavily invested in the success of their advisor. I would also like to thank Jahan Dawlaty for the time we spent in our first year of graduate school, and early days in the lab, wrestling with the many complexities of quantum and statistical mechanics.

I would like to thank the rest of the Marohn Group during my time here, Erik Muller, Tina Ng, Micheal Jaquith, Showey Yazdanian, Steve Hickman, Boyan Penkov, and Eric Moore. Thanks to Showey and Steve for infusing the lab with new excitement and for good times outside of Baker.

Much of my exposure to the broader scientific community came through interactions with fellow MRFMers during conferences and lab visits. Thanks to John Sildes at UW Washington for having such vision, although some days I wished he never would have thought up this crazy experiment! Dan Rugar and John Mamin at IBM Almaden, for being helpful with the nuts and bolts of getting MRFM to work, and for writing some of the best scientific papers I've ever read. Doran Smith at the Naval Research Laboratory for everything from DSP to hardware advice. Thanks to the rest of the MRFM community. I hope to encounter such a collaborative group of scientists working towards a common goal elsewhere. It has been immensely rewarding.

Thanks to my committee, Professors Paul McEuen, David Zax, and Roger Loring for their time and comments. Thanks especially to Roger for his collaboration on the theory portion of the friction work and for a well taught graduate course in statistical mechanics. Thanks to Dave for advice about radio frequency electronics.

### Family

Thanks to my parents. I have been incredibly fortunate to grow up with your support, and the experiences I was given. The farther I get from home, the more I realize how lucky I have been. Thanks for everything you taught me, and thanks for all those wonderful years on the farm! Thanks also for directing me towards Beloit. Thanks to my sister, Erika, for supporting me here at Cornell and to my grandparents MM, David, Oma and Opa.

### Friends

My time in Ithaca has been about so much more than science because of the group of people here I've been fortunate enough to spend time with. Thanks to Greg and Victoria, Yutan and Beth, Aviva, Vivian, Kurt, Abhijit, Scott, Tom, Andrea, Lisa and Joanna, Ethan, Rob and Kristen, Yang Guang, Steve and Erin. Thanks to Kyle Jackson and Devin Brown of the MacCormack Secure center. Jane, thanks for pushing me to do better and for a real glimpse of another part of the world.

Thanks to Ranjan Roy, the most talented educator I have encountered. Ranjan taught me what it means to understand a concept and changed the way that I learn.

Hope, thanks for your insatiable curiosity, energy, and positive outlook. I've been fortunate to spend so much time with such a gifted thinker and writer. Thanks for the endless conversations weaving poetry, economics, science, and art into one. Also, for the Central American adventures, past and future; somehow, things look better riding in the back of a rusty truck across El Salvador. I can't wait for the Big City.

## TABLE OF CONTENTS

<b>1</b>	<b>Introduction</b>	<b>1</b>
1.1	Background and history . . . . .	1
1.1.1	Protein structure: X-ray diffraction and NMR . . . . .	1
1.1.2	Magnetic resonance imaging . . . . .	2
1.1.3	Scanned probe microscopy . . . . .	2
1.2	MRFM basics . . . . .	3
1.2.1	Force from a single spin . . . . .	5
1.2.2	Cantilever force sensitivity . . . . .	5
1.2.3	Basic signal-to-noise . . . . .	6
1.3	Why force detection? . . . . .	7
1.4	Previous MRFM measurements . . . . .	8
1.4.1	Future directions for MRFM . . . . .	10
1.5	Summary and outline . . . . .	11
<b>2</b>	<b>Theoretical background</b>	<b>13</b>
2.1	Nuclear Magnetic Resonance . . . . .	13
2.1.1	Bloch Equations . . . . .	13
2.1.2	The rotating frame . . . . .	14
2.1.3	Spin-lock . . . . .	14
2.1.4	Adiabatic rapid passage . . . . .	14
2.2	Relaxation . . . . .	16
2.2.1	Phenomenological relaxation . . . . .	16
2.2.2	Quantum mechanical relaxation . . . . .	16
2.3	Cantilever dynamics . . . . .	18
2.3.1	Minimum detectable force . . . . .	19
2.3.2	Minimum detectable frequency shift . . . . .	20
2.3.3	Relaxation of a classical oscillator . . . . .	21
<b>3</b>	<b>Force-gradient detected nuclear magnetic resonance</b>	<b>22</b>
3.1	Force-gradient detection . . . . .	22
3.1.1	Signal to noise . . . . .	22
3.1.2	Comparison to OSCAR . . . . .	24
3.2	Apparatus design . . . . .	26
3.2.1	Nanopositioner . . . . .	28
3.2.2	Radio frequency electronics . . . . .	28
3.2.3	Cantilever and fiber alignment . . . . .	33
3.3	Measurement and signal . . . . .	35
3.4	Second generation apparatus . . . . .	36
3.4.1	Basic design . . . . .	36
3.4.2	Material consideration and heat sinking . . . . .	42
3.4.3	Attocube positioning . . . . .	42
3.4.4	Fiber gluing . . . . .	43
3.4.5	Cryogenic electrical considerations . . . . .	44
3.4.6	Cantilever driving and frequency demodulation . . . . .	44
3.5	Noise floor measurements . . . . .	45
3.6	Signal and cyclic CERMIT . . . . .	47
3.6.1	Experimental setup . . . . .	47
3.6.2	CERMIT signal . . . . .	51
3.7	Conclusions . . . . .	54
3.8	Future directions . . . . .	54

<b>4 Introduction to noncontact friction</b>	<b>56</b>
4.1 Noncontact friction and MRFM . . . . .	56
4.2 Noncontact friction in other fields . . . . .	56
4.3 Dielectric fluctuations and friction . . . . .	57
4.4 Fundamentals of friction: fluctuation-dissipation . . . . .	57
4.4.1 Fluctuation-dissipation for cantilevers . . . . .	58
4.4.2 Phenomenology of friction in force microscopy . . . . .	59
4.5 Previous work . . . . .	61
4.5.1 Experiments . . . . .	61
4.5.2 Theory . . . . .	61
4.6 Preliminary observations . . . . .	62
<b>5 High sensitivity dissipation microscope</b>	<b>64</b>
5.1 Introduction . . . . .	64
5.2 Microscope design . . . . .	64
5.2.1 Perpendicularity . . . . .	64
5.2.2 Cantilever and fiber alignment . . . . .	64
5.2.3 Piezo tube scanner . . . . .	67
5.2.4 Microscope super structure . . . . .	69
5.2.5 Chamber and vibration isolation . . . . .	69
5.3 Cantilever design and fabrication . . . . .	71
5.3.1 Cantilever design . . . . .	71
5.3.2 Cantilever fabrication protocol . . . . .	74
5.3.3 Tip metalization . . . . .	77
5.4 Initial data and microscope calibration . . . . .	77
5.4.1 Measuring friction . . . . .	77
5.4.2 Surface approach . . . . .	79
5.4.3 Friction versus voltage . . . . .	79
5.4.4 Surface location determination . . . . .	80
5.4.5 Friction versus distance . . . . .	81
5.4.6 Frequency measurements . . . . .	82
5.4.7 Scanning . . . . .	85
5.5 Conclusions . . . . .	86
<b>6 Dielectric fluctuations and the origins of noncontact friction</b>	<b>87</b>
6.1 Introduction . . . . .	87
6.2 Measurement protocol . . . . .	87
6.2.1 Sample preparation . . . . .	87
6.3 Friction over dielectrics . . . . .	90
6.3.1 Thickness dependence . . . . .	90
6.3.2 Estimating capacitance . . . . .	93
6.3.3 Estimating $S_E(\omega_c)$ . . . . .	95
6.4 Screening by metals and substrate dependence . . . . .	95
6.5 Adsorbates . . . . .	98
6.6 Friction at $V_{ts} = \phi$ . . . . .	98
6.7 Conclusions . . . . .	100
6.8 Cantilever frequency fluctuations . . . . .	100
6.9 Future directions . . . . .	100
<b>7 Theory of noncontact dielectric friction</b>	<b>102</b>
7.1 Introduction and hypothesis . . . . .	102
7.2 Outline of the calculation . . . . .	102
7.2.1 Linear response . . . . .	102
7.2.2 Electrostatics: infinitely thick film . . . . .	104

7.2.3	Electrostatics: films of finite thickness . . . . .	104
7.2.4	Dynamics . . . . .	104
7.3	Calculating friction . . . . .	106
7.3.1	Friction over an infinite film . . . . .	106
7.3.2	Friction over a finite film backed by a conductor . . . . .	106
7.3.3	Dielectric spectroscopy . . . . .	106
7.4	Comparison with experiment . . . . .	107
7.4.1	Ratios . . . . .	107
7.4.2	Further considerations . . . . .	111
7.5	Discussion . . . . .	113
7.5.1	Relevance to MRFM . . . . .	115
<b>A</b>	<b>Solution to Bloch equations for <math>T_1 = T_2</math></b>	<b>116</b>
A.1	Solution to the Vector Equation of Motion . . . . .	116
<b>B</b>	<b>Langevin relaxation of a classical oscillator</b>	<b>118</b>
B.1	Introduction . . . . .	118
B.2	Onsager's regression . . . . .	118
B.2.1	Correlation functions . . . . .	118
B.2.2	Regression hypothesis formalized . . . . .	121
B.3	Fluctuation-dissipation theorem . . . . .	122
B.4	Response functions . . . . .	123
B.5	Langevin formalism . . . . .	124
B.6	Harmonic oscillator . . . . .	126
B.6.1	Laplace transforms . . . . .	126
B.6.2	Solution to equation of motion . . . . .	127
B.6.3	White noise . . . . .	128
B.6.4	Exponential Bath Correlations . . . . .	128
<b>C</b>	<b>Second generation MRFM probe</b>	<b>130</b>
C.1	Filling liquid helium . . . . .	130
C.1.1	Swept field magnet . . . . .	130
C.1.2	Cryogen filling protocol . . . . .	130
C.2	Probe design . . . . .	132
<b>D</b>	<b>Magnetometry calculations</b>	<b>141</b>
D.1	Calculation of frequency shift . . . . .	141
D.1.1	Checks . . . . .	141
D.1.2	Results . . . . .	141
D.1.3	Comments . . . . .	141
D.1.4	Frequency shifts . . . . .	143
<b>E</b>	<b>Spectral theorems and spectral conventions</b>	<b>145</b>
E.1	Exact form of equation 4.11 . . . . .	145
E.2	Conventions . . . . .	145
E.3	The Wiener-Khinchin Theorem . . . . .	146
<b>F</b>	<b>Dissipation microscope design</b>	<b>147</b>
<b>G</b>	<b>Cantilever fabrication recipe</b>	<b>156</b>
G.1	Topside processing . . . . .	156
G.1.1	Tip thinning . . . . .	156
G.1.2	Definition of cantilevers . . . . .	156
G.2	Backside processing . . . . .	157

<b>H Dielectric spectroscopy measurements</b>	<b>158</b>
H.1 Custom capacitors . . . . .	158
H.2 Results . . . . .	158
<b>References</b>	<b>161</b>

## LIST OF TABLES

1.1	Forces from single spins . . . . .	5
1.2	Minimum detectable forces . . . . .	6
3.1	Attocube piezo displacements . . . . .	43
3.2	Magnetization densities for GaAs and PS . . . . .	52
5.1	Perpendicular geometry minimum approach distance due to angular misalignments . . . . .	66
5.2	Fabricated cantilever dimensions and calculated specifications . . . . .	73
6.1	Physical properties of PMMA, PVAc, PS . . . . .	90
7.1	$\epsilon'(\omega_c)$ and $\epsilon''(\omega_c)$ for PMMA, PVAc and PS . . . . .	106

## LIST OF FIGURES

1.1	MRFM Schematic . . . . .	3
1.2	Tip sphere and sample . . . . .	4
1.3	Perpendicular Geometry . . . . .	9
2.1	Rotating Frame . . . . .	15
2.2	Fluctuating field power spectrum. . . . .	18
2.3	Cantilever position fluctuation power spectrum . . . . .	19
3.1	CERMIT Schematic . . . . .	23
3.2	CERMIT signal estimate . . . . .	24
3.3	CERMIT probe . . . . .	27
3.4	Magnet parallel to width geometry . . . . .	28
3.5	MRFM coarse approach . . . . .	29
3.6	Coarse approach steps . . . . .	30
3.7	RF tank circuit . . . . .	31
3.8	RF tank resonance frequency versus $C_t$ . . . . .	32
3.9	CERMIT cantilever SEM . . . . .	34
3.10	Schematic of fiber cantilever alignment . . . . .	35
3.11	CERMIT frequency shift time transients . . . . .	37
3.12	CERMIT signal versus field . . . . .	38
3.13	Schematic of second generation MRFM probe . . . . .	39
3.14	Second generation MRFM probe pictures . . . . .	41
3.15	Temperature versus time during cooling to 4K . . . . .	42
3.16	Cantilever frequency power spectra . . . . .	46
3.17	77K frequency noise power spectra . . . . .	48
3.18	4K frequency noise power spectrum . . . . .	49
3.19	CERMIT experimental setup . . . . .	50
3.20	Time domain CERMIT signal . . . . .	51
3.21	cyclic CERMIT slow modulation . . . . .	53
3.22	ARP induced frequency transient . . . . .	53
3.23	Estimate of CERMIT signal from nanofabricated magnet . . . . .	55
4.1	Schematic of noncontact friction. . . . .	60
4.2	Noncontact friction comparison between sharp and blunt cantilevers . . . . .	63
5.1	Dissipation microscope . . . . .	65
5.2	Cantilever perpendicularity and angular alignment . . . . .	65
5.3	Cantilever and fiber holder . . . . .	66
5.4	Piezo tube scanner . . . . .	68
5.5	Microscope super structure . . . . .	70
5.6	Microscope chamber and vibration isolation . . . . .	71
5.7	Picture of the chamber, vibration isolation and superstructure . . . . .	72
5.8	Friction versus cantilever dimensions at constant $Q$ . . . . .	73
5.9	Cantilever frequency versus length at constant thickness . . . . .	74
5.10	Schematic of cantilever tip design . . . . .	75
5.11	Basic cantilever fabrication . . . . .	76
5.12	Scanning electron micrographs of a cantilever . . . . .	77
5.13	Cantilever ringdown . . . . .	78
5.14	Friction versus tip-sample voltage . . . . .	79
5.15	$Q$ versus piezo extention: surface extrapolation . . . . .	80
5.16	Surface location errors at high levels of noncontact friction . . . . .	81
5.17	$\Gamma$ versus $d$ over Au(111) . . . . .	82
5.18	Block diagram of the dissipation experiment . . . . .	83

5.19	Cantilever $f_0$ versus $V_{ts}$ for $d = 30, 100, 200\text{nm}$	84
5.20	$1.5\mu\text{m}^2$ frequency image	86
6.1	Schematic of the measurement	88
6.2	Friction measured at $\pm 0.5\text{V}$	89
6.3	Film thickness verses solution concentration	91
6.4	Friction over PMMA, PVAc and PS at constant film thickness	92
6.5	Decreasing $S_E(\omega_c)$ with film thickness	93
6.6	Thickness dependence of friction over dielectrics	94
6.7	Capacitance calculation	95
6.8	Estimated capacitance and $S_E(\omega_c)$ over Au(111)	96
6.9	Thickness dependence of friction over dielectrics	97
6.10	Fluctuating field screened by metals	97
6.11	Friction over Au and PS	98
6.12	Friction over Au and PS	99
6.13	Cantilever frequency fluctuations over PMMA and PVAc	101
7.1	Schematic of noncontact dielectric friction	103
7.2	Reaction field from a test dipole	103
7.3	Schematic of noncontact dielectric friction	105
7.4	Comparison between measured and predicted friction	108
7.5	Theory and experiment: friction ratios at constant $h$	109
7.6	Friction ratios PMMA/PVAc from $d = 7 - 60\text{nm}$	110
7.7	Measured thickness dependence of noncontact friction for $d = 10\text{nm}$	111
7.8	Calculated thickness dependence of noncontact friction for $d = 5\text{nm}$	112
7.9	Calculated $\Gamma_s$ as a function of $d$ and $h$ over PMMA	113
7.10	Comparison of capacitance estimates	114
7.11	Dynamic heterogeneity hypothesis	114
B.1	Onsager regression hypothesis	119
B.2	Correlation functions	120
B.3	Oscillator in contact with a bath	125
B.4	Lineshape of a classical oscillator	129
C.1	Schematic of probe super structure	133
C.2	Top view of CERMET probe	134
C.3	Mounting plate CAD	135
C.4	Microscope stage CAD	136
C.5	Cantilever holder CAD	137
C.6	Sample holder CAD	138
C.7	Magnet parallel to width stage schematic	139
C.8	Magnet parallel to width stage CAD	140
D.1	Magnetometry SNR as a function of magnet width	142
D.2	Magnetometry frequency shift verses magnet dimensions	144
F.1	Overview of dissipation microscope CAD	148
F.2	CAD for parts (a) and (b)	149
F.3	CAD for parts (c) and (d)	150
F.4	CAD for parts (e) and (f)	151
F.5	CAD for parts (g) and (h)	152
F.6	CAD for parts (i),(j) and (k)	153
F.7	CAD for part (l)	154
F.8	CAD for part (l)	155

H.1	Capacitor evaporation jig for dielectric spectroscopy . . . . .	159
H.2	Custom thin film capacitors for dielectric spectroscopy . . . . .	159
H.3	Custom capacitor holder for dielectric spectroscopy . . . . .	160
H.4	Measured $\hat{\epsilon}'(\omega)$ and $\tan \delta$ for PMMA and PVAc . . . . .	160

## CHAPTER 1 INTRODUCTION

*Professor Bloch has told you how one can detect the precession of the magnetic nuclei in a drop of water. Commonplace as such experiments have become in our laboratories, I have not yet lost a feeling of wonder, and of delight, that this delicate motion should reside in all the ordinary things around us, revealing itself only to him who looks for it. I remember, in the winter of our first experiments, just seven years ago, looking on snow with new eyes. There the snow lay around my doorstep - great heaps of protons quietly precessing in the earth's magnetic field. To see the world for a moment as something rich and strange is the private reward of many a discovery. But I am afraid it has little bearing on the sober question we must, as physicists, ask ourselves: What can we learn from all this about the structure of matter?*

- E.M. Purcell (1952)

In the decades after Purcell posed this question nuclear magnetic resonance (NMR) became a mainstay of fundamental physics, analytical chemistry, and structural biology by permitting the elucidation of the atomic structure of matter. Fifty years later, we continue to explore the possibilities that magnetic resonance offers for determining how atoms arrange themselves.

This thesis presents work in a field which seeks to expand the applicability of magnetic resonance by detecting magnetic resonance not inductively, as Purcell and Bloch initially demonstrated, but as a force. In 1991 Professor John Sidles proposed magnetic resonance force microscopy (MRFM) [1] as a method to detect magnetic resonance from individual nuclei. Sidles' motivation came from the many difficulties associated with determining the detailed atomic structure of proteins, which he saw as the central stumbling block to understanding the origins of disease. Sidles' proposal for single nucleus magnetic resonance imaging would alleviate those difficulties by imaging protein structure directly, one molecule at a time.

At single nucleus sensitivity, MRFM would represent both a new tool for determining protein structure and a general method for the interrogation of matter at the atomic scale. Such measurements would enable the elucidation of the atomic structure of small quantities of non-crystalline material, something which remains out of reach for all currently available analytical techniques. In addition, at single-nucleon sensitivity, MRFM could be exploited to explore fundamental quantum measurement processes. MRFM could be used to readout the quantum state of single nuclear spin in a solid-state quantum computer. Nuclear spins are attractive as quantum bits due to their generally long coherence times and the well established techniques for manipulating their quantum states.

### 1.1 Background and history

Given that stated goal of MRFM is to provide a new route for determining of the atomic structure of matter we begin with a brief overview of the most common existing techniques for determining atomic structure: x-ray crystallography and liquid-state NMR. We then briefly summarize two analytical techniques which enable MRFM: magnetic resonance imaging (MRI) and scanned probe microscopy.

#### 1.1.1 Protein structure: X-ray diffraction and NMR

Much of the existing detailed information about how biological systems work on a molecular level comes from knowledge of the angstrom scale atomic structure of the relevant molecular architectures. Such detailed information is fundamental to understanding the mechanisms of the vast array of interactions occurring between macromolecules in biological systems and is required to develop drugs that exhibit specific interactions with proteins and nucleic acids.

The first macromolecular structure to be determined with angstrom scale resolution was hemoglobin in 1958 using x-ray crystallography. [2] This accomplishment was recognized with a Nobel Prize in Chemistry awarded in 1962 to Max Ferdinand Perutz and Sir John Cowdery Kendrew. Since then, a total of more than 35000 structures have been determined by x-ray crystallography. [3] The central challenge for crystallographers is coaxing biological molecules to form ordered solids amenable to x-ray analysis and crystallization remains the primary obstacle to the rapid determination of large numbers of distinct protein structures. In addition, many protein topologies are poorly suited to x-ray analysis. For example, transmembrane proteins are often comprised of distinct hydrophilic domains which are presented to the cytoplasm and extracellular environment and hydrophobic domains which reside in the lipid bilayer. As a result, expressing these proteins in high concentration often results in aggregation. Of the more than 40000 known structures fewer than 250 are transmembrane proteins. [4]

Atomic scale macromolecular structures have also been determined by liquid state NMR. Of the 40000 known protein structures more than 6000 have been determined by NMR. Conventional NMR exploits the long coherence times of nuclear magnetic moments in liquids and low energy radio frequency photons to non-invasively identify atomic connectivity in proteins. NMR of biological molecules is a rich field; dramatic advances have included Fourier-transform spectroscopy, Nuclear Overhauser Effect measurements, and innumerable multidimensional experiments. Still, elucidating a protein structure by liquids NMR places severe restrictions on the structures that can be studied. First, it requires that the protein be expressible and soluble in millimolar concentrations. In addition, proteins bigger than about 50 kDa become difficult to study.

Solid-state NMR (ssNMR) can in principle provide detailed structural information, especially since dipolar couplings are retained, but obtaining spectra at sufficiently high resolution remains too difficult to permit general application of the technique. [5] Interestingly, ssNMR has provided the only detailed structures of amorphous amyloid fibrils important in the study of Alzheimer's disease. [6] Despite these advances, and the many important structures which have been determined, NMR remains limited in its applicability to the study of macromolecular biomolecules.

Both x-ray crystallography and liquids NMR have yielded much detailed information about the complex structure of biological macromolecules. Yet remains unknown, especially molecular structures which do not form crystals or are not soluble at high concentration. In 2003 the National Research Council presented one of the major challenges facing chemistry: to develop an analytical technique which can "determine the detailed atomic structure of a small amount of non-crystalline material." [7]

### 1.1.2 Magnetic resonance imaging

In addition to providing detailed structural information magnetic resonance has been exploited for the non-invasive imaging of matter. MRI is a technique pioneered by Paul Lauterbur and Sir Peter Sheppard, awarded a Nobel in Medicine in 2003. Lauterbur was the first to suggest invoking a field gradient to spatially localize magnetic resonance thereby facilitating imaging. [8] Conventional MRI allows for three dimensional, non-invasive, chemically specific imaging with resolution as small as tens of microns. Still, imaging on the molecular length scale remains infeasible with current technology due to low sensitivity.

MRFM exploits Lauterbur's idea of using a magnetic field gradient to spatially localize the force signal. While conventional MRI utilizes gradients on the order of  $10\text{T/m}$  over the length scale of tens of centimeters and MRFM exploits gradients of  $10^5\text{T/m}$  and greater over hundreds of nanometers, the essential concept is the same. As will be shown here, the large gradients present in an MRFM experiment enable both nanometer scale spatial localization and the detection of magnetic resonance as a force.

### 1.1.3 Scanned probe microscopy

Another technology which enabled both the advent of MRFM and its continued development is scanned probe microscopy. The much documented development of scanning tunneling microscopy (STM) by Binnig and Rohr in 1980 ushered in a new era of surface science marked by the development of an array of probe based surface analysis techniques, including atomic force microscopy (AFM). [9] AFM uses a micromachined cantilever, with a nanoscale tip brought into contact with the surface of a sample. The deflection of the micromachined oscillator, due to the interaction between the tip and the sample, is measured to high precision producing a high resolution map of the surface. These instruments have yielded images of surfaces with atomic resolution.

AFM laid the theoretical and experimental groundwork for the routine detection of small forces. AFM opened a new route to the detection of very small forces using micromachined oscillators and developed technology for the high precision detection of cantilever motion. However, typical atomic force microscope cantilevers are capable of detecting forces in the  $100\text{fN}$  range while the forces present in a high sensitivity MRFM experiment are only a few attonewtons ( $10^{-18}\text{N}$ ). Much of the work in this thesis is directed towards understanding the fundamental processes which govern the force sensitivity of cantilevers.

A wide variety of scanned probe techniques have been developed, including: electric force microscopy (EFM), near-field scanning optical microscopy (NSOM), chemical force microscopy (CFM), friction force microscopy (FFM), and magnetic force microscopy (MFM). With the exception of EFM and NSOM, the majority of these techniques are strictly surface measurements yielding no information about the underlying substrate. MRFM represents a subsurface scanned probe technique with the additional advantage of chemical specificity.

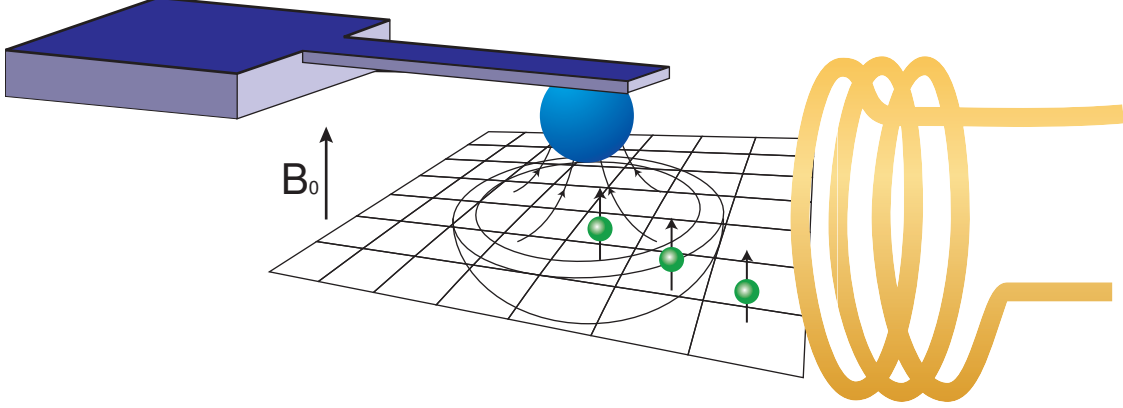


**Figure 1.1:** Schematic of a basic MRFM experiment. A cantilever with a magnetic tip is brought close to the sample of interest which contains the target spins (green spheres). A large polarizing field is applied ( $B_0$ ). A nearby radio-frequency coil is used to manipulate the quantum state of the magnetic moments near the tip. The high field gradient from the magnetic tip creates a slice of the sample for which the magnetic resonance condition is satisfied - shown here as a bowl shaped region.

## 1.2 MRFM basics

MRFM seeks to address the clear deficiency in the currently available techniques for interrogating matter at the atomic length scale by providing a method for the imaging of individual molecules. MRFM achieves this goal by merging the chemical and spatial specificity of MRI with the inherent high sensitivity of AFM. MRFM detects magnetic resonance as a force, or a force-gradient, on a magnet-tipped cantilever. Figure 1.1 shows the basic setup of an MRFM experiment.

A magnet-tipped cantilever is brought close to a sample containing nuclear or electron spin magnetic moments. A large externally applied field ( $B_0$ ) serves to polarize the sample spins. A nearby radio frequency (RF) coil is used to manipulate the sample spins by conventional magnetic resonance techniques. The sample spins couple to the magnetic particle via the gradient-dipole interaction. The field gradient from the magnetic particle further serves to localize the resonance condition spatially as shown by the bowl shaped region in figure 1.1.

To illustrate the key features of the experiment we begin with a simple estimation of the force in the MRFM measurement shown in figure 1.1. While this estimation will contain several rough approximations, it captures the key considerations in an MRFM measurement. We will conclude with an estimate of the force present in a single-spin measurement and a comparison with the force sensitivity of several different cantilevers.

Consider a spherical magnetic particle of radius  $a$  and distance  $d$  from the surface of the sample as shown in Figure 1.2. The force between the particle and the sample spins within the sensitive slice is given by the gradient-dipole interaction

$$\mathbf{F} = (\boldsymbol{\mu} \cdot \nabla) \mathbf{B} \quad (1.1)$$

where  $\mathbf{F}$  is the force,  $\boldsymbol{\mu}$  is the total magnetic moment in the sensitive slice, and  $\mathbf{B}$  is the field from the magnetic particle. Note that for this equation, and the remainder of this thesis, variables in **bold** denote vectors.

Since the external field is applied along  $z$  we assume that  $\boldsymbol{\mu} = (0, 0, \mu_z)$ . Note that this assumes a random phase approximation applies to the spins within the sensitive slice and that this approximation will break down for sufficiently small ensembles of spins. For this estimation we neglect small ensemble effects. In this case equation 1.1 simplifies to

$$F_z = \mu_z \frac{\partial B_z}{\partial z}. \quad (1.2)$$

Equation 1.2 contains two parts: the magnetization in the sensitive slice ( $\mu_z$ ) which is set by the properties of the sample and the field gradient produced by the tip ( $\partial B_z / \partial z$ ) which is set by the magnetic properties and size of the tip. We consider these in turn.

In this large ensemble limit,  $\mu_z$  will be the Curie law magnetization density times the volume of the sensitive slice. In the high temperature limit, where  $k_B T \gg \gamma B_0$  with  $k_B T$  the average thermal energy and  $\gamma$  the gyromagnetic ratio of the target spins, this will be given by

$$\mu_z \approx \frac{\mu^2 B_0}{k_B T} \rho V_{slice} \quad (1.3)$$

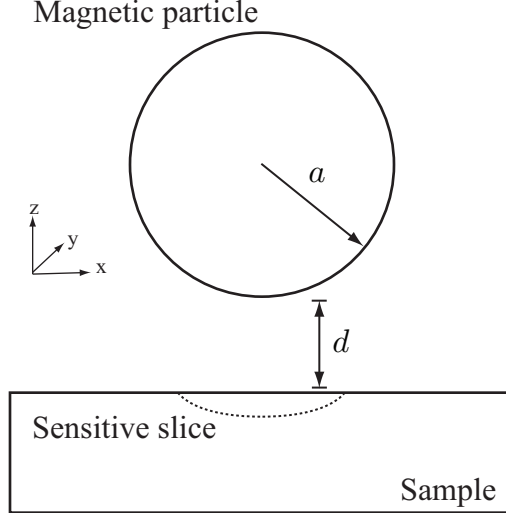


**Figure 1.2:** A spherical magnetic particle of radius  $a$  a distance  $d$  from the surface of the sample. Both the external field ( $B_0$ ) and the cantilever motion lie along  $z$ . The dotted line within the sample indicates the region where the resonance condition is satisfied, the sensitive slice.

where  $V_{slice}$  is the volume of the sensitive slice,  $\rho$  is the spin density and  $\mu$  is the magnetic moment of the target spins. This magnetic moment is given by  $\mu = \gamma\hbar\sqrt{s(s+1)}$  where  $s$  is the spin quantum number and  $\hbar$  is Plank's constant. Note that we are again assuming a large ensemble of spins where statistical fluctuations in the polarization are small compared to the thermal polarization. Generally,  $V_{slice}$  will depend on several parameters in the experiment including  $d$ , the rf power, tip magnet size, and method of inverting the spin magnetization. The thickness of the slice will be inversely proportional to the gradient from the tip and its extent in the  $x$  and  $y$  directions will be approximately the radius of the magnet,  $a$  in figure 1.2.

Having estimated the size of the magnetic moment responsible for the observed force, we now approximate the gradient from the tip. If we assume that the tip is a spherical magnetic particle, the field from the tip can be calculated analytically. This approximation serves well for a variety of magnetic tip geometries since it represents the lowest order term in a multipole expansion of more complex magnet shapes. The field from a saturated spherical particle is given by

$$\mathbf{B} = \frac{\mu_0}{4\pi} \left( \frac{3(\mathbf{m} \cdot \mathbf{r})\mathbf{r}}{r^5} - \frac{\mathbf{m}}{r^3} \right) \quad (1.4)$$

where

$$\mathbf{m} = \frac{4\pi}{3} a^3 \mathbf{M} \quad (1.5)$$

is the magnetic moment of the tip. Here  $\mu_0 = 4\pi \times 10^{-7} \text{ T m/A}$  and  $\mathbf{M}$  is the tip magnetization. If the magnetic particle is saturated by the applied field then,  $\mathbf{M} = M_z$ . [10] To simplify our analysis we consider the field in the  $z$ -direction a distance  $d$  directly below the tip (figure 1.2)

$$B_z = \frac{2\mu_0 M}{3} \frac{a^3}{(a+d)^3}. \quad (1.6)$$

The gradient of the field in the  $z$ -direction is then given by

$$\frac{\partial B_z}{\partial z} = -2\mu_0 M \frac{a^3}{(a+d)^4}. \quad (1.7)$$

In the spirit of this rough approximation we take this gradient to be constant over the volume of the slice. Combining this with equations 1.2 and 1.3 we obtain

$$F_z \approx \frac{-2\mu^2 B_0 \rho V_{slice}}{k_B T} \mu_0 M \frac{a^3}{(a+d)^4}. \quad (1.8)$$

**Table 1.1:** Force on a cobalt magnetic particle with radius 15nm placed 5nm from a single spin for a variety of spin species.

Spin	Magnetic Moment [J/ T]	Force [N]
Electron	$-928.476 \times 10^{-26}$	$3.9 \times 10^{-16}$
$^1\text{H}$	$1.410 \times 10^{-26}$	$5.9 \times 10^{-19}$
$^{13}\text{C}$	$3.550 \times 10^{-27}$	$1.5 \times 10^{-19}$
$^{15}\text{N}$	$-1.431 \times 10^{-27}$	$6.0 \times 10^{-20}$

The least well defined quantity in equation 1.8 is  $V_{slice}$ . Proceeding in the signal estimate requires some knowledge of the region of the sample magnetization being inverted by the rf irradiation. This can be estimated given some knowledge of the specific measurement, and will be considered in more detail later in this thesis.

### 1.2.1 Force from a single spin

In order to develop some intuition for the forces involved in an MRFM experiment we now estimate the force on a cantilever from a single spin. We assume the spin to be polarized along  $z$  at the time of measurement, and note that the volume of the slice no longer figures into the calculation. For a spin a distance  $d$  from the surface of the magnetic particle

$$F_z = -2\mu_{spin}\mu_0 M \frac{a^3}{(a + d)^4} \quad (1.9)$$

where  $\mu_{spin}$  is the magnetic moment of the target spin. If we take a cobalt magnet ( $\mu_0 M = 1\text{T}$ ) with  $a = 15\text{nm}$  placed  $d = 5\text{nm}$  from the target spin we can easily calculate the resulting force for a variety of magnetic moments. The results are shown in Table 1.1.

These forces are incredibly small. For comparison the force required to break a single covalent bond is on the order of  $10^{-9}\text{N}$  and the Coulomb repulsion between two electrons spaced  $1\mu\text{m}$  apart is about  $200\text{aN}$ ! These comparisons naturally raise a question of central importance to MRFM: how small are these forces in comparison to the force sensitivity of a typical cantilever?

### 1.2.2 Cantilever force sensitivity

The force sensitivity of a cantilever will be discussed in detail later in this thesis. Here we state the theoretical minimum detectable force for a harmonic oscillator, which can be derived from classical statistical mechanics, and calculate this minimum for a variety of typical cantilevers. The minimum detectable force is given by:

$$F_{min} = \sqrt{S_F(f_0)b} = \sqrt{\frac{2kk_B Tb}{\pi Q f_0}} \quad (1.10)$$

where  $S_F(f_0)$  is the spectral density of force fluctuations on resonance,  $k$  the spring constant,  $b$  the measurement bandwidth,  $Q$  the quality factor [unitless], and  $f_0$  the resonance frequency. The minimum detectable force for several oscillators taken from the literature are listed in table 1.2. Table 1.2 demonstrates two significant points. First, the commercial SiN cantilever has the poorest force sensitivity. This is due to the generally lower  $Q$  and higher  $k$  for SiN cantilevers. Second, while these theoretical force sensitivities approach those required for single spin detection (table 1.1) they do not in all cases take into account the spurious surface interactions between the tip and the sample which generally lower the quality factor. Despite these cautions, the measured sensitivities that constructing a force sensor for single electron and single proton MRFM has been realized experimentally.

**Table 1.2:** Theoretical minimum detectable forces for several oscillators. Note that the minimum detectable force values assume that the cantilever experiences no spurious interactions with a nearby surface which might degrade  $Q$  and that the detection of the cantilever's motion is thermally limited, meaning that the detector sensitivity is smaller than the thermal motion expected from the equipartition theorem. The nanotube oscillator is a doubly clamped single walled carbon nanotube with a detector limited the force sensitivity of  $\sim 20\text{fN}$ . For the first three oscillators the theoretically predicted force sensitivities have been observed experimentally.

Cantilever	$k$ [N/m]	$f_0$ [Hz]	$Q$	$T$ [K]	$F_{min}$ [N/ $\sqrt{\text{Hz}}$ ]	Citation
SiN	0.001	5000	$10^4$	300	$7 \times 10^{-16}$	
Cornell Si	$60 \times 10^{-6}$	850	$4.6 \times 10^4$	4.4	$8 \times 10^{-18}$	[11]
IBM Si	$260 \times 10^{-6}$	4975	$15 \times 10^4$	0.110	$5.8 \times 10^{-19}$	[12]
Nanotube	$4 \times 10^{-4}$	$5 \times 10^6$	100	300	$20 \times 10^{-18}$	[13]

### 1.2.3 Basic signal-to-noise

Having considered the basic ingredients of an MRFM experiment, namely the expected signal and the expected noise, we can calculate the signal-to-noise ratio (SNR) for an MRFM experiment. Combining equations 1.2 and 1.10 we have:

$$SNR = \frac{\mu_z \frac{\partial B_z}{\partial z}}{\sqrt{S_F(f_0)b}}. \quad (1.11)$$

Equation 1.11 provides insight into the factors to governing the sensitivity of MRFM measurements. Equation 1.11 also allows us to take a careful look at the experimental parameters which we must consider in order to maximize the SNR in any MRFM experiment. We examine these in turn.

$\mu_z$ , as stated, is the magnetic moment of the nuclei, or the ensemble of nuclei being detected. For a large ensemble of spins at equilibrium this will be the net magnetic moment given by the Curie law (equation 1.3). This polarization can be enhanced using techniques such as optical pumping [14], cross polarization, or dynamic nuclear polarization. For very small ensembles the statistical polarization will be large compared to this Curie law magnetization. [15–17] These small ensemble effects will become important when  $\sqrt{N}$ , where  $N$  is the number of spins in the ensemble, approaches the Curie law polarization. The Curie law polarization is  $10^{-3} \times N$  for protons at 4K and at typical fields of a few Tesla. In this small ensemble regime the statistical polarization (the net polarization resulting from these fluctuations) can easily be orders of magnitude larger than the Curie law polarization giving an increase  $\mu_z$ . This increase comes with an associated cost resulting from the fact that the *sign* of the statistical fluctuations is random. So while these fluctuations result in larger  $\mu_z$ 's, the direction of the magnetization is unknown. Therefore the sign of the resulting signal is unknown. This means that one must average signal *power* rather than the raw signal. Therefore, for measurements where the single shot SNR  $< 1$ , where averaging is necessary, the SNR increases as  $b^{1/4}$  rather than  $b^{1/2}$ . [18] If the single shot SNR  $> 1$  this will not be a serious limitation.

Second, we consider the gradient from the tip,  $\partial B_z / \partial z$ . As mentioned this gradient increases as the size of the tip decreases. This makes small magnetic tips desirable. It also presents a central technical challenge in MRFM. How can we custom fabricate high sensitivity oscillators with very small magnetic tips? Also, how small can we make our magnetic tips before they begin to lose their ferromagnetic properties? Another important consideration is the tip-sample separation,  $d$ . As  $d$  decreases, the field gradient increases (equation 1.7), but the surface noise also increases, thereby undesirably increasing  $S_F(f_c)$  in equation 1.11. This compromise has played a central role in recent MRFM measurements at the highest levels of sensitivity.

Third, the spectral density of force fluctuations at the cantilever frequency,  $S_F(f_0)$ , sets the noise in the measurement. We can gain insight into the origins of these fluctuations by rewriting the second equality in equation 1.10. Using the fact that the friction the cantilever experiences,  $\Gamma = k/\omega Q$  we have

$$S_F(f_0) = 4\Gamma k_B T. \quad (1.12)$$

We note that equation 1.12 takes the form of a standard fluctuation-dissipation relationship for a linear system. Equation 1.12 makes clear that the important figure of merit for a cantilever's force sensitivity is the friction that it experiences with its environment,  $\Gamma$ . For a cantilever in an MRFM measurement this friction has two contributions. The intrinsic

friction,  $\Gamma_0$ , is due to losses the cantilever experiences without any external interactions present. The origins of these losses remain unknown, although measurements indicate that they are likely dominated by surface effects and not losses through the base of the cantilever. [19–21] In an MRFM measurement a second dissipation mechanism contributes to  $\Gamma$ . Losses between the tip of the cantilever and the nearby sample due to noncontact interactions contribute surface induced friction,  $\Gamma_s$ . While measurements of this effect have been made previously, [22] no clear mechanism for these effects had been elucidated prior to the work presented here. In addition,  $\Gamma_s$  has been the dominant source of noise in the highest sensitivity MRFM measurements to date. [18] Since total friction is additive,  $\Gamma = \Gamma_0 + \Gamma_s$  and generally for small  $d$ ,  $\Gamma_s > \Gamma_0$ , this effect is significant for MRFM. While we have successfully fabricated cantilevers with the necessary sensitivity for single-spin detection (table 1.10), we are finding that this sensitivity is significantly degraded when the magnetic particle is brought close to the sample. This effect will be discussed in detail in the second half of this thesis, as it remains central challenge for MRFM measurements.

Finally,  $b$ , the bandwidth of the measurement is set by the coherence lifetime of the spins. This coherence time will depend on the details of the spin manipulation necessary for the desired detection protocol. Some detection protocols require long spin-lock lifetimes [23], while others require long spin-lattice relaxation times. [11] The spin relaxation time varies from sample to sample, with the spin-lock lifetime generally much shorter than the spin-lattice relaxation time. Requiring long spin-lock lifetimes for example, restricts the samples which can be studied by MRFM. As a rule of thumb, the spin coherence time must be longer than the cantilever period. For the audio cantilevers used in most of the high sensitivity MRFM measurements thus far this means a coherence time of greater than 10ms is necessary for detection to be feasible. If the oscillator frequency can be successfully increased, or the detection protocol altered, this restriction may be lifted or at least diminished in severity.

### 1.3 Why force detection?

Given the claim that force detected magnetic resonance offers the possibility of increased sensitivity in the detection of NMR it is reasonable to ask how force detection compares to conventional inductive detection. Why should we expect any improvement in sensitivity from force detection? This question has been addressed in the literature. [24] Here we summarize these findings and comment on the comparison.

Conventional, inductively detected magnetic resonance transduces the precession of magnetic moments into an electrical signal in a coil. The coil of wire is generally a component in an rf ‘tank’ circuit which behaves as a harmonic oscillator. This oscillator creates and annihilates a field with the motion of the magnetic moment. NMR has been detected with reasonably high sensitivity by inductive detection using micron scale coils. [25] The sensitivity of these measurements has been on the order of  $10^{12}$  protons/ $\sqrt{\text{Hz}}$ . One can derive a ‘spring constant’ for a coil which relates the strength of the created field to the size of the magnetic moment inducing that field. [24] This spring constant is completely analogous to the cantilever’s mechanical spring constant,  $k$ . In the case of a cantilever, the spring constant relates the mechanical displacement of the magnetic tip to the magnetic moment responsible for that displacement. Therefore, MRFM acts essentially as a mechanical transducer which physically moves the magnetic field rather than creating and annihilating it. The analogy of the spring constant between a coil and a cantilever affords an analytical comparison of the signal produced on each due to an identical magnetic moment, but in order to compare sensitivity we must also compare the noise.

For a cantilever, the noise in the measurement is given by Equation 1.10 which allows a calculation of the random fluctuations which the spin induced mechanical motion of the oscillator must overcome in order to be measured. As mentioned, at the heart of these fluctuations lies the friction that the cantilever experiences, both intrinsic ( $\Gamma_0$ ) and surface induced ( $\Gamma_s$ ). In the case of a coil, the random fluctuations of the current in the coil, or the Johnson noise, sets the sensitivity of the measurement.

Therefore a complete comparison between inductive and mechanical detection of magnetic resonance requires knowledge of their associated spring constants and of the noise mechanisms which set the sensitivity. Since these noise mechanisms are unknown, one cannot formulate a general theory for the sensitivity of mechanical detection. Determining the sensitivity of mechanical detection must be done experimentally. Therefore, any meaningful comparison between mechanical and inductive detection must be done empirically. Such comparisons indicate that mechanical oscillators have been constructed which are softer electrical oscillators affording significantly higher sensitivity for mechanical detection. To date, mechanical detection represents the most sensitive *general* route to detecting magnetic resonance which has been experimentally realized. [18]

## 1.4 Previous MRFM measurements

In the 15 years since John Sidles proposed MRFM, there have been numerous theoretical and experimental advances. We summarize these advances here to provide context for the work that follows.

The first MRFM signal was presented in 1992. [26] In this early experiment at IBM Almaden a force was generated between a micron scale cantilever with a small sample of 2,2-diphenyl-1-picrylhydrazyl (DPPH) glued to the tip containing unpaired electron spins and a millimeter scale ferromagnetic particle. The spins were manipulated using a method now known as cyclic saturation. In cyclic saturation the magnetization in the sensitive slice is saturated by the rf irradiation. The rf irradiation is turned on and off at the resonance frequency of the oscillator producing a time dependent  $\mu_z$  which generates a force at the cantilever resonance. This protocol works well for electrons where the  $T_1$  and  $T_2$  are very short compared to the cantilever period. Generally, for nuclear spins where these relaxation times are milliseconds to seconds long this manipulation protocol will not work.

In 1994 the IBM researchers developed a detection protocol which was amenable to the detection of nuclei and successfully detected magnetic resonance as a force from nuclear magnetic moments. [27] In this experiment the magnetization of the sample was again inverted cyclically at the resonance frequency of the oscillator using a technique known as adiabatic rapid passage (ARP). In ARP the magnetization is inverted in the rotating frame by sweeping the rf frequency from far above the spin resonance to far below the resonance. This results in an inversion of  $\mu_z$  which can be repeated cyclically to produce a force resonant with the oscillator. In order to successfully invert the nuclei many times they must have a sufficiently long relaxation time in the rotating frame, this relaxation time is known as  $T_{1\rho}$ . The experiment was done on ammonium nitrate salts, which have  $T_{1\rho} \approx 3\text{s}$  at room temperature allowing for many ARP inversions before the magnetization is lost to relaxation.

In the same year the IBM group presented the first images from a magnetic resonance force microscope. [28] These images were essentially force maps of the sample translated into spin density images. The resolution of these images was a few microns. As a result of this low resolution and the stringent sample restrictions of the cyclic-ARP detection protocol, no general applications for imaging were proposed. As yet, no one has found a clear application for MRFM at the micron scale.

In 1996 IBM presented the first low temperature MRFM measurements, made on calcium fluoride due to its long  $T_{1\rho}$  at 20K. [29] This was an important advance as the thermomechanical noise in the oscillator scales as  $\sqrt{T}$  (equation 1.10). In addition to demonstrating that a low temperature apparatus could be built, the IBM group demonstrated a variety of classic NMR experiments could be done by MRFM. These experiments included nutation, spin-locks, and inversion recovery measurements.

At this time important advances in cantilever technology began. The Kenny group at Stanford presented the first fabrication of ultrasensitive oscillators capable of detecting forces in the attonewton range. [30] Prior to this work, conventional AFM cantilevers had been used in MRFM experiments limiting the measurement sensitivity. These new cantilevers had spring constants in the  $10^{-6} - 10^{-4}\text{N/m}$  range and resonance frequencies in the kHz. These cantilevers were fabricated from single crystal silicon. The Marohn group presented the second successful fabrication of these high sensitivity oscillators. [31]

Over the last 6-8 years the use of high sensitivity audio frequency cantilevers has brought MRFM to the highest levels of sensitivity. One of the major breakthroughs has been the use of ultrasensitive cantilevers in a geometry where the motion of the cantilever is parallel to the surface of the sample, figure 1.3. In this geometry cantilevers with very small spring constants can be positioned very close to the surface without experiencing snap-in to contact. [32]

This perpendicular geometry meant that standard force detection protocols would no longer work since the net force on the tip is zero for a homogenous distribution of spins. As a result, MRFM measurements shifted from detecting forces to detecting force-gradients. A force-gradient measurement detects the spin signal through a small change in the cantilever's effective spring constant which results in a shift in the cantilever's mechanical resonance frequency.

The first method presented for the detection of magnetic resonance as a force-gradient was OSCAR (**O**scillating **C**antilever **A**diabatic **R**apid passages). In OSCAR the spins are adiabatically inverted by the cantilever motion when resonant rf irradiation is applied. [33] While OSCAR was initially demonstrated using the conventional geometry (figure 1.1), it also allows for frequency shift detection with soft cantilevers in the perpendicular geometry provided there is an asymmetry in the spin distribution below the tip. The initial demonstration of OSCAR boasted a sensitivity of about 100 electron spins in a gamma-irradiated silica sample. By gamma-irradiating silica one can create dangling silicon bonds which contain unpaired electron spins. It is these spins which are detected by MRFM. This sample offers two advantages. First, the spin density can be set by controlling the dose of gamma rays. Second, at sufficiently low spin density the spin-lock lifetime,  $T_{1\rho}$  is known to be long.

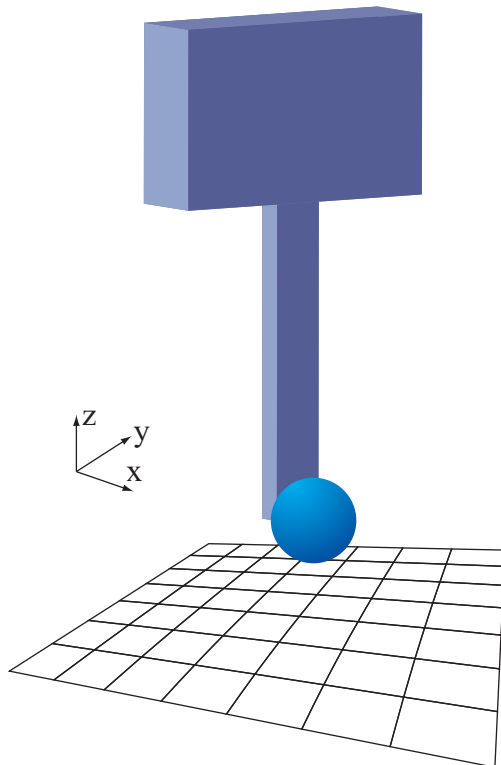


**Figure 1.3:** The perpendicular geometry. The motion of the cantilever is parallel to the surface of the sample in the  $x$  direction. This geometry facilitates the use of soft cantilevers which have low spring constants in the  $x$  direction ( $10^{-5}\text{N/m}$ ), and very high spring constants in the  $z$  direction ( $100\text{N/m}$ ). Note that for a homogeneous distribution of spins the net force on the cantilever in the direction of motion will be zero.

Although OSCAR facilitated the detection of very small force-gradients it was susceptible to low frequency noise. It was, in effect, a DC frequency shift measurement. As a result, the IBM group introduced ‘interrupted-OSCAR’ or i-OSCAR, where the phase of the cantilever frequency shift is flipped periodically by turning the rf irradiation off for half of a cantilever cycle. This produced a coherent frequency shift at nonzero frequency (typically a few tens of hertz) and moved the signal away from the high levels of noise at DC. This elegant solution was, and is, only a partial fix to the problem of low frequency noise, as discussed below.

In 2003, exploiting the i-OSCAR protocol the IBM group detected an equivalent of 6 electron spins by MRFM. [32] The sensitivity demonstrated by this experiment represented a major advance for the field. The spin signal in this experiment arose from roughly 40 electron spins with a noise floor equivalent to about 6 electrons.

With the advent of soft cantilevers and frequency shift measurements the detection of small ensembles of spins became feasible by MRFM. As discussed in section 1.2.3, the detection of small ensemble statistical fluctuations are important. The IBM group demonstrated the initial detection of and control of these fluctuations in a regime where the single shot SNR > 1. [15, 17]

The culmination of more than a decade of research by the IBM group resulted in the detection of a single electron spin in a sample of gamma-irradiated silica. [18] The single-spin measurement represented a major breakthrough in MRFM, enabled by a host of technical advances over the preceding 13 years. The measurement exploited i-OSCAR and required averaging over a period of weeks to achieve an SNR  $\approx 3$ . It is worth emphasizing that this was truly a single spin measurement, as opposed to the measurement of say, 10 spins with an SNR > 10. There was only one spin in the sensitive slice and because the gamma-irradiated silica in this experiment was so dilute with spins that the researchers spent considerable time just locating the unpaired electron for study! Attempts have been made to improve this detection time, which required 13 hours of averaging per point. [34] As yet MRFM has not achieved single shot readout of the quantum state of an individual spin.

MRFM has also seen a host of experimental and theoretical advances which are not explicitly related to attaining high sensitivity detection. For example, the Meier group at ETH Zurich has presented a series of papers demonstrating that a variety of spectroscopic methods from solid state NMR can be applied to MRFM, at least for situations where the gradient from the magnetic particle is relatively small. [35, 36] In addition, Dan Weitekamp at Caltech has proposed several techniques for employing the sensitivity of force detection using methods amenable to spectroscopy [37], or methods for polarizing the spins by coupling them to a mechanically cold oscillator. [38]

#### 1.4.1 Future directions for MRFM

MRFM must face a host of remaining technical challenges . While single-spin detection has been achieved, the primary goal of MRFM, to become a generally applicable tool for imaging matter at the atomic scale, remains a challenge. We now discuss the most important of these challenges.

The limitations of frequency shift detection are clear. Generally, noise is larger at lower frequencies due to  $1/f$  noise sources of unknown origin. These noise sources make it difficult to detect DC frequency shifts, or coherent frequency shifts near zero frequency, while retaining thermally limited detection. This is to say, for frequency shift detection, deleterious sources of noise typically associated with tip-surface interactions are limiting the measurement sensitivity. In contrast, force detection is often thermally limited, even at very small tip-sample separations. Therefore, it is advantageous to generate a spin signal coherent with  $f_0$ . The difficulties here are twofold. First, rapid, coherent manipulation of magnetization by the rf requires long relaxation times, typically long spin-lock lifetimes ( $T_{1\rho}$ ). This undesirably limits the number of samples readily amenable to study by MRFM. Second, coherent manipulation by intense rf fields often generates significant heat in the cryogenic apparatus raising the temperature and thus lowering the sensitivity of the measurement. MRFM would benefit greatly from a manipulation protocol limited by generally long  $T_1$  processes, which will not unrealistically restrict the possible samples, and has a relatively low rf duty cycle or an exceedingly efficient mechanism for producing the rf fields. Alternatively, one expects that  $T_{1\rho}$  will increase with the intensity of the applied field. Therefore, efficient generation of large amplitude rf fields may make long coherent manipulations of spin magnetization possible for a large number of samples.

A second major challenge is the fabrication of magnetic tips. As we have seen, small magnetic tips produce higher field gradients and thus higher per spin forces or force-gradients. The IBM group has successfully ion-beam milled magnetic tips on high sensitivity cantilevers to dimensions of around 100nm. Making smaller tips will require either challenging electron beam lithography or exotic methods such as chemical self assembly.

While deleterious surface interactions that dominate force-gradient MRFM measurements making direct force detection more attractive, force detection remains limited by noncontact friction between the tip and the surface of the sample.

This thesis represents a first, and significant, step towards understanding this noncontact interaction, still considerable work remains. For example, it is empirically clear that noncontact friction is minimized for cantilever tips near metal surfaces. There remains substantial disagreement between measurements of noncontact friction over metals [22] and theories which seek to describe those measurements. [39, 40] A central unanswered question is the role of atomic and molecular adsorbates in noncontact friction. As yet, no careful ultra-high vacuum measurements have been made to test this possibility.

The efficient generation of rf fields also remains a challenge in MRFM. While superconducting resonators have been employed successfully [41] they are limited to operating below the critical field of the superconductors, typically  $\sim 1000\text{G}$ . Operating at low field,  $< 1000\text{G}$ , where these superconducting resonators function does not limit the spin polarization if one operates within the statistical regime where the polarization is dominated by  $\sqrt{N}$  fluctuations. Still, the applied field does serve to saturate the magnetic particle allowing for the highest possible gradients. Therefore, operating in such a low field can compromise SNR by lowering the gradient from the tip.

The IBM group has recently pursued the mechanical generation of rf fields simply by shaking scale magnets at radio frequencies. Mechanical generation of rf fields will be very efficient because it does not require flowing current through a resistive wire. The major obstacle has been producing enough motion at cryogenic temperatures. Since the rf field produced will be the gradient from the small magnet times the amplitude of motion, generating this large amplitude is crucial for success. This approach to rf generation recognizes the important fact that for MRFM we need not generate large fields over large volumes since the region of spins having an effect on the cantilever is small. In current designs much of the power directed at rf generation is wasted by creating fields in regions of space where spins are not resonant.

These challenges highlight the connectedness between the many subsystems in an MRFM experiment. While any single strategy may optimize a specific part of the experiment for SNR, often a simultaneous compromise is necessary. Finding an optimum balance among all relevant parameters remains the central challenge for MRFM. Since many of these parameters, such as surface noise, are not understood theoretically empirical information is paramount for the success of any measurement.

## 1.5 Summary and outline

This thesis presents work addressing these central challenges of MRFM. First, we present the first demonstration of an entirely new MRFM detection protocol, CERMIT (**C**antilever **E**nabled **R**eadout of **M**agnetization **I**nversion **T**ransients). CERMIT is a technique for detecting magnetic resonance as a force-gradient by inverting the nuclei in the sensitive slice and measuring the resulting change resonance frequency of the cantilever. This method offers two distinct advantages over previous methods, including OSCAR. First, the detection bandwidth in CERMIT is limited by  $T_1$ , the spin-lattice relaxation time. Since  $T_1$  will generally be very long at cryogenic temperatures CERMIT lifts the restriction on MRFM that it only be applied to samples with long spin-lock lifetimes ( $T_{1\rho}$ ). This is a significant advance especially if MRFM is to achieve broad applicability as an imaging tool. At the time, our initial demonstration of this technique represented the most sensitive nuclear MRFM measurement ever made with a sensitivity of  $6 \times 10^5$  polarized protons/ $\sqrt{\text{Hz}}$ .

As mentioned in section 1.4.1 noncontact friction sets the ultimate limits on the sensitivity of force detection. As a result the mechanisms of noncontact friction are of central importance to the MRFM community. We have shown that dielectric fluctuations lead to noncontact friction. Using high sensitivity, custom fabricated, single crystal silicon cantilevers we measured energy losses over poly(methyl methacrylate), poly(vinyl acetate), and polystyrene thin films. We have developed a new theoretical analysis, relating noncontact friction to the dielectric response of the film, which is consistent with our experimental observations. This work constitutes the first direct, mechanical detection of noncontact friction due to dielectric fluctuations. It also represents the first time that a theory of noncontact friction has been experimentally validated.

**Chapter 2** discusses the basic theories of NMR including the Bloch equations, Bloembergen-Pound-Perell theory for relaxation, and adiabatic rapid passage. In addition, we elucidate the equations of motion for a harmonic oscillator as they pertain to scanned probe microscopy, including an intuition for the relaxation of a classical oscillator.

**Chapter 3** is structured in three parts. The first part discusses the design and construction of our MRFM apparatus including the fabrication of our custom nanopositioning system and rf electronics. We then discuss our CERMIT measurement and present and analyze the results. We conclude this chapter with a discussion of the second generation MRFM apparatus, pointing out specific design principles learned from our first probe. We then present preliminary data from this instrument concerning noise floors in frequency shift measurements. We conclude with CERMIT signal obtained with this apparatus and our first demonstration of coherent frequency modulation via a cyclic-CERMIT protocol. We end with conclusions and future directions.

**Chapter 4** begins our discussion of noncontact friction by providing the necessary background information. Previous experiments in the field are discussed as well as the connection between noncontact friction and MRFM. The relevance of noncontact friction to a variety of fields is established, and the broad importance of dielectric fluctuations is presented. We also present our preliminary observations with respect to noncontact friction in high sensitivity force microscopy.

**Chapter 5** outlines the custom dissipation microscope and cantilevers which were designed and constructed for the purpose of studying noncontact friction. General experimental considerations are made for the measurement of noncontact friction including methods of measuring noncontact friction and for determining the location of the sample surface.

**Chapter 6** presents experimental results establishing, for the first time, that dielectric fluctuations can result in noncontact friction. Additional measurements relevant to previous theoretical proposals for the mechanism of noncontact friction are also presented. Future directions and applications of this measurement are considered.

**Chapter 7** presents the theory of noncontact friction due to dielectric fluctuations explaining the data presented in Chapter 6. We show remarkable agreement between our measurements and a simple theoretical formalism we develop. Our formalism allows us to predict the noncontact friction due to dielectric fluctuations over any dielectric given only knowledge of the bulk dielectric response. Included in this presentation are limitations and assumptions of the proposed formalism and the estimations used to compare this theory to our experiments.

## CHAPTER 2

### THEORETICAL BACKGROUND

Here we present the basic theoretical framework for this thesis. These concepts will facilitate the presentation of MRFM and noncontact friction. This chapter is broken into two main parts. First, the necessary theory of nuclear magnetic resonance including the Bloch equations, adiabatic rapid passage, and relaxation theory. Second, the basic theory of cantilever dynamics and measurement including minimum detectable force and force-gradient concepts.

### 2.1 Nuclear Magnetic Resonance

We begin with a purely classical description of nuclear magnetic moments in an applied field, this will facilitate our discussion of the primary spin manipulation protocol in MRFM - adiabatic rapid passage. These basic NMR techniques are covered in detail in [42] and to a lesser degree in [43].

#### 2.1.1 Bloch Equations

The Bloch Equations are a classical, phenomenological explanation of the dynamics of a magnetic moment in an applied field. These equations contain no *explicit* spin-spin interaction, but such phenomenological approaches lend a great deal of intuition for how spins behave. This intuition is well suited for most MRFM experiments, but often breaks down when quantum mechanical properties of the spin ensemble become important.

We begin with the motion of an isolated dipole in an external magnetic field. This treatment is remarkable in that the motion of a classical dipole is very often a good approximation to the dynamics of the ensemble average of a large number of spins. For an ensemble of noninteracting spins, one may treat the motion of the ensemble average using this formalism. Assume that the dipole is fixed in space and that the field acts only to apply a torque to the dipole. We assume no explicit form of the external field. The equation of motion may be written as

$$\dot{\mathbf{L}} = \boldsymbol{\mu} \times \mathbf{H}(t). \quad (2.1)$$

Where  $\mathbf{L}$  is the angular momentum of the dipole due to the field and the dot denotes a derivative with respect to time. We know that the dipole moment  $\boldsymbol{\mu}$  is equivalent to the torque times the gyromagnetic ratio of the dipole in the field. Thus,

$$\dot{\boldsymbol{\mu}} = \boldsymbol{\mu} \times \gamma \mathbf{H}(t). \quad (2.2)$$

Now, suppose that the dipole is in a large static field and a smaller oscillating field perpendicular to the static field. The total field from equation 2.2 may be written in the following form

$$\mathbf{H}(t) = H_0 \hat{\mathbf{z}} + H_{1x} \cos(\omega t) \hat{\mathbf{x}}. \quad (2.3)$$

The oscillating term in equation 2.3, which is due to the applied radio frequency, may be decomposed into clockwise and counterclockwise rotating components. That is, we may write a linearly polarized wave as an equal superposition of circularly polarized waves. The second term on the right hand side of equation 2.3 becomes

$$\begin{aligned} H_{1x} \cos(\omega t) \hat{\mathbf{x}} &= H_1 [\cos(\omega t) \hat{\mathbf{x}} + \sin(\omega t) \hat{\mathbf{y}}] \\ &\quad + H_1 [\cos(\omega t) \hat{\mathbf{x}} - \sin(\omega t) \hat{\mathbf{y}}]. \end{aligned} \quad (2.4)$$

Notice that the two waves rotate in the opposite sense. One wave will rotate in the same sense as the precession of the spins in the static field while the other will rotate counter to it. The wave rotating counter to the spins will be far from resonance, therefore we exclude it. No generality is lost in this exclusion as the counter rotating wave differs from the properly rotating wave by only a negative sign. Thus, the analysis that follows may be easily repeated for the counter rotating wave. Also, notice that we have split the intensity of the linearly polarized wave in two while constructing the superposition; explicitly

$$H_{1x} = 2H_1. \quad (2.5)$$

Finally, we have

$$\mathbf{H}(t) = H_0 \hat{\mathbf{z}} + H_1 [\cos(\omega t) \hat{\mathbf{x}} + \sin(\omega t) \hat{\mathbf{y}}]. \quad (2.6)$$

Now, returning to equation 2.2 we have the following equation of motion for a spin in a static field being irradiated by a perpendicular oscillating field

$$\frac{d\boldsymbol{\mu}}{dt} = \boldsymbol{\mu} \times (\gamma H_0 \hat{\mathbf{z}} + \gamma H_1 [\cos(\omega t) \hat{\mathbf{x}} + \sin(\omega t) \hat{\mathbf{y}}]). \quad (2.7)$$

### 2.1.2 The rotating frame

We now transform to a frame of reference that rotates along with  $H_1$  about the  $\hat{z}$  axis. One can readily see that both the rotating field and the static field will be stationary in such a reference frame. In making this transformation, care must be taken in treating the rotation of the unit vectors in the stationary, or lab frame. The time evolution of the unit vectors in the lab frame is described by

$$\dot{\hat{x}} = \hat{x} \times \boldsymbol{\omega}. \quad (2.8)$$

Where  $\boldsymbol{\omega}$  is frequency of the rotating frame. We use  $\boldsymbol{\omega}$  here because we wish to use a frame which rotates at the frequency of the applied field. Furthermore, define the following notation:

$$\frac{\delta \boldsymbol{\mu}}{\delta t} = \hat{x} \frac{d\mu_x}{dt} + \hat{y} \frac{d\mu_y}{dt} + \hat{z} \frac{d\mu_z}{dt}. \quad (2.9)$$

Using both equation 2.8 and equation 2.9 we see that

$$\dot{\boldsymbol{\mu}} = \frac{\delta \boldsymbol{\mu}}{\delta t} + \boldsymbol{\omega} \times \boldsymbol{\mu}. \quad (2.10)$$

Using this relationship and the fact that the applied field in the rotating frame may be written as  $H_1 \hat{x}$ . We find the following expression for the equation of motion of a dipole

$$\dot{\boldsymbol{\mu}} = \boldsymbol{\mu} \times \left( (H_0 - \frac{\omega}{\gamma}) \hat{z} + H_1 \hat{x} \right). \quad (2.11)$$

Typically, we then define an effective field in the rotating frame as

$$\mathbf{H}_{\text{eff}} = (H_0 - \frac{\omega}{\gamma}) \hat{z} + H_1 \hat{x}. \quad (2.12)$$

Equation 2.11 describes the motion of a classical magnetic moment in a frame rotating with angular velocity  $\omega$ . The result is best understood graphically (figure 2.1). Using this we can reduce all of the spin dynamics to a simple classical vector equation as follows

$$\dot{\boldsymbol{\mu}} = \gamma(\boldsymbol{\mu} \times \mathbf{H}_{\text{eff}}). \quad (2.13)$$

Equation 2.13 is extraordinarily powerful in that it describes the motion of an ensemble of noninteracting spins under the influence of a resonant field. It can be shown that these dynamics follow the quantum mechanical expectation value of an ensemble of non-interacting spins.

### 2.1.3 Spin-lock

One common experiment which can easily be visualized in the classical rotating frame is the spin-lock. Imagine that a short pulse or rf irradiation is applied along  $\hat{x}$  in the rotating frame. If the pulse is of the appropriate duration the magnetization will precess in the  $y - z$  plane until it lies exactly along  $\hat{y}$ , this is called a  $\pi/2$  pulse. Note that if the phase of the rf irradiation is rapidly shifted by  $\pi/2$  the magnetization will lie along the rf field in the rotating frame. The magnetization is then said to be ‘locked’ along the applied rf field.

The magnetization that has been brought into the  $x - y$  plane by the  $\pi/2$  pulse is the Curie Law magnetization associated with  $H_0$ , which now lies along the much smaller field  $H_1$ . Intuitively, and correctly this is not an equilibrium situation. The magnetization will decay until it reaches a new Curie Law equilibrium associated with the much smaller field  $H_1$ . This relaxation process, called spin-lattice relaxation in the rotating frame, is discussed in section 2.2.2. Note that in the lab frame both the rf and the spin magnetization are rotating in the  $x - y$  plane at the Larmor frequency.

### 2.1.4 Adiabatic rapid passage

Adiabatic rapid passage is a technique for inverting magnetization by using continuous rf irradiation with the appropriate frequency modulation. This technique was originally used when NMR was a continuous wave (CW) technique, but has found wide application in MRFM. Notice that, if we turn on rf irradiation far from resonance (as is depicted in figure 2.1)  $\mathbf{H}_{\text{eff}}$  is nearly parallel to  $H_0$ . As the frequency of irradiation is increased towards resonance the  $H_0 - \frac{\omega}{\gamma}$  term

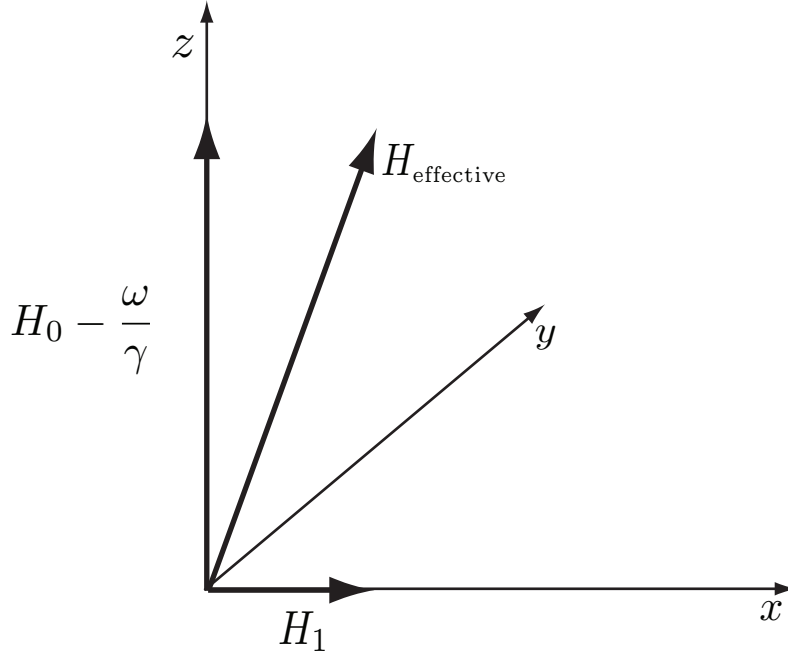


**Figure 2.1:** A schematic of the effective field,  $H_{\text{effective}}$ , in the rotating frame. Notice that the applied field ( $H_0$ ) is diminished by a factor proportional to the frequency of the rf irradiation. For the case shown here  $H_0 > \omega/\gamma$ , meaning that we are far from resonance. At resonance,  $H_0$  vanishes and  $\mu$  undergoes precession about  $H_1$  in the  $y-z$  plane.

in equation 2.12 begins to vanish, and  $H_{\text{eff}} \rightarrow H_1 \hat{x}$ . If we continue to increase  $\omega$  the effective field becomes large again, now in the  $-\hat{z}$  direction. It can be shown [42] that if the change in  $\omega$  is sufficiently slow the magnetization will follow the effective field. If this condition, called the adiabatic condition, is satisfied the magnetization will be inverted by the rf frequency sweep protocol just outlined. Rigorously, the adiabatic condition is given by

$$\frac{d\omega}{dt} \ll \gamma^2 H_1^2. \quad (2.14)$$

To gain an intuition for the adiabatic condition imagine that the rf frequency sweep just outlined is broken up into discrete steps. That is,  $\omega$  is stepped discretely from far below resonance to far above resonance. Prior to the rf being turned on the magnetization will be directed along  $\hat{z}$ . The rf is then turned on at frequency  $\omega_1$  (the first point in our frequency sweep) far below resonance and  $H_{\text{eff}}$  makes a small angle with the  $z$ -axis. The magnetization will then precess about  $H_{\text{eff}}$  as described by equation 2.2. This precession will happen on a cone around  $H_{\text{eff}}$  with an angle defined by (see figure 2.1):

$$\theta = \tan^{-1} \left[ \frac{H_1}{H_0 - \frac{\omega_1}{\gamma}} \right]. \quad (2.15)$$

It is clear that the closer  $\omega_1$  is to resonance the larger the angle  $H_{\text{eff}}$  will make with the  $z$ -axis and the larger cone of precession of the spins about  $H_{\text{eff}}$ . The adiabatic condition is essentially the statement that the frequency of the rf is changed slowly enough that the precession of magnetization about  $H_{\text{eff}}$  remains small, so that the bulk of the magnetization lies along the effective field.

Maintaining adiabaticity in frequency sweeps is a central issue in MRFM experiments. Equation 2.15 tells us that inverting nuclei of small gyromagnetic ratio requires slower frequency sweeps and larger  $H_1$  fields. Similarly, for a given nucleus, halving the frequency sweep time requires a four-fold increase in the rf field. This will become important when we consider generating rf fields in a cryogenic apparatus.

## 2.2 Relaxation

The equations of motion that we have described so far do not include relaxation. In any real system nuclei will experience dissipative interactions that cause them to diverge from their classical precession about the effective field. These interactions arise from a variety of sources, from dipole-dipole interactions with neighboring nuclei to magnetic interactions with electrons. Generally, the dominant interactions responsible for spin relaxation are sample specific and vary greatly between solids and liquids. [44, 45] Spin relaxation is the basis for much of what NMR can tell us about the dynamical properties of matter. In MRFM relaxation sets the time scale on which we can manipulate the spin magnetization and read-out those manipulations via the cantilever.

We will consider two formalisms of the theory of relaxation in NMR. The first simply heuristically adds relaxation terms to the classical equations of motion shown above. The second roughly outlines the calculation of transitions induced by field fluctuations present at the nucleus, this will require that we consider spins quantum mechanically.

### 2.2.1 Phenomenological relaxation

We can add intuitively reasonable terms to equation 2.11 to describe relaxation phenomenologically. To do this it is simplest to consider each vector component of equation 2.13. Using  $\mu = \{\mu_x, \mu_y, \mu_z\}$  we can add terms to each component to describe relaxation

$$\frac{d\mu_z}{dt} = -\gamma\mu_z H_1 + \frac{\mu_0 - \mu_z}{T_1}, \quad (2.16)$$

$$\frac{d\mu_x}{dt} = \gamma\mu_y(H_0 - \frac{\omega}{\gamma}) - \frac{\mu_x}{T_2}, \quad (2.17)$$

$$\frac{d\mu_y}{dt} = \gamma\left(\mu_z H_1 - \mu_x(H_0 - \frac{\omega}{\gamma})\right) - \frac{\mu_y}{T_2}. \quad (2.18)$$

The final terms in equations 2.16, 2.17 and 2.18 are responsible for relaxation. The final term in equation 2.16 is responsible for relaxation along the applied field  $H_0$ , this process is governed by the time  $T_1$ , known as the spin-lattice relaxation time. The relaxation time present in equations 2.17 and 2.18,  $T_2$ , causes any magnetization that persists in the  $x - y$  plane to ‘de-phase’ in time. This process is generally much faster than  $T_1$ , the reason for this will become apparent in the next section.

Exact solutions for the equations of motion including relaxation are possible under a variety of regimes. For example, where  $T_1 \gg T_2$  or  $T_1 = T_2$ . For the latter case, see appendix A.

### 2.2.2 Quantum mechanical relaxation

In general treating spin relaxation quantum mechanically is complex due to the many interactions for any given system and the resulting complicated Hamiltonian. Here we will give a rough sketch of the quantum mechanical method for calculating relaxation times, this will provide us with intuition for relaxation as it pertains to MRFM experiments. For a complete derivation of the effects discussed here see [42, 44].

To begin consider a spin Hamiltonian with two contributions.  $\mathcal{H}_0$  describes the externally applied fields (which will become static in the rotating frame) and  $\mathcal{H}_r(t)$  which describes the stochastic, time dependent field at the spin due to its interactions with the lattice. This portion of the Hamiltonian has zero mean,  $\langle \mathcal{H}_r(t) \rangle = 0$ . The total Hamiltonian is then,

$$\mathcal{H} = \mathcal{H}_0 + \mathcal{H}_r(t). \quad (2.19)$$

We can then write the time evolution of the density matrix,  $\sigma$  using the Liouville-von Neumann equation

$$\frac{d\sigma}{dt} = -i[\mathcal{H}_0 + \mathcal{H}_r(t), \sigma]. \quad (2.20)$$

We now transform into a quantum mechanical description in the rotating frame by applying the appropriate unitary rotation operators to  $\mathcal{H}$ . As with the classical case, this transformation removes the time dependence of the spin system due to  $\mathcal{H}_0$ , and is often called the interaction representation. For an arbitrary operator  $\mathcal{Q}$  this transformation is

$$\tilde{\mathcal{Q}} = e^{i\mathcal{H}_0 t} \mathcal{Q} e^{-i\mathcal{H}_0 t}. \quad (2.21)$$

Transformation of equation 2.20 [44] results in:

$$\frac{d\tilde{\sigma}(t)}{dt} = -i\langle[\tilde{\mathcal{H}}_r(t), \tilde{\sigma}(t)]\rangle, \quad (2.22)$$

where  $\langle \dots \rangle$  denotes an ensemble average over the system. Equation 2.22 can then be expanded to second order. We truncate the series at second order by assuming that  $\tilde{\sigma}(0)$  does not deviate significantly from  $\tilde{\sigma}(t)$ . This expansion is obtained by integrating equation 2.22 and recursively substituting the result into the remaining integral. This process is sometimes referred to as a Dyson expansion in the NMR literature. We assume that the correlation time of the fluctuations in  $\tilde{\mathcal{H}}_r(t)$  is short compared to the time over which we are considering changes in  $\tilde{\sigma}$ , this assumption allows us to drop the first order term in the expansion as it averages to zero. With some algebraic manipulations outlined elsewhere [44] we have the time dependence of the density matrix

$$\tilde{\sigma}(t) - \tilde{\sigma}(0) = - \int_0^t dt' \int_0^{t'} dt'' \langle [\tilde{\mathcal{H}}_r(t'), [\tilde{\mathcal{H}}_r(t'', \tilde{\sigma}(0)]] \rangle. \quad (2.23)$$

To move forward requires that we consider the explicit form of  $\tilde{\mathcal{H}}_r(t)$ . Most generally we can write

$$\mathcal{H}_r(t) = \sum_{\alpha} V_{\alpha} F_{\alpha}(t). \quad (2.24)$$

where  $V_{\alpha}$  is a general spin operator and  $F_{\alpha}(t)$  is a random function of time with zero mean. The  $V_{\alpha}$ 's are spin operators that oscillate at different frequencies in the interaction representation. In the interaction representation these spin operators become  $\tilde{V}_{\alpha} = e^{i\omega t} V_{\alpha}$ . Geometrically they correspond to spin operators with components orthogonal to  $\mathcal{H}_0$ , which cause a rotation of  $\sigma$  at time  $t_0$  corresponding to the magnitude of  $F_{\alpha}(t_0)$ . The sum in equation 2.24 adds the contribution of each of these operators in the interaction representation to the total stochastic portion of the Hamiltonian. This formalism serves to break the fluctuating field into components each inducing rotations of the density matrix in time as  $F$  fluctuates.

Since  $\langle \tilde{\mathcal{H}}_r(t) \rangle = 0$  it is clear that  $\langle F_{\alpha}(t) \rangle = 0$  and that correlations in  $F_{\alpha}(t)$  are the important quantity when considering relaxation. We define the associated correlation function as

$$\langle F_{\alpha}(t) F_{\beta}(t') \rangle = G_{\alpha\beta}(t - t'). \quad (2.25)$$

Putting these definitions into equation 2.23 and using the fact that the spectral density is the Fourier transform of the correlation function it can be shown that

$$\frac{d\tilde{\sigma}}{dt} \approx - \sum_{\alpha} [V_{\alpha}, [V_{\alpha}^{\dagger}, \tilde{\sigma}(0)]] J_{\alpha}(\omega_{\alpha}), \quad (2.26)$$

where  $J_{\alpha}$  is the spectral density of fluctuations resulting from the random function  $F_{\alpha}$ . To arrive at equation 2.26 requires several assumptions. First, this equation is valid only for time scales which are *both* slow compared to correlation time of the field fluctuations and fast compared to the time evolution of the density matrix.

Equation 2.26 gives us a route to calculating the time dependence of any physical variable of the spin system as a result of fluctuating fields being experienced by the ensemble. This is accomplished in the usual way, by tracing the operator with the density matrix as follows:

$$\frac{d}{dt} \langle \mathcal{Q} \rangle = \text{Tr}\{\mathcal{Q} \frac{d\tilde{\sigma}}{dt}\}. \quad (2.27)$$

For example, to calculate the spin-lattice relaxation time we would trace  $I_z$  with the density matrix, because spin-lattice relaxation refers to relaxation along the  $z$ -axis. By evaluating this trace it can be shown that the spin-lattice relaxation time scales with the fluctuating field spectral density at the Larmor frequency,

$$\frac{1}{T_1} \propto J(\omega_0). \quad (2.28)$$

Via a similar argument it can be shown that the spin-lattice relaxation time in the rotating frame, discussed in section 2.1.3 is proportional to field fluctuations at the Rabi frequency,  $\omega_{Rabi} = -\gamma H_1$ ,

$$\frac{1}{T_{1\rho}} \propto J(\omega_{Rabi}). \quad (2.29)$$

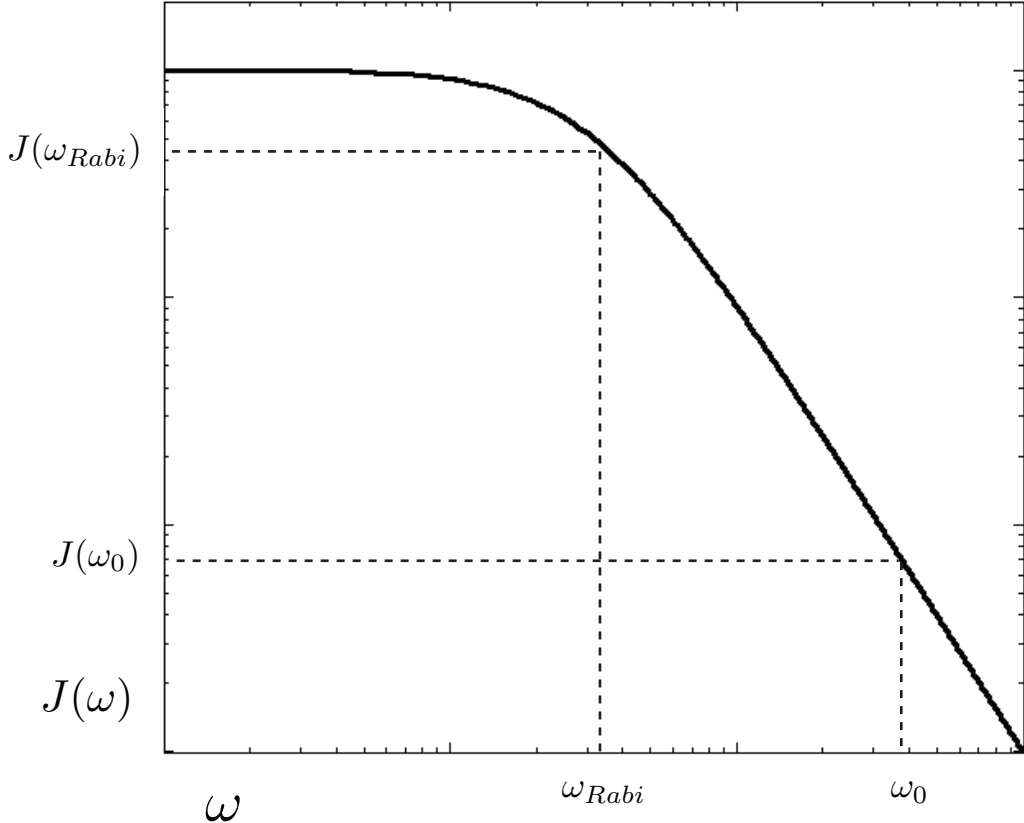


**Figure 2.2:** A sketch of a typical fluctuating field Lorentzian power spectrum. The Rabi  $\omega_{Rabi}$  and Larmor  $\omega_0$  frequencies are labeled, as are their corresponding field spectral densities. Note the log-log scale.

This would be obtained by setting the static Hamiltonian to  $I_x$ , which is the case in the presence of on resonance rf irradiation as outlined in section 2.1.3. To further build an intuition for how fluctuating fields effect various NMR relaxation times figure 2.2 sketches a typical fluctuating field power spectrum. A Lorentzian power spectrum is common, corresponding to processes with exponentially decaying correlation functions. By simply examining figure 2.2 and equations 2.28 and 2.29 it is clear that generally  $T_{1\rho} < T_1$ .

We are now in a position to consider relaxation of spin magnetization during an ARP sweep. Section 2.1.4 discussed the inversion of magnetization by sweeping the rf frequency through the spin resonance. In the rotating frame this amounts to sweeping the effective field from nearly along  $z$ , through the  $x$ -axis, and along  $-z$ . It is clear from the preceding argument that when the effective field is along  $z$  the relaxation will proceed as a  $T_1$  process, but when the magnetization is locked along  $H_1$  in the  $x$ -direction the relaxation proceeds as  $T_{1\rho}$ . One would intuitively expect that the relaxation time one would observe for an ARP sweep, sometimes called  $\tau_m$ , would be somewhere between  $T_{1\rho} < \tau_m < T_1$ . This intuition is correct, but in practice  $\tau_m$  is closer to  $T_{1\rho}$  than  $T_1$ .

Knowledge of the  $\tau_m$  relaxation time for the system under study is key to the success of MRFM measurements. If the applied ARP sweep takes a time longer than  $\tau_m$  then significant magnetization will fail to be inverted, reducing the signal. Still, as outlined in section 2.1.4 the slower the frequency sweep the more adiabatic, and therefore complete, the magnetization inversion. Finding a happy medium between spin relaxation and adiabaticity of inversion is an important factor in MRFM.

### 2.3 Cantilever dynamics

The force sensor used in most, but not all [37], MRFM experiments is a singly clamped beam. In many cases, the cantilever is fabricated from single crystal silicon. Such micromechanical oscillators are very well described as under

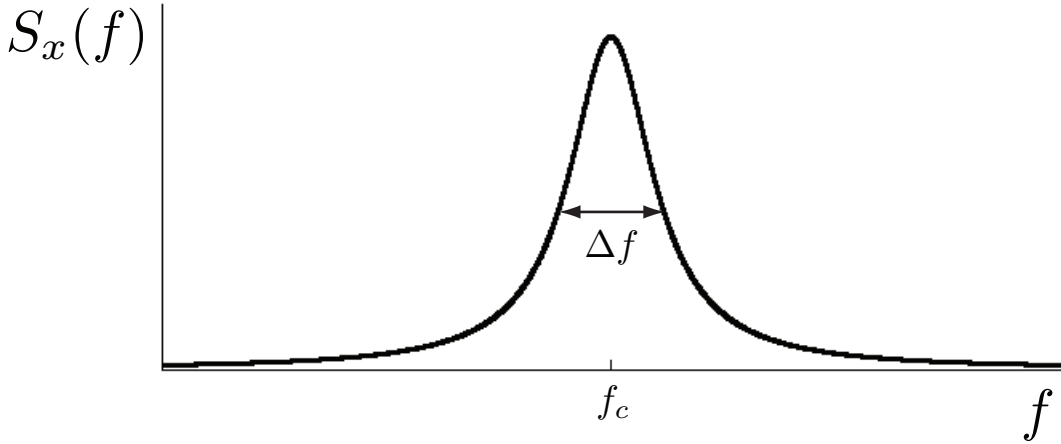


**Figure 2.3:** An analytical expression for the power spectrum of cantilever position fluctuations plotted versus frequency. The full width at half maximum (FWHM) of the Lorentzian peak centered at  $f_c$  is  $\Delta f$ . The power spectrum of position fluctuations has units of [ $\text{m}^2/\text{Hz}$ ]

damped simple harmonic oscillators. Here we summarize the formalism for understanding the dynamics of harmonic oscillators, and for understanding the thermomechanical noise limits in measuring small forces and shifts in fundamental frequency. We then discuss dissipation in these oscillators.

The cantilevers used in this thesis are, for small oscillations about equilibrium, well described as damped harmonic oscillators

$$m\ddot{x} + \Gamma\dot{x} + kx = F(t), \quad (2.30)$$

where  $m$  is the mass,  $\Gamma$  is the damping coefficient,  $k$  is the spring constant and  $F(t)$  is any time-dependent driving force. For all of the measurements described here, nonlinear contributions to the cantilever dynamics were found to be negligible. We begin with a simple and intuitive derivation of the minimum detectable force for a harmonic oscillator described by equation 2.30. We then discuss the minimum detectable frequency shift which is closely related to the minimum detectable force.

### 2.3.1 Minimum detectable force

To arrive at an expression for the minimum detectable force of a harmonic oscillator in contact with a bath we consider the random motion of the oscillator due to its interaction with the bath. The notion of minimum detectable force is the force required to cause a displacement equal to these random thermal fluctuations. To begin, we consider the power spectrum of the *position* fluctuations,  $S_x(f)$ . A note, in this section, as opposed to section 2.2.2 we will use frequency in units of cycles per second as opposed to radians per second. This facilitates direct comparison to measurements in the lab. It can be shown that the cantilever's position fluctuations will be a Lorentzian centered at the cantilever resonance frequency,  $f_c$ , as depicted in figure 2.3.

If the cantilever position fluctuations must obey Parseval's theorem [46, 47],

$$\langle x^2 \rangle = \int_0^\infty S_x(f) df \quad (2.31)$$

which relates the total power in  $S_x(f)$  to the rms fluctuations of the cantilever. Classical statistical mechanics also gives us a prediction for what these root-mean-square fluctuations should be. For any system where the energy is squared in a generalized coordinate and the sum over states in the partition function may be approximated as an integral, the equipartition theorem states

$$\frac{1}{2}k\langle x^2 \rangle = \frac{1}{2}k_B T \quad (2.32)$$

where  $k$  is the spring constant, and  $k_B T$  is the average thermal energy. By equating 2.31 and 2.32 we have

$$\int_0^\infty S_x(f) df = \frac{k_B T}{k}. \quad (2.33)$$

We can estimate the integral on the left hand side of equation 2.33 graphically as a rectangle of width  $\Delta f$  and height  $S_x(f_c)$ . The value of this integral can be related to the quality factor of the harmonic oscillator. The quality factor is a unitless measure of an oscillator's dissipation given by

$$Q = \frac{f_c}{\Delta f} = \frac{k}{2\pi f_c \Gamma}. \quad (2.34)$$

Combining these two facts with equation 2.33 we have

$$S_x(f_c) = \frac{Qk_B T}{kf_c} = \frac{k_B T}{2\pi f_c^2 \Gamma}. \quad (2.35)$$

The second equality amounts to a fluctuation-dissipation theorem for the harmonic oscillator, relating the dissipation experienced by the oscillator,  $\Gamma$ , to the position fluctuations of that oscillator,  $S_x(f_c)$ . We note that this is completely analogous to the Einstein relation for a free particle, where the diffusion constant  $D = k_B T / \Gamma$ . This relationship is discussed in detail in chapter 4.

In order to calculate the minimum detectable force for a harmonic oscillator we need to connect the position fluctuations experienced by the oscillator to the force fluctuations which are responsible. To do this we first assume that the force fluctuations arising from the bath are white, that is they have a constant power spectrum out to a frequency much higher than  $f_c$ . We then need a constant of proportionality between position fluctuations and force fluctuations. By units analysis, we have

$$S_F(f) = \frac{k^2}{Q^2} S_x(f) \quad (2.36)$$

where  $S_F(f)$  is the spectral density of force fluctuations having units of  $N^2/\text{Hz}$ . By the white power spectrum assumption we know that  $S_F(f)$  is a constant at all frequencies. Plugging equation 2.36 into equation 2.35 we find

$$S_F = \frac{kk_B T}{Qf_c}. \quad (2.37)$$

Any measurement must occur in some finite bandwidth,  $b$ . For a fixed bandwidth measurement the minimum detectable force is then given by

$$F_{min} = \sqrt{S_F b} = \sqrt{\frac{kk_B Tb}{Qf_c}}. \quad (2.38)$$

We refer to equation 2.38 as the thermally limited force sensitivity of the cantilever.

### 2.3.2 Minimum detectable frequency shift

In OSCAR and CERMIT the spin signal is present as a small frequency shift in the cantilever's fundamental frequency,  $f_c$ . Therefore, we will also be interested in the minimum detectable frequency shift for a cantilever. A rigorous derivation of the minimum detectable frequency shift for a harmonic oscillator subject to white thermal noise can be found in the literature [48], here we present only an intuitive argument.

Cantilever frequency shifts in MRFM experiments are due to small changes in the cantilever's spring constant,  $k$ , related to the frequency by

$$f_c = \sqrt{\frac{k}{m}}. \quad (2.39)$$

Consider a small change in the fundamental frequency,  $\delta f$ , due to a small change in the spring constant,  $\delta k$ ,

$$f_c + \delta f = \sqrt{\frac{k + \delta k}{m}}. \quad (2.40)$$

The right hand side of equation 2.40 can be expanded and truncated to first order resulting in,

$$\frac{\delta f}{f_c} \approx \frac{\delta k}{2k}. \quad (2.41)$$

Small changes in frequency are therefore proportional to small changes in spring constant. We have related the minimum detectable frequency shift to the minimum detectable change in spring constant. The spring constant has units of N/m, which is a force-gradient. For a harmonic oscillator the spring constant is a measure of the curvature of the harmonic potential. So a frequency shift measurement is a measurement of the curvature of the oscillator's potential. In frequency shift detection we self oscillate the cantilever to some pre-set amplitude and fit the sinusoidal displacement in time to determine the frequency. It is intuitive that the larger this amplitude of oscillation the better the measurement of the curvature of the potential, and therefore the lower the minimum detectable frequency shift. By this intuition, and examining the units we claim that:

$$\delta k_{min} = \frac{F_{min}}{x_{rms}} \quad (2.42)$$

where  $x_{rms}$  is the rms oscillation amplitude of the cantilever. Using this with equations 2.38 and 2.41 we have:

$$\delta f_{min} = \sqrt{\frac{f_c k_B T b}{x_{rms}^2 Q k}}. \quad (2.43)$$

### 2.3.3 Relaxation of a classical oscillator

Equation 2.38 can be rewritten in terms of friction experienced by the cantilever as,

$$F_{min} = \sqrt{4\Gamma k_B T}. \quad (2.44)$$

where  $\Gamma$  is the friction experienced by the oscillator. From equation 2.44 it is clear that for force or force-gradient measurements the cantilever's friction sets the thermomechanical limits on sensitivity. There are typically two contributions to the friction experienced by the cantilever, intrinsic friction ( $\Gamma_0$ ) due to coupling between the cantilever motion and internal degrees of freedom of the oscillator or the environment. The cantilever may also experience surface induced noncontact friction ( $\Gamma_s$ ) due to interactions between the cantilever tip and the nearby surface in an experiment. These two contributions are additive

$$\Gamma = \Gamma_0 + \Gamma_s. \quad (2.45)$$

For most MRFM experiments to date the second term in equation 2.45 has been dominant. The second half of this thesis discusses the concept of noncontact, surface induced friction in detail. For a rigorous derivation of how friction effects the dynamics of a classical oscillator see appendix B.

## CHAPTER 3

### FORCE-GRADIENT DETECTED NUCLEAR MAGNETIC RESONANCE

This chapter discusses successful experiments in force-gradient detected nuclear magnetic resonance. [11] The chapter is structured as follows. First, we present the basic idea of the experiment and a comparison with OSCAR. We then present the custom instrument focusing on the nanopositioning and radiofrequency components. Third we present the results from the experiment. Finally the design and construction of a second generation apparatus is outlined, as well as noise measurements and the successful detection of NMR. We also present preliminary results for a coherent version of our CERMIT protocol.

#### 3.1 Force-gradient detection

As discussed in chapter 1 this thesis presents an entirely new, general, route to detecting magnetic resonance. CERMIT measures magnetic resonance as a change in the mechanical spring constant of the cantilever. In CERMIT we operate the cantilever in the perpendicular geometry, as discussed previously this facilitates the use of low spring constant cantilevers. For a homogeneous distribution of spins the net force on the cantilever in the direction of motion will be zero in this geometry. This leads us to consider equation 1.1 more carefully. As before assume that the spins are polarized along  $z$ , but now consider the term resulting in a force in the  $x$  direction, which in the perpendicular geometry is the direction of cantilever motion. The force in this direction is:

$$F_x = \mu_z \frac{\partial B_x}{\partial z}. \quad (3.1)$$

Using the Maxwell equation  $(\nabla \times B)_y = 0$  we can rewrite equation 3.1 in terms of derivatives with respect to  $x$ . We may then take a derivative of the force acting on the cantilever with respect to  $x$  arriving at a force-gradient:

$$\frac{dF}{dx} = \mu_z \frac{\partial^2 B_z}{\partial x^2} + \frac{\partial \mu_z}{\partial x} \frac{\partial B_z}{\partial x}. \quad (3.2)$$

The first term in equation 3.2 is nonzero governs signal in a CERMIT experiment. A schematic of the experiment is shown in figure 3.1. We invert nuclei below the tip using an adiabatic rapid passage, the inverted magnetization interacts with the second derivative of the tip field resulting in a force-gradient on the cantilever and therefore a frequency shift. The cantilever frequency then decays to its previous value in a time  $T_1$  as the inverted nuclei repolarize along the applied field. The second term in equation 3.2 contributes an additional frequency shift which is observed in the OSCAR experiment. This term requires that the spin magnetization change with the motion of the oscillator and therefore can be neglected in a CERMIT experiment. [49]

We can formalize the spring constant change which occurs in a CERMIT experiment as shown in figure 3.1 as,

$$\delta k = \sum_i \mu_z(\mathbf{r}_i) \frac{\partial^2 B_z(\mathbf{r}_i)}{\partial x^2}. \quad (3.3)$$

where the sum over  $i$  runs over all spins inverted by the ARP sweep. As shown in figure 3.1 the frequency shift induced by spins interacting with the second derivative of the tip field will last for a time  $T_1$  as the spins repolarize along the applied field. The signal in a CERMIT experiment therefore lasts for  $T_1$ . This is the central strength of CERMIT detection. Where most techniques, such as OSCAR, rely on cyclic ARP's at the cantilever frequency where the detection time is set by  $\tau_m$ , CERMIT detects the inverted nuclei for a time  $T_1$ . As shown in figure 2.2,  $T_1$  will generally be longer than  $\tau_m$ , this fact makes CERMIT more widely applicable. In addition, since we need not continually manipulate the spin magnetization during detection the rf duty cycle will be significantly lower for a CERMIT experiment than for experiments that require constant rf irradiation such as cyclic ARP's. A lower rf duty cycle dramatically reduces the heat load placed on cryogenic probe. This is critical since rf heating has been shown to be sensitivity limiting in nuclear MRFM experiments. [17]

##### 3.1.1 Signal to noise

We can make a simple extension of the formalism outlined in chapter 1 to estimate the signal in a CERMIT experiment. Again, the rough estimate here serves not as a precise calculation but as a guideline for experiments. From equation 3.3 we require an estimate for the second derivative of the field from the tip over the region of inverted magnetization.

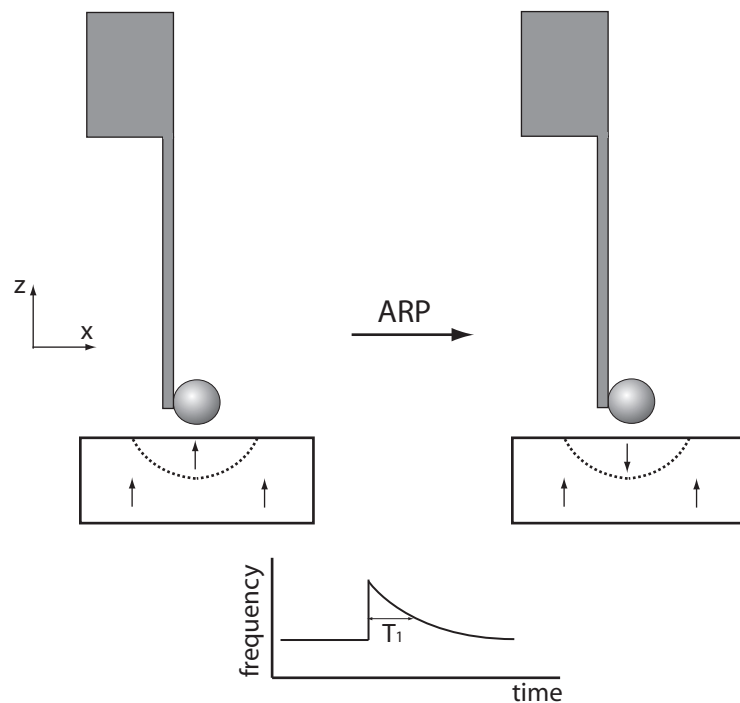


**Figure 3.1:** Schematic of the CERMIT experiment. The cantilever moves parallel to the sample in the  $x$  direction. The cantilever is self oscillated using positive feedback. The spins directly below the cantilever are inverted using an ARP sweep generated by an rf coil (not shown). Upon inversion, the cantilever experiences a frequency shift due to the first term in equation 3.2. The cantilever frequency then relaxes back to its value prior to the ARP sweep in a time  $T_1$  as shown.

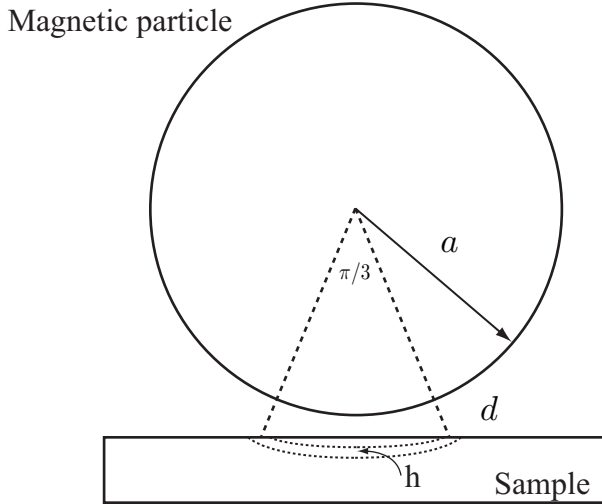


**Figure 3.2:** Magnetic particle of radius  $a$  a distance  $d$  away from the surface of the sample. The inverted region of the sample has a thickness  $h$  and is subtended by an arc of length  $\pi/3$  about the center of the magnet.

For a sphere of radius  $a$  the second gradient a distance  $d$  below the tip is given by

$$\frac{\partial^2 B_z}{\partial x^2} = \frac{16\mu_0 M}{a^2} \left( \frac{a}{a+d} \right)^5. \quad (3.4)$$

Assume that the inverted region of space is approximately a spherical shell. To estimate the volume of that spherical shell, illustrated as the region enclosed by dotted lines in figure 3.2, consider the gradient at the center of the region of inversion. Here we must consider the gradient in the  $z$  direction given by equation 1.7. First, assume that the shell is approximately a distance  $d$  from the tip. The thickness of the shell will be given by the width of the ARP sweep, converted to units of field using the gyromagnetic ratio, divided by the gradient. Define the width of the ARP sweep as  $\Delta\omega/\gamma$ . Then the slice thickness  $h$  will be

$$h = \frac{\Delta\omega}{\gamma \partial B_z / \partial z}. \quad (3.5)$$

To get a volume we need to estimate the area of the sphere on which the inverted region lies. For a region like the one sketched in figure 3.2 this area will be approximately  $\pi(a+d)^2$ . The total magnetization in the inverted region will then be the volume of the inverted region times the magnetization density, which in this approximation can be written as

$$\mu_z = \rho_m \pi (a+d)^2 \frac{\Delta\omega}{\gamma \partial B_z / \partial z}, \quad (3.6)$$

where  $\rho_m$  is the magnetization density as before. Plugging this into equation 3.3, using equation 1.7 and 3.4 and assuming that the second derivative of the field is approximately constant over the region of inverted magnetization we arrive at an estimate for the spring constant change due to the nuclei inverted by the ARP

$$\delta k = 8\pi(a+d) \frac{\Delta\omega}{\gamma} \rho_m. \quad (3.7)$$

It is important to put this result into context. This is not intended as a scaling law, as approximations will break down under certain regimes, such as small magnets with large regions of inverted magnetization. Still, it does allow us to obtain very quick rough estimates of the expected signal given an experimental set of parameters. Note that this calculation is also only valid for the situations where the polarizing field is applied along the length of the cantilever, the  $z$  direction if figure 3.1. To consider other geometries we need only to modify equation 3.4.

### 3.1.2 Comparison to OSCAR

We can briefly compare the expected SNR in a CERMIT experiment to the OSCAR protocol. The simplest way to obtain a reliable comparison is to juxtapose these two methods in the single spin limit. Briefly, OSCAR works by

inducing a cantilever frequency shift due to interactions with the spins. Rather than applying ARP sweeps to invert the nuclei, OSCAR inverts magnetization by exploiting the cantilever motion to sweep the effective field in the rotating frame. If the rf is on at a fixed frequency a spin at a fixed point in space will see the effective field swept from above resonance to below resonance as the cantilever moves through half a cycle. [33] OSCAR exploits the second term in equation 3.2, using the spin magnetization to create a position dependent force on the cantilever. While the rf is on, the spins remain locked to the cantilever motion for a time  $\tau_m$  as discussed previously. The spring constant change in an OSCAR experiment is given by

$$\delta k_{\text{OSCAR}} = \frac{4\mu_s}{\pi x_{pk}} \frac{\partial B_z}{\partial x}, \quad (3.8)$$

where  $x_{pk}$  is the peak displacement of the cantilever and  $\mu_s$  is the magnetic moment of the spin. [32] It is important to note that the derivative  $\partial B_z/\partial x = 0$  at a point directly below the tip. The gradient is symmetric with respect to the cantilever motion in the  $x$  direction. Therefore, OSCAR requires either a spatial asymmetry in the spin distribution below the tip, or statistical fluctuations in magnetization which result in a detectable difference between the magnetization to the left and the right of the cantilever equilibrium position in the direction of the cantilever motion.

The gradient important for OSCAR is given by

$$\frac{\partial B_z}{\partial x} = \mu_0 M a^3 \left( \frac{3x}{(x^2 + (a+d)^2)^{5/2}} - \frac{15(a+d)^2 x}{(x^2 + (a+d)^2)^{7/2}} \right), \quad (3.9)$$

where  $x$  is the lateral distance between the center of the magnet and the spin,  $a$  is the magnet radius as before and  $d$  is the distance from the magnet to the spin in the vertical direction (figure 3.2). A numerical maximization of the gradient can then be used to find the optimal position for a single spin with respect to the equilibrium position of the cantilever given a fixed distance between the tip magnet and the spin in the  $z$  direction ( $d$ ). We find that  $\partial B_z/\partial x$  is a maximum for  $a = 3d$  and  $x \approx 1.5d$ , where  $x$  is the lateral distance from the center of the magnet to the location of the spin. For these values equation 3.8 simplifies to

$$\delta k_{\text{OSCAR}} = -0.288 \mu_s \frac{\mu_0 M}{\pi x_{pk} d}. \quad (3.10)$$

We can then divide this quantity by the thermally limited noise equation 2.42 to achieve a single spin SNR for the OSCAR protocol of

$$SNR_{\text{OSCAR}} = 0.288 \mu_s \frac{\mu_0 M}{\pi d F_{\min}}. \quad (3.11)$$

A minus sign has been dropped for clarity. Note that the SNR for OSCAR does not scale with the drive amplitude of the cantilever.

We can undertake a similar analysis for CERMIT. Here the second gradient of the field is important which is maximized directly below the tip. At this point the second gradient is given by equation 3.4. The second derivative obtains a maximum for  $a = 3d/2$ . At this value the spring constant change is given by

$$\delta k_{\text{CERMIT}} = 0.55 \frac{\mu_s \mu_0 M}{d^2}. \quad (3.12)$$

We calculate the signal to noise in the same fashion

$$SNR_{\text{CERMIT}} = 0.55 \mu_s \frac{\mu_0 M x_{pk}}{d^2 F_{\min}}. \quad (3.13)$$

A direct comparison can now be made between OSCAR and CERMIT by dividing the signal to noise ratios for each. Noting that each SNR calculation assumes an optimized tip radius which will not be the same for both techniques, we have

$$\frac{SNR_{\text{CERMIT}}}{SNR_{\text{OSCAR}}} = 2\pi \frac{x_{pk}}{d}. \quad (3.14)$$

Equation 3.14 is greater than one, making CERMIT advantageous, for  $x_{pk}/d > 1/6$ . For larger cantilever amplitudes, and single spin measurements, CERMIT achieves a larger SNR than OSCAR. At small cantilever oscillations OSCAR provides greater sensitivity than CERMIT by virtue of the fact that OSCAR SNR is independent of drive amplitude. Note also that we are assuming that spin inversion is completely adiabatic. In addition, for a fixed separation  $d$  an optimized

tip for CERMIT is smaller by a factor of 2. We know empirically that smaller tips experience smaller noncontact friction conferring an additional advantage to CERMIT.

Ultimately a comparison between techniques requires some empirical knowledge which cannot be captured in analytical scaling laws such as equation 3.14. For example, if the adiabatic condition is more difficult to satisfy for one technique than the other then increased  $H_1$  will be necessary at the expense of increased probe heating. As discussed below,  $1/f$  frequency noise will require coherent spin signals. OSCAR is readily amenable to producing coherent spin signals using the interrupted-OSCAR protocol. Preliminary results for coherent versions of the CERMIT are presented here but will require further improvement. In addition, the bandwidth of the measurement will be set by the dominant spin relaxation time for the detection scheme chosen. For some samples, such as  $\gamma$ -irradiated quartz, this will not be a major restriction for either detection protocol, but for real samples may afford CERMIT an additional advantage.

Having established a theoretical basis for force-gradient detected NMR by the CERMIT protocol we now discuss the experimental apparatus.

### 3.2 Apparatus design

One challenge of designing and constructing an MRFM apparatus is obtaining reliable alignment between the cantilever, fiber, coil and sample under cryogenic conditions. The most stringent alignment requirement is between the 20 $\mu\text{m}$  pad on the cantilever and the optical fiber used to detect cantilever displacement. Also, alignment typically must be attainable by hand, not requiring elaborate motors or external motion control. Once this alignment can be obtained the reliability of each subsystem must be established. Common problems such as rf failure, sample cracking or a motionless nanopositioner will cause experimental failure. Here we discuss the design of a proof of concept probe used to demonstrate the CERMIT technique.

The custom built probe used to demonstrate CERMIT is shown in figure 3.3. The geometry of this probe was chosen such that the applied magnetic field exerted no torque on the cantilever due to the tip magnet. [50] This was accomplished as shown in figure 3.4 by aligning the magnetic moment of the tip magnet with the width of the cantilever. This geometry is crucial since in the initial experiment we use a large, 10 $\mu\text{m}$  tip magnet which will interact strongly with the applied field in any other geometry. This geometry also avoids field induced dissipation which results from changing flux through the cantilever over a cycle of oscillation. This dissipation, of unknown origin can reduce the cantilever  $Q$  by a factor of 10 or more. [51]

The superstructure of the probe is outlined elsewhere. [47] Briefly, the probe was mounted on stainless steel vacuum lines, supported by blackbody radiation shielding baffles, and placed in the bore of a 9T swept field superconducting magnet. The swept field magnet resided in a 90 liter liquid helium dewar. All optical and electric connections passed through these vacuum lines to a small chamber which supported the vacuum lines and sits atop the dewar. The chamber contained feedthroughs for all optical and electrical signals. The probe contained two optical fibers, one for interferometric detection of cantilever displacement and the other to monitor the nanopositioning system's motion. The components of the apparatus are now discussed in turn.

A detailed view of the experiment is shown in figure 3.3 (c). The custom built nanopositioner allowed the sample to be placed within a few nanometers of the cantilever tip as discussed below. Electrical contact was maintained with the sample, typically with a silver painted wire, which was electrically isolated from the rest of the probe by a small piece of sapphire. The rf coil was placed a few hundred microns away from the cantilever as shown in figure 3.3 (c). The rf coil was part of a tuned and matched tank circuit which was assembled on a printed circuit board discussed below. The cantilever was aligned to an optical fiber and affixed using either 5 minute epoxy or super glue. A wire was silver painted to the back of the cantilever die supplying electrical contact. A wire for capacitive driving of cantilever motion was glued to the printed rf circuit board and pointed at the cantilever. A small oscillating voltage applied between this wire and the cantilever excited cantilever motion capacitively. The wire needed only be within a few millimeters to excite motion with voltages of about 100mV. The coil and fiber were manipulated spatially using kinematic mounts discussed elsewhere. [47] These mounts were not found to be effective in aligning various components of the experiment as they did not provide sufficient range of motion. In addition, the three orthogonal directions of motion in a kinematic mount as designed here were strongly coupled, making precise alignment very difficult. As discussed below, the fiber was originally designed to be aligned using a kinematic mount but this was found to be unreliable when cooling.

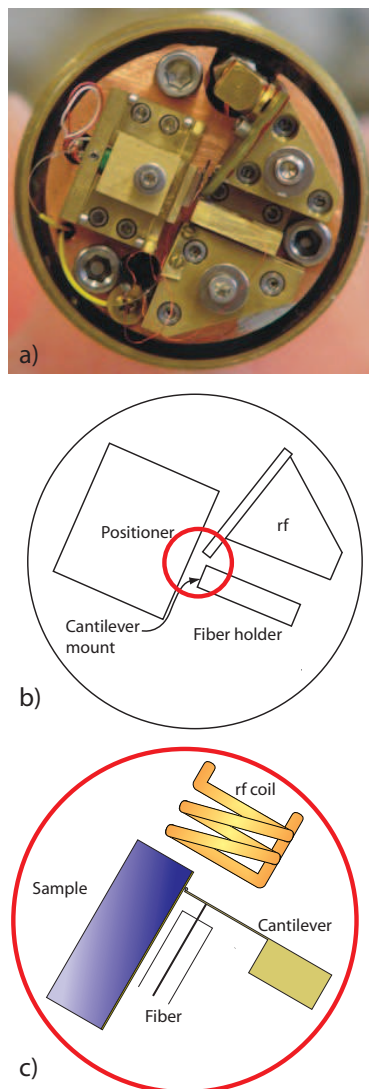


**Figure 3.3:** First generation CERMIT probe. a) Photograph of the probe. All components custom machined from brass are mounted on an OHFC copper plate. The OHFC plate is in direct contact with the liquid helium in the cryostat. The applied field is directed into the page. b) Labeled outline of components pictured in a). Details of each component are discussed in the text. c) Close-up schematic of region emphasized by the red circle in b). Note that the motion of the cantilever occurs in a plane perpendicular to the direction of the applied field. The entire setup is enclosed by a  $7^\circ$  grease seal can.

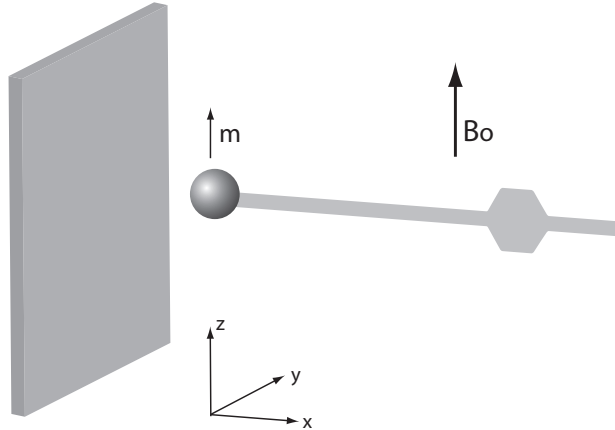


**Figure 3.4:** A schematic of the magnet parallel to width geometry. The magnetic moment of the tip magnet is parallel to the width of the cantilever ( $z$  direction). The cantilever oscillation occurs in the  $\pm y$  direction. The applied field is along  $z$ . In this geometry  $m \times B_0 = 0$  regardless of cantilever position, resulting in no torque on the cantilever due to the applied field. In addition, flux through the cantilever shaft has been shown to induce field dependent cantilever dissipation of unknown origin, this source of dissipation is not present in the magnet parallel to width geometry as discussed in the text.

### 3.2.1 Nanopositioner

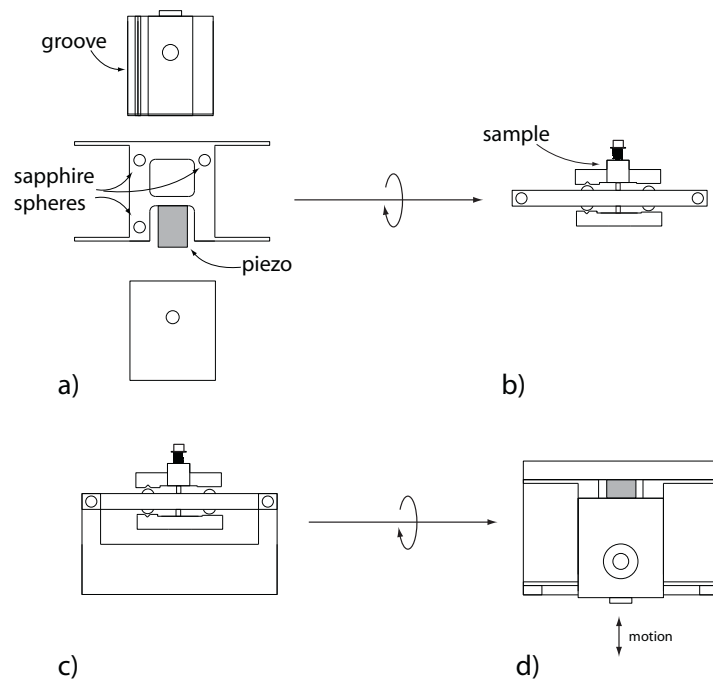
A schematic of the custom machined nanopositioning system used in the experiment is shown in figure 3.5. This design was taken from a previous one in our group [52] but was adapted to operate perpendicular to gravity. The positioner used a stick-slip principle which is discussed in detail elsewhere. [53] Briefly, a sawtooth voltage pulse was sent to the piezo ceramic element. On the slower rising edge of the pulse the piezo extended against the spring feet of the part shown in the center of figure 3.5 (a). Due to the slow piezo extension the two plates which are spring loaded move with the center piezo actuated part. This is referred to as the stick phase of the motion. On the rapid falling edge of the sawtooth the piezo motion was too rapid for the spring loaded plates to move with the center part, the friction between the sapphire spheres and the brass plates is overcome, and they slide on the sapphire spheres shown in figure 3.5 (a)-(d). This is the slip phase of the motion. The net result is forward motion of the plates which are spring loaded about the center part.

Figure 3.6 shows typical performance for this positioner at cryogenic temperatures. Considerable time was spent adjusting the spring loaded tension on the sliding plates to achieve optimal performance. Piezo ceramic elements like those discussed in [52] were used. Piezos were rated to 150V (Thorlabs), and appeared to degrade over a period of 6 months. Positioner performance was found to depend highly on the condition of the sliding surfaces. Extra care was taken in machining the groove and flat. Sliding surfaces were found to improve dramatically upon careful polishing with Wenol metal polish. Polishing was accomplished by spreading a small amount of Wenol on a piece of paper laid on a hard flat metal surface. By rubbing the sliding surfaces of the brass parts on the piece of paper coated with Wenol very uniform polishing was obtained.

The positioner typically operated with  $\sim 10$ V pulses at room temperature,  $\sim 40$ V pulses at 77K and  $\sim 80$ V pulses at 4K. Steps as small as 8nm were achieved at all temperatures. Larger voltage pulses could be used resulting in larger step sizes as shown in figures 3.6 (b) and (c). Sample heat sinking was done by running a 0.005 inch thick strip of copper from beneath the sapphire plate on which the sample is mounted to the 4K copper plate on which the positioner was mounted.

### 3.2.2 Radio frequency electronics

As discussed previously efficient generation of radio frequency fields for MRFM is a challenge. Intense fields must be generated to overcome the internal spin Hamiltonian experienced by nuclei in solids. High intensity fields are often accompanied by heating especially when generated by flowing current through resistive metals. In addition, MRFM places severe space restrictions on the design of rf circuitry as the rf coil must be positioned within a few hundred microns of the cantilever, fiber and sample.



**Figure 3.5:** The custom nanopositioning system used in CERMIT. a) Three components which makeup the positioner all custom machined from brass. The center part was actuated by a piezo. Three 1/16 inch holes each had a pair of sapphire spheres press fit into them. These spheres then protrude from this part and provide sliding points for the other two parts which are spring loaded as shown in b). The spring loading shown in b) forced the two aligned sets of sapphire spheres to ride in the groove labeled in a). The remaining sphere slid on a polished surface. The spring loaded parts are mounted in a holder which occupied the position labeled in figure 3.3 (b). The direction of motion for the positioner is labeled in d).

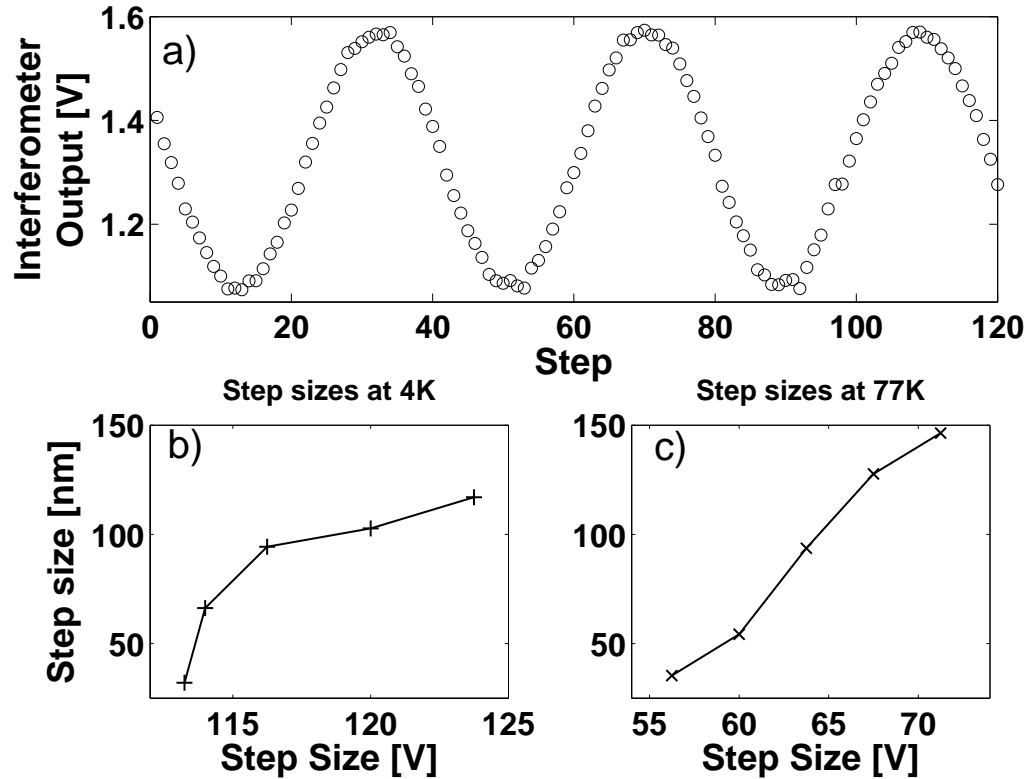


**Figure 3.6:** Characterizing the nanopositioner at low temperature. a) Interferometrically detected steps at 80K. The wavelength of the laser was 780nm, making the distance between each peak 390nm. The steps were approximately 8nm each. Details of the interferometer are discussed in [54]. b) Step size characterized at 4K as a function of peak voltage of the pulse sent to the piezo. c) Step sizes characterized at 77K.

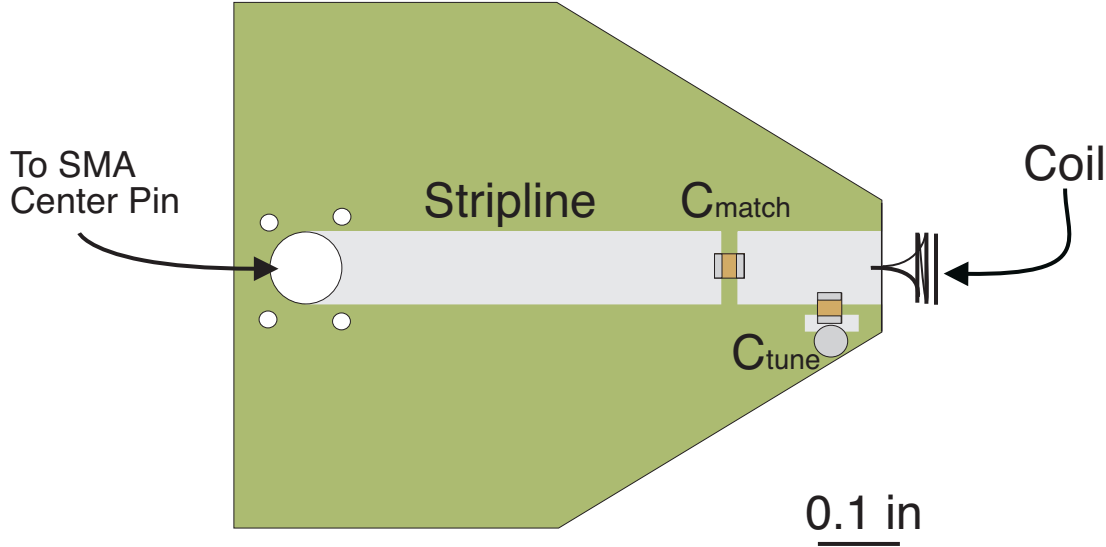


**Figure 3.7:** rf tank circuit. The printed circuit board contains holes drilled for SMA connector attachment to a microstripline. The match capacitor was in series with the stripline. The tune capacitor was in parallel with one side soldered to a via which maintains electrical connection to the ground plane. The board was FR-4 laminate from [www.pcbexpress.com](http://www.pcbexpress.com) with a 1MHz relative dielectric constant  $k$  of 4.4 at room temperature. The matching and tuning capacitors were soldered in by hand. The backside of the board was a ground plane. The coil diameters ranged from 200 – 600 $\mu\text{m}$ .

A previous design [47] featured a  $\lambda/2$  line to remove tuning and matching capacitors from the neighborhood of the cantilever. This design did not perform satisfactorily, generating only  $4.7 \text{ G}/\sqrt{\text{W}}$  in the rotating frame as determined by nuclear spin nutation experiments. Microcoils have been used in conventional NMR experiments for some time. [55–58] To improve our system, we adapted a design from the literature [59–61] using microstriplines on printed circuit boards to make the entire rf circuit compact and easy to assemble.

A schematic of the rf tank circuit is shown in figure 3.7. A parallel-tune series-match circuit was employed. In this configuration the inductance of the coil and the tuning capacitor act as a harmonic oscillator, and this portion of the circuit is often referred to as the “tank.” The matching capacitor is used to adjust the input impedance of the tank circuit to the characteristic  $50\Omega$  necessary for efficient coupling to rf electronics. The resonance frequency of a parallel tuned tank circuit is given by:

$$\omega_0 = \frac{1}{\sqrt{C_t L}}, \quad (3.15)$$

where  $L$  is the inductance of the coil and  $C_t$  is the capacitance of the tuning capacitor. The tank circuit behaves as a harmonic oscillator with  $Q = \omega_0 L / r$  where  $r$  is the resistance of the coil. The tuning capacitor was a Panasonic 0402 ceramic chip capacitor (Digikey). The matching capacitor  $C_m$  was a mica chip 0805 multilayer capacitor (Digikey). Using the mica capacitor in the matching position was critical for low temperature reliability of the tank circuit as ceramic capacitors failed upon thermal cycling. The reason for the reliability of ceramic capacitors in the tuning position, but not in the matching position remained unknown. The stripline width was calculated using a formalism from the literature [61] to obtain a  $50\Omega$  characteristic impedance with the ground plane. Coupling to the stripline was achieved using a  $50\Omega$  SMA connector soldered into the printed circuit board containing the stripline.

Typically, in an NMR experiment the tuning and matching capacitors are adjustable allowing precise setting of the coil resonance frequency and careful matching. In this design this was not possible since manual tuning would require mechanical access to the capacitors and would not allow the use of small ceramic and mica capacitors. Tuning was not a problem since we operated in a swept field magnet, which allowed the applied magnetic field to be set to the field appropriate for the coil frequency. Therefore, the coil needed only be tuned to a frequency corresponding to a field below 9T for the nucleus under study. Still, we needed to match the tank circuit to  $50\Omega$ . This was done by trial and error. A rule of thumb for matching circuits at room temperature is  $C_m \sim 0.1 C_t$ . Since we desired the circuit to be matched at 4K this rule of thumb did not generally apply to this circuit. Experience dictates that a circuit which is 50% under matched

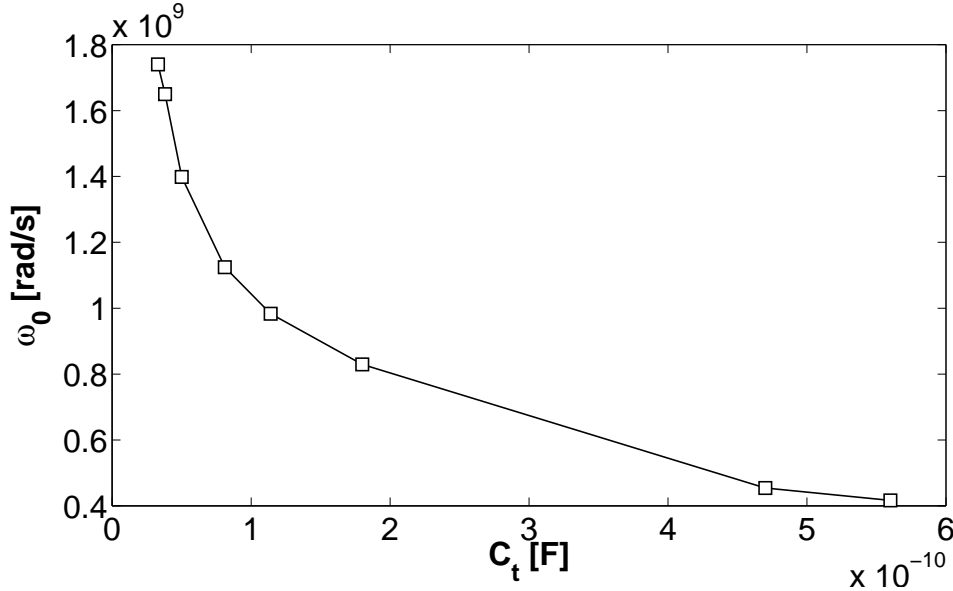


**Figure 3.8:** Tank resonance frequency versus  $C_t$  for a 3 turn 500 $\mu\text{m}$  diameter coil wound from 25 $\mu\text{m}$  thick copper wire. Fitting this data to equation 3.15 an inductance of 9.7nH was extracted. The calculated inductance for these parameters was 5.1nH. The difference between calculated and measured inductance is likely due to stray inductance associated with the legs of the coil that are soldered to the circuit board as discussed in the text.

at room temperature will be approximately matched at 4K. By under matched we mean that the matching improves upon cooling. Trial and error matching was done rapidly by soldering match capacitors onto the printed circuit board and dunking the entire circuit directly into liquid nitrogen while connected to an rf sweeper (Morris, model 505NV+). At 77K the circuit should deviate approximately 10% from a perfect match to achieve a good match at 4K. As an example, a 2.5 turn 350 $\mu\text{m}$  ID coil constructed from 100 $\mu\text{m}$  diameter copper wire (MWS industries, free sample) was tuned and matched using  $C_t = 560\text{pF}$  and  $C_m = 15\text{pF}$  at  $\omega_0 = 81.4\text{MHz}$  at 4K. The 4K match for these parameters was very good, within 1%.

Coil dimensions were chosen to optimize the field produced by the coil. In general, the inductance of the coil needs to be large enough so that it dominates any stray inductance to facilitate tuning. Making a coil with many turns will produce a large inductance but will also produce a large resistance reducing the  $Q$  of the coil and increasing heating. Since the first turn of the coil, the turn closest to the sample in figure 3.3 (c), makes the largest contribution to the field at the sample increasing the number of turns will not increase the field at the sample. A good rule of thumb is to keep the length of the coil  $h$  approximately equal to the diameter  $2R$  and to have a minimum of two turns, this allows for sufficient coil inductance for tuning while minimizing turns which do not contribute to the field at the sample. In general we would like to use as thick a wire as possible to reduce coil resistance but the overall coil dimensions place a restriction on the diameter of the wire  $d_{\text{wire}}$  to use since it is optimal to space turns one wire diameter apart to reduce inter-turn capacitance in the coil. [62] Therefore, if we construct a three turn coil with  $2R = 350\mu\text{m}$  the diameter of the wire should be  $d_{\text{wire}} = 350\mu\text{m}/5 = 75\mu\text{m}$  (where we divide by 5 since there are 3 turns and 2 inter-turn spaces). Note that any estimate of the resistance of the coil must include the inter-turn capacitance, the self inductance of the wire and the skin depth effect. [62]

The stray capacitance in the circuit arising typically between turns in the coil and contributing to the coil tuning was measured using the following protocol. The circuit was made to resonate at two frequencies by changing the tuning capacitor between two values  $C_1$  and  $C_2$

$$f_1 = \frac{1}{2\pi\sqrt{L(C_1 + C_s)}}, \quad (3.16)$$

$$f_2 = \frac{1}{2\pi\sqrt{L(C_2 + C_s)}}, \quad (3.17)$$

where  $C_s$  is the stray capacitance and  $f_1$  and  $f_2$  are the resonance frequencies of the circuit as measured using a spectrum

analyzer. The stray capacitance and the inductance  $L$  are then

$$C_s = \frac{C_2 - n^2 C_1}{n^2 - 1}, \quad (3.18)$$

$$L = \frac{1}{4\pi^2 f_1^2} \frac{n^2 - 1}{C_2 - C_1}. \quad (3.19)$$

The measured inductance could be used in calculating  $H_1$  generated by a given coil.

Construction of coils was done by hand. Wire for winding coils was uninsulated copper wire. To wind a coil, uninsulated copper wire with a diameter equal to the desired inner diameter of the coil was selected. This winding wire was stretched firmly and held in place using special c-clamps such that the coil could be wound around this wire without obstruction. The small diameter wire, typically  $60 - 100\mu\text{m}$ , was then wrapped around the taught wire while looking through an optical microscope. The turns of the coil were manipulated into position by gently pulling on the free, unwound, ends of the coil wire until they appeared as desired. In this way coil turn spacing was controlled. Once the coil winding was completed a small dab of superglue applied to the coil attached it to the winding wire. This allowed one to manipulate the coil "legs" - the portions of the coil wire which will be soldered to the printed circuit board. With the coil glued to the winding wire the legs were bent into position and trimmed to the appropriate length. The legs should be cut as short as possible to minimize the total resistance of the coil which contributes to heating. The coil could then be unglued using acetone. By cutting the winding wire near the coil, the coil then could be removed from the winding wire. Under a microscope the coil was then held by the legs using tweezers and soldered into position on the circuit board. Care was taken during soldering not to destroy the coil. Coils could be easily cleaned by careful sonication in methanol. Coils were mechanically and electrically robust to direct dunking in liquid nitrogen.

The design of this tank circuit was well suited for a lumped element analysis of circuit properties. The lumped element approximation takes the voltage to be approximately constant across the circuit at any given point in time. This approximation is valid when the physical size of the circuit components are less than about  $\lambda/10$  where  $\lambda$  is the wavelength of the rf irradiation being transmitted by the circuit as was the case here. We make these approximations with the intention of estimating the magnitude of the field generated by the coil. While calculating the current in the coil for a tuned and match circuit is notoriously difficult, some rules of thumb are useful for estimating the current in the coil and the resulting  $H_1$  field which is generated. [62] The current in the coil is often taken to be

$$i_{coil} = \sqrt{\frac{Z_0}{r}} i_{line}, \quad (3.20)$$

where  $i_{coil}$  is the current in the coil,  $Z_0 = 50\Omega$  is the input impedance of the tank,  $r$  is the resistance of the coil and  $i_{line}$  is the current in the line.  $i_{line} = \sqrt{\frac{P}{Z_0}}$  where  $P$  is the power input into the circuit. We can estimate the resistance of the coil using the quality factor, frequency and calculated inductance. The quality factor can be estimated by inspecting the full width at half max ( $\delta\omega$ ) of the coil resonance on a spectrum analyzer,  $Q = \omega/\delta\omega$ . We then have

$$i_{coil} = \sqrt{\frac{PQ}{\omega_0 L}}. \quad (3.21)$$

The field in the rotating frame a distance  $d$  from the center of the first turn of the coil of radius  $R$  will be

$$\frac{H_1}{\sqrt{P}} = \frac{\mu_0}{2} \sqrt{\frac{Q}{\omega_0 L}} \left( \frac{R^2}{(R^2 + d^2)^{3/2}} \right). \quad (3.22)$$

Typical parameters for a coil will be  $Q = 40$ ,  $L = 5\text{nH}$ ,  $\omega_0 = 80\text{MHz}$ ,  $R = 175\mu\text{m}$  and  $d = 250\mu\text{m}$  resulting in an  $H_1 = 55 G/\sqrt{W}$ . This estimate is comparable to fields found in the literature for similar designs. [29,61,63] Despite this accordance this estimate should be taken with caution. A host of factors can contribute to reduced  $H_1$  such as improper alignment, poor matching and heating which will increase the coil resistance. The only convincing assay for  $H_1$  field strength is to perform a nutation experiment and calculate the rf field from the Rabi frequency and the known gyromagnetic ratio of the nucleus. Nutation experiments have not yet been performed with the rf electronics outlined here.

### 3.2.3 Cantilever and fiber alignment

The cantilever used in the CERMIT experiment is shown in figure 3.9. The cantilever was custom fabricated from single crystal silicon at the Cornell Nanoscale Science and Technology Facility (CNF) using a silicon on insulator fabrication process discussed elsewhere. [31,49,64] The cantilever was  $400\mu\text{m}$  long,  $4\mu\text{m}$  wide and  $0.34\mu\text{m}$  thick with a spring

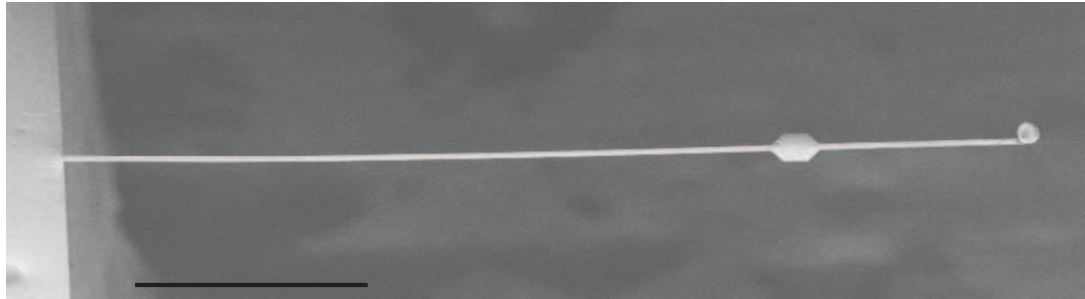


**Figure 3.9:** A scanning electron micrograph of the cantilever used to detect magnetic resonance as a force-gradient. The sphere at the tip of the cantilever was a 9 $\mu\text{m}$  in diameter nickel sphere glued by hand. The scale bar is 100 $\mu\text{m}$ .

constant measured by the thermal method of 60 $\mu\text{N/m}$ . The cantilever had a fundamental frequency of 854Hz and a  $Q$  of 43900 at a tip-sample separation of 160nm and a temperature of 4.4K.

### Magnetic particle gluing

The magnetic particle on the tip was a 9 $\mu\text{m}$  nickel sphere glued manually. Spherical nickel powder was obtained from Novamet. The gluing process was executed as follows. Using optical translation stages oriented such that the cantilever could be held in a geometry perpendicular to a polished metal surface (figure 1.3). These stages achieved motion using micrometer screws allowing manipulation on about a 5 $\mu\text{m}$  length scale. A small amount of the Novamet nickel power was spread on the polished metal surface using a metal spatula. It was important that the spheres be spread with low enough density to allow the isolation of individual spheres. The entire apparatus was then viewed through a long working distance microscope (Center for Nanoscale Systems, Cornell University). Under the microscope the cantilever was positioned over a region of where the spheres were sufficiently far apart and no large clumps of powder were present. A small dab of well mixed 45 minute epoxy was then put down nearby the cantilever using a sharp dental tool or toothpick. The cantilever was then moved over the glue dab and slowly lowered until the tip of the cantilever was observed to “snap” into the glue dab. Too much glue on the tip of the cantilever caused curling or multiple spheres to be glued to the tip. The cantilever was then brought down over a the desired nickel sphere. Long working time epoxy allowed for careful selection of spheres. In [11] 5 hour epoxy was used and the particle was oriented in a 5T magnet such that the magnetization pointed along the width of the cantilever as in figure 3.4. Orienting the particle was done to avoid any component of the particle magnetization from lying in a direction perpendicular to the applied field, resulting in a torque on the cantilever. Torque on the cantilever due to the applied field were observed with non-spherical SmCo particles glued to cantilever tips, this effect was likely due to the shape anisotropy of these irregular particles. However, it has since been determined that when using spherical nickel particles this orientation step is not necessary greatly simplifying tip preparation. After gluing was complete, magnetic particles were inspected under a high magnification short working distance optical microscope or by SEM to ensure that the particle protruded slightly from the tip such that the magnet would be closest to the surface in an experiment.

There are several important points to note with respect to gluing magnetic particles to cantilevers. First, the success of gluing particles depends on the shape of the silicon at the tip of the cantilever. For all successful gluing attempts the cantilever tip was narrower than the shaft of the cantilever. Meaning a small “tongue” region, typically 1 $\mu\text{m}$  wide and 3 – 5 $\mu\text{m}$  long, was patterned into the cantilever shape during the fabrication process. Having this small region reduced the amount of glue used in the gluing process and kept the glue from spreading up the shaft of the cantilever as it minimized its surface tension. Unsuccessful attempts were made to glue 1 – 2 $\mu\text{m}$  particles using the method outlined above. The central difficulty with these smaller particles was getting them to separate on the polished metal surface. The particles tended to cluster and each gluing attempt resulted in multiple spheres at the tip rather than just a single sphere as is desirable in an experiment. Ultimately, nanofabrication of magnetic tips will have to replace the methods outlined here.

### Cryogenic cantilever fiber alignment

One of the biggest drawbacks to the fiber interferometer for detecting cantilever displacements was retaining alignment between the cantilever and the fiber under cryogenic conditions. The cantilever was fabricated with a hexagonal pad

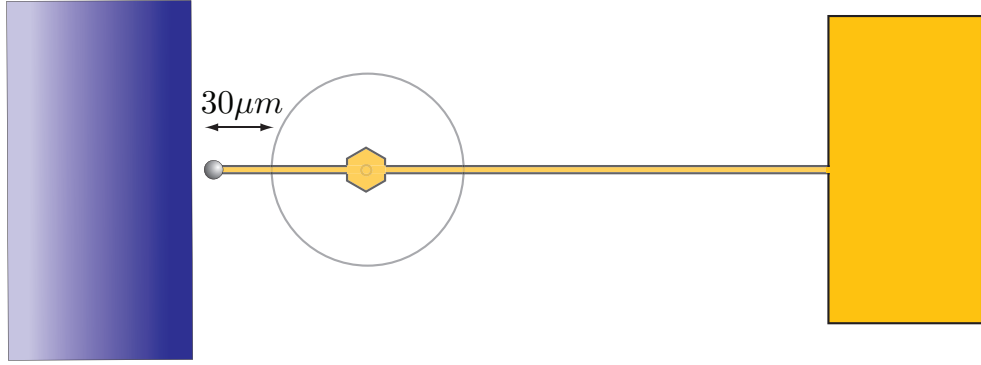


**Figure 3.10:** A top down view of cantilever-fiber alignment, drawn to scale. The distance between the edge of the fiber and the tip of the cantilever is  $30\mu\text{m}$ . To ensure that the cantilever tip can come close to the surface this small gap cannot be obstructed by any fiber holding mechanism. The problem can be minimized if the distance the fiber must traverse across the sample is kept to a minimum.

$20\mu\text{m}$  across (figure 3.9) which serves as a reflector for interferometric detection. The core of the optical fibers used in this thesis were  $5\mu\text{m}$  in diameter (Metrotek, Corning 1310nm single-mode 900 $\mu\text{m}$  SM jacket). Misalignment occurred readily between this small core and the pad on the cantilever as materials contracted upon cooling. In the perpendicular geometry the problem was compounded by restrictions placed on the fiber holding mechanism. Figure 3.3 (c) illustrates the difficulty. The fiber traversed a portion of the sample in order to be placed within about  $80\mu\text{m}$  of the cantilever. Any mechanism which holds the fiber could not obstruct the cantilever from being allowed to approach the surface as shown in figure 3.10. These problems were addressed by gluing the fiber directly to the cantilever mount. Minimizing the distance between the fiber holding mechanism and the cantilever was crucial for maintaining alignment with cooling. It was shown through iterated experiments that gluing the fiber as close as possible to the cantilever produced the best alignment. Very thin layers of glue adhering the fiber to the metal allowed for the stringent spatial requirement shown in figure 3.10 to be met. In subsequent designs, discussed below, it was shown that Stycast 2850 FT epoxy (Lakeshore) produced the most reliable fiber cantilever alignments.

### 3.3 Measurement and signal

The cantilever was brought to a height of  $160\text{ nm}$  above the sample surface using our custom-built, low-temperature coarse approach mechanism. [52] The sample was GaAs, coated with  $20\text{ nm}$  of gold. This sample was chosen because its NMR relaxation times were well characterized at low temperature by MRFM. [14] The voltage between sample and cantilever was set to  $0.4\text{ V}$ , a value found by ring-down time to minimize the noncontact friction between the cantilever and the sample surface. [22] The noncontact friction was observed, as expected, to be parabolic in this tip-sample voltage. A  $500\text{ }\mu\text{m}$ -diameter radio-frequency (rf) coil tuned and matched as discussed above with a  $Q$  of about  $90$  at  $4\text{ K}$  was positioned nearby. The wire used in this coil construction was  $25\mu\text{m}$  in diameter making winding and soldering especially challenging. As outlined above, it is now believed that thicker wire reduces coil resistance and therefore heating as well as making construction far easier. The rf was synthesized with a digital arbitrary waveform generator (Wavetek, model 302) operating at an intermediate frequency of  $2 - 3\text{MHz}$  and was upconverted to  $88\text{ MHz}$  using single sideband mixing (SMC mixer, model SMK-34-15). Cantilever displacement was observed with a fiber optic interferometer [54, 65], the output of which was phase shifted and used to capacitively drive the cantilever into self oscillation using a positive feedback loop [47, 48, 64] to a root-mean-square (rms) amplitude of  $x_{\text{rms}} = 176\text{ nm}$ . The cantilever frequency was monitored by sending the output of the loop to a commercial frequency counter(Stanford Research Systems, model 620).

Spins were inverted as discussed in section 2.1.4 using  $1\text{MHz}$  ARP frequency sweeps. The region of inverted spins lies between two constant- $B_z$  contours determined by the initial and final frequency of the ARP. The total field experienced by the spins depends on both the tip field and the applied field.  $B_{\text{total}} = B_{\text{tip}} + B_0$ . The region where the resonance condition was satisfied could be moved spatially by adjusting the applied field.

Figure 3.11 shows the cantilever response when ARP sweeps were delivered at various applied magnetic fields. The sweep generally had no discernible effect on the cantilever frequency when the rf was out of resonance with the sample spins ( $7.050\text{ T}$ , filled circles, figure 3.11). Occasionally, a small, short-lived shift was observed after one or both of the

sweeps (7.025 T, open circles). The appearance of these responses was unpredictable, likely because they depend on the phase of the cantilever at the time of the sweep as discussed below, these transients can become appreciable in experiments requiring many ARP sweeps be applied. It was noted that DC voltages applied to the ground pin on the rf coax effected the cantilever frequency in a way consistent with an electrostatic interaction. This is to be expected, since the leg of the coil soldered to ground is in close proximity with the cantilever.

At 6.775T (open triangles) the sweep produced an inverted region of spins, causing a  $-70\text{ mHz}$  jump in the cantilever frequency. This shift corresponds, via equation 2.41, to a force gradient of about  $10\text{nN/m}$ . At 6.900T a positive frequency shift was observed. When a second, identical sweep was applied to return the spins to equilibrium, the recovery of the cantilever frequency was imperfect, consistent with an incomplete restoration of sample magnetization. Due, for example, to spins whose  $z$  magnetization was partially destroyed at the endpoints of the ARP sweeps. One issue which may have been important was the phase of the rf sweeps. Considering that the rf sweeps are 1MHz they nearly completely span the resonance of the coil. Therefore, the rf must be undergoing considerable phase shift due to the phase dependent response of the coil. The effect of these phases has not been fully explored, but errors in complete recovery similar to those addressed by compensated  $\pi$  pulses might have contributed.

Figure 3.12 is a plot of the cantilever frequency shift versus external magnetic field. The lineshape is composed of a negative, low-field peak and a smaller, positive, high-field peak. The high-field peak is due to spins in the high-gradient region near the tip (upper inset). Here,  $\partial^2B_z/\partial x^2$  is strongly positive and the spins are pointing down, for an overall positive shift (see equation 3.3). The signal collected in this field range is from a small volume of spins localized near the tip. and is of interest for imaging experiments [66,67]. At point “a” in figure 3.12, which is derived from the 6.900 T transient in figure 3.11, the shift of  $38\text{mHz}$  corresponds to a change in force gradient of  $5.3 \times 10^{-9}\text{ N/m}$ . Spins contributing to this signal experience, we estimate, a  $\partial^2B_z/\partial x^2$  of  $2 \times 10^{10}\text{ T/m}^2$ . Given that the Curie law magnetic moment of  $^{71}\text{Ga}$  is  $1.06 \times 10^{-29}\text{ J/T}$  per nucleus at  $4.4\text{ K}$  and  $7\text{ T}$ , the signal at “a” is due to  $2.5 \times 10^{10}$  nuclei.

The negative peak in figure 3.12 is due to spins further away from the tip (lower inset) which interact with weaker, negative side lobes of  $\partial^2B_z/\partial x^2$ . These spins experience a much smaller first derivative of the tip field and therefore a much larger volume of spins is inverted by the ARP sweep, resulting in a larger signal despite the smaller second derivative. This is analogous to the “zero-tip-field resonance” observed by Suter *et al.* [68] in electron spin resonance experiments.

The sensitivity of this experiment was limited by a background frequency jitter (Allan variance) of  $2\text{mHz}$  in a one hertz measurement bandwidth, equivalent to fluctuating force gradient with spectral density  $S_k = 3 \times 10^{-10}\text{ N/m}\sqrt{\text{Hz}}$ . The associated minimum detectable nuclear magnetic moment, for spins directly below the tip, is  $\mu_{\min} = 1.5 \times 10^{-20}\text{ J/T}$  in a one hertz bandwidth. This is equal to the Curie-law magnetic moment from  $1.4 \times 10^9\text{ }^{71}\text{Ga}$  nuclei occupying  $(0.54\text{ }\mu\text{m})^3$  in GaAs. While the position noise of the undriven cantilever was consistent with thermomechanical fluctuations, as estimated from a calculated spring constant and the measured temperature, the observed  $S_k$  is six times higher than the thermomechanical limit [48]. There are many possible reasons for non-thermal frequency noise including insufficient vibration isolation or frequency fluctuations due to spurious electric fields originating at the sample surface.

In principle, magnetic moment sensitivity can be increased by decreasing magnet diameter and tip-sample separation. In practice, however, sensitivity at small tip-sample separations is limited by surface induced cantilever dissipation [22]. Still, with our current  $S_k$  and separation of  $160\text{ nm}$ , using a  $\partial^2B_z/\partial x^2$ -optimized tip diameter of  $0.48\text{ }\mu\text{m}$  improves the magnetic moment sensitivity to  $\mu_{\min} = 3300\text{ }\mu_p$  (in terms proton magnetic moments). A further factor of six gain in sensitivity can be obtained by lowering the force gradient noise to the thermal limit.

## 3.4 Second generation apparatus

Difficulties with alignment of the coil and the cantilever, the cantilever and the fiber along with the sample necessitated the re-design of the CERMIT probe. The goals behind this redesign were to construct a simple probe without additional functionality, such as 3D scanning, but with dramatically increased overall reliability.

### 3.4.1 Basic design

A schematic of the basic design is shown in figure 3.13. All parts were machined from grade II annealed titanium unless otherwise noted. Material selection is discussed below. The design exploits the commercially available nanopositioning systems from Attocube. These systems are much more robust to freezing than our custom design and minimize backlash. The Attocube moved the cantilever left and right in the plane of the page in figure 3.13. By moving the left the Attocube approached the cantilever to the sample with the coil positioned nearby. In addition, this probe was not built in the

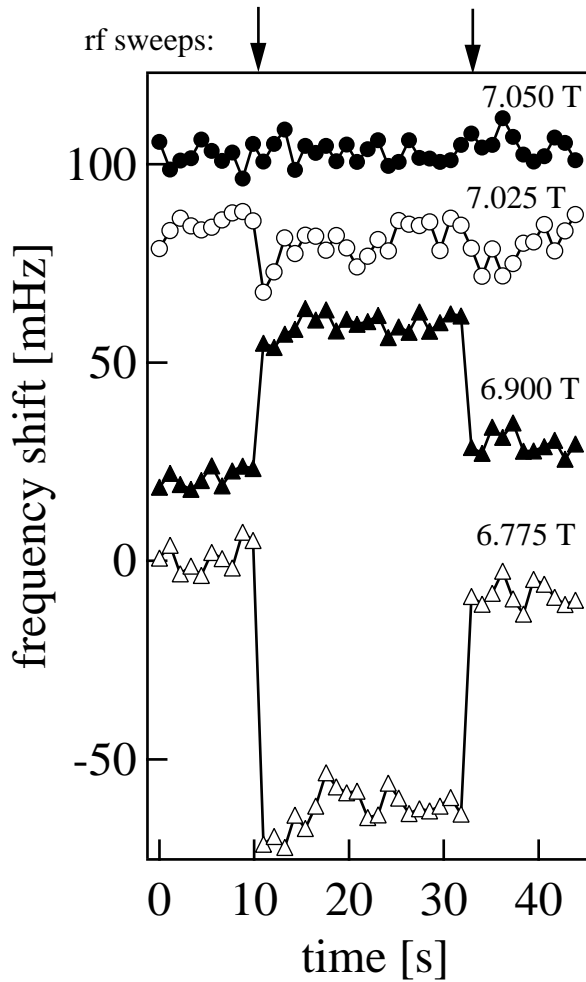


**Figure 3.11:** Cantilever resonance frequency shift transients at various fields. Traces are offset vertically for clarity. The times at which rf sweeps (see text) were delivered are indicated by arrows above. Each sweep consisted of a 20ms long 1 MHz frequency ramp centered at 88.075 MHz (the rf coil's resonance frequency and the magnetic resonance frequency for  $^{71}\text{Ga}$  at 6.785 T). Only 25 mW of rf was required to produce an estimated  $B_1 = 12$  G. The rf was turned on only during the sweep.

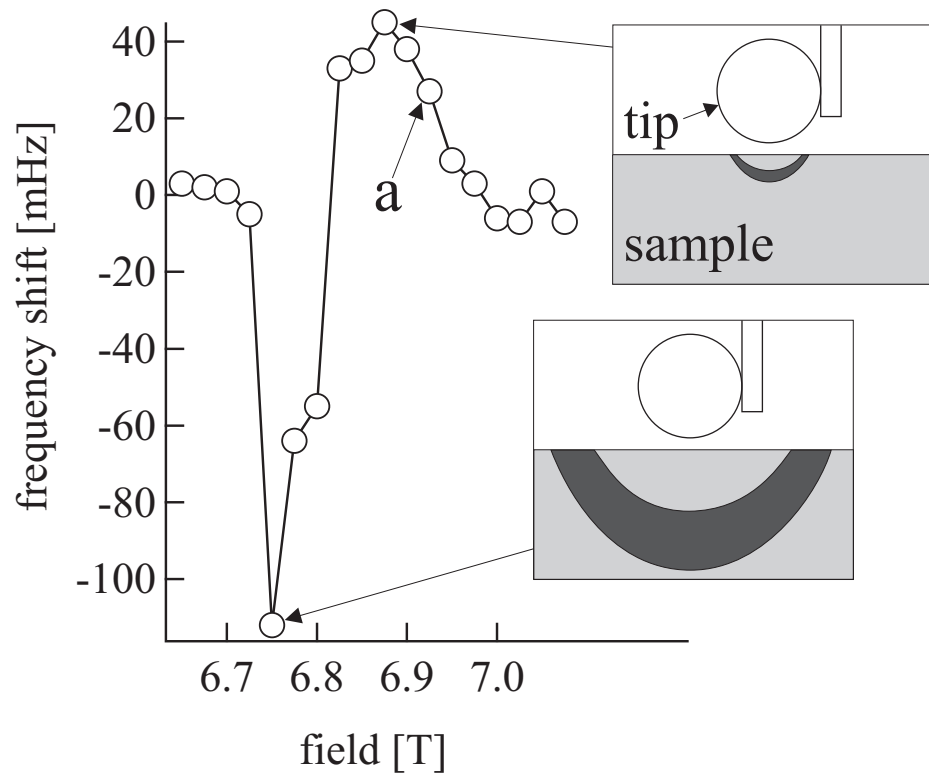


**Figure 3.12:** Cantilever frequency shift as a function of field, obtained from frequency transient data (figure 3.11) by averaging the 10 values before the first rf sweep and subtracting the result from the average of the first 10 values after the sweep. The insets show the tip in relation to the region of inverted spins (shaded) at two external field values, sliced along the tip magnet's equator in a plane normal to the external field, the  $x - y$  plane in figure 3.4.

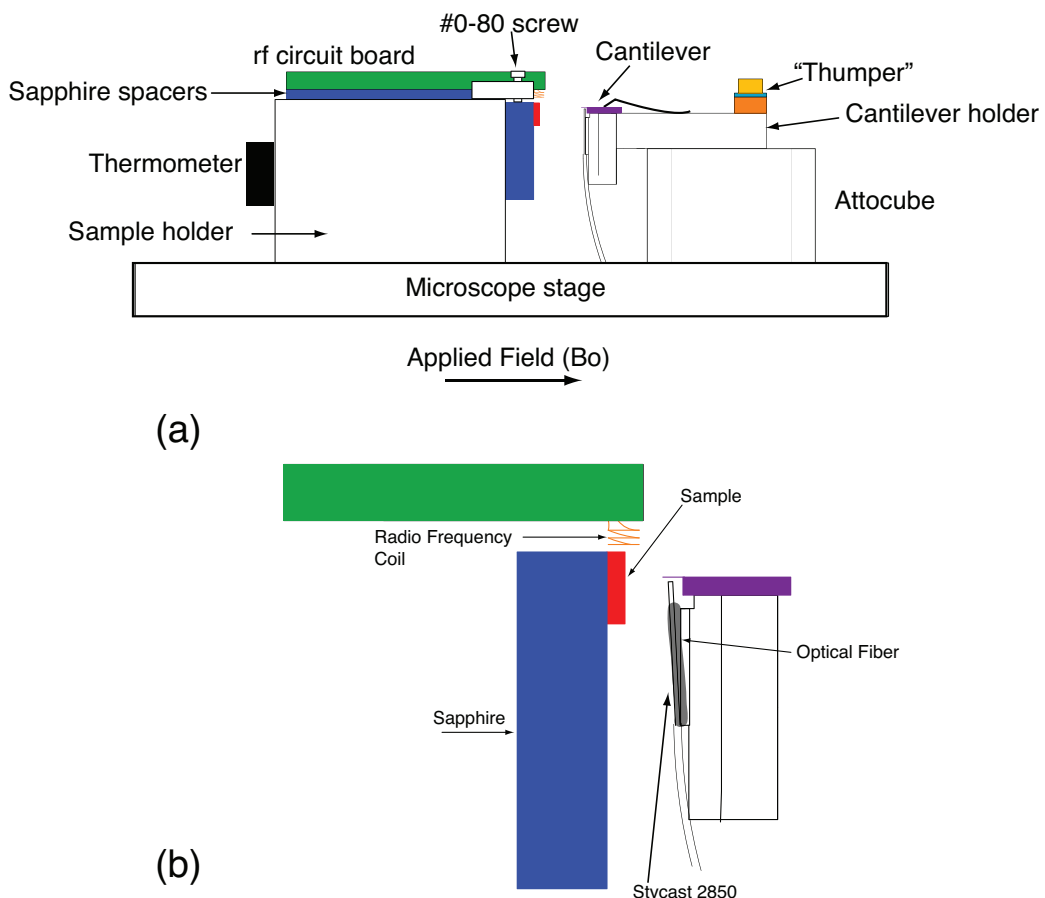


**Figure 3.13:** Schematic of the design.(a) shows an overall view of the design including sample holder, rf circuit board, sample, cantilever, commercial Attocube positioner, and “thumper” for cantilever driving. For scale, the Attocube is approximately 1/2 inch from left to right. (b) an enlarged view of the cantilever, rf coil and sample alignment scheme. Note the angle of the fiber mitigating the problem illustrated in figure 3.10. For a discussion of the design see the text.

geometry shown in figure 3.4. We anticipate that using nanofabricated magnetic tips with dimensions on the 50nm length scale will have negligible interaction with the applied field  $B_0$ . If this is not the case, we have also designed a second microscope stage which positions the entire microscope as shown here but in the geometry shown in figure 3.4. CAD drawings for the entire probe are contained in appendix C.

Beginning with figure 3.13 (a), the titanium block on the left provided physical support for the thermometer (black), rf circuit (green) and sample (red) as shown. The thermometer was a calibrated Lakeshore Cernox low temperature thermometer (model CX-1050-CU). The printed circuit board was custom ordered as discussed above. Coupling to the circuit was achieved using a solder mount SMA connector (Digikey) which is not shown. Contact between the coil and the topside stripline was made with a small via hole facilitating the coil geometry shown. The rf board was mounted to the sample holder using #2 – 56 screws which are not shown. The sample (red) was glued to a sapphire slab (blue - Meller Optics) using super glue to facilitate low temperature thermal contact while maintaining electrical isolation. The vertical position of this sapphire slab was set using the #0 – 80 set screw shown. An additional set screw was present, but not shown, on the opposite side of the rf board. The rf circuit sat on small sapphire spacers (Meller optics, overstock). The thickness of these spacers combined with the position of the #0 – 80 screws sets the coil sample spacing.

As discussed previously it was critical that the coil be as close as possible to the spins which are being detected by the cantilever. The position of the cantilever was fixed in this design by the height of the Attocube and the thickness of the cantilever holder which sat atop the Attocube (model ANPx50 LT) as shown in figure 3.13 (a). There was some uncertainty with respect to the position of the coil due to the length of the legs which are soldered to the circuit board. Since the coils were constructed by hand this length is not well determined. Therefore, to control the coil to cantilever spacing in the vertical direction shown in figure 3.13 (a) we relied on the sapphire spacers shown and on manual adjustment of the coil by bending its legs. This process of alignment was found to be adequate in precision and in ease of use. Sapphire spacers ranging over many thicknesses between 0.01 and 0.06 inches were purchased (Meller Optics, overstock listing). By varying the thickness of these spacers the coil cantilever separation was set. Setting this separation must be done for each new rf coil that is constructed. To do this we constructed an rf coil and mounted it onto the sample holder as shown in figure 3.13 (a) and approached the cantilever using the Attocube while observing the approach with an optical microscope. The coil cantilever separation could then be inspected and the size of the spacers changed accordingly. Cantilever coil separations between 100 – 200 $\mu\text{m}$  were obtained in this way.

The sample and sapphire slab were held onto the sample holder using a brass clip (not shown). Once the coil cantilever separation was set, the sample holder could be removed and the sample and sapphire slab mounted using this clip. The sample coil separation could then be precisely controlled using the #0 – 80 screws shown and discussed above. The clip was electrically isolated from the sample holder using nylon spacers and washers, electrical contact was made with the clip by soldering a wire to the edge. Electrical connection between the sample, which was typically coated with a thin layer of metal, was made by silver paint between the sample surface and the clip. Care was taken to avoid putting silver paint on the region where the cantilever would contact the surface. This connection was found to be robust at cryogenic temperatures and reliable upon temperature cycling. The nylon washers isolating the clip from the sample holder were also found to be robust to many temperature cycles, but may require replacement on an annual basis.

The cantilever holder facilitated cantilever fiber alignment. This was achieved as discussed above by gluing the fiber directly to the cantilever holder using Stycast 2850 FT epoxy as shown in figure 3.13 (b). The fiber cleaving and gluing process is outlined below. The cantilever was electrically grounded by a wire soldered to the clip shown in figure 3.13 (a). The cantilever holder also held the piezo “thumper” which facilitated cantilever driving shown in figure 3.13 (b) on the right hand side of the holder. The thumper excited cantilever motion by sending vibrations through the cantilever holder. The piezo and small brass mass that comprised the thumper sat atop a small copper clip which attached to the cantilever holder via two #2 – 56 screws. This copper clamp also served to attach a strip of 99.9999% pure copper 0.002 inch thick foil (Alfa Aesar) to the 4K copper block on which the entire microscope was mounted. Thin foil was necessary as not to impede positioner motion.

Images of the probe discussed here are shown in figure 3.14. The sample clip, along with nylon washers used for electrical isolation, can be seen in figure 3.14 (a) as can the 0.02” thick strip of copper used to heat sink the sample and rf discussed below. All electrical connections were made with Samtec plugs which have been shown to be reliable at low temperature and high vacuum. Electrical connections can be seen in figure 3.14 were made at two points, one at the end of the microscope stage and a second set of connectors at the circular copper microscope mounting plate. The probe presented did not utilize the variable temperature insert restricting measurements to 4K.

The entire microscope stage was bolted to a copper mounting plate inside a 7° grease sealed copper can with an O.D. of 2.75” comprising the vacuum space. The grease seal can be seen in figures 3.14 (a) and (c). The entire can was mounted on stainless pump lines and lines for wiring, rf coax, optical fibers and the turbo molecular pump (Pfeiffer).

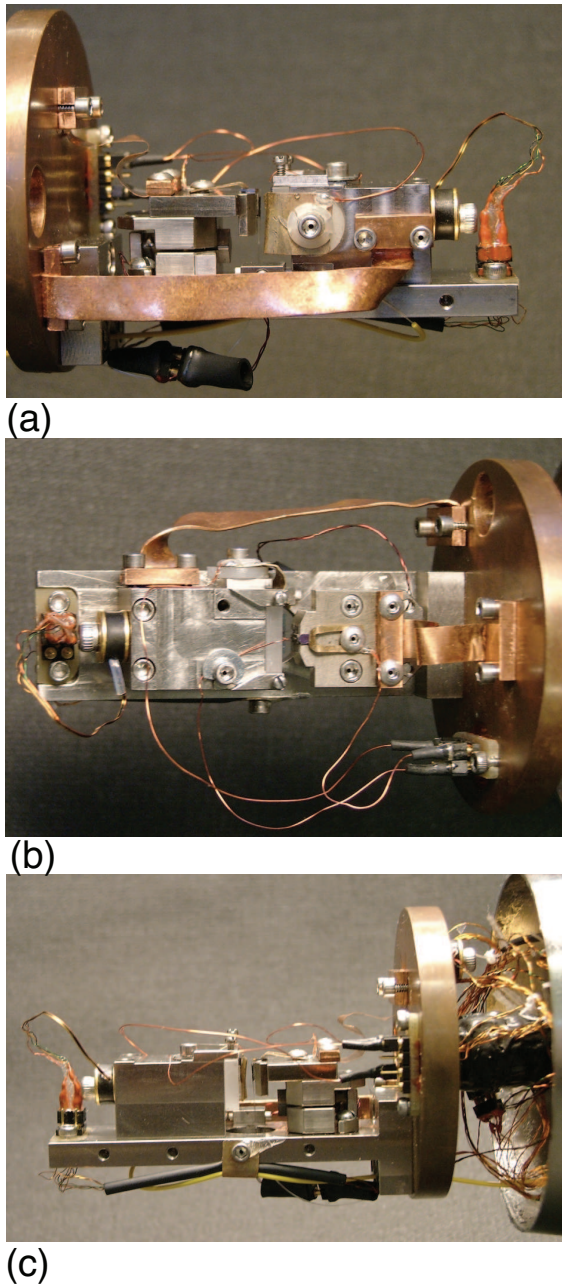


**Figure 3.14:** Three views of the second generation MRFM probe. The rf board and coaxial cable have been removed for clarity. (c) presents the same view as that drawn in figure 3.13 (a).

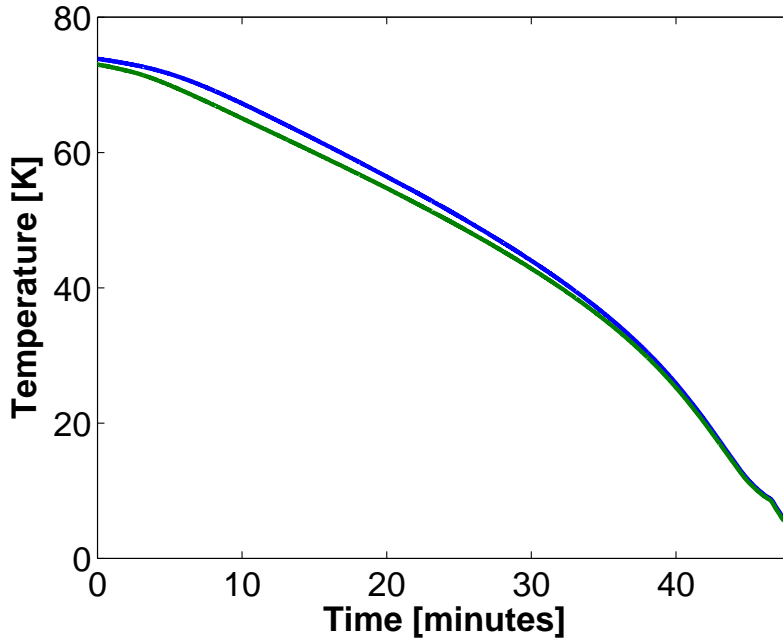


**Figure 3.15:** Temperature as measured by two Cernox thermometers during cooling from 77K to 4K. Green: temperature measured at the sample holder with the heat sink installed as shown in figure 3.14 (a), note that the probe is under vacuum. Blue: temperature measured at the copper mounting plate (the copper disc visible on the right side of figure 3.14 (b)). Cooling was measured during a liquid helium transfer.

These thin walled stainless steel tubes were welded to a top flange which bolted to the top flange of the 90L helium dewar containing the swept field superconducting magnet. The pump lines also supported copper baffles shielding the probe from black body radiation. The details of the probe superstructure are contained in appendix C.

### 3.4.2 Material consideration and heat sinking

As mentioned the entire microscope was machined from grade II annealed titanium. Titanium is a superior material for microscope construction due to its low thermal contraction and slightly higher thermal conductivity as compared to stainless steel. [69] Titanium has historically been used for constructing UHV low temperature STM and MFM systems. [70–72] Grade II annealed titanium was chosen here to specifically match the commercial Attocube system for thermal contraction. Several grades of titanium are available. The industrial standard is Ti-6Al-4V (titanium alloy: 6% aluminium, 4% vanadium) which is a very hard, light and strong material. Unfortunately, Ti-6Al-4V is so hard (C32 on the Rockwell Hardness Scale) that machining, especially of small parts, is difficult. Grade II annealed titanium (Jessop Specialty Products) is a B98 on the Rockwell Scale as it lacks vanadium, making it machinable while retaining the desirable thermal properties.

At cryogenic temperatures heat sinking is critical. As mentioned high purity copper strips were connected between the sample holder and the cooled copper microscope plate (figure 3.14 (a)). Thinner strips of copper foil were used for heat sinking the cantilever holder as shown in figure 3.14 (a)-(c). These strips were annealed in high vacuum at 650°C for 6 hours (Cornell Center for Materials Research annealing oven) to further remove impurities which lower thermal conductivity by scattering conduction electrons. Contact area between these strips and the titanium sample and cantilever holder was maximized by coating the surfaces with apiezon N-grease. Cooling curves as measured by two thermometers, one at the sample holder and another at the copper mounting plate, are shown in figure 3.15

### 3.4.3 Attocube positioning

This new probe design utilized the first commercially available cryogenic and vacuum compatible nanopositioning system. These positioners work on the same basic slip-stick principle discussed above. We observed the motion of

**Table 3.1:** Piezo displacements and capacitance for the Attocube ANPx50 positioner at three different temperatures. Capacitance was measured using the ANP150 step controller.

Temperature [K]	Piezo displacement [nm/V]	Piezo capacitance [nF]
300	130	900
77	50	280
4	27	170

the Attocube positioner with nanometer precision using an additional fiber optic interferometer. For the ANPx50 LT positioner used here typical piezo displacements (under the influence of DC voltages) and piezo capacitance are shown in table 3.1.

Using the ANC150 step controller (Attocube) step sizes of  $\sim 25\text{nm}$  were obtained at room temperature with 8V steps, at 77K with 14V steps and at 4K with 20V steps. These step sizes were not found to be long term reliable and therefore are listed here as only approximate. In fact, the positioner was found to degrade in performance over time. The reason for this degradation remained unknown but might have been due to dust on the sliding surfaces or condensation on the piezo during probe warm-ups. At the time of this writing the positioner was being repaired by Attocube.

The major disadvantage to using these positioners was their extreme fragility. Any torque applied to the piezo delaminated the layers which are glued together. This de-lamination resulted in total positioner failure. To avoid this it was critical to handle the positioner such that no torque is applied to the piezo as per the Attocube instructions. To do this it was necessary to mount the cantilever holder on the Attocube prior to mounting the Attocube to the microscope stage. Future designs might consider using the more robust ANPx51 or ANPx101 positioners to avoid this difficulty.

### 3.4.4 Fiber gluing

Repeated misalignments between the cantilever and the optical fiber used to detect its motion upon cooling in the previous instrument were a central concern. The design adopted here, shown in figure 3.13 (b), solved this issue.

In this design the fiber was glued directly to the cantilever holder using Stycast 2850 FT epoxy. The region where the fiber was glued to the titanium cantilever holder was approximately 0.15 inches long in the vertical direction in figure 3.13. Fiber cleaving was achieved by stripping approximately 3 inches of fiber down to the polymer coating with about 1 inch of exposed glass fiber at the end. The fiber was then taped to a flexible metal ruler in two places, at the end of the fiber and at any point on the polymer coated region. Approximately 0.1 inch from where the polymer coating ends and the glass begins the fiber was lightly scribed using a diamond scribe. The ruler was then bent by hand until the fiber snapped at the scribe point resulting in a cleaved fiber end. With the New Focus amplifier gain set to  $10^4 \times 1$  and the bandwidth open from DC to well above  $f_0$  a voltage of 1V or greater from the reflection at the cleave was sufficient to provide high sensitivity cantilever displacement detection. Using a commercially available fiber cleaver was also feasible although it was typically more difficult to control the location of the cleave with respect to the end of the polymer coating.

The cleaved fiber was then glued to the cantilever holder using helping hands. The helping hands were clamped firmly to the edge of the lab bench. The cleaved optical fiber was held in one clip of the helping hands and the cantilever holder in the other. A cantilever die should be temporarily adhered to the cantilever holder in the same place that the actual cantilever will sit using grease. The placement of this die allowed the estimation of cantilever fiber separation prior to gluing. Under the microscope the cleaved fiber was placed along the surface of the cantilever holder as shown in figure 3.13 (b). Before gluing the fiber several things should be noted. The distance between the cleaved end of the fiber and the top of the cantilever die, where the cantilever will be located, should be approximately  $80\mu\text{m}$ . The angle between the fiber and the cantilever holder should be positive as shown in figure 3.13 (b). Stycast epoxy was then applied sparingly to form a thin sheet around the fiber and onto the cantilever holder. The epoxy not only covered the glass region of the fiber but also a short portion of the polymer coated region of the fiber. If the glass portion of the fiber exited the glue at the bottom it was found not be robust to handling. In addition, if a full 2 inches of the yellow  $900\mu\text{m}$  jacket was not removed from the fiber as mentioned above, the stiffer yellow jacket induced added stress at the point where the fiber exited the glue and the fiber was found to break. Stycast 2850 FT required a minimum of 12 hours to dry. The drying process was often aided by placing a 100W conventional light bulb nearby.

Future designs of the cantilever holder might include a method to rigidly clamp the fiber by this thicker, yellow jacket

yet still allow gluing of the fiber with Stycast. Using the protocol outlined here cantilever fiber alignment was maintained over dozens of cooling cycles without failure and the Stycast and titanium combination was demonstrated to be robust to many ( $> 10$ ) thermal cycles.

### 3.4.5 Cryogenic electrical considerations

Electrical wiring must be thermally tied to a large mass which is efficiently cooled at 4K to avoid heat leaks. The thermal conductivity of electrical wiring should be minimized. To do this we used 36 AWG wire (Lakeshore, WSL-36-450) for individual connections and “quad twist” wires (Lakeshore) for 4-terminal thermometer connections. All wires were wrapped twice around the central cooper cylinder which held the microscope mounting plate. The cylinder was in direct contact with liquid helium. The wires were secured with Stycast 2850 FT. Unfortunately, it was determined that 36 AWG wires were unable to support the large currents supplied by the ANC150 Attocube controller. Therefore, larger gauge (20 AWG) wire was run separately and wrapped around the same central copper cylinder to run the Attocube.

Radio frequency signals were transmitted using copper clad, stainless steel conductor, cryogenic compatible coaxial cable (Astrolab, model 3100ST). Since rf signals travel only on first few microns of a conductor due to the skin depth effect a copper cladding is sufficient. These coaxial cables minimize the heat leak by being comprised of predominantly low thermal conductivity stainless steel. This semi-rigid coax was connectorized with SMA plugs (Astrolab, part 29044 or 29043 which required the arduous insertion of a “snap-ring”) Attempts to connectorize these cables with standard, noncryogenic, plugs failed upon thermal cycling.

### 3.4.6 Cantilever driving and frequency demodulation

Previous work utilized capacitive electrical driving of the cantilever motion as described in section 3.2. Capacitive driving resulted from forces between the drive wire and the cantilever due to electric field interacting with capacitively induced charge on the cantilever. AC voltages applied to the cantilever drive wire then resulted in oscillatory motion. Positive feedback was used to self oscillate the cantilever in this way. During an experiment it was also desirable to null the tip-sample contact potential [53] by applying a DC voltage between the cantilever and the sample. By setting this voltage appropriately the charge on the tip of the cantilever could be nulled. This occurred when the surface induced dissipation was a minimum as a function of this tip-sample voltage. However, it was determined that the capacitive drive efficiency, the cantilever amplitude resulting from a fixed amplitude AC voltage applied to the drive wire, was lowest when the *tip-sample* voltage was set to the voltage that minimized the surface dissipation. In CERMIT, or any high sensitivity MRFM experiment, SNR is maximized at the tip-sample voltage that minimizes the noncontact friction. At this minimum voltage, driving capacitively was nearly impossible requiring large voltages be applied to the drive wire to achieve even small displacements. It was believed that the electric field from the capacitive drive wire interacted strongly with the charge on the tip of the cantilever to drive the oscillator. Thus, nulling the tip charge reduced the driving efficiency. This mechanism was not explored in detail. Instead, we engineered mechanical driving of the cantilever using piezo actuators.

The thumper was a small piece of piezo ceramic (Piezo systems, model T120-A4E-602) which expanded and contracted vertically in figure 3.13 (a). Leads were soldered to the small piezo part manually. Leads and piezo electrodes were electrically isolated from the rest of the probe by coating with epoxy and high vacuum sealant (Vacseal). The piezo was then glued to the copper clamp with super glue as shown in figure 3.13 (a). Atop the piezo sat a small cylinder of brass serving as the mass for the thumper. As the piezo oscillated with an applied bias the inertia of the thumper sent vibrations through the cantilever holder that drove cantilever oscillations. Using small (100mV rms) voltages this design excited large cantilever amplitudes. Furthermore, connecting this piezo element to the output of an analog positive feedback circuit resulted in cantilever self oscillation. [53] Three thumper sizes were constructed small (0.4g), medium (0.7g) and large (1.4g). The small thumper provided insufficient driving force requiring that large voltages be sent to the driving piezo. The large thumper provided such large driving forces that voltages of only a few mV were needed to achieve large displacements. The medium size provided the best compromise of sizable drive amplitudes at moderate voltages. The medium size mass also was shown to drive the cantilever sufficiently at 4K.

When designing new cantilever driving protocols it was important to check the phase response of the cantilever to the drive signal as a function of frequency. For the harmonic cantilevers used in this thesis we expect the phase of the cantilever to be  $0^\circ$  with respect to the drive frequency when the oscillator is driven below resonance and a  $180^\circ$  phase shift between the drive and the oscillator response above resonance. To check that this was the case with the thumper design presented here the frequency of the cantilever drive was swept through the cantilever resonance while the phase of

the oscillator response was measured using a lockin amplifier (Stanford Research Systems, SR830). The drive signal was generated by a function generator (National Instruments, PCI FGen) and used as an external reference for the lock-in amplifier. The response was as expected for a harmonic oscillator. [53]

Measuring cantilever frequency shifts was accomplished previously using a commercial frequency counter (Stanford Research Systems, SR620). While the frequency counter achieved low noise frequency determination by using stable reference oscillators, the hardware did not allow high bandwidth cantilever frequency measurements. This limitation was due to the fact that measurements of frequency using the SR620 required either direct query via GPIB, at a maximum bandwidth of 100Hz, or measuring the voltage on an analog output which is proportional to the frequency measurement. The analog output was updated at a rate of only 60Hz. For coherent MRFM measurements, such as iOSCAR or cyclic versions of the CERMIT protocol, where the spin signal appears at nonzero frequencies of a few 10's of Hertz, rapid cantilever frequency demodulation was necessary.

In frequency shift MRFM it was not necessary to determine the cantilever frequency in real time as is often necessary in AFM where real-time feedback is used. Therefore, frequency demodulation could occur post-experiment and be employed in software. [73] To do this the cantilever was put under self oscillation at a fixed amplitude by an analog feedback circuit and the cantilever signal digitized at a high bandwidth ( $\sim 100\text{kHz}$ , 16 bit resolution) using a DAQ board (National Instruments, PCI 6209, shielded BNC 2090 breakout box). Approximately 60 seconds of data were read in at this rate. We worked with two algorithms to demodulate the frequency in software. The first was a nonlinear least squares fit of the cantilever sinusoid implemented in FORTRAN code executed by LabVIEW. The fitting algorithm and LabVIEW code was supplied by Dan Rugar. The nonlinearity of the fitting was found to be robust under situations of low frequency jitter, but failed in cases where the cantilever frequency fluctuated more than about 1 part in  $10^5$ . A second algorithm, implemented in Matlab and executed via a Matlab code node in LabVIEW fit the phase of the cantilever a function of time. This *linear* least squares fit was shown to be robust under all regimes for demodulating cantilever time domain data and was less computationally intensive due to the fit linearity.

Typical cantilever frequency demodulations are shown in figure 3.16. It was also shown that the rms frequency jitter measured by integrating the power spectra agreed with that measured using the SR620 frequency counter at the appropriate bandwidth, indicating that the power spectra were not folding in noise. For the Matlab protocol discussed above, two filters were implemented in software. The first was a filter on the Fourier transform of the raw cantilever signal. This filter served to knock out higher cantilever harmonics and therefore was set as wide as possible without including fourier components at or greater than  $2f_c$ . The second filter was the frequency demodulation Nyquist condition. This condition set the time domain bin size that the cantilever phase versus time was fit to a line. The Nyquist frequency of the frequency demodulation  $f_N$  and the time domain bin size  $T$  of the phase fitting are related by,

$$f_N = \frac{1}{2T}. \quad (3.23)$$

This Nyquist frequency was set smaller than the filter on the cantilever Fourier Transform. Typical Nyquist frequencies of frequency demodulation were  $100 - 500\text{Hz}$ . Due to time constraints in inverting the nuclei coherent spin signals higher than  $\sim 50\text{Hz}$  were unlikely, making these Nyquist frequencies reasonable in an MRFM experiment.

### 3.5 Noise floor measurements

As discussed in section 1.4.1 frequency shift detection will often be limited by non-thermal frequency noise, meaning frequency noise has typically been observed to be higher than predicted by equation 2.43. Initial measurements of frequency noise spectra, like those shown in figure 3.16 with the cantilever close to the surface agreed with this conclusion.

In general we observed two trends with respect to cantilever frequency noise and cantilever tip composition. First, smaller tips resulted in lower frequency noise as well as lower noncontact friction. Second, metal tips resulted in lower frequency noise as well as lower noncontact friction than semiconductor tips. This indicated that sharp metal tips are best in terms of noise. To assay the noise present in measurements made in the second generation probe we made friction and frequency noise power spectrum measurements as a function of temperature using identical cantilevers. The cantilevers used in this study were single crystal  $\langle 100 \rangle$  silicon  $400\mu\text{m}$  long,  $4\mu\text{m}$  wide, and  $0.34\mu\text{m}$  thick. [74] The tip region of these cantilevers was  $1\mu\text{m}$  wide resulting in a silicon area  $1\mu\text{m} \times 0.34\mu\text{m}$  being presented to the sample surface in the perpendicular geometry. In our noise floor measurements the tips were not metallized and no magnet was present. Work remained in progress to fabricate nanoscale magnetic tips overhanging the ends of these cantilevers, therefore the bare silicon represented a worst case noise floor since we expect metal, magnetic tips to experience less friction and frequency jitter than bare silicon tips as discussed above. Overhanging magnetic tips are ideal from a noise perspective

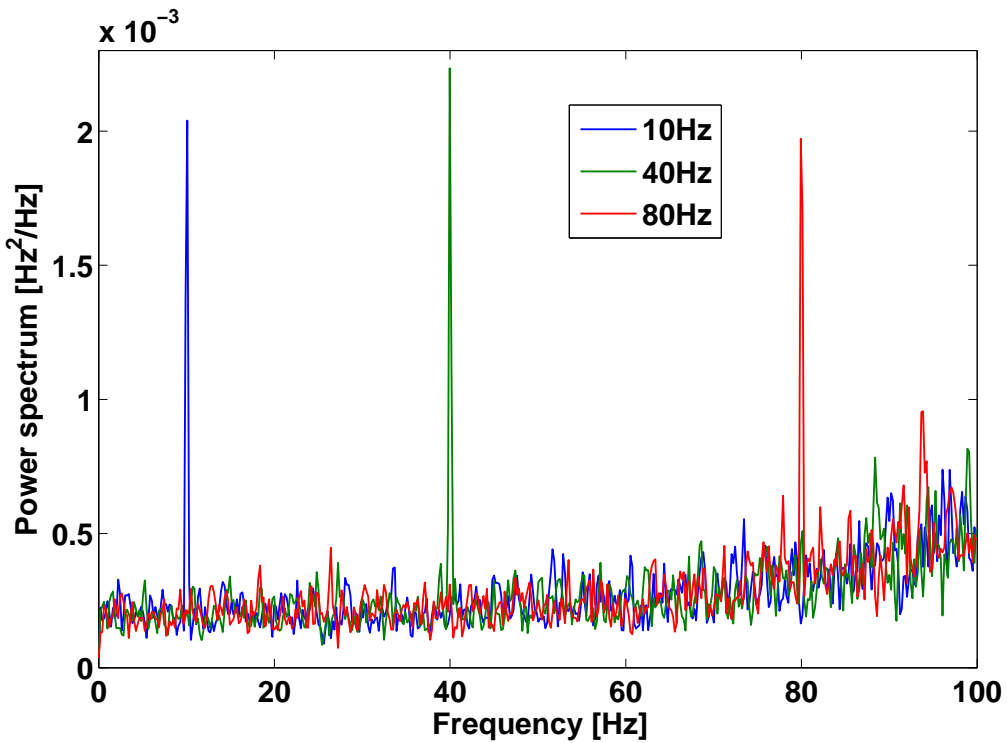


**Figure 3.16:** Cantilever frequency power spectra resulting from cantilever frequency demodulation employed in FORTRAN. For each of the three traces the cantilever frequency was modulated electrostatically. The frequency of the applied modulations were 10, 40, and 80Hz. As expected, peaks are observed at the modulation frequencies in the power spectra. Note the rising noise floor with frequency which is due to detector noise and goes  $\propto f^2$ . [65] The cantilever frequency was demodulated at 200Hz resulting in the Nyquist cut-off frequency of 100Hz.

because they effectively move the higher noise silicon portion of the tip further from the surface of the sample. Figure 3.17 shows frequency noise spectra out to a frequency of 100Hz. The spectral density of frequency fluctuations due to thermal fluctuations is given by

$$S_f^{1/2} = \sqrt{\frac{f_c k_B T}{x_{rms}^2 Q k}} \sim [\text{Hz}/\sqrt{\text{Hz}}]. \quad (3.24)$$

Small discrepancies between the thermal limit and the measured frequency noise can arise from errors in the measurement of  $k$  and  $Q$ . From figure 3.17 we conclude that aside from the  $1/f$  component of the noise the frequency detection is thermally limited at 77K. The dramatic  $1/f$  noise observed at a tip-sample separation of 50nm illustrates the SNR enhancement that can be obtained by coherent spin detection protocols such as iOSCAR or cyclic versions of CERMIT as discussed below. These protocols move the spin signal from zero frequency to finite frequency where the noise floor is lower. The precise origin of the  $1/f$  noise is unknown.

Equation 3.24 predicts a  $\sqrt{T}$  scaling of noise with temperature. Upon cooling to 4K we have not observed this expected reduction in noise (figure 3.18). The data shown in figure 3.18 is a frequency noise spectrum for a cantilever with a hand glued spherical magnetic particle at the tip. For bare silicon cantilevers, like the one used in figure 3.17, we observe a larger difference between the measured noise and the thermal limit (data not shown). We have explored a variety of reasons for the discrepancy between the observed frequency noise at 4K and the thermal limit calculated using equation 3.24. First, we observe a reduction in frequency noise with increasing cantilever drive amplitude as predicted by equation 3.24. Increases in noise with amplitude would suggest nonlinearities becoming appreciable in cantilever dynamics, this appears not to be the case. Second, we measured frequency noise as a function of interferometer laser power and found a small reduction in baseline noise with increasing laser power. This reduction is due to reduction in detector noise with increasing light intensity. [65] Lower frequency noise with higher laser power suggests that laser driving is not adding noise to the cantilever frequency measurement. The non-thermal noise at 4K may be due to tip-sample interactions which were dominant at 77K or to noise in the feedback electronics which only becomes appreciable at the lower thermal limits near 4K. The cantilever position fluctuations scaled as expected by the equipartition theorem suggesting that inadequate heat sinking was not an issue. Also, noise in the tip-sample voltage would induce frequency fluctuations beyond the thermal limit.

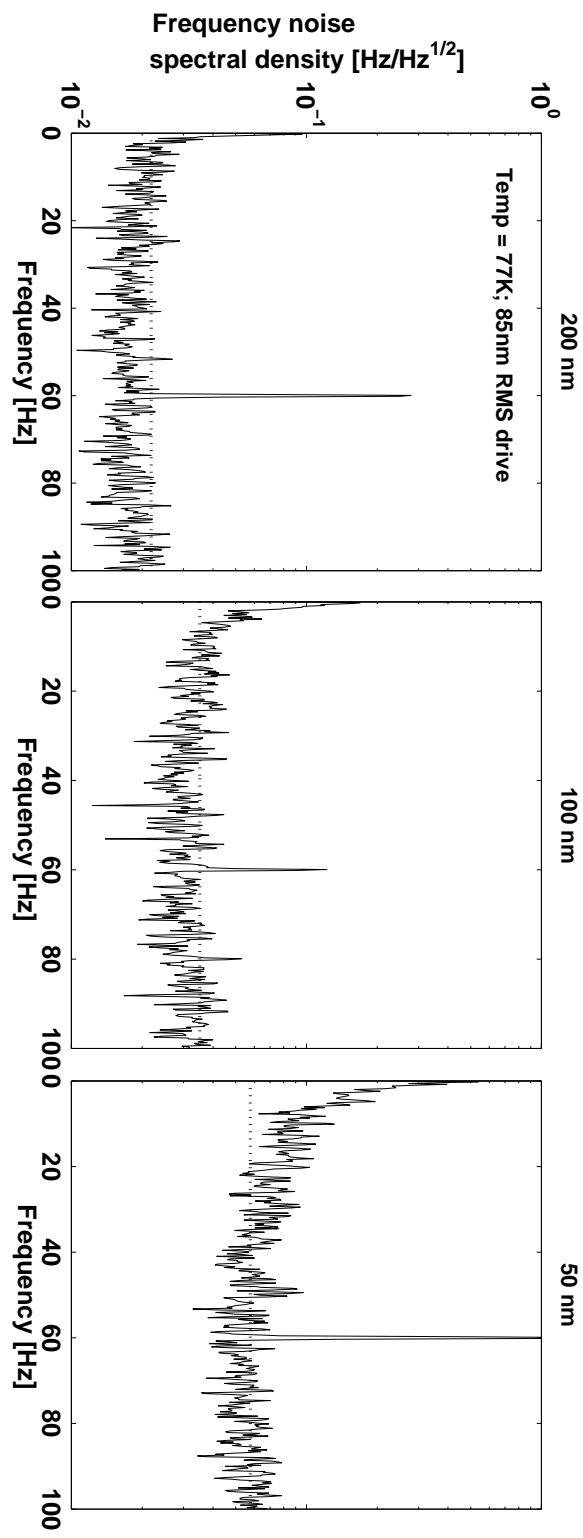
### 3.6 Signal and cyclic CERMIT

Our previous CERMIT experiment [11] was reproduced using the second generation apparatus discussed here. In addition, we obtained preliminary data for a coherent cyclic CERMIT detection protocol where the spin magnetization is modulated at a predetermined frequency. Experimentally, we have demonstrated dramatic advances in instrument reliability. We also made improvements in hardware which will facilitate MRFM experiments requiring rf irradiation synchronous with the cantilever motion. The experimental setup is discussed here.

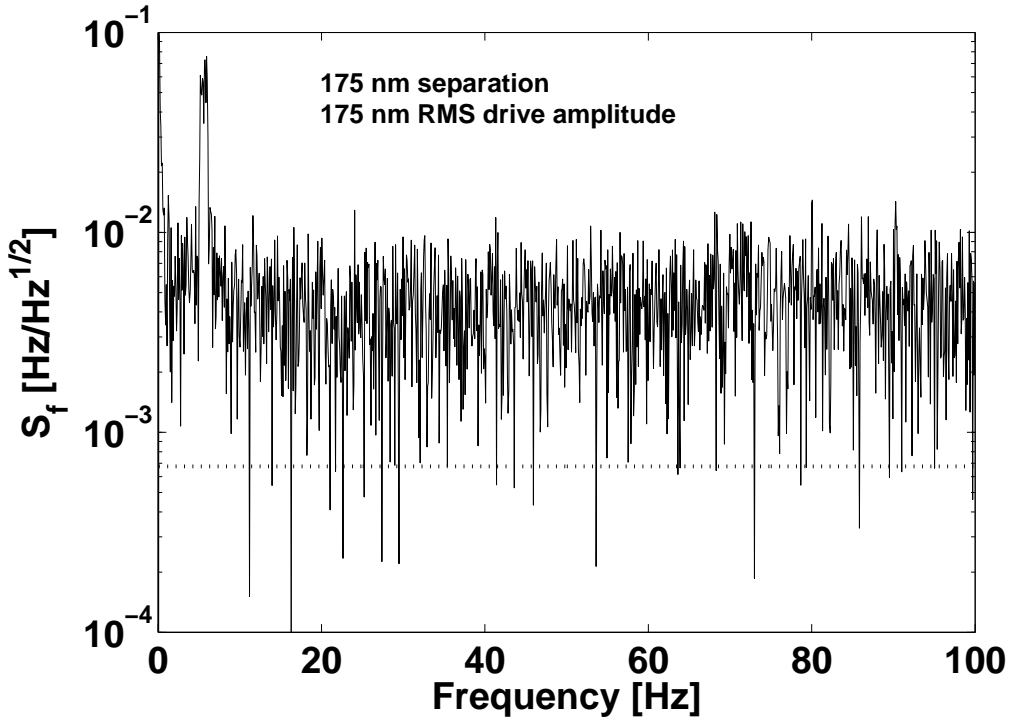
#### 3.6.1 Experimental setup

Figure 3.19 shows a schematic of the setup for a CERMIT experiment. The optical fiber used to interferometrically detect cantilever motion used a 90/10 optical coupler. One branch of the coupler contained the diode laser which was driven by a low noise current source (ILX Lightwave, LDX 3620). The laser diode temperature was set by a temperature controller (ILX Lightwave, LDM 4980) allowing for interferometer tuning. The laser was rf injected to lower laser noise. The other leg of the coupler was sent to an optical receiver and amplifier (New Focus, model 2011FC) which contained a photodiode and a variable bandwidth amplifier. [54] The output of the amplifier produced the cantilever signal and was sent to the feedback electronics and an analog input channel of the NI DAQ PCI board. The feedback circuit locked to the Brownian motion of the cantilever and resulted in self oscillation imparted by the thumper piezo, to an amplitude controlled by an externally set voltage.

Prior to an experiment the cantilever was approached to the surface. Approaching was accomplished by stepping the Attocube forward  $\sim 300\text{nm}$  at a time and measuring the cantilever frequency. The process was repeated until the frequency was observed to change observably due to interactions with the surface. When the surface was visible as a change in  $f_c$  the cantilever was stepped forward followed by a slow voltage ramp which was approximately twice as long as the distance taken in steps prior to the ramp. During the slow voltage ramp the cantilever frequency was monitored with the surface being indicated by an abrupt change in the cantilever frequency. The precise location of the surface was determined by measuring  $Q$  versus piezo extension, extrapolating the data to a point of  $Q = 0$  and assigning this



**Figure 3.17:** Frequency noise power spectra at a temperature of 77K at three tip-sample separations (200nm, 100nm, and 50nm) with a blank silicon cantilever tip 1 $\mu\text{m}$  wide and 0.34 $\mu\text{m}$  thick. The horizontal dotted lines are the thermally limited noise floor as calculated by equation 3.24. The increasing thermal limit is due to noncontact friction reducing the cantilever  $Q$ . Note the onset of  $1/f$  noise at closer separations and the 60Hz Fourier component due to electrical noise.



**Figure 3.18:** Cantilever frequency noise power spectrum at 4.4K and a tip sample separation of 175nm with an 8 $\mu$ m diameter magnetic particle glued to the tip. The peak observed at 10Hz is due to noise in the amplifier being used to apply the tip sample voltage and could be eliminated by using a lower noise voltage source.

location to the surface. The process of surface location is discussed in detail later in section 5.4.4. Once the surface was located, the voltage sent to the piezo was low pass filtered to minimize noise and the cantilever was positioned at a fixed distance from the surface, typically 150 – 250nm for a micron size tip, using a DC voltage applied to the Attocube piezo. The cantilever was placed under self oscillation at a present amplitude of  $\sim 100$ nm or more.

For CERMIT we required an rf frequency sweep of approximately 1MHz in length centered around the rf coil resonance. The rf was synthesized using a Wavetek 302 arbitrary waveform generator. A sinusoid with time dependent frequency was loaded into the Wavetek memory via GPIB using LabVIEW. The Wavetek sample clock was of unknown phase noise, therefore the low phase noise HP rf source was used as an external clock since phase noise will dephase magnetization. The frequency of the clock set the sampling frequency of the waveform loaded into the Wavetek buffer via GPIB. ARP sweeps were typically 10 – 20ms long beginning at 1MHz and ending at 2MHz. The Wavetek was set to an external trigger mode releasing an ARP sweep when triggered by a TTL signal from the pulser (Berkeley Nucleonics, model 565). The Wavetek generated both the in-phase and quadrature channels for the ARP sweep. The ARP generated by the Wavetek was mixed up to the frequency appropriate to the rf coil resonance. For GaAs experiments this frequency was typically 80MHz. This frequency was attained using single sideband mixing with the appropriate carrier frequency. Note that phase errors in the in-phase and quadrature signals from the Wavetek will result in improper mixing and appreciable alternate sidebands. In addition, it is important to zero fill the ARP waveforms at the beginning and end so that waveforms begin and end with zero voltage applied to the Wavetek outputs. Nonzero voltage applied to mixer inputs, by the Wavetek outputs, resulted in carrier bleed through and probe heating. If necessary the output of the mixer may be put through an rf amplifier (Kalmus, model 320-FCP-CE) adding 44 dB to the rf power. A complete schematic of the experimental setup is shown in figure 3.19. The superconducting magnet was ramped to the appropriate field for resonance to be observed.

The measurement then proceeded as follows. The cantilever signal acquisition at high bandwidth was triggered by a TTL pulse from the pulser output on channel A. At a specified time later a second pulse, this time on pulser channel B, was sent to the external trigger of the Wavetek releasing an ARP sweep to the mixer and therefore the rf coil, inverting the spins. In some cases, a second pulse on channel B was sent to the Wavetek triggering a second ARP from the Wavetek

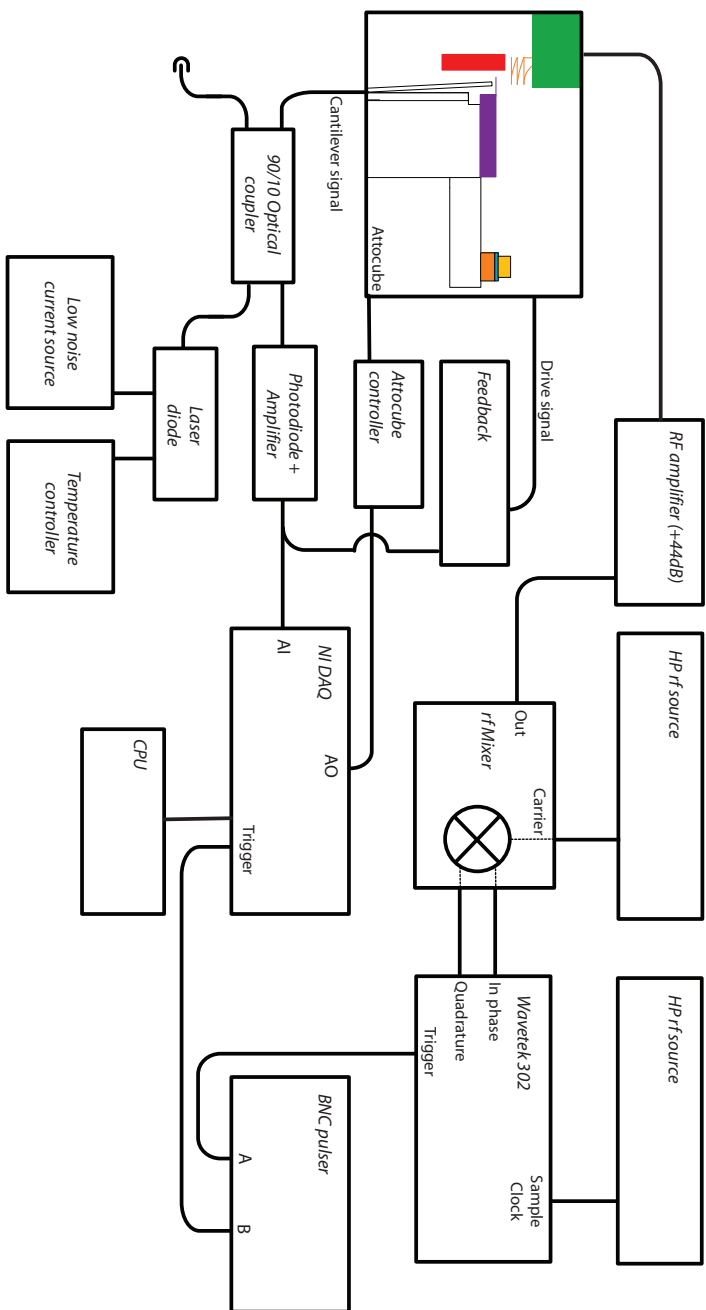
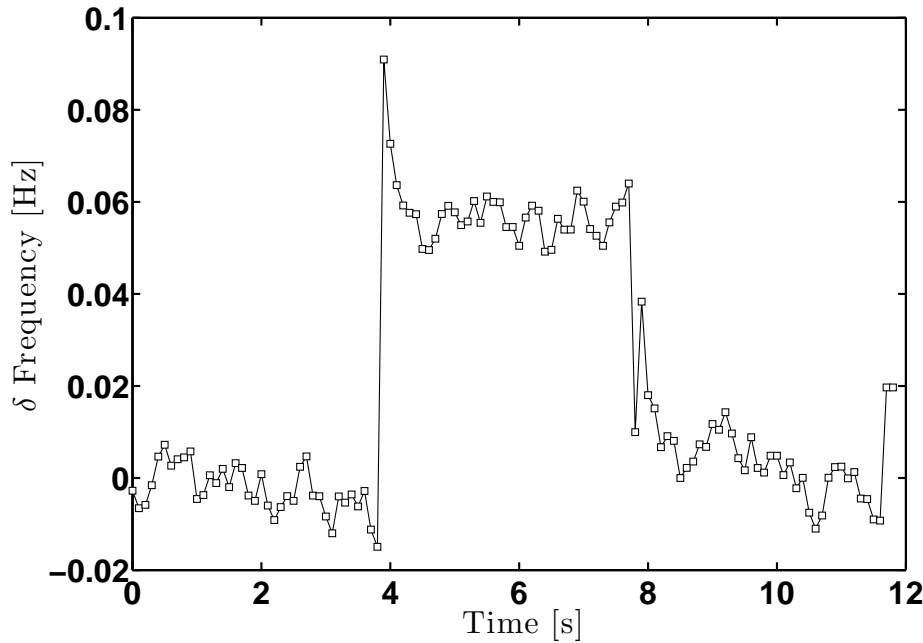


Figure 3.19: Experimental setup for a CERMIT. Details are contained in the text.



**Figure 3.20:** CERMIT signal from the second generation probe from  $^{69}\text{Ga}$  nuclei at an applied field of 8.61T and a temperature of 4.4K. ARPs were triggered by the pulser at 4s and at 8s. The cantilever frequency was demodulated in software as described with a Nyquist frequency of 5Hz. The noise floor at this demodulation bandwidth was 5.3mHz yielding a signal to noise ratio of 10.8.

resulting in the recovery of spin magnetization along the applied field.

Before and after the ARP frequency sweeps were sent to the probe, the cantilever signal was digitized at a high rate. The resulting data was post processes as discussed above and the cantilever frequency as a function of time, along with the frequency power spectrum, was displayed. Any frequency shifts due to force-gradient MRFM could then be observed. Successive transients could also be averaged if necessary.

The entire experiment was executed via custom software written in LabVIEW and saved directly as a Matlab data structure using a Matlab code node within LabVIEW. Acquisitions of the cantilever signal digitized at 100kHz for more than 60s resulted in system slow downs and crashes due to excessive RAM consumption.

### 3.6.2 CERMIT signal

Figure 3.20 illustrates signal arising from  $^{69}\text{Ga}$  nuclei and acquired using the experimental setup described above and shown in figure 3.19. The gyromagnetic ratio for  $^{69}\text{Ga}$  is 10.237 MHz/T which is a 60% naturally abundant isotope of Gallium. At this temperature and field  $^{69}\text{Ga}$  has a Curie law magnetization density of 0.106J/Tm<sup>3</sup>. The rf coil resonance frequency was 87.250MHz, the match was within 1% at 4.4K. The ARP sweeps were 1MHz wide spanning the coil resonance. The rf frequency was swept in the same direction each time. Therefore, the second inversion resulted from an anti-locked ARP where the magnetization vector was pointing in the opposite direction from the effective field in the rotating frame.

An  $\sim 8\mu\text{m}$  nickel particle was hand glued to the tip of the cantilever as described previously. Due to the large size of the tip the experiment occurred in the magnet parallel to the width of the cantilever as shown in figure 3.4. The geometry was accomplished using a different microscope stage than the one pictured in figure 3.14. The stage used here is shown in figure C.8. The tip sample separation was 275nm where, at high field, the cantilever  $Q$  was 32000. The spring constant was  $2.2 \times 10^{-4}\text{N/m}$  and the cantilever was self oscillated 175nm rms.

**Table 3.2:** Number density and magnetization density per tesla for protons in polystyrene and the three NMR active isotopes in GaAs.  $^{69}\text{Ga}$  is 60.4% abundant and  $^{71}\text{Ga}$  is 39.6% abundant.

Isotope/Sample	Density $\rho$ [ $\#/m^3$ ]	Magnetization Density/Field [J/T $^2$ m $^3$ ]
$^1\text{H}/\text{Polystyrene}$	$2.2 \times 10^{28}$	0.166
$^{69}\text{Ga}/\text{GaAs}$	$1.33 \times 10^{28}$	0.012
$^{71}\text{Ga}/\text{GaAs}$	$8.7 \times 10^{28}$	0.013
$^{75}\text{As}/\text{GaAs}$	$2.2 \times 10^{28}$	0.0046

## DC CERMIT

The spin induced frequency shift of 56.1mHz shown in figure 3.20 corresponds to a spring constant change of  $1.5 \times 10^{-8}\text{N/m}$ . Looking back at our rough estimate for the spring constant change in a CERMIT experiment we note that for these parameters equation 3.7 gives  $\delta k = 4.3 \times 10^{-8}\text{N/m}$  within a factor of 3 of the measured value! The ARP sweep of 1MHz corresponds to an effective field sweep of 0.1T which is a bowl of spins approximately 800nm deep. We estimate the second gradient over that region to be  $2.5 \times 10^{10}\text{T/m}^2$ . We therefore attribute the frequency shift to a total magnetic moment of  $6 \times 10^{-19}\text{J/T}$ . The Curie law magnetization per nucleus is  $8 \times 10^{-30}\text{J/T}$ , meaning that the signal results from  $8 \times 10^{10}$  nuclei and that the minimum number of measurable nuclei was  $8 \times 10^9$ . Therefore, the sensitivity of these measurements was comparable to our previous experiment. We observed MRFM signal from both  $^{69}\text{Ga}$  and  $^{71}\text{Ga}$  ( $\gamma = 13.607\text{ MHz/T}$ ) , with the coil tuned at 87MHz  $^{75}\text{As}$  ( $\gamma = 7.2899\text{ MHz/T}$ ) was not accessible in our 9T system. Magnetization and number densities for several isotopes are given in table 3.2. Note in figure 3.20 that the cantilever frequency did not immediately stabilized after the ARP sweep but first underwent a transient spike. We believe that this was not due to a spin interaction with the magnetic tip, but instead due to an electrostatic interaction with the coil. Also, note that the cantilever frequency did not appear to completely recover after the ARP at 8 seconds. This might have been due to incomplete inversion of the spin magnetization. Incomplete recovery might be due to violations of the adiabatic condition during rapid passage or due to regions of spin magnetization being saturated by rf irradiation, resulting in a net magnetization of zero in those regions.

## cyclic CERMIT

Due to the  $1/f$  noise as shown in figure 3.17 it would be advantageous to make the CERMIT signal appear at nonzero frequency where the noise floor is lower. To do this we applied repeated ARP sweeps to the sample at predetermined intervals  $\tau$ . The spin signal should then appear at  $1/2\tau$  in the power spectrum of the cantilever frequency fluctuations since the magnetization returns to its initial direction every other ARP sweep. To show that repeated inversions of sample magnetization could be observed we applied an ARP sweep every 3 seconds for 27 seconds. The resulting cantilever frequency as a function of time is shown in figure 3.21. The application of ARP sweeps resulted in short lived transients in the cantilever frequency. These transients have been removed from the data shown in figure 3.21. These transients are typically much larger than the observed frequency shift due to the CERMIT effect. An example of the rapid shift in cantilever frequency due the application of ARP's is shown in figure 3.22. Transients were observed as both positive and negative frequency shifts.

To produce spin signals at higher frequencies requires more rapid modulation of the spin magnetization. Measurements were undertaken with  $\tau = 0.2\text{s}$  which would result in a spin signal at 2.5Hz in the cantilever frequency power spectrum. RF transients in these data sets dominated the cantilever frequency in the time domain. These transients made data analysis difficult since they obscured the spin induced frequency shifts. Attempts to remove these transients without disturbing the cantilever power spectrum were not successful. Clean cantilever modulation will require careful consideration of the origin of these transients.

One problem with modulated detection methods using ARP's was that the width of the ARP in time rapidly approaches the ARP repeat time,  $\tau$ , at spin modulation frequencies where the signal to noise advantage of modulation is present. For example, to modulate the magnetization at 10Hz requires the application of an ARP sweep every 50ms. If the ARP sweep is 10 – 20ms long then much of the detection time is spent on spin inversions. This negates, to some extent, one of the advantages of the CERMIT protocol which is to detect the spins when the rf is turned off and to minimize the time the spin spends locked to  $H_1$  where relaxation is rapid. In addition, it was not determined if the length of time that the rf is on effects the cantilever frequency transient response.

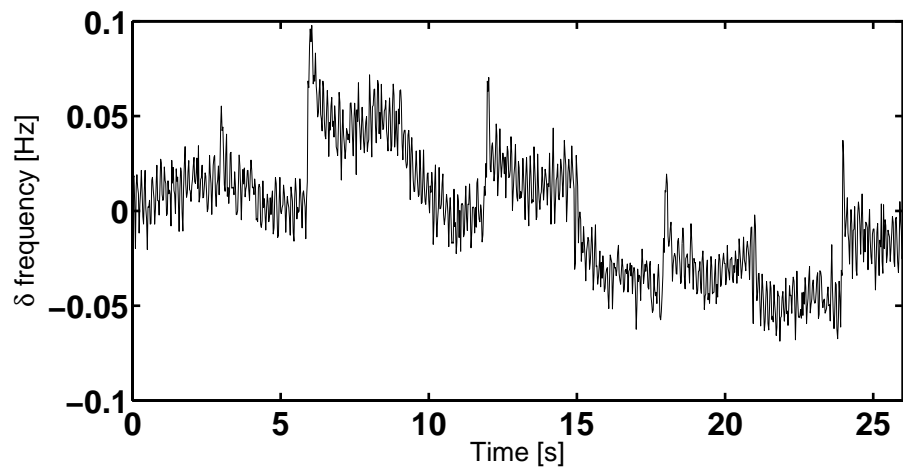


**Figure 3.21:** Slow modulations of the cantilever frequency. An ARP sweep was applied every 3 seconds. The ARP sweeps were 10ms long. Clear steps in the cantilever frequency are visible. This modulation frequency was too low to be observed in the power spectrum of the time domain frequency data due to  $1/f$  noise, but demonstrates that multiple inversions are possible. Short lived transients in the cantilever frequency induced by the ARP sweeps have been removed as discussed in the text.

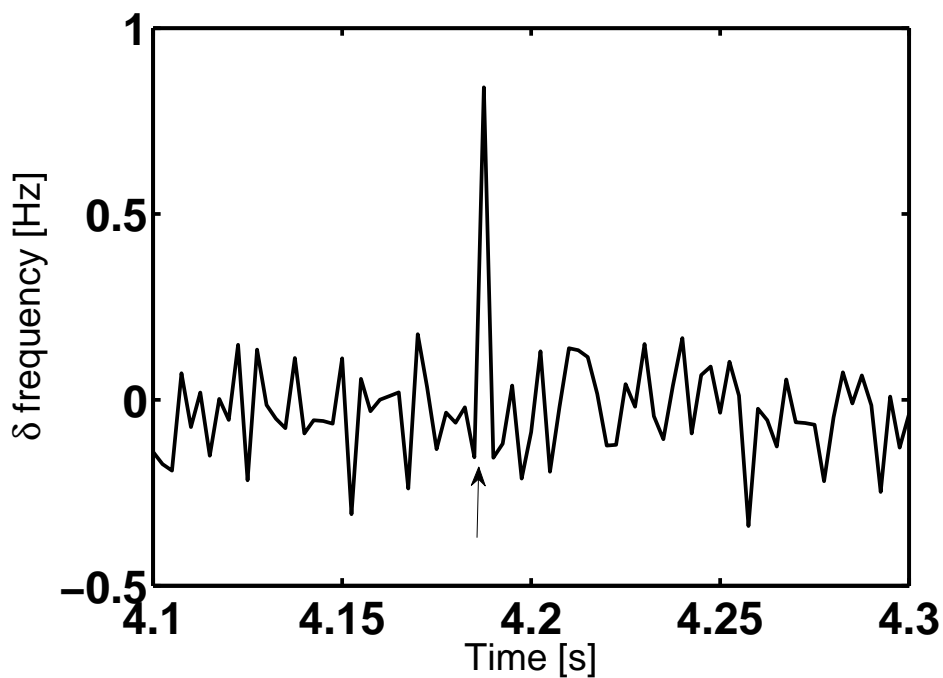


**Figure 3.22:** An example of the transient response of the cantilever frequency to the application of an ARP sweep. The ARP was applied at the time marked with an arrow.

The optimal protocol may therefore be a combination between the OSCAR inversion and the CERMIT detection. In this protocol the spins would be inverted using the OSCAR mechanism where the rf is turned on when the cantilever is at an extremum of its motion and turned off when it reaches the opposite extremum. In OSCAR the rf the irradiation frequency is not swept, as it is the motion of the cantilever which inverts the effective field in the rotating frame. [33] Since the cantilever frequency was 1522Hz this would require the rf be on for only  $\sim 300\mu\text{s}$ . This reduction in time comes at the expense of making the adiabatic condition more difficult to satisfy and therefore higher rf power or smaller volumes of inverted nuclei. The modulated experiment could then proceed by flipping magnetization periodically using the OSCAR protocol, detecting the inversion using the CERMIT protocol and demodulating the cantilever frequency to observe the spin signal in the power spectrum. Very recently such a protocol was successfully implemented. [75] Mamin *et. al* detected nuclear magnetic resonance in  $\text{CaF}_2$  with a sensitivity of 1200 nuclei at a base temperature of 600mK. They successfully imaged patterned  $\text{CaF}_2$  on the tip of the cantilever with a resolution of 90nm.

### 3.7 Conclusions

We have demonstrated the detection of magnetic resonance as a force-gradient using the CERMIT protocol. This protocol confers two major advantages. First, the spin signal may be detected for a time  $T_1$  and does not require a long spin-lock lifetime, allowing its application to many samples not previously accessible to MRFM measurement. Second, the rf duty cycle was greatly reduced with respect to other protocols, reducing the heat load on the cryogenic apparatus. We have demonstrated a detection sensitivity of  $\sim 10^9$   $^{69}\text{Ga}$  nuclei equivalent to  $10^5$  polarized proton magnetic moments.

We have successfully demonstrated the effect in a proof of concept apparatus and constructed an entirely new apparatus with increased reliability and usability making future experiments significantly easier to perform.

### 3.8 Future directions

As outlined, a cyclic CERMIT protocol will increase the signal to noise in the force-gradient detection demonstrated here. Clean modulation of spin magnetization will be required to achieve this, as might be obtained by inverting nuclei using OSCAR.

There are two remaining technical challenges which must be addressed: understanding the mechanisms of noise which set the force sensitivity of a cantilever and the construction of small magnetic tips. The former is the subject of the latter half of this thesis. The latter is currently under investigation. [74] Decreasing the tip magnet increases the field gradient and second gradient increasing the per spin signal while decreasing the total signal. At the time of this writing we were fabricating magnetic tips with electron beam lithography having dimensions  $600\text{nm} \times 200\text{nm} \times 1000\text{nm}$ . Using our noise measurements we can simulate the expected signal numerically from these magnets and project an SNR for the CERMIT protocol. The results are shown in figure 3.23. Even with the well above thermal noise we predict an SNR of  $\sim 4$  for these magnets.

The central advantage of CERMIT is its exploitation of the long  $T_1$  relaxation and its obviating the need for long, coherent spin manipulations. This advantage could be exploited to study a variety of samples, for example organics, not previously studied by high sensitivity MRFM. While applications of MRFM have been limited, and with even modest increases in sensitivity high resolution imaging might open exciting routes to apply MRFM to chemical and biological systems.

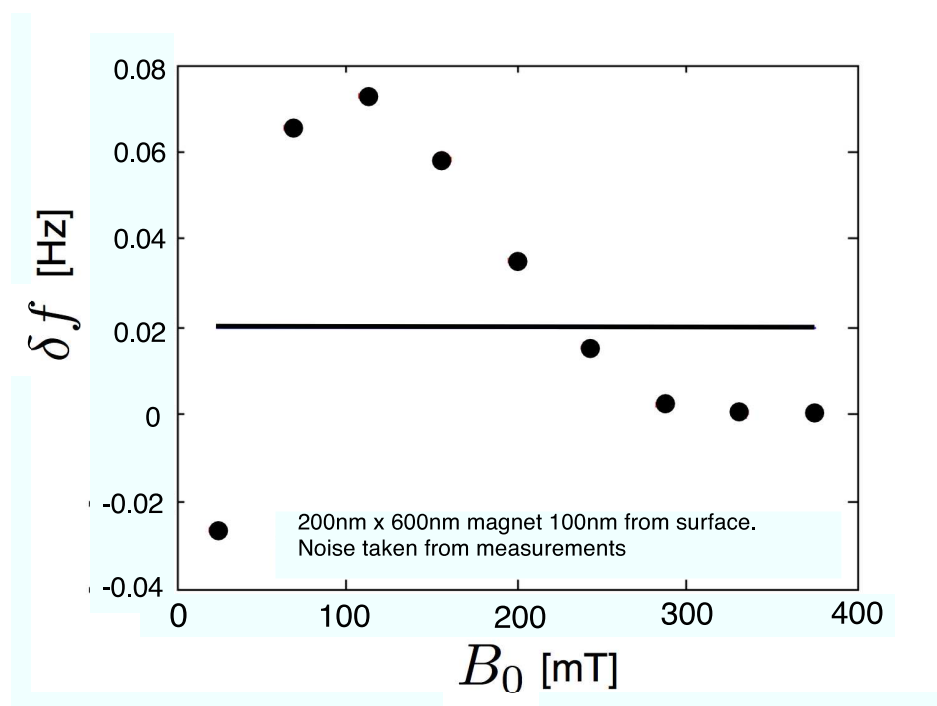


**Figure 3.23:** Numerical estimate of CERMAT frequency shift for magnet dimensions shown. The horizontal line is the measured noise level in a 1Hz bandwidth at 100nm tip sample separation. Each point results from a 1MHz ARP sweep.

## CHAPTER 4

### INTRODUCTION TO NONCONTACT FRICTION

With the advent of high sensitivity, low spring constant, audio frequency cantilevers, the detection of attonewton forces became a possibility for the first time. [30,31] These cantilevers initiated the detection of attonewton forces while simultaneously becoming susceptible to a new regime of noncontact friction. These cantilevers possess low intrinsic friction,  $\Gamma_0 = 10^{-11} - 10^{-13}\text{Ns/m}$  given by:

$$\Gamma = \frac{k}{\omega_0 Q} \quad (4.1)$$

with  $Q = \pi\tau f_0$ ,  $\omega_0 = 2\pi f_0$ ,  $k$  the spring constant and  $\tau$  the  $1/e$  decay time with which cantilever oscillations damp out. For audio frequency cantilevers, low intrinsic friction is achieved through reducing  $k$  while maintaining as high a  $Q$  as possible.

The remaining chapters of this thesis present our efforts to understand noncontact friction between the tip of a high sensitivity cantilever and a nearby sample surface. Here we report the first experimental demonstration that noncontact friction can arise from dielectric fluctuations within the sample. [76] We also present the first experimentally validated theory of noncontact friction which describes friction over dielectric substrates. [77] This chapter presents the relevance of noncontact friction to MRFM and the relevance of noncontact friction to fields other than force microscopy. The chapter concludes with an intuition for the fluctuation-dissipation theorem and a basic, phenomenological understanding of noncontact friction. We continue by outlining previous theoretical and experimental work to understand the effect and preliminary measurements of noncontact friction in our laboratory.

#### 4.1 Noncontact friction and MRFM

For MRFM to be successful we must detect some of the smallest forces ever measured (table 1.1). Equation 2.44 sets the ultimate limits on force and force-gradient detection by a classical harmonic oscillator.  $\Gamma$ , the friction experienced by the cantilever, is the figure of merit when evaluating the sensitivity of an oscillator. As mentioned in section 1.2.3, cantilevers in MRFM experiments experience two types of friction: intrinsic friction  $\Gamma_0$  and noncontact friction  $\Gamma_s$  between the tip of the cantilever and the surface of the sample. These contributions to the cantilever friction are additive. Therefore equation 2.44 may be written as,

$$F_{\min} = \sqrt{4(\Gamma_0 + \Gamma_s)k_B T}. \quad (4.2)$$

It has been universally observed that  $\Gamma_s$  increases with decreasing tip-sample separation. For the highest sensitivity MRFM measurements  $\Gamma_s > \Gamma_0$ , allowing noncontact friction to limit the sensitivity of the measurement. [11,17,18,32,34] This is in contrast to most force microscopy experiments where  $\Gamma_0 \gg \Gamma_s$  making noncontact interactions negligible. Increases in friction with smaller separations are detrimental to MRFM where signal increases with decreasing tip sample separation due to increasing field gradients. Essentially what we have done is to carefully engineer high sensitivity cantilevers, only to have that sensitivity destroyed in the context of an experiment by deleterious tip-sample interactions! In principle, there is some optimum tip-sample separation with respect to MRFM signal to noise. However, as yet no comprehensive theory for noncontact friction has been put forth, making the determination of this optimum working distance empirical. More importantly, efforts to minimize noncontact friction cannot proceed rationally without a detailed understanding of the mechanism. It is not known how noncontact friction scales with the frequency of the cantilever  $f_c$ , making it impossible to rationally design the oscillator to minimize this interaction. Understanding the mechanism of noncontact friction is of critical importance if MRFM is to reach the force sensitivities required for single nucleus detection.

#### 4.2 Noncontact friction in other fields

While noncontact friction has become sensitivity limiting for MRFM, it has also played a role in a variety of seemingly disparate fields. Noncontact friction has emerged as a phenomenon central to the dynamics of micro and nanomechanical systems. Studies of fundamental physical phenomena such as the Casimir effect using micromechanical systems are often limited by noncontact friction. [78,79] Micromechanical systems have also been proposed as tools to study gravitation at very small length scales. [80] Noncontact friction is especially important as we work to make mechanical oscillators with higher quality factors for industrial applications. [19]

In addition to micromechanical systems, noncontact friction has been observed in many systems where charge is diffusing or moving relative to a nearby surface. In experiments with trapped atoms near surfaces noncontact friction

has been shown to be a relaxation mechanism for these systems proposed as a route to quantum computation. [81, 82] Other examples include electrons in 2D quantum wells [83] and charge diffusion in self assembled monolayers on metal surfaces. [84, 85]

### 4.3 Dielectric fluctuations and friction

Our work has demonstrated that noncontact friction between the tip of a cantilever and a nearby substrate can result from dielectric fluctuations. The first implication that dielectric fluctuations could result in friction came from studies of ion mobility in aqueous solutions. For spherical objects moving through a medium, the viscous drag is described to first order by the Stokes formula, where drag scales linearly with the size of the particle. [86] This was found to be adequate to describe an ion's drag as it moved through a fluid under the influence of an electric field, so long as the radius of that ion was sufficiently small. At larger atomic radii, the drag experienced by ions was shown experimentally to increase more rapidly than predicted by the Stokes formula. [87] The extra contribution to the friction was shown over a period of several years to result from interactions between the ions and dielectric fluctuations in the solvent. [88–92]

Dielectric fluctuations have also been shown to be important in the dynamics of biological molecules. [93] In this smaller body of work, fluctuations in water have been shown to play an important role in the function of proteins as they sample dynamic conformations in time. [94] In addition, dielectric fluctuations are, in some cases, responsible for decoherence in Josephson qubits. These qubits are proposed as a route to quantum computation which requires long coherence times to facilitate calculations. [95]

Dielectric fluctuations have been a subject of study in their own right for some time. [96–98] Much work has been completed to understand the dynamics of polar molecules in the condensed phase. Dielectric fluctuations have been a subject of study with respect to dynamics in glass forming materials where it is thought that concerted motion of multiple domains is important in the formation and stability of glasses. Dielectric impedance spectroscopy, discussed in more detail later in this thesis, has been used extensively attempting to untangle complex dynamics in glass forming materials [95] by studying these materials in the bulk while varying the microscopic structure or composition of the sample. [99–101] Glass transitions in thin polymer films have been studied for suspended polymer films. [102] The effects of confinement and surfaces on dynamics have also been studied. [103]

Dielectric fluctuations have also been measured directly using scanned probe microscopy. Vidal-Russell and Israeloff detected dielectric fluctuations as low frequency fluctuations in the fundamental frequency of a cantilever near a dielectric surface. [104–109] They observed telegraph noise that they attributed to concerted motion of domains in PVAc near the glass transition. These measurements concentrated on low frequency fluctuations in the cantilever resonance frequency, typically  $< 1\text{Hz}$ , arising from dielectric fluctuations. These measurements, along with data acquired via solid-state NMR [110–112], are representative of the handful of studies elucidating microscopic dynamics in polymers near the glass transition. It remains an experimental challenge to interrogate glassy dynamics.

To understand the relationship between dielectric fluctuations and friction we must first consider the fundamental physical processes that lead to friction, namely stochastic forces.

### 4.4 Fundamentals of friction: fluctuation-dissipation

Friction has been fundamentally linked to random forces since Einstein's seminal paper in 1905. [113] The result of his work, the Einstein relation, describes the Brownian motion a free particle,

$$D\Gamma = k_B T \quad (4.3)$$

where  $D$  is the diffusion constant and  $\Gamma$  is the friction or dissipation exerted on the particle due to its interactions with the environment. Equation 4.3 was the first in a class of relations generally referred to as fluctuation-dissipation relations. The Einstein relationship holds for a free particle with zero average potential energy. A simple intuition for equation 4.3 is helpful in understanding friction in general and noncontact friction in particular. A complete discussion and derivation can be found in [86].

To appreciate the Einstein relation consider a free particle in a fluid. Intuitively we know that the particle will undergo random motions. Einstein realized that those random motions were a consequence of the random forces exerted on the particle by the fluid. The diffusion constant, with units of  $[\text{m}^2/\text{s}]$ , is a measure of the mean squared deviation of the particle's position, from its starting position, per unit time. The larger the diffusion constant, the faster the particle leaves its initial position.  $\Gamma$  is the friction or dissipation that the particle experiences as it moves through the

fluid, corresponding to the viscous drag opposing the particle's motion. The Einstein relation tells us that the more drag a particle experiences from its environment the more slowly it will diffuse. The link between friction and diffusion comes from the random forces arising between the particle and its environment. Random forces cause diffusion simply by knocking the particle around. The same random forces also dissipate energy as we move the particle through the medium. The larger these random forces are the more dissipation, or drag the particle experiences. Loosely, in a high friction regime the particle frequently encounters large forces from the environment which overcome its inertia and force it to change direction, thus confining the particle to a small region of space. In a low friction regime the particle experiences only small forces from the environment and therefore can traverse long distances between two events which change its direction. The particle therefore can diffuse long distances. These heuristic arguments will be formalized below.

#### 4.4.1 Fluctuation-dissipation for cantilevers

Following arguments similar to those presented in section 2.3.1 we can derive an expression analogous to the Einstein relation for a cantilever. Throughout this derivation we assume that the cantilever experiences white noise from the bath and that the system is linear. A cantilever can be treated as a particle bound by a harmonic potential. For a free particle, diffusion can persist indefinitely resulting in arbitrarily large deviations from the starting position. For a bound particle, this must not be the case, for persistently larger deviations from the equilibrium position would require more and more energy, but we assume that the system is in equilibrium therefore the expectation value of the total energy must be constant in time.

Begin with the equipartition theorem (equation 2.32). Calculate the mean squared displacement of the oscillator using Parseval's theorem (equation 2.31) using the same approximation as before for the integral and we have,

$$\langle x^2 \rangle = S_x(f_c) \frac{f_c}{Q} \quad (4.4)$$

where  $S_x(f_c)$  is the spectral density of the position fluctuations at resonance. Using the definition of the quality factor in terms of cantilever friction (equation 4.1) and plugging  $\langle x^2 \rangle$  into the equipartition theorem we have:

$$k \left( S_x(f_c) \frac{2\pi f_c^2 \Gamma}{k} \right) = k_B T. \quad (4.5)$$

Rearranging we get,

$$S_x(f_c) \Gamma = \frac{k_B T}{2\pi f_c^2}. \quad (4.6)$$

Equation 4.6 is analogous to the Einstein relation for a cantilever with  $S_x(f_c)$  playing the role of the diffusion constant.  $S_x(f_c)$  gives us a measure of the magnitude of the equilibrium fluctuations of the cantilever at its resonance frequency due to interactions with its environment. Equation 4.6 says that higher friction (lower  $Q$ ) oscillators exhibit smaller on-resonance fluctuations while lower friction (higher  $Q$ ) oscillators exhibit larger on-resonance fluctuations. One often missed implication of equation 4.6 is the fact that lower friction oscillators, and therefore higher sensitivity oscillators, undergo larger fluctuations due to interactions with their environment than high friction, low sensitivity, oscillators. One might intuitively believe that smaller fluctuations, that is smaller  $S_x(f_c)$ , would be better for measuring small forces because a small deflection might be easier to detect, but this is not the case. To see why, consider the response of the oscillator to a coherent on-resonance force. The response  $x$  of the cantilever will be

$$x = \frac{k}{F} Q. \quad (4.7)$$

where  $F$  is the applied force. Using equation 4.6 we can calculate the on-resonance equilibrium fluctuations of the cantilever due to its interaction with its environment,

$$x_{min} = \sqrt{S_x(f_c)b} = \sqrt{\frac{k_B T}{2\pi f_c^2 \Gamma}} = \sqrt{\frac{Q k_B T b}{k f_c}}. \quad (4.8)$$

where  $b$  is the bandwidth of the measurement. By taking the ratio of equations 4.7 and 4.8 we see that the signal to noise ratio for an on resonance position measurement goes as,

$$SNR \propto \sqrt{Q}. \quad (4.9)$$

We know from equation 4.6 that higher  $Q$  oscillators exhibit larger fluctuations, but equation 4.9 also tells us that high  $Q$  oscillators yield better SNR than low  $Q$  oscillators. The reason for this is that while lower friction results in larger position fluctuations, the response of the oscillator to an on resonance force increases more rapidly than the fluctuations as friction decreases.

The minimum detectable force for a harmonic oscillator is theoretically *independent of frequency*. That is, the SNR for an on resonance force and a periodic force applied far from  $f_0$  will be identical. The scaling shown in equation 4.9 for position fluctuations holds regardless of the frequency of the applied force. This should not be surprising given that the system is assumed to be driven by white noise. In practice, the off resonance thermal motion will be small, and therefore require a more sensitive detection scheme. It is therefore often advantageous to detect on resonance forces where the noise in the measurement will be limited by the Brownian motion and not the detector noise floor.

### Stochastic forces

Underlying our discussion of fluctuations and friction are random forces. Stochastic forces between the cantilever and its environment result in the position fluctuations  $S_x(f_c)$ . By transforming equation 4.6 from position fluctuations to force fluctuations we can derive a more familiar expression for the dissipation experienced by a harmonic oscillator. Recalling the relationship between position fluctuations and force fluctuations given by equation 2.36 and plugging that relation into equation 4.6 we have,

$$\left(\frac{Q}{f_c}\right)^2 S_F(f_c) \Gamma = \frac{k_B T}{2\pi f_c^2}. \quad (4.10)$$

where  $S_F(f_c)$  is the fourier component of the force fluctuations at the cantilever frequency. This relationship simplifies to,

$$\Gamma \approx \frac{1}{k_B T} S_F(f_c). \quad (4.11)$$

Equation 4.11 is often called the fluctuation-dissipation theorem, in this case for the classical harmonic oscillator. Our derivation resorted to some approximations, the correct relationship between friction and force fluctuations is given in appendix E. This relation tells us that the friction experienced by the cantilever depends linearly on the spectral density of the force fluctuations at the resonance frequency of the oscillator. Equivalent relationships can be derived rigorously using the Langevin formalism as discussed in appendix B. This relationship holds as written only for underdamped oscillators where the cantilever ringdown time  $\tau >> 1/f_c$ . Equation 4.11 provides a basis for considering theoretical and experimental studies of noncontact friction.

#### 4.4.2 Phenomenology of friction in force microscopy

Returning to the problem of noncontact friction discussed in section 4.1 where we noted that the friction experienced by the cantilever is dominated by interactions with the surface of the sample. Equation 4.11 tells us that interactions between the tip of the cantilever and the surface must be increasing the spectral density of force fluctuations at the cantilever resonance frequency. Therefore, to understand the mechanism of noncontact friction between the cantilever and the sample we must uncover the origins of these force fluctuations.

Consider the tip of a cantilever close to a surface as shown in figure 4.1. The tip of the cantilever in this case does not have a magnetic particle attached, but the fundamental physics of noncontact friction is unchanged. As discussed in chapter 3, we are able to apply a bias between the tip and the sample. This applied bias will result in some charge induced on the tip of the cantilever  $+q$ , and the sample,  $-q$ . The charge on the tip is given by

$$q = C(V_{ts} - \phi) \quad (4.12)$$

where  $C$  is the tip-sample capacitance and  $\phi$  is the contact potential difference (CPD) between the tip and the sample. [53] We then propose that there is a time-random electric field,  $\delta E_x(t)$  in the direction of cantilever motion which originates from the sample. At this point we do not speculate as to the origin of this electric field, we require only that it be random and originate from the sample. There will then be a random force exerted on the cantilever tip in the direction of motion

$$\delta F_x(t) = q\delta E_x(t). \quad (4.13)$$

We then need only to take the spectral density of these force fluctuations at the cantilever frequency to calculate the resulting friction via equation 4.11. This spectral density will be the real portion of the Fourier transform of the

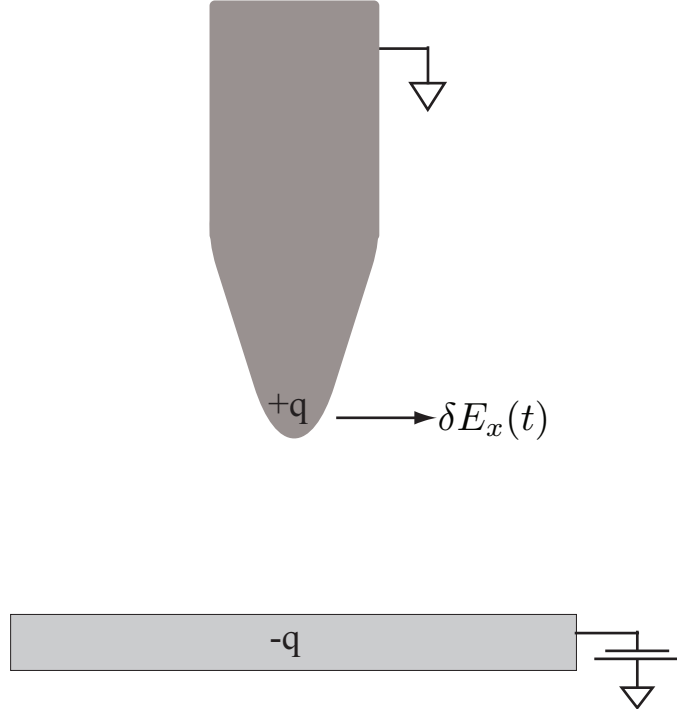


**Figure 4.1:** A cantilever tip close to the surface of a conducting sample. The motion of the cantilever is in the plane of the page. We may apply a bias ( $V_{ts}$ ) between the tip of the cantilever and the sample.

autocorrelation function of these force fluctuations,

$$S_F(\omega_c) = 4 \int_0^\infty dt \cos(\omega t) \langle \delta F_x(t) \delta F_x(0) \rangle. \quad (4.14)$$

The factor of 4 is explained in appendix E. Plugging into equation 4.13 we have

$$S_F(\omega_c) = 4q^2 \hat{C}'_{xx}(\omega_c) \quad (4.15)$$

with  $\hat{C}'_{xx}(\omega) = \int_0^\infty dt \cos(\omega t) \langle \delta E_x(t) \delta E_x(0) \rangle$  the Fourier transform of the electric field fluctuations. Using the exact form of equation 4.11 (appendix E) and our expression for the tip charge, the friction may be written as

$$\Gamma = \frac{C^2(V_{ts} - \phi)^2}{k_B T} \hat{C}'_{xx}(\omega). \quad (4.16)$$

An equivalent phenomenology was first presented in [22]. What we have accomplished is a translation of the question from how friction arises in a tip-sample system like the one depicted in figure 4.1 to how electric field fluctuations might arise from the sample in such a system. Stipe *et. al* [22] do not speculate as to the exact mechanism of field fluctuations between high sensitivity cantilevers and metals.

### Tip charge

Equation 4.16 raises the important question - what if there is no charge on the tip of the cantilever? That is, what if we dial the tip sample voltage to the CPD making  $V_{ts} - \phi = 0$ ? Will the noncontact friction vanish? The CPD between two materials is essentially the difference in their ionization potential. For the metallized cantilever tips considered in this thesis the tip metal is polycrystalline. The contact potential is a function of the crystal plane. Since the tips used here contain multiple facets they are also comprised of multiple contact potentials. Since we can apply only a single voltage  $V_{ts}$  to the cantilever we imperfectly match the CPD, resulting in some charge on the tip. In principle this will be case for any cantilever tip which is finite in size which must include edges with contact potentials different from the

bulk surface sites. Therefore, any metal tip will contain some, if very small, amount of charge when brought close to a surface.

We may also consider nonconducting probes near surfaces. For such probes this phenomenology will not apply directly. Insulating probes may be macroscopically neutral, but may be subject to polarizing fields and therefore time dependent induced polarization which may also result in friction. [40] Practically, the fabrication of charge free insulators is technically difficult. This difficulty may be best reflected by the fact that the lowest levels of noncontact friction ever measured have been between two metal objects. [22, 76]

## 4.5 Previous work

Previous efforts to understand noncontact friction have focused on either measuring the magnitude of friction experienced by a cantilever or theoretical work postulating mechanisms for fluctuating forces arising between objects in close proximity.

### 4.5.1 Experiments

Early work on noncontact friction focused on exploiting it to measure electrical properties of semiconductors locally. Denk and Pohl [114] were the first to image semiconductor heterostructures using dissipation force microscopy. Using high sensitivity cantilever in the perpendicular geometry Stowe *et. al* were able to measure doping levels in silicon by noncontact friction. [115] Imaging was achieved with 100nm spatial resolution.

Initial work directed towards understanding noncontact friction using high sensitivity cantilevers by Stipe *et. al* measured dissipation using a conducting probe over metal and quartz substrates at tip-sample separations down to 2 nm and temperatures from 4 – 300K. [22] Friction over  $\gamma$ -irradiated quartz samples, of interest to electron spin MRFM experiments, was found to be orders of magnitude higher than that over metals. Noncontact friction was found to decrease with temperature by approximately a factor of 6 from 300K to 77K and by another factor of 6 between liquid nitrogen temperature and 4K. Interestingly, friction over Au(111) was found to be 7 orders of magnitude larger than predicted by Coulomb drag theories. [116] Coulomb drag theories sought to explain noncontact friction by calculating the  $i^2r$  losses as the induced surface charge,  $-q$  in figure 4.1, moved during cantilever oscillations. Stipe *et. al*'s measurements made it clear that there must be other mechanisms of noncontact friction present in the measurement.

Stipe *et. al* [22] further showed that previous measurements of noncontact friction [117] were flawed due to their measurement scheme. They showed that measurements of noncontact friction required the direct measurement of cantilever decay times or fluctuation correlation times, and that fitting the power spectrum of cantilever fluctuations could result in large measurement errors.

Most of the theoretical work on noncontact friction since 2001 has been directed towards understanding the high levels of friction measured between the gold coated tip and the gold sample in [22].

### 4.5.2 Theory

Theoretical work on noncontact friction has focused on explaining the origins of electric field fluctuations over surfaces.

In 1998 Persson *et. al* [116] considered two infinite slabs of conductors separated by a small distance and in parallel relative motion. This study treated the fluctuations quantum mechanically and their resulting fields classically. The authors concluded that friction due to quantum fluctuations falls off rapidly as  $\Gamma \propto e^{-2Gd}$  where  $G$  is the reciprocal lattice basis vector and  $d$  is the separation; while friction due to thermal fluctuations went as  $1/d^6$  for surface contributions and  $1/d^4$  for bulk fluctuations.

Further developments were presented in 2002 by Volokitin and Persson. [118] Here the authors generalized their previous result to a small particle with arbitrary dispersive and absorptive dielectric properties moving parallel to a metal surface. The field was treated classically and used to calculate the force of friction on a dipolar particle. The friction was found to have a quadratic dependence on voltage in both [116] and [118]. Persson extended this analysis to perpendicular motion [119] so as to be relevant to standard AFM experiments. Here he presented for the first time the possibility of resonant photon tunneling between the tip and the sample enhancing the noncontact friction.

Zurita-Sanchez *et. al* describe another derivation of friction resulting from fluctuating thermal fields. [40] This treatment was novel, addressing an oscillating neutral particle classically and the field quantum mechanically. The authors found that the friction depended on fourth order correlation functions between the induced dipole in the particle, and the electric field or the electric field-gradient. Four such correlation functions were derived and their physical origins

discussed and contribution to the friction calculated numerically. The authors concluded that the large discrepancy between theory and experiment in, for example [22], was due to the composition of the *substrate* on which the metal film was evaporated. Our measurements call this conclusion into question, but do not provide an unambiguous test of their theory.

Recently, it has been postulated by Volokitin and Persson [120] that in certain cases thermal fields could become resonant with modes in the surface, thereby promoting photon tunneling and thus dissipation between the cantilever and the surface. This mechanism requires that the surface contain modes which are of low enough energy (frequency) to be excited by thermal fields. This condition is said to be met by semiconductor surface plasmons and possibly certain adsorbate vibrational transitions. [39] At yet, no measurements of noncontact friction have been made using high sensitivity cantilevers in ultrahigh vacuum. Without these measurements the contribution to noncontact friction by surface adsorbates, which are certainly present in our measurements, cannot be determined.

Most recently, Chumak et. al [79] calculated both the electrostatic force and the dissipation from a charged sample such as  $\gamma$ -irradiated silica on a cantilever. They considered the effect of the Casimir force. They claim that the Casimir force is of appreciable magnitude for low resistivity substrates. These forces are calculated for cylindrical, spherical and ellipsoidal tip shapes. More general formulations, applying to neutral polarizable objects moving near surfaces, have also been put forth. [121]

Since the publication of the work presented in this thesis, fully quantum mechanical derivations of noncontact friction including dielectrics and 2-D electronic systems have been presented. [122, 123]

Aside from measurements by Stipe *et. al* no measurements prior to the work presented here had explored the mechanism of noncontact friction at very high levels of sensitivity. In fact, no theory of noncontact friction had been experimentally validated.

## 4.6 Preliminary observations

Our work on noncontact friction was motivated by both the necessity of understanding the effect and the limitations it places on MRFM sensitivity and the lack of data to test theories of noncontact friction. Prior to constructing an apparatus specifically to measure noncontact friction using high sensitivity oscillators we made some observations with respect to tip composition and noncontact friction.

Figure 4.2 compares noncontact friction between sharp and blunt silicon cantilevers over a metal surface. The sample was thermally evaporated gold on RCA cleaned silicon substrates. Thermal evaporation proceeded at a rate of 0.01nm/s with a 5nm chromium adhesion layer and 200nm of gold. The surface was characterized by conventional AFM and was found to have a roughness of 0.6nm rms. The sharper cantilever experienced dramatically lower friction. This indicated that smaller magnetic tips, which are advantageous to MRFM due to their higher gradients, will experience lower noncontact friction near a surface. Further measurements have shown that metal tips experience lower friction than semiconducting doped silicon tips. These measurements indicated that the optimal tip for an MRFM experiment would be a small magnetic particle protruding from the end of the cantilever. The protrusion would work to effectively move the high friction, semiconducting silicon far away from the sample surface while allowing  $d$ , the distance from the magnet to the target spins, to be as small as possible. Figure 4.2 shows that even for a very large silicon tip the silicon need only be a few hundred nanometers from the surface to minimize the noncontact friction. Therefore the magnet must protrude approximately 200nm to minimize surface friction due to interactions between the silicon of the cantilever shaft and the surface.

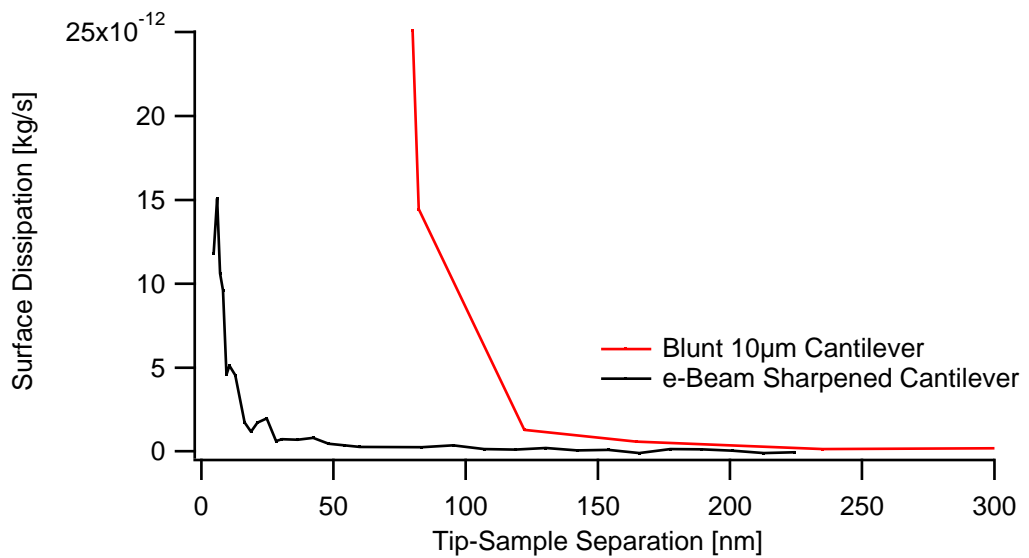


**Figure 4.2:** Surface induced dissipation  $\Gamma_s$  measured as a function of tip sample separation for two cantilevers at room temperature. The black line is dissipation experienced by an cantilever with tip dimensions  $\sim 100\text{nm} \times 340\text{nm}$  fabricated using electron beam lithography. The red line is dissipation experienced by a cantilever with a  $10\mu\text{m} \times 340\text{nm}$  tip fabricated by optical lithography. Both cantilevers are made of doped single crystal silicon. The intrinsic friction  $\Gamma_0$  has been measured far from the surface and subtracted off, yielding only the surface induced contribution to the total friction. Friction was measured over thermally evaporated gold surfaces with a roughness of  $0.6\text{nm rms}$  as measured by conventional AFM. Friction was measured by the ringdown method as discussed in the text.

## CHAPTER 5

### HIGH SENSITIVITY DISSIPATION MICROSCOPE

#### 5.1 Introduction

With the goal of understanding the mechanism of noncontact friction between a high sensitivity cantilever and the surface of a sample we constructed a custom, high vacuum, room temperature force microscope. While high sensitivity MRFM experiments are typically carried out at low temperature there is considerable evidence that the dominant mechanism of noncontact friction is the same at 300K and 4K. [22] Furthermore, by constructing a room temperature microscope we were able to design a system which is simple, facilitating rapid sample and cantilever exchange. We anticipated that many measurements would be undertaken with a variety of samples and cantilevers making reasonable turn around times for sample exchange a necessity. Also, low temperature measurements could be carried out in our MRFM apparatus discussed in section 3.4. Our room temperature microscope utilized high sensitivity cantilevers with metalized non-magnetic tips to study noncontact friction at tip-sample separations of 2nm and greater.

The present chapter is comprised of three sections. We begin by outlining the microscope design and construction discussing cantilever fiber alignment, sample scanning, chamber design and vibration isolation. We then discuss the design and fabrication of cantilevers with low intrinsic levels of friction including the fabrication protocol and design stipulations. Finally, we detail early measurements obtained with the microscope including system calibrations.

#### 5.2 Microscope design

Figure 5.1 (a) shows a picture of the microscope not including the chamber or vibration isolation systems. Details of the microscope super structure are discussed below and in appendix F. Figure 5.1 (b) shows a schematic of the cantilever close to the surface in the perpendicular geometry. Note that the motion of the cantilever is parallel to the surface of the sample. The microscope allows control of the tip sample separation with nanometer scale precision using an Attocube nanopositioner. In addition, we may apply a bias between the cantilever and the sample. This bias is important for controlling the charge on the tip  $q$  as discussed in section 4.4.2.

##### 5.2.1 Perpendicularity

One of the central design restrictions for our dissipation microscope was cantilever perpendicularity. As discussed in section 1.4 low spring constant cantilevers must be approached to the surface of the sample in a perpendicular geometry to allow tip-sample separations of just a few nanometers. Still, if the angle between the surface normal and the cantilever, illustrated in figure 5.2 as  $\alpha$ , is too large the cantilever will snap in to contact long before the tip of the cantilever has approached very close to the surface. This distance of closest approach  $d_{min}$  depends on  $\alpha$ , the cantilever spring constant in the  $x'$  direction and the surface forces present which induce snap-in. In practice estimating the surface forces which induce snap in to contact is difficult making estimates of  $d_{min}$  only approximate. A detailed discussion of surface forces present, and a complete derivation is presented in [64] and will not be reproduced here. If we wish to study noncontact friction at small tip sample separations, a simple estimate of  $d_{min}$  is important in guiding our microscope construction where we must take care to minimize  $\alpha$ .

Table 5.1 shows some values of  $d_{min}$  estimated for cantilever spring constants which have been fabricated in our laboratory. Note that even a  $2^\circ$  misalignment can cause  $d_{min}$  to be large for small spring constant cantilevers. In practice it is not difficult to align two objects to within a couple of degrees, therefore we expect that if we are able to construct a microscope with  $\alpha \leq 2^\circ$  we should be able to approach a  $k \sim 10^{-4}$  cantilever to within a couple of nanometers before experiencing snap-in. While studying noncontact friction at separations of less than 2nm is important for studies of the Casimir force, we set out to undertake experiments elucidating longer range interactions, which bear directly on MRFM sensitivity. Therefore, tip-sample separations of  $\sim 2$ nm were determined to be sufficient.

##### 5.2.2 Cantilever and fiber alignment

Optical fiber cantilever alignment was a critical and challenging design task for cryogenic force microscopes. Our room temperature apparatus did not need to satisfy the stringent alignment conditions discussed in section 3.4.4 but it still needed to satisfy the geometrical consideration shown in figure 3.10. We also required that the cantilever oscillation

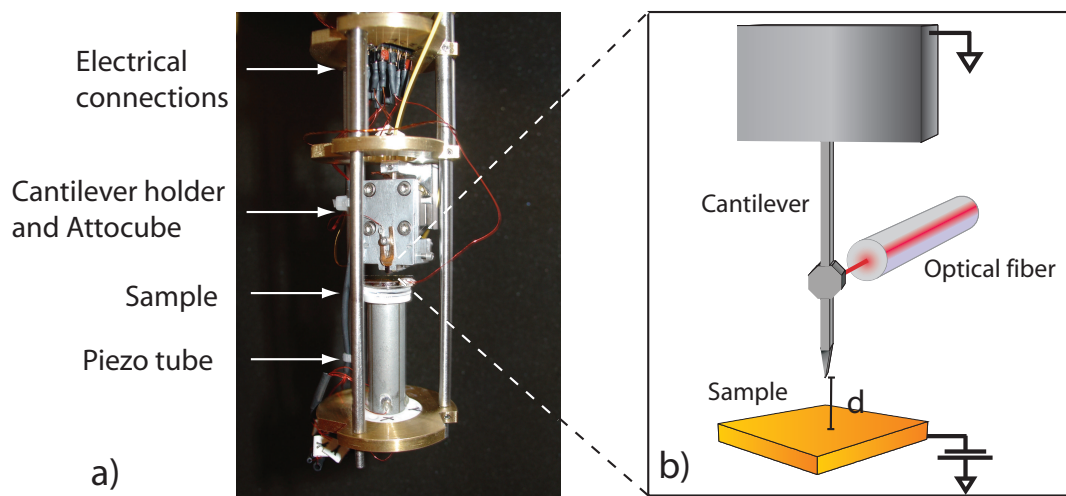


**Figure 5.1:** A photograph and schematic of the dissipation microscope. a) A photograph of the microscope with electrical connections, cantilever holder and attocube, sample, and scanning piezo tube labeled. b) An enlarged schematic view of the cantilever and the sample. The optical fiber for interferometric detection of cantilever displacement is labeled. Note that a bias can be applied between the cantilever and the sample.

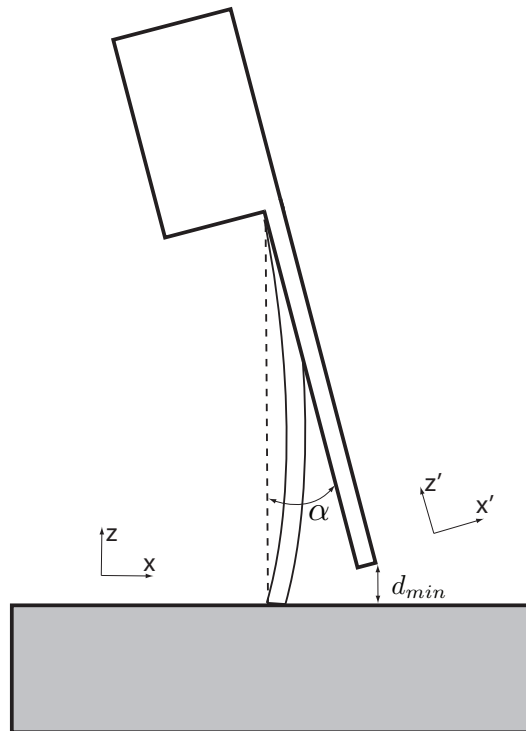


**Figure 5.2:** The effect of angular misalignment for a cantilever in the perpendicular geometry. The angle  $\alpha$  is exaggerated for clarity.  $d_{min}$  is the distance of closest approach for a given  $\alpha$  before snap in to contact occurs due to surface forces. The cantilever moves in the  $\pm x'$  direction.

**Table 5.1:**  $d_{min}$  for single crystal silicon cantilevers of three different spring constants for angular misalignments of  $1^\circ$  and  $2^\circ$ . Data are taken from [64] figure 2.5.

$k$ [N/m]	$\alpha$ [degrees]	$d_{min}$ [nm]
$10^{-3}$	1	1
	2	1.5
$10^{-4}$	1	2
	2	3
$10^{-5}$	1	4
	2	6
$10^{-6}$	1	8
	2	13

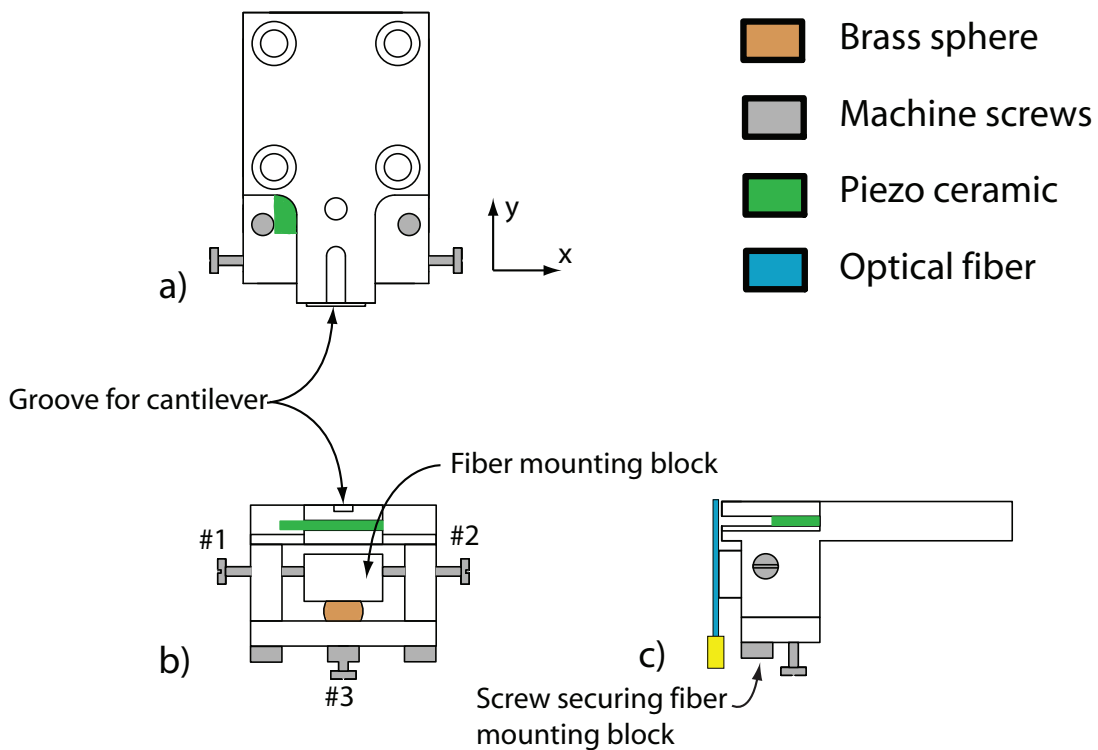


**Figure 5.3:** Schematic of the cantilever and fiber holder designed for the dissipation microscope. a) A top down view of the holder. The four holes were used to mount the holder to the Attocube using #2 – 56 screws. The cantilever points down in this view and the motion was in and out of the page. Electrical connections were made to the drive piezo on the left side. The optical fiber is omitted for clarity. b) A head on view of the holder, the cantilever pointing out of the page. The brass sphere is visible. Optical fiber omitted for clarity. c) Side view of the holder, with optical fiber shown glued to the metal block. Alignment is discussed in the text.

be induced mechanically due to the interactions between the capacitive driving and the tip-sample voltage discussed in section 3.4.6.

A schematic of the cantilever and fiber holder is shown in figure 5.3. The cantilever was placed in the groove (depicted in figure 5.3 (a) and (b)) and the edge of the cantilever die pushed against the machined edge of the groove. The cantilever was held down with a clip (not shown) which also supplied electrical contact to the cantilever die. The fiber alignment mechanism worked as follows. The fiber was glued to the fiber mounting block labeled in figure 5.3 as described in section 3.4.4 with the exception that 5 minute epoxy is used in place of Stycast. Three #0 – 80 machine screws, labeled #1 – 3 in figure 5.3 (b) facilitated motion of the fiber mounting block in the  $\pm x$  and  $-y$  directions as labeled in figure 5.3 (a). The fiber mounting block was attached securely to a 1/8 inch brass sphere by a screw which passed through the sphere and threaded into the block, this screw is labeled in figure 5.3 (c). The motion of the fiber mounting block on the brass sphere was facilitated by a small counter sink in the fiber mounting block (not shown) which resulted in a “ball and socket” style joint between the sphere and the mounting block. Using this simple mechanism several hundred microns of fiber motion was attained. Cantilever fiber alignments could be performed rapidly and cantilever perpendicularity was guaranteed since the cantilever die was aligned directly with the machined surface of the groove. To assure perpendicularity special care was paid to milling machine alignment prior to machining the part. The holder was made from aluminum to minimize the weight carried by the Attocube.

Cantilever driving was achieved by applying an AC voltage to the piezo shown in green in figure 5.3 (a)-(c). As shown the cantilever is at the end of a 0.25 inch lever arm. The piezo expands in the vertical direction in figure 5.3 (c). The slot where the piezo resides was machined using a 0.03125 inch thick slotting saw. The 0.02 inch thick piezo was custom cut on a diamond band saw and electrical connections were made by soldering wires to the electrodes. The piezo was then insulated by repeated spraying with high vacuum sealant (Vacseal). The piezo was installed by painting the inside of the slot with epoxy and then sliding the piezo in position and allowing the glue to dry. This piezo driving design offers several advantages over previous designs [53]. First, the cantilever was not in direct contact with the piezo, making electrical isolation between the two straightforward. Most importantly, changing the cantilever required no ungluing and re-gluing of the drive piezo making cantilever changes rapid. Cantilever oscillations could be induced with small voltages  $\approx 100\text{mV rms}$ . The phase response of the cantilever driving was measured as discussed in section 3.4.6. The response of the resonance was found to be reliable with the appropriate phase relationship. No mechanical resonances were observed in the microscope below 50kHz.

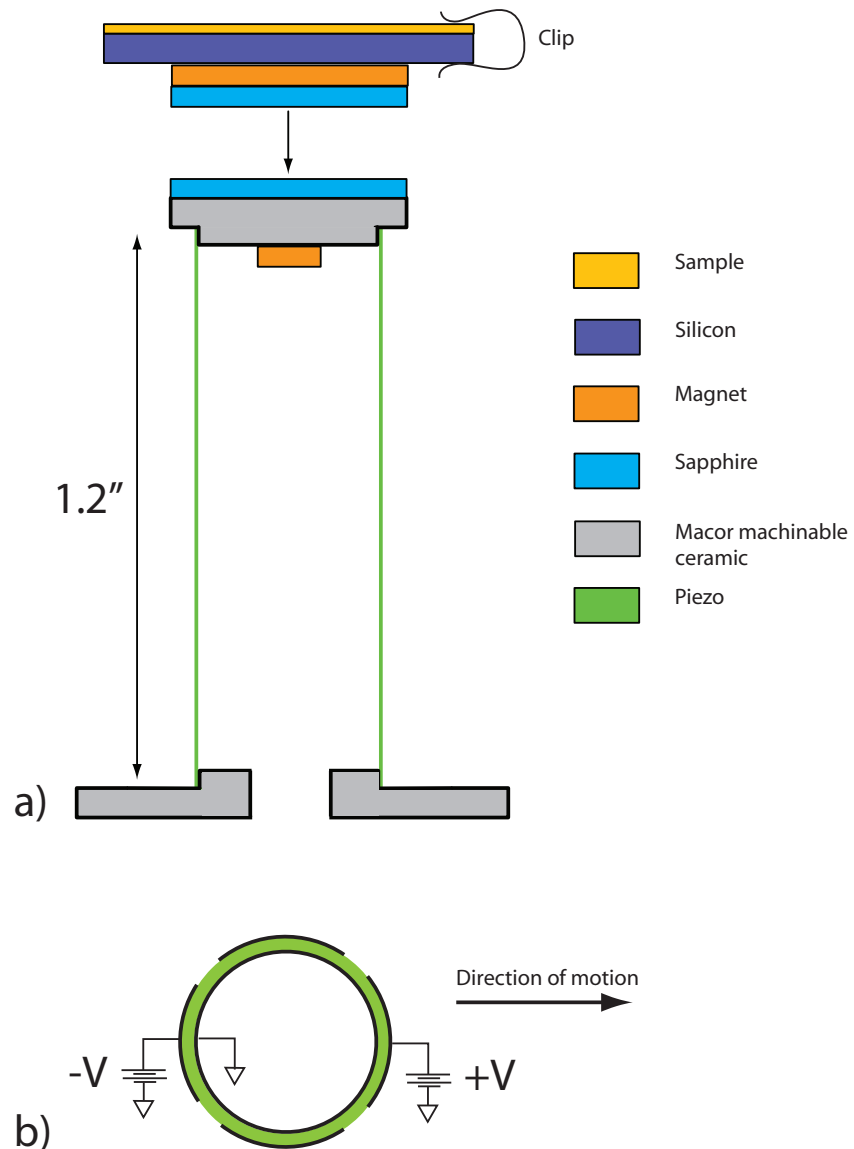
### 5.2.3 Piezo tube scanner

Figure 5.4 shows a schematic of the custom piezo tube scanner constructed for the dissipation microscope. The piezo tube (Physik Instrumente, model PT-130.24) had quartered electrodes on the outside and a single grounded electrode on the inside. Opposite voltages applied to opposing electrodes with the center electrode grounded resulted in motion in the direction of the positive voltage as shown in figure 5.4 (b). Maximum operating voltage was  $\pm 200\text{V}$ . Motion in the orthogonal direction was obtained by applying voltages to the orthogonal electrodes. The motion of the tube was calibrated using a fiber optic interferometer and found to move 50nm per volt applied to the electrodes, corresponding to a scan range of  $\pm 10\mu\text{m}$  in all directions. The directions were shown to move independently.

The scanner was assembled by custom machining parts, shown in grey in figure 5.4 (a), from Macor machinable ceramic (Corning) which is electrically insulating, allowing us to isolate the high voltage electrodes from the rest of the microscope. Machining Macor required very slow machine speeds and sharp cutters to avoid cracking. The piezo tube was affixed to the Macor parts using super glue. At the sample end of the tube a polished sapphire disk (thickness = 0.04in, Meller Optics) was super glued to the Macor cap (figure 5.4 (a)).

To mount a sample on the scanner the sample, typically epitaxial Au(111) on mica, was carefully glued to a 0.5 in  $^2$  piece of 0.5mm thick silicon wafer. The wafer was then glued, using 5 minute epoxy to a disc shaped rare earth magnet (thickness = 0.0625 in, The Magnet Source) which was in turn affixed to a second sapphire disk (thickness = 0.04in) as shown in figure 5.4 (a). The bottom Macor part had a 0.25 inch hole allowing a small rare earth magnet to be dropped into the tube. The sample-silicon-magnet-sapphire was then set on top of the scanner sapphire. The attractive force between the two magnets held the sample to the scanner. Note that there was no glue between the two sapphire disks. Coarse positioning of the sample could then be accomplished by applying rapid voltage pulses to the piezo tube and exploiting a stick-slip mechanism similar to the functioning of the Attocube system. [53]

Electrical contact was made with the sample surface by a clip around the sample and the silicon wafer. A wire soldered to this clip made the electrical connection.



**Figure 5.4:** A schematic of the piezo tube scanner and the tube electrodes. a) The scanner moves the sample in the plane perpendicular to the page. The total range is  $20\mu\text{m}$  at room temperature with maximum voltages of  $\pm 200\text{V}$ . A connectorized wire is soldered to the clip providing electrical contact to the sample. Drawn to scale. b) Top down view of the piezo tube showing quartered outer and continuous inner electrodes. Voltages applied as shown result in motion to the right.

### 5.2.4 Microscope super structure

Figure 5.5 shows a schematic of the microscope super structure. The microscope hangs from soft edge welded bellows to isolate the experiment from ambient vibrations. The structure of the microscope consisted of brass discs joined together by three stainless steel rods. The stainless steel rods slide through holes in the brass discs and are secured by three set screws per disc. There are four brass discs, viewed in profile in figure 5.5 and visible in figure 5.1 (a). From the top down in figure 5.5 these four discs held electrical connections, support the Attocube and cantilever holder, stabilize and stiffen the structure, and hold the piezo tube scanner and sample respectively.

Cantilever sample perpendicularity as discussed above was set by how parallel the brass discs holding the Attocube and scanner could be set. To facilitate the reproducible and precise alignment of these two brass discs, stops were machined into the stainless steel rods on which the discs were mounted. To do this the rods were machined in two parts as shown in figure 5.5. The top section of the stainless rods were 5/32 inch in diameter and thread into a larger brass mass which was attached to the bottom of the bellows. The end of these rods were drilled a tapped for #4 – 40 screws. The subsequent section of stainless rod was 1/8 inch in diameter and threaded to screw precisely into the larger top section of the upper rod. The disc holding the Attocube was machined with 1/8 inch holes such that it could slide freely over the 1/8 inch portion of the rods but stopped at the joint between the 5/32 and 1/8 inch rods, thereby providing a precise stopping point for the disc. The ends of the 1/8 inch rods were turned down to 3/32 inch in diameter providing a stop for the brass disc containing the scanner. All dimensions on the stainless steel rods were machined to 0.004 inches assuring angular misalignments to a degree or better. Machining of the stainless steel rods was crucial to perpendicularity. All tapping and threading was done on the lathe using spring loaded followers. A small counter bore on the #4 – 40 threaded holes in the bottom of the 5/32 inch rods allowed the thinner rod screw in flush to the upper rod providing a seamless stop for the brass disc. All discs were secured with three #2 – 56 set screws. Details of the superstructure are given in appendix F.

### 5.2.5 Chamber and vibration isolation

Our room temperature high vacuum force microscope required careful vibration isolation to allow the cantilever to be approached to within 2nm of the surface reliably. Two sources of vibrations were of concern: ambient vibrations in the building and vibrations traveling down the pump lines from the turbo molecular pump. A schematic of the overall design is shown in figure 5.6. As shown in figure 5.5 the microscope hangs from a flexible bellows. The estimated mechanical resonance of the microscope on these flexible bellows was approximately 5Hz chosen so as not to coincide with the mechanical resonance of the commercial vibration isolation system. The custom vacuum chamber (Nor-Cal) contained three NW50 viewports and one pumpline. The chamber and the pumpline were securely bolted to the top plate of an aluminum box containing 250 lbs lead shot. Lead shot was acquired from the group of Prof. Seamus Davis. The lead shot and chamber sat on a commercial vibration isolation system (Minus-k technologies, model 250BM-3) with a mechanical resonance frequency of  $\sim 0.6\text{Hz}$  laterally and  $\sim 0.7\text{Hz}$  vertically approximated by eye with a metronome. These mechanical resonances were near the 0.5Hz specification for the Minus-k system and present a significant improvement over typical air table or active feedback systems.

The vacuum pump vibration isolation system design was taken from [69]. Briefly, a rigid vacuum line from the chamber joined a “T” joint as shown in figure 5.6. Both sides of the “T” were attached to soft high vacuum edge welded bellows (BellowTech). The lower bellows were capped. The cap was then clamped to the 100 lbs mass. A stainless steel rod, threaded on both ends extended from the clamped cap through the lower bellows, the “T” and the upper bellows to a custom machined brass part where the opposite end of the rod is screwed into the center of the pumpline. The custom brass part centered the rod while allowing air to pass along the sides. This brass part was then clamped firmly to the 100 lb mass as well. In this way the “T” was free to move against the action of the soft bellows but was indirectly supported by the central rod. The 100 lbs mass was a plywood box filled with sand. The sand box sat on sorbothane elastomers (MSC). Sorbothane elastomers were used because sand was generally poor at isolating low frequency vibrations due to the high coefficient of static friction between grains, the soft sorbothane elastomers allowed the large mass to move more readily with the low frequency oscillations that dominate building vibrations. The entire system was pumped out using a turbo pump with a rotary vane backing pump (Pfeiffer). Typical base pressures measured near the pump were  $10^{-6}\text{ mbar}$ .

To facilitate working on the microscope we engineered a structure surrounding the chamber and pumpline with a plywood table just above the chamber. A section of the table just above the chamber could be removed. Upon removal the top flange of the chamber the microscope could be lifted out and placed on a hook allowing it to hang freely above the table. The removable section of table could then be replaced allowing unobstructed work space for sample or cantilever

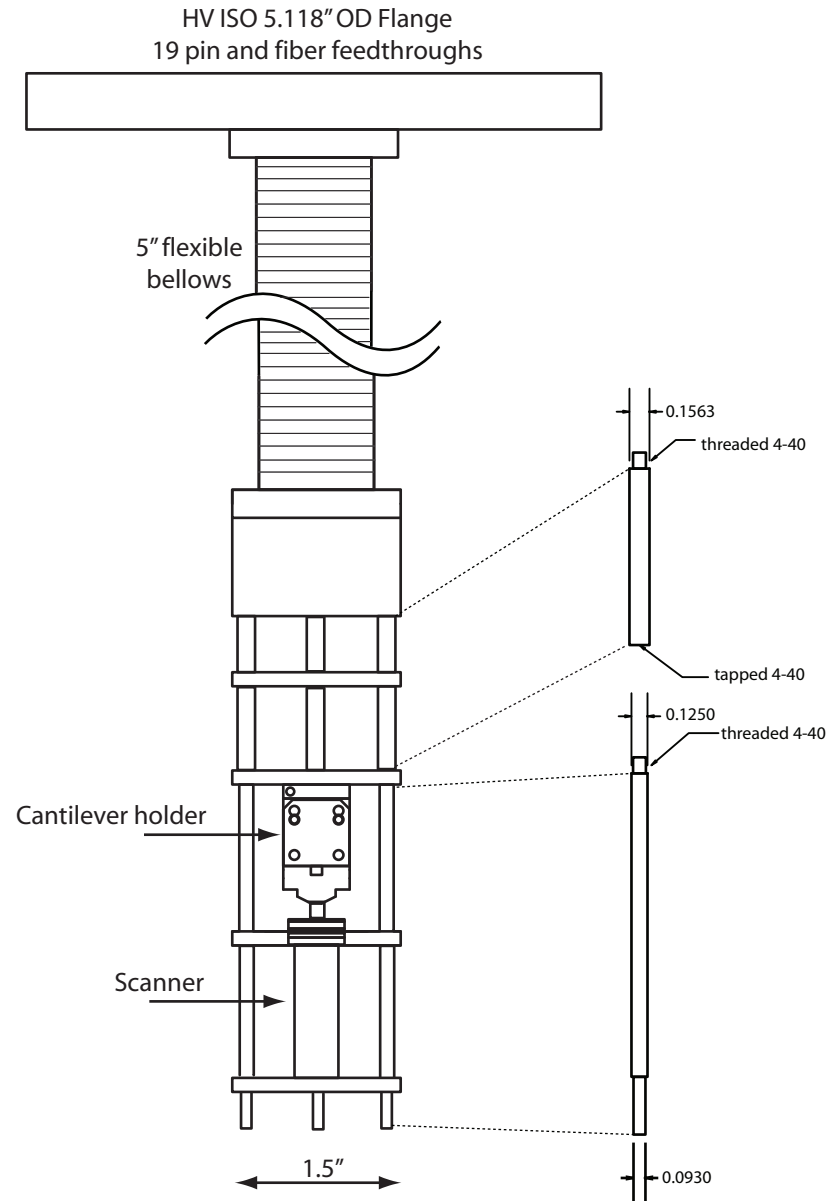


**Figure 5.5:** A schematic of the microscope as pictured in figure 5.1 (a). The cantilever holder is viewed from the same perspective as shown in figure 5.3 (a). The microscope hung from a flexible bellows which was attached to the top flange of the vacuum chamber discussed below. Details of the design and construction are discussed in the text.

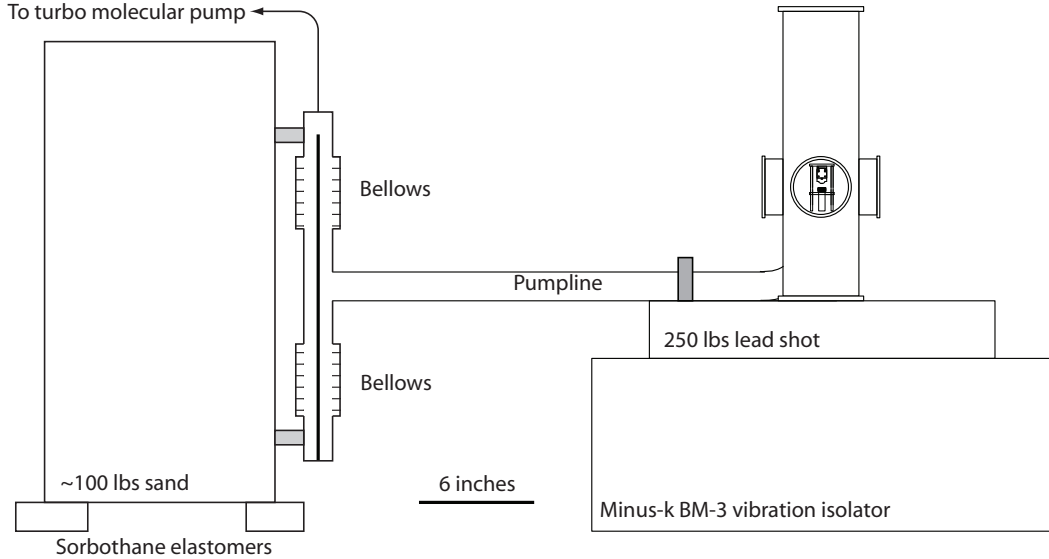


**Figure 5.6:** Schematic of the microscope high vacuum chamber and vibration isolation system. The chamber (figure F.8) was bolted to a 17 inch square aluminum box containing ~ 250 lbs of lead shot. The box sat on a Minus-k commercial vibration isolation system. The pumpline was isolated from turbo pump vibrations using flexible high vacuum bellows attached to a 100 lb mass which rested on sorbothane elastomers. The microscope is visible through the chamber viewport. All high vacuum connections used NW40 hardware. Clamps are shown in grey. Details are presented in the text.

exchange. Figure 5.7 shows a photograph of the apparatus including the table, chamber and vibration isolation. The instrument rack was situated directly to the right as was the computer.

### 5.3 Cantilever design and fabrication

The extraordinary sensitivity of the experiments presented here was a result of the custom fabricated low spring constant cantilevers. These cantilevers had been fabricated previously, [31, 124] and used to detect attonewton [125] and even zeptonewton [12] forces. Detailed cantilever fabrication protocols using silicon-on-insulator (SOI) wafer technology have been outlined previously. [49, 64]

We fabricated cantilevers specifically to study noncontact friction over a variety of substrates in our high vacuum apparatus outlined above. These low spring constant cantilevers were engineered to be used in the perpendicular geometry shown in figure 5.1 with their motion detected interferometrically.

#### 5.3.1 Cantilever design

Engineering cantilevers for high force sensitivity is equivalent to engineering cantilevers with low intrinsic friction (equation 4.1). Our goal in designing these cantilevers was to minimize the quantity

$$\Gamma = \frac{k}{\omega_0 Q}. \quad (5.1)$$

We can express this in terms of the cantilever length  $l$ , width  $w$  and thickness  $t$  as follows

$$\Gamma = 0.29 \frac{wt^2}{l} \frac{12\sqrt{\rho E}}{Q} \quad (5.2)$$

with the density  $\rho = 2330 \text{ kg/m}^3$  and the Young's modulus  $E = 150 \text{ GPa}$ . Equation 5.2 tells us to make cantilevers thin, narrow and long to minimize the friction assuming that  $Q$  does not scale with the cantilever dimensions. We know, in general, that  $Q$  does depend on dimensions and tends to decrease with an increasing surface to volume ratio. If we

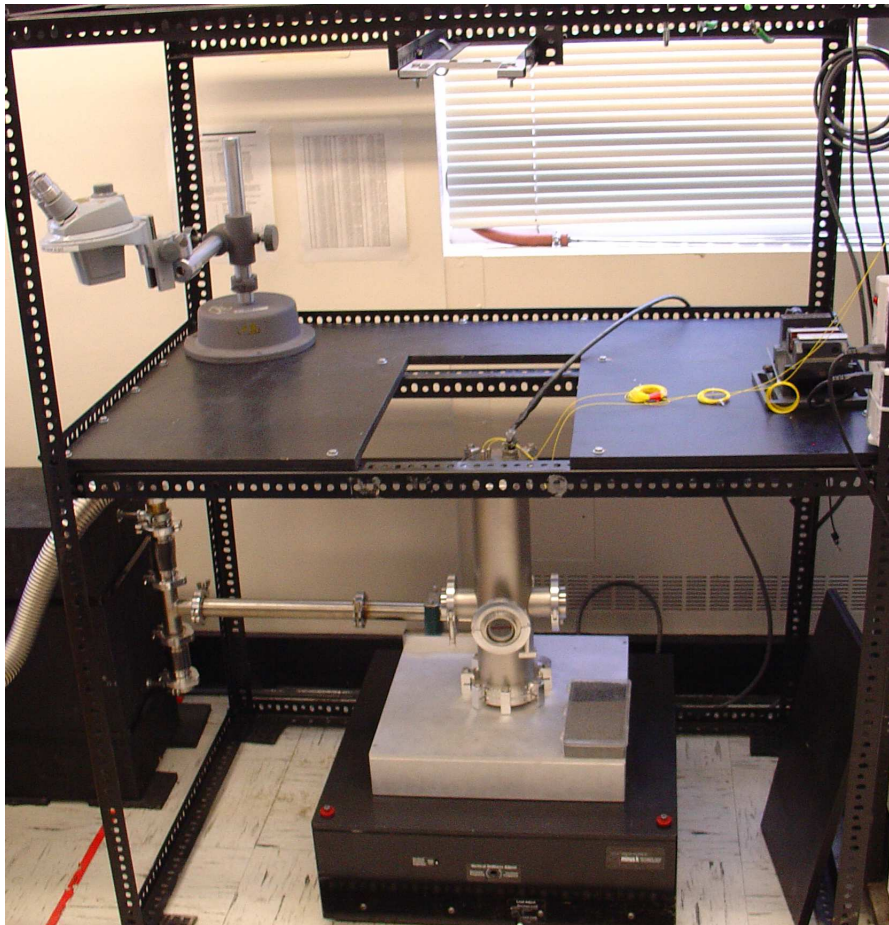


**Figure 5.7:** A photograph of the chamber, vibration isolation system and working space. The top flange of the chamber could be raised through the table and hung on the aluminum hook (top, center) for sample exchanges. The 19-pin cable and yellow optical fibers are visible.

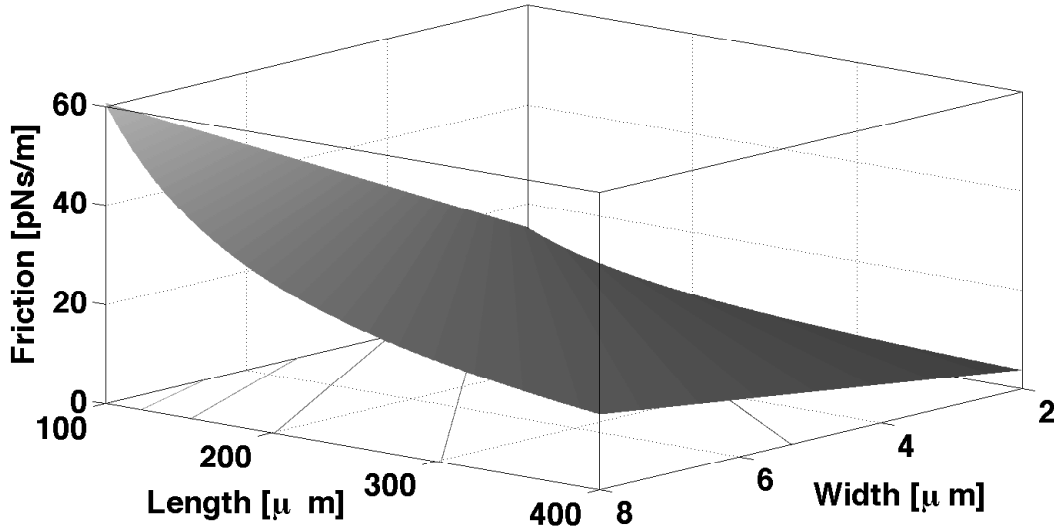


**Figure 5.8:** Equation 5.2 plotted as a function of cantilever length and width for  $Q = 10000$ . Cantilever thickness is  $0.34\mu\text{m}$  set by the SOI wafers readily available at the time of fabrication.

**Table 5.2:** Calculated cantilever parameters for fabricated cantilevers.  $t = 0.34\mu\text{m}$  and quality factor taken to be 10000.

$l [\mu\text{m}]$	$w [\mu\text{m}]$	$f_0 [\text{kHz}]$	$k [\text{mN/m}]$	$\Gamma_0 [\text{pNs/m}]$
175	3	14.3	3.4	13
200	4	11	3	15
225	5	8.7	2.7	16
250	6	7	2.3	18
275	7	5.8	2	19

assume  $Q$  to be a constant over cantilever dimensions similar to those used previously in our laboratory we can predict the friction levels experienced by cantilevers as a function of their dimensions using equation 5.2. Figure 5.8 shows equation 5.2 plotted for typical cantilever widths and lengths for constant  $Q$  and  $t$ . It is clear that fabricating cantilevers with intrinsic friction  $\Gamma_0$  of a few tens of pNs/m is feasible with current technology. In contrast, a typical contact mode silicon nitride AFM cantilever with  $k = 0.01\text{N/m}$ ,  $\omega_0/2\pi = 2\text{kHz}$  and a  $Q$  of  $10^4$  will have  $\Gamma_0 \sim 10^{-9}\text{Ns/m}$ .

In theory, it is advantageous to make our cantilevers as long and thin as possible. In doing so the cantilever frequency will decrease as

$$f_0 = \frac{3.516}{2\pi} \frac{t}{l^2} \sqrt{\frac{E}{12\rho}}. \quad (5.3)$$

Due to  $1/f$  noise of unknown origin at very low frequencies it is not advantageous to make  $f_0$  too small. Also, we typically observe  $Q = \pi\tau f_0 \sim 10^4$  at room temperature. For such high quality factor cantilevers the ringdown time will become long as  $f_0$  decreases. For example, a cantilever with  $f_0 = 500\text{Hz}$  and a  $Q = 10000$  will have a ringdown time  $\tau = 6.3\text{s}$ ! At cryogenic temperatures we have observed ringdowns in excess of 20 seconds. In order to measure friction as a function of distance we would like to be able to acquire cantilever ringdowns as rapidly as possible to facilitate many measurements in a reasonable amount of time. We therefore decided to construct cantilevers with resonance frequencies in the  $5 - 10\text{kHz}$  range resulting in  $\tau < 1\text{s}$ .

From table 5.2 it appears that shorter cantilevers are better given our restriction on the cantilever frequency. In

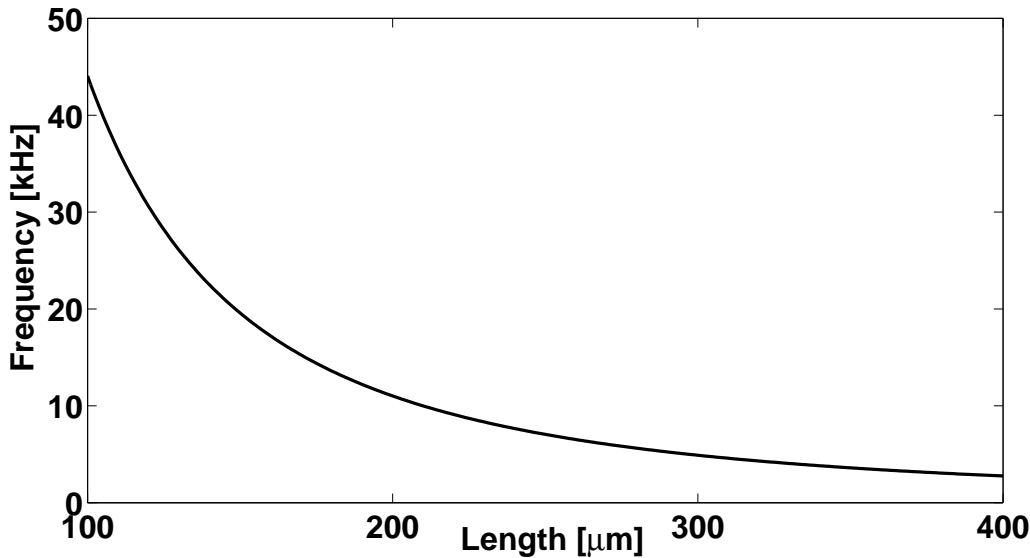


**Figure 5.9:** Equation 5.3 plotted for cantilevers from  $100\mu\text{m}$  to  $400\mu\text{m}$  long as in figure 5.8 and  $t = 0.34\mu\text{m}$ .

general this is true, but the length of the cantilever was restricted by the size of the optical fiber ( $125\mu\text{m}$ ) and the geometrical considerations shown in figure 3.10. In addition as the reflector pad is moved down the shaft of the cantilever the difference between the measured oscillation amplitude and the tip amplitude increases dramatically. If we were to retain the Brownian motion limited detector noise floor we could not arbitrarily move the pad of the cantilever towards the base. With these restrictions in mind cantilevers with the dimensions shown in table 5.2 were fabricated.

These cantilevers were also fabricated with in-line tips using a protocol from the literature [124]. To decrease the overall tip radius the tip region of the cantilever was thinned from  $340\text{nm}$  to  $\sim 100\text{nm}$  using a reactive ion etch, as discussed in the next section. The final cantilever design is shown in figure 5.10.

### 5.3.2 Cantilever fabrication protocol

The cantilever fabrication process is outlined in figure 5.11. For a detailed discussion of the cantilever fabrication protocol see [49, 64] and appendix G. Briefly, we started with an SOI wafer comprised of a  $340\text{nm}$  thick single crystal silicon device layer and a  $400\text{nm}$  thick buried oxide layer, both on top of a  $525\mu\text{m}$  silicon handle layer, as shown in figure 5.11 (a). To accomplish the thinning of the tip region as shown in figure 5.10 we exposed and etched a  $50\mu\text{m}^2$  regions which would later become the tip. These regions were then thinned using a reactive ion etch (RIE). By using an RIE we sacrificed the uniformity of tip thickness which ranged from  $80 - 120\text{nm}$  across the wafer, figure 5.11 (b). We then exposed and etched the cantilever into the device layer silicon, figure 5.11 (c). Exploiting a trick presented in [124] we then exposed and etched the cantilever pattern a second time with a  $2\mu\text{m}$  lateral offset in the optical stepper mask. The tip of the cantilever therefore resulted from the *intersection* of these two etched edges processes resulting in small radii of curvature. The cantilevers were then encapsulated in  $\text{SiO}_2$  by depositing thermal oxide on top of the etched cantilevers. The handle layer of silicon was then etched through from the back using a deep reactive ion etch (DRIE). The cantilevers were released using an aqueous hydrofluoric acid etch from which the wafer was carefully transferred to high purity chromatography grade methanol and a critical point drying machine. Typical yields were 50% although in one case a yield of 97% was obtained resulting in 204 cantilevers on a single wafer! SEMs of a typical cantilever and tip are shown in figure 5.12

Two problems were encountered which are worth mentioning here. First, exposure of the device layer silicon to oxygen plasma seemed to result in cantilever curling after release. Curling was dramatic and rendered the cantilevers useless due to poor perpendicularity. Second, Bosch process polymer from the DRIE step was observed on the cantilevers after release on one occasion; this was mitigated using a harsh oxygen plasma etch just prior to finishing the DRIE etch. The

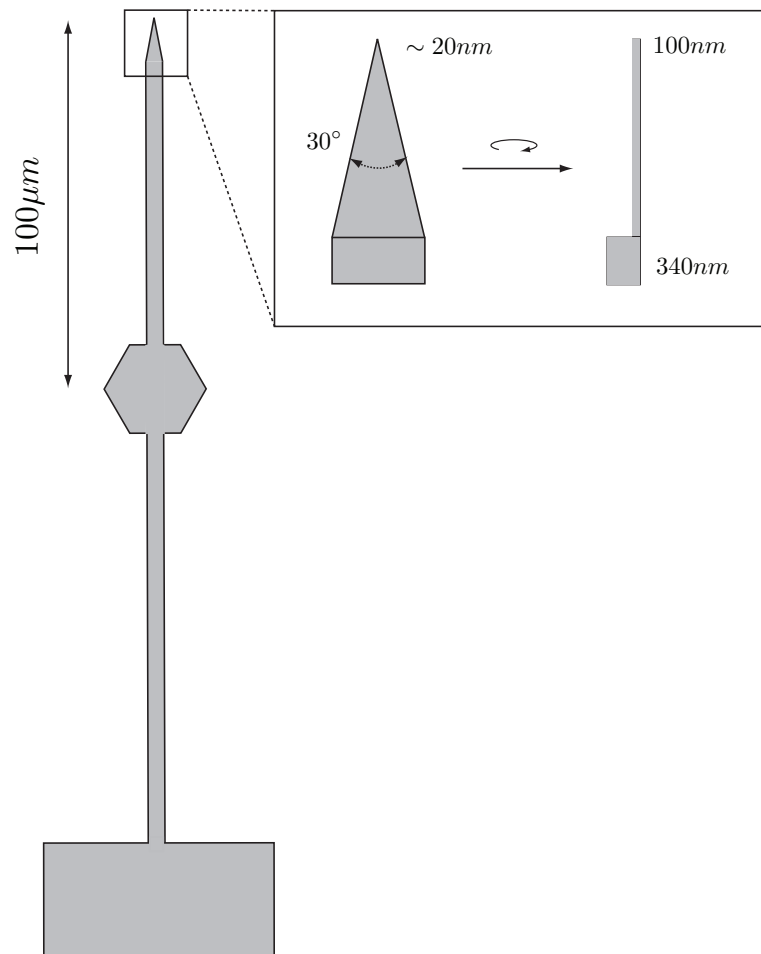


**Figure 5.10:** Schematic of the cantilever including the thinned tip region. The inline tip makes an angle of thirty degrees and typically has a radius in the neighborhood of 20nm. The reflector pad is  $100\mu m$  from the tip.

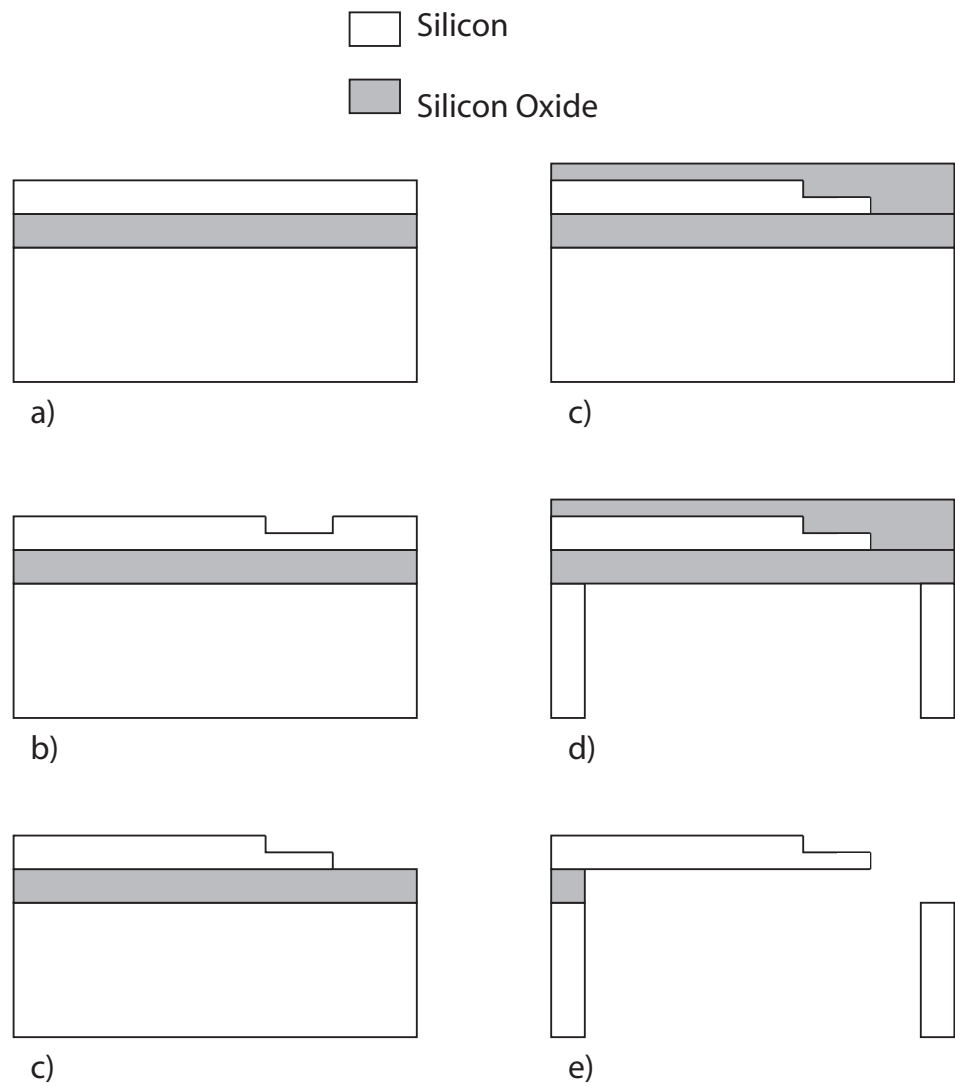


**Figure 5.11:** A simple outline of the cantilever fabrication starting with an SOI wafer (a) and resulting in a high sensitivity cantilever (e). Process is discussed in the text.

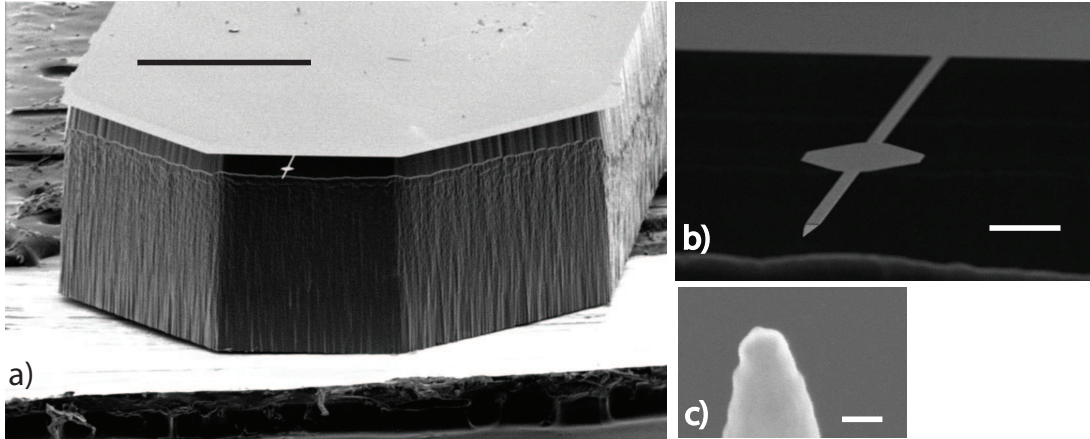


**Figure 5.12:** Scanning electron micrographs of a cantilever. a) The cantilever and die. The die results from the handle layer of silicon in figure 5.11. The scale bar is 0.5mm. b) Zoomed in on the cantilever itself. The scale bar is 10 $\mu$ m. c) A high resolution SEM of the cantilever tip. The scale bar is 50nm.

cantilever fabrication process is described in detail in appendix G.

### 5.3.3 Tip metalization

To simplify the analysis of our experiments we metalized the tips of our cantilevers. Tip metalization presented several challenges. We first tried sputtering a thin layer of gold over the entire cantilever but found that the metal present on the reflector pad resulted in laser induced cantilever oscillations tens of nanometers in amplitude even at modest interferometer laser powers. The advantage to sputtering was the uniform coverage of metal across the cantilever which prevented curling of the cantilevers. In order to metalize just the tip region to avoid the laser driving of the cantilever we used a shadow masking technique [64, 124]. A custom jig was machined which held 4 cantilevers simultaneously. Each cantilever could be positioned such that the shaft and reflector pad of the cantilever were shielded by a razor blade while the tip region was exposed. The jig could be mounted in the electron gun metal evaporators with the direction of evaporation being such that only the tip region of the cantilever was coated. To avoid cantilever curling the geometry of the evaporation jig was such that the metal was evaporated on the thin edge of the cantilever visible in the blow up in figure 5.10. It was critical to place the cantilever as close as possible to the razor blade edge so that no metal was evaporated onto the shaft or pad of the cantilever. Tip metalization proceeded by evaporating 15nm of platinum onto the tip region of the cantilevers held by the jig.

## 5.4 Initial data and microscope calibration

With the microscope and cantilevers constructed, we evaluated system performance and determined optimal protocols for measuring friction, surface approach, surface location determination and typical behavior of friction versus applied bias and tip-sample separation. We also explored cantilever frequency changes as a function of tip-sample separation and obtained spatial images of cantilever frequency shifts at constant tip-sample separations down to 30nm with spatial resolution of  $\sim 80$ nm.

### 5.4.1 Measuring friction

The total friction experienced by the cantilever is the sum of the surface induced dissipation and the intrinsic dissipation. Far from the surface the total friction  $\Gamma$  is comprised solely of the intrinsic cantilever friction  $\Gamma_0$ . Several methods for measuring cantilever friction have been presented in the literature [22, 117]. Dorofeyev *et. al* measured friction by measuring the power spectrum of cantilever position fluctuations and then fitting those spectra to the expected Lorentzian line shape from which the quality factor can be deduced. Their measurements were controversial due to their dramatic disagreement with theory. Stipe *et. al* measured friction three different ways as a function of tip sample separation. First, they oscillated the cantilever on resonance using positive feedback. They then rapidly grounded the driving piezo and

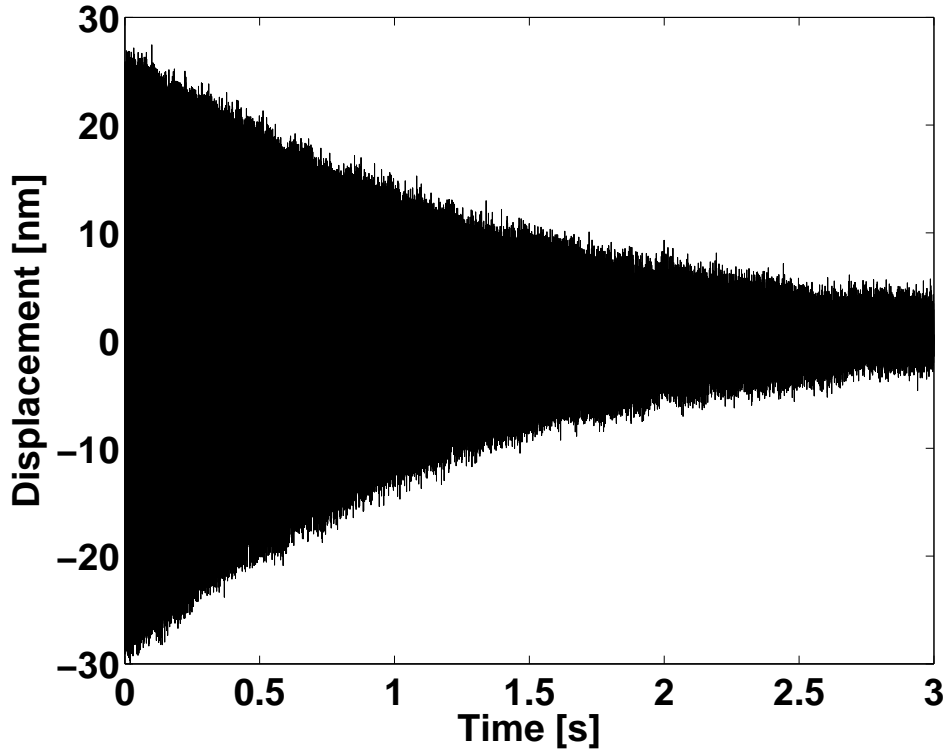


**Figure 5.13:** A typical cantilever ringdown. The signal to the drive piezo is grounded abruptly and the resulting decay to equilibrium is shown.

recorded the cantilever decay to equilibrium. The exponential decay to equilibrium was fit, the time constant extracted and the friction calculated. Second, they recorded the cantilever fluctuations in time for several minutes and calculated  $\langle x^2(t)x^2(t + \tau) \rangle$  which can be shown to decay with the same time constant as the cantilever ringdown. Finally, they duplicated the power spectrum fitting method presented in [117]. Stipe *et. al* found that the first two methods agreed for tip sample separations greater than 2nm while the method of Dorofeyev *et. al* resulted in  $4000\times$  more friction at small separations. The IBM group led by Dan Rugar attributed the difference to small anharmonicity near the surface. Stowe *et. al* [115] measured friction by measuring the oscillating force required to maintain a certain cantilever amplitude under positive feedback. This method required that they measure the  $Q$  once by ringdown to calibrate the force required and then simply measure the oscillating voltage used to maintain the cantilever amplitude at a fixed value as the friction increased.

While the calibrated method presented in [115] makes friction measurements possible in milliseconds rather than seconds it relies on the positive feedback circuitry to maintain a linear relationship between the driving force and the cantilever  $Q$  in a variety of conditions. For example, as the cantilever frequency changes due to surface interactions, analog bandpass filters in the feedback electronics might alter the required drive signal amplitude to maintain a fixed oscillation amplitude and this process may not correspond to a reduction in cantilever  $Q$ . Therefore, we chose to measure the cantilever friction using the ringdown method. This method allowed the most rapid *and* reliable measurement of friction. A typical ringdown is shown in figure 5.13

The  $1/e$  decay time for the envelope of the decay shown in figure 5.13 could be extracted and the friction calculated by

$$\Gamma = \frac{2k}{\tau\omega_0^2}. \quad (5.4)$$

The envelope of the ringdown was obtained by squaring the time domain signal, low pass filtering it in software to remove the oscillations at  $\omega_0$ , and then taking the square-root of the signal. The resulting envelopes could be fit. Fitting in real-time, during an experiment became cumbersome due to the slow convergence of the fit routines. To rapidly extract the

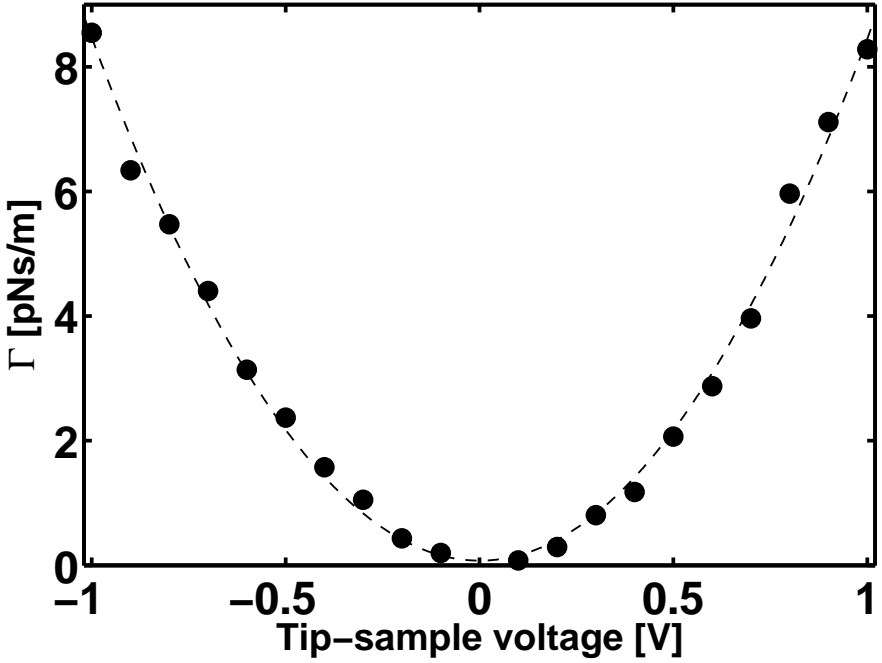


**Figure 5.14:** Total friction  $\Gamma$  as a function of the applied tip-sample voltage  $V_{ts}$  measured at a tip sample separation  $d \sim 30\text{nm}$ . The dotted line is a least-squares fit to a quadratic from which the contact potential  $\phi$  was extracted.

decay time it was shown that direct extraction of the  $1/e$  decay time was possible and reliable. To do this the ringdowns were processed as described, then a point  $(x_0, t_0)$  was chosen on the decay envelope and the value  $x_0/e$  calculated. The time domain string was then scanned for a point close to  $(x_0/e, t_1)$  resulting in  $\tau = t_1 - t_0$ . The results of this method were shown to coincide with envelope fitting method, to within the noise of the  $\tau$  measurement, over all friction regimes present in the experiment.

#### 5.4.2 Surface approach

To approach the cantilever to the surface, a large bias ( $\sim 4\text{V}$ ) was applied between the tip and the sample and the cantilever frequency monitored as the Attocube was stepped forward. When the cantilever approached within about  $50\mu\text{m}$  the frequency increased due to electrical interactions with the surface. The approach then proceeded more carefully by stepping a small amount and extending the Attocube piezo using a slow voltage ramp while measuring the cantilever frequency. The stepping distance was set to  $< 1/2$  the distance traversed by the voltage ramp. The presence of the surface was noted by an extremely rapid change in the cantilever frequency. The approximate surface location was determined by the position of this rapid frequency change.

#### 5.4.3 Friction versus voltage

Equation 4.16 predicts a quadratic dependence of the measured friction on the tip-sample bias  $V_{ts}$ . Positioning the cantilever a few tens of nanometers from the approximate surface location and measuring friction as a function of  $V_{ts}$  resulted in the data shown in figure 5.14, which was observed to be parabolic as expected. By fitting the measured data to a quadratic the contact potential  $\phi$  was extracted. If the cantilever was not positioned close enough to the surface the curvature of the resulting parabola became small, due to a small tip-sample capacitance, and the error in  $\phi$  correspondingly large. Therefore it was shown to be critical to approach within a few tens of nanometers to obtain reliable values of  $\phi$ .

For all of the samples presented in this thesis a parabolic dependence of friction on the applied bias was observed.

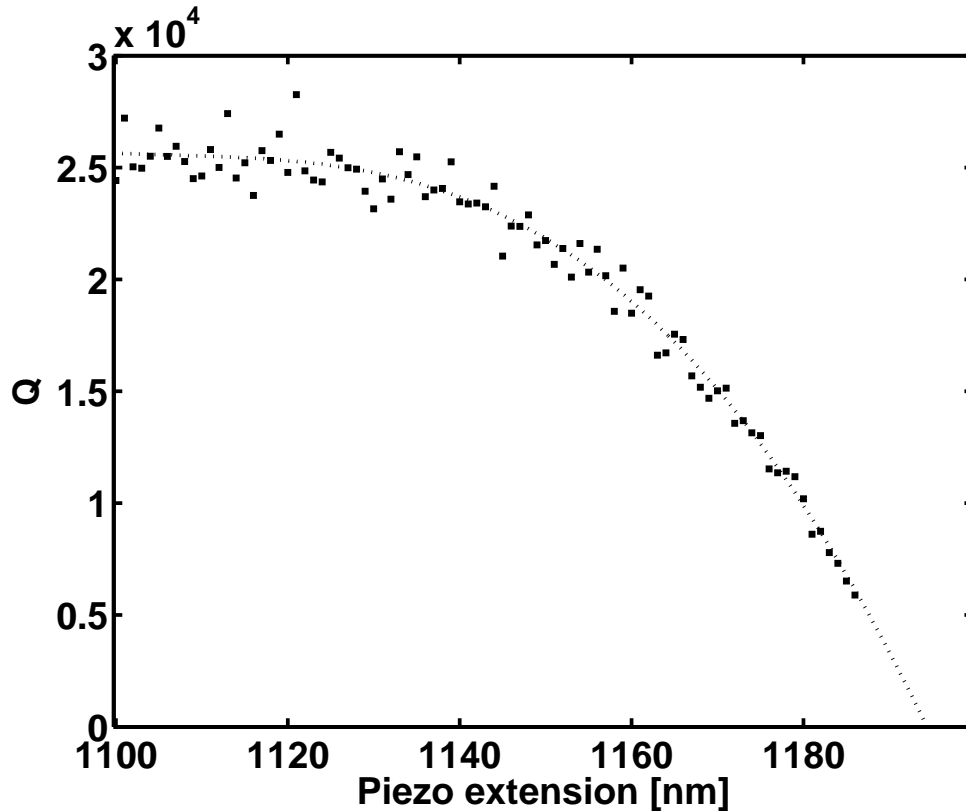


**Figure 5.15:** Cantilever  $Q$  measured as the tip of the cantilever was brought close to the surface of the sample. The dotted line is a fourth-order polynomial fit to the data. The surface was taken to be the point at which this line crossed the  $x$  axis.

#### 5.4.4 Surface location determination

To determine the surface location with greater precision the cantilever was positioned within approximately 100nm of the suspected surface location from the frequency data discussed above. The DC voltage supplied to the Attocube, to facilitate this positioning, was low pass filtered to reduce cantilever position noise due to voltage fluctuations across the piezo. The cantilever quality factor was measured as the tip of the cantilever was moved closer to the surface in 1 – 2nm increments. Due to noncontact friction between the tip and the sample the quality factor decreased with decreasing tip sample separation as shown in figure 5.15. The surface location was determined by extrapolating this data to the point of  $Q = 0$  which was taken to be the surface location. This extrapolation was accomplished by fitting the  $Q$  versus distance data to a fourth-order polynomial. A typical fit is shown in figure 5.15.

To determine the validity of our method for surface location determination we also determined the surface location by contacting the surface directly. To do this we first measured the surface location as described above. We then turned the cantilever drive off and approached the surface slowly. When the tip of the cantilever contacted the surface the position of the reflector pad moved abruptly as the cantilever flexed against the surface. We took the surface location to be the point at which the cantilever position change began. We found that this method correlated well with the  $Q$  versus distance measurement, so long as the tip sample bias was small, and the cantilever was not experiencing excessive noncontact friction. The disadvantages to determining surface location by touching the surface were the possibility of depositing significant charge on the surface and tip damage.

To determine the reliability of the  $Q$ -extrapolation method for finding the surface location we measured the the cantilever  $Q$  versus tip-sample separation at  $0.1V \leq V_{ts} - \phi \leq 1V$  and determined the surface location as outlined above. The results are presented in figure 5.16. For  $V_{ts} < 0.4V$  the projected surface location remained constant. At higher  $V_{ts}$  the apparent, extrapolated surface location moved due to the higher friction experienced at higher  $V_{ts}$ . After completing this series of measurements the surface location as measured for  $V_{ts} < 0.4V$  was corroborated by contacting the surface

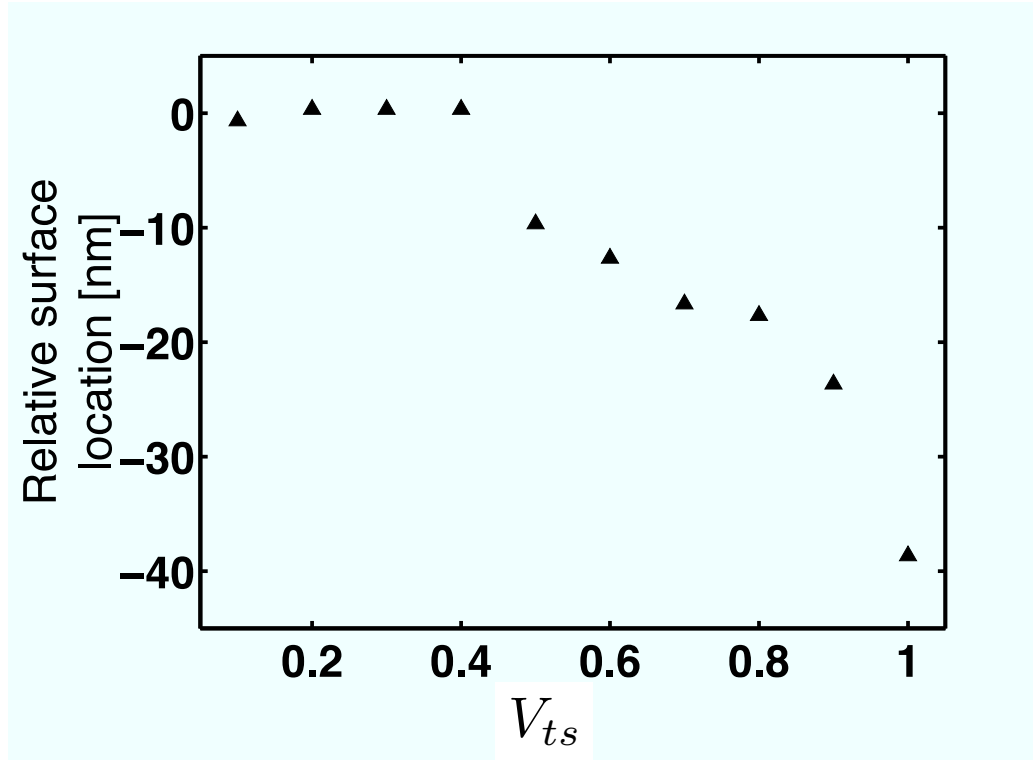


**Figure 5.16:** Relative surface location as measured by extrapolating  $Q$  versus  $d$  at various  $V_{ts}$ . A negative normalized surface location means that the surface was predicted to be closer than it actually is.

directly. Therefore, to obtain a reliable surface location from  $Q$  extrapolation it was necessary to make measurements at sufficiently low  $V_{ts}$ . For all samples studied here finding a  $V_{ts}$  low enough to obtain a reliable surface location was possible. This may not generally be the case for samples which exhibit unusually high friction even at small  $V_{ts}$ , or for very large cantilever tips where the surface location should be validated by contact between the tip and the surface if possible.

The end of the data acquisition for the data shown in figure 5.15 occurred when the cantilever  $Q$  reached a threshold level set externally by the user. It was shown that the location of the surface as determined by extrapolation did not depend on this threshold value.

#### 5.4.5 Friction versus distance

Typically, after measuring  $\phi$  and the surface location we measured  $\Gamma(d)$  at a fixed  $V_{ts} - \phi$ . Data is shown in figure 5.17 at  $V_{ts} - \phi = 0.5V$  exhibiting the universal increase in  $\Gamma_s$  with decreasing  $d$ . In order to make comparisons across samples it was critical to obtain precise and reproducible measurements of  $\phi$  and the surface location.

The measurement of friction as a function of distance proceeded as follows. The voltage applied to the Attocube piezo was supplied by the analog output of a DAQ PCI board (National Instruments, model PCI 6025E). Higher noise was generally observed when applying this voltage through an amplifier. At each point the cantilever was put under self oscillation by a positive feedback loop. The amplitude of oscillation was controlled to a present value of  $\sim 30\text{nm rms}$  by a PID feedback loop in software. The cantilever frequency was then measured and recorded using a commercial frequency counter (Hewlett-Packard, model 53131A). To record a ringdown, the NI DAQ board digitized the interferometer signal and subsequently grounded the output of the cantilever self oscillation circuit by supplying a TTL signal to a leaf switch. The resulting cantilever ringdown was then recorded and analyzed as outlined above. The cantilever was then allowed to return to its present oscillation amplitude and the Attocube piezo ramped slowly forward to the next point. A 200 point acquisition typically required 45 minutes to complete. All software was custom written in LabVIEW. Fitting of the cantilever  $Q(d)$  was implemented in Matlab. A block diagram of the experiment is shown in figure 5.18.

To ensure that no electrical noise was leaking through the switch and altering the cantilever ringdown time unnaturally,

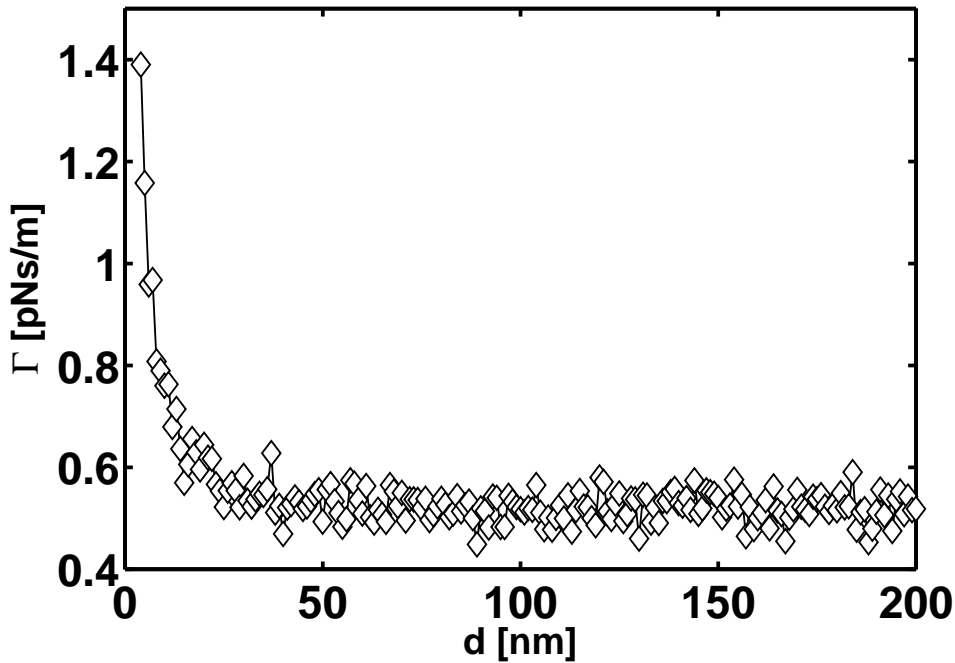


**Figure 5.17:** Total friction versus distance measured at  $V_{ts} - \phi = +0.5V$  over epitaxial Au(111) in high vacuum at room temperature.  $\Gamma_0 = 5 \times 10^{-13}\text{Ns/m}$ . Cantilever was  $250\mu\text{m}$  long, with  $k = 0.0007\text{N/m}$  and  $Q = 31000$ . Tip was metallized with platinum as discussed above.

the cantilever Brownian motion was measured via a lockin amplifier with the output of the feedback circuit grounded with the switch and again with the feedback circuit completely disconnected from the drive piezo. The Brownian motion was found to be identical under these two conditions, allowing us to conclude that the switch was effective in isolating the drive piezo from the feedback electronics.

For the data shown in figure 5.17 the final ringdown was taken 2nm from the surface of the sample. From this closest approach and table 5.1 our angular misalignment discussed previously was approximately  $1^\circ$  as expected. For the cantilever used to generate figure 5.17,  $\Gamma_0 = 5 \times 10^{-13}\text{Ns/m}$ . The noise in the friction measurement, taken as the standard deviation of the data far from the surface, was  $\Gamma_0 = 5 \times 10^{-14}\text{Ns/m}$  making these friction measurements some of the most sensitive ever reported. We have not systematically analyzed the noise in the friction measurement. Intuitively, cantilever position fluctuations during the cantilever ringdown will result in measurement to measurement variation in the friction. Therefore, we expect that low frequency Fourier components in the position noise to dominate the noise in the friction measurement. It is interesting to note that the noise in the friction measurement decreases with increasing friction as can be observed in figure 5.15. This makes sense because in a higher friction environment low frequency position fluctuations will be damped out more rapidly resulting in less noise in the friction measurement. It remains to make this argument rigorously.

#### 5.4.6 Frequency measurements

In conventional AFM and EFM, imaging can be achieved using cantilever frequency and phase information. We have explored the cantilever frequency response in the high sensitivity perpendicular geometry presented here. In general, we found that the frequency behavior of the cantilever was significantly less reproducible and prone to spurious effects than the friction measurements.

For example, the contact potential difference  $\phi$  is typically determined by measuring the cantilever frequency as a function of the applied tip-sample bias and fitting the resulting parabolic dependence. [53, 54, 64] The typical cantilever frequency behavior is shown in figure 5.19. At large separations we observed the expected parabolic dependence of frequency on the applied bias. [64] As the cantilever approached closer than  $\sim 150\text{nm}$  the parabolic response was lost. At

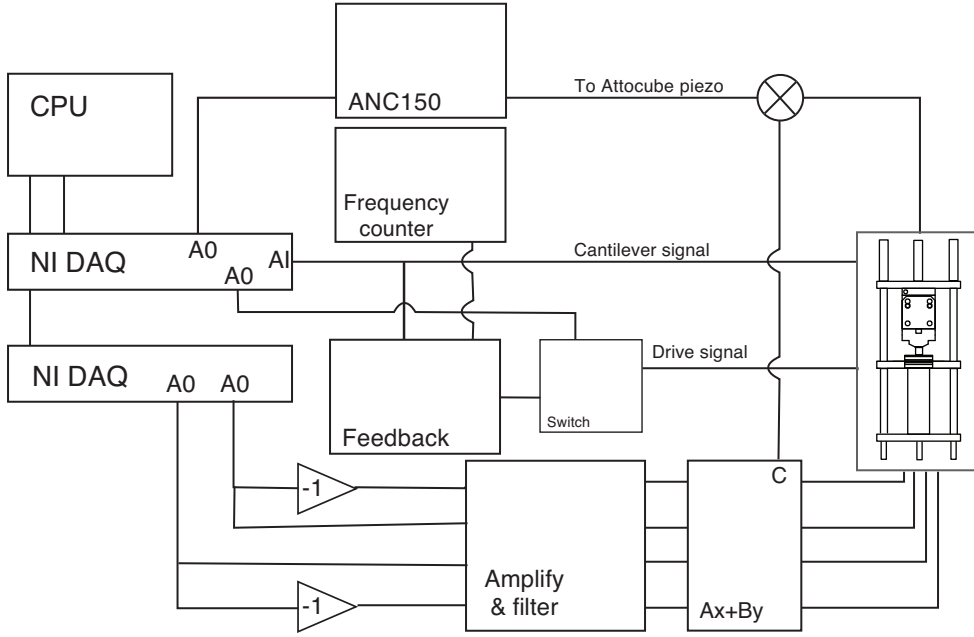


**Figure 5.18:** A Block diagram of the experiment. The details are discussed in section 5.4.5 and 5.4.7. The NI DAQ analog outputs are labeled “AO” and the inputs “AI”.

$d = 100\text{nm}$  the frequency dependence on the applied bias was inconsistent, changing over different sample locations. For some samples, at very close separations  $d < 20\text{nm}$ , inverted parabolas, with negative curvature, were observed. We can qualitatively understand this observation by exploiting an analysis presented in [64]. Stowe gives the change in frequency experienced by a cantilever in the perpendicular geometry near a surfaces as

$$\delta f = \frac{f_0}{2k} \left( \frac{\partial F_x}{\partial x} - \frac{F_z}{l} - \frac{\partial F_z}{\partial z} \theta^2 - 2 \frac{\partial F_z}{\partial x} \theta \right), \quad (5.5)$$

with  $\mathbf{F} = (F_x, F_y, F_z)$  is the force on the tip with  $x$  is the direction of cantilever motion and  $z$  is the surface normal. Additionally,  $l$  the length of the cantilever,  $k$  and  $f_0$  the force constant and fundamental frequency respectively, and  $\theta$  the angular misalignment between the cantilever and surface discussed previously. Note that  $\delta f = f_0 - f$ . The first term is frequency shifts arising from spatial heterogeneity across the sample, the second term is often called the “pendulum” term resulting from forces pulling the cantilever towards the surface. The last two terms are force-gradients arising from angular misalignments.

In general we expect  $\frac{\partial F_x}{\partial x}$  arising from the mechanism outlined by Stowe, to be zero, for the very flat spin cast thin films and epitaxial gold surfaces studied here. In addition, far from the surface the force-gradients arising from sample tilt ( $\theta$ ) will be small and we expect the term  $F_z/l$  to dominate. The force in the  $z$ -direction and a flat sample is given by [53]

$$F_z = -\frac{1}{2} \frac{\partial C}{\partial z} V_{ts}^2, \quad (5.6)$$

with  $C$  the tip-sample capacitance. Therefore, for large  $d$  we have

$$\delta f = \frac{f_0}{4kl} \frac{\partial C}{\partial z} V_{ts}^2 \quad (5.7)$$

and,

$$f = f_0 - \frac{f_0}{4kl} \frac{\partial C}{\partial z} V_{ts}^2. \quad (5.8)$$

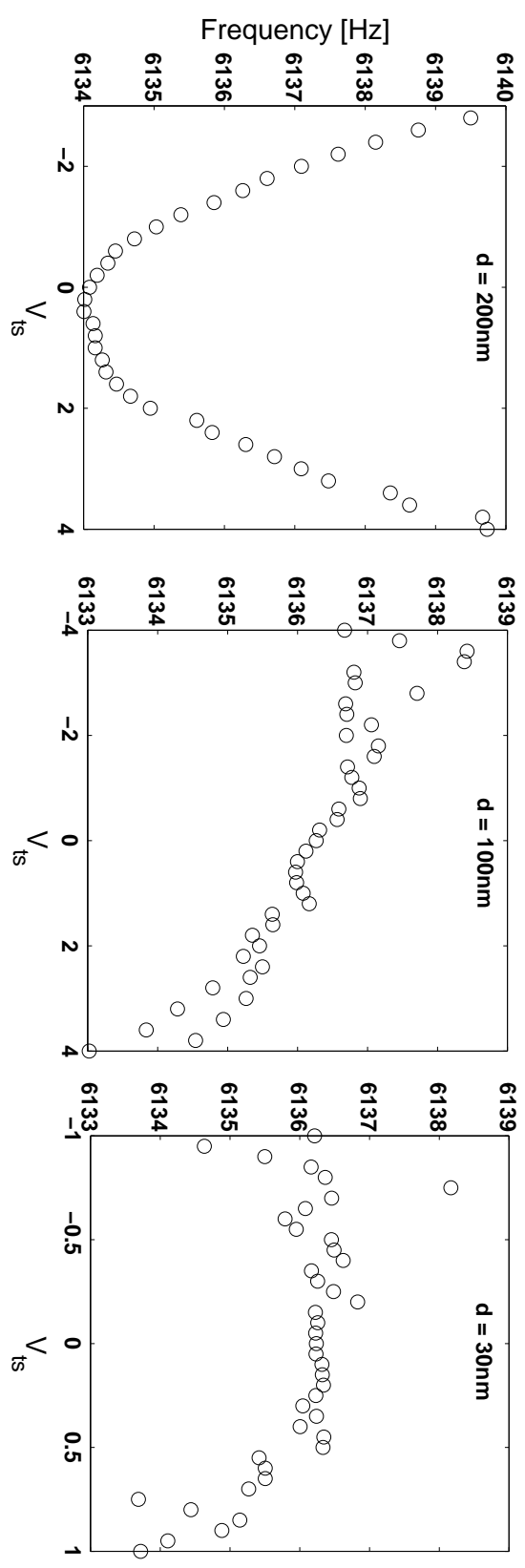


**Figure 5.19:** Cantilever resonance frequency as a function of  $V_{ts}$  measured at tip sample separations of 30, 100 and 200nm over Au(111). Note the expected parabolic dependence at larger tip-sample separations. At small separations an inverted parabolas were observed (data not shown).

To determine the sign of  $\frac{\partial^2 f(V_{ts})}{\partial V_{ts}^2}$  we need to consider the sign of the capacitance derivative. Generally, capacitance will be a decreasing function of  $z$ , where  $z$  is the tip-sample separation, making the derivative negative and the second term overall positive. Therefore, at far separations over planar samples and small angular misalignments we expect equation 5.8 to hold and the parabola to have a positive second derivative with respect to  $V_{ts}$  as we observe for  $d = 200\text{nm}$  in figure 5.19.

As the tip sample separation decreases the force-gradients resulting from the angular misalignment of the cantilever will increase. It is reasonable to assume that the third term will be larger than the last term in equation 5.5 for very small  $d$ . The third term contains the  $z$  derivative of  $F_z$  and the resulting frequency shift will be

$$f = f_0 - \frac{f_0}{4kl} \frac{\partial^2 C}{\partial z^2} V_{ts}^2. \quad (5.9)$$

Again, consider  $C(z)$ , if the first derivative is negative and the function is decreasing with  $z$ , we expect the second derivative to have opposite sign from the first derivative. This holds for most reasonable functional forms of  $C(z)$  including the logarithm. We therefore expect the curvature of  $f(V_{ts})$  to be *negative* for small  $d$  as observed.

In the intermediate regime, for  $30\text{nm} \leq d \leq 100\text{nm}$  some superposition of terms is governing the cantilever frequency and the nonparabolic nature of  $f(V_{ts})$  results as can be seen in figure 5.19. It is noted that the first term in equation 5.5 predicts a *linear* dependence of the frequency on the tip charge if one considers this term as arising from spatially inhomogeneous surface forces. Qualitatively, a linear dependence, with the appropriate slope is observed for  $d = 100\text{nm}$  in figure 5.19. As a result of this behavior, using cantilever frequency to extract meaningful information about the interaction between the tip and the surface can be difficult. This results largely from the fact that changes in cantilever frequency arise from force gradients at or near DC. Friction, on the other hand, is sensitive to fluctuations coherent with  $f_0$  only making measurements less prone to local variations and low frequency noise.

#### 5.4.7 Scanning

Using the piezo tube, sample scanning was also possible. As discussed in section 5.2.3, voltages of opposite polarity applied to opposing tube electrodes result in motion. One difficulty with scanning surfaces was the presence of sample tilt. Small sample tilts were not avoidable. To maintain a constant tip-sample separation while scanning a tilted plane required the implementation of a custom summing circuit which made the voltage setting the Attocube position a function of the  $x$  and  $y$  voltages being sent to the piezo tube electrodes. In general the equation of a plane is given by

$$Ax + By = C. \quad (5.10)$$

Using the summing circuit mentioned, with voltages corresponding to  $A$  and  $B$  under the user control, we were able to scan an arbitrary plane by sending the resulting voltage  $C$  to the Attocube piezo. In this way, the Attocube extension was made a function of the tube scanner position. The details of this method are contained in [54]. The scanning voltages were supplied by an additional DAQ board (National Instruments, model PCI 6052E). Two analog output channels supplied voltages specified by the custom scanning software. These voltages were then buffered and split into four channels two of which were inverted. All four of these channels were amplified using bipolar piezo amplifiers (Piezomechanik, model SVR 350-3bip). The output of these amplifiers was finally low pass filtered again to reduce mechanical noise in the probe. A block diagram of the experiment is shown in figure 5.18.

To determine the coefficients  $A$  and  $B$ , custom software was written which approached and made contact between the cantilever and the surface at three locations. From this data the tilt of the sample plane could be determined and initial values for  $A$  and  $B$  estimated. Additional small adjustments were necessary to facilitate scanning at tip sample separations down to  $30\text{nm}$ .

Using this method, images of cantilever frequency as a function of sample position could be recorded. Images of spatial variation in friction were not recorded due to the long acquisition time for large numbers of cantilever ringdowns. Rapid imaging of dissipation could be accomplished using the method of measuring friction proportional to the cantilever drive signal at constant amplitude as outlined above. An example of a frequency shift image is shown in figure 5.20. The frequency image was acquired by measuring the cantilever frequency using the HP frequency counter at each point in the scan. Frequency variations in the image are orders of magnitude larger than the noise in the frequency measurement. The origin of these variations remains unclear, although extensive measurements have been made. [53]

The spatial resolution of the microscope was limited by both the tip radius and the drive amplitude. The convolution of these two effects resulted to a resolution of  $\sim 80\text{nm}$  in figure 5.20

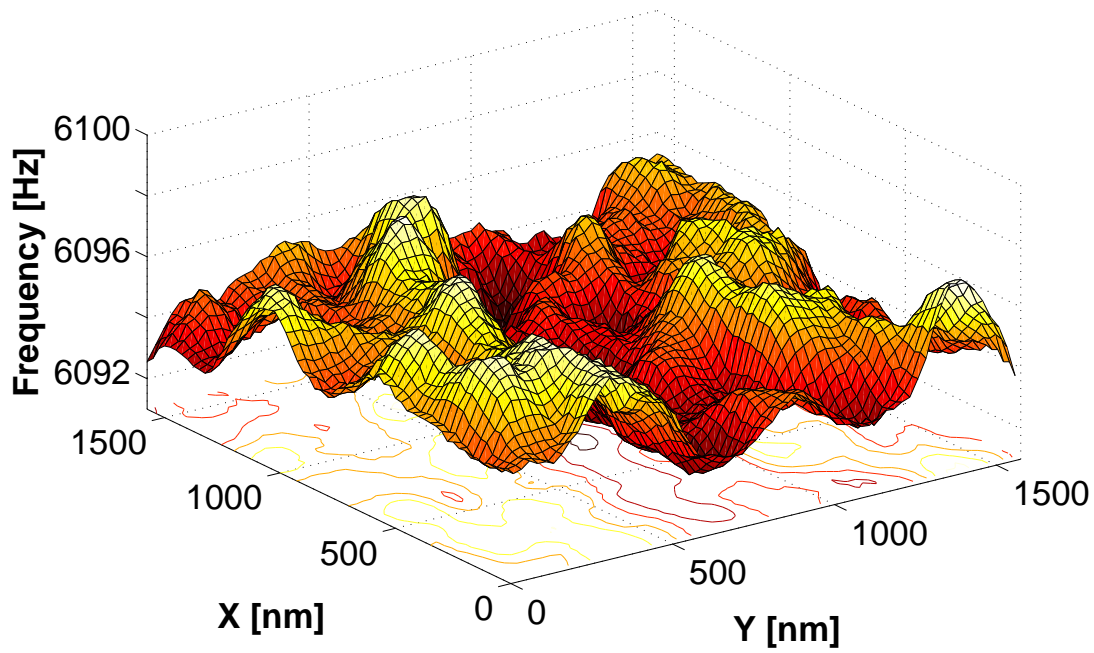


**Figure 5.20:** A  $1.5\mu\text{m}^2$  cantilever frequency image comprised of  $64^2$  points with  $V_{ts} = +0.35\text{V}$  and  $d \sim 30\text{nm}$ . Sample is 100nm thick polystyrene film doped with 10% TPD and spin cast on Au(111).

## 5.5 Conclusions

We have presented the design, construction and calibration of a custom high vacuum dissipation force microscope. We have constructed high sensitivity cantilevers with nanometer scale in-line tips for use in the perpendicular geometry to study noncontact friction between the tip of the cantilever and the sample surface. We have validated a robust protocol for measuring friction, determining the surface location, measuring the contact potential and scanning the sample.

## CHAPTER 6

### DIELECTRIC FLUCTUATIONS AND THE ORIGINS OF NONCONTACT FRICTION

#### 6.1 Introduction

Here we describe measurements published in [76]. For this study we used a single, high-sensitivity silicon cantilever to measure friction over a variety of thin films. The cantilever used in this study was 250 $\mu\text{m}$  long, 5 $\mu\text{m}$  wide, and 340 nm thick, with a spring constant  $k = 7 \times 10^{-4}$  N/m and a fundamental resonance frequency of  $\omega_c/2\pi = 7.385$  kHz. [31] The tip region of the cantilever was thinned from 340nm to  $\sim 100$ nm using a reactive ion etch as described above. The cantilever tip has a radius of  $\sim 30$ nm and was coated with a thin layer of platinum using the shadow mask technique described elsewhere. [124]

Briefly, recall the friction formalism presented previously. Since the dependence of the friction on applied bias was quadratic in all samples, figure 5.14, and the cantilever Brownian motion agreed with the equipartition theorem, the assumption of linear response was valid [22]. The sample induced friction could therefore be attributed to electric field fluctuations and calculated using the fluctuation-dissipation theorem,

$$\Gamma_s = \frac{q^2 S_E(\omega_c)}{4k_B T}, \quad (6.1)$$

where  $q = C(V_{ts} - \phi)$  is the charge on the tip,  $C$  is the tip sample capacitance,  $\phi$  is the contact potential difference between the tip and the sample,  $k_B$  is Boltzmann's constant,  $T$  is the temperature, and

$$S_E(\omega_c) = 4 \int_0^\infty \cos(\omega_c t) \langle \delta E_x(t) \delta E_x(0) \rangle dt \quad (6.2)$$

is the power spectrum at the cantilever resonance frequency of the electric field fluctuations experienced by the tip due to the sample. Here  $\delta E_x(t)$  is the electric field component parallel to the sample surface, in the direction of the cantilever motion. Our measurements explored the dependence of this fluctuating electric field on the chemistry of the sample.

#### 6.2 Measurement protocol

For each sample, we began by locating the sample surface. We took zero height,  $d = 0$ , as the height at which the cantilever quality factor extrapolated to zero. By using this method we avoided any triboelectric charging of the sample surface. At no point in the measurements did the tip of the cantilever contact the sample surface. We next measured  $\Gamma$  versus  $V_{ts}$  at a fixed tip-sample separation of about 30nm. We then measured  $\Gamma$  as a function of  $d$  at  $V_{ts} = \phi \pm 0.5$  V starting at a tip sample separation of approximately 200nm. In all measurements presented here, the  $V_{ts} - \phi = \pm 0.5$  V traces agreed to within the noise of the friction measurement (figure 6.2), indicating that the contact potential was not a function of the tip-sample separation over the measured range, typically  $d = 3 - 200$ nm. Our conclusion was verified by measuring  $\Gamma(V_{ts})$  in a few samples as a function of  $d$ ; the voltage at the  $\Gamma(V_{ts})$  minimum,  $\phi$ , was always independent of the tip-sample separation. In all samples, friction was measured at different locations and was found to be spatially invariant and independent of the local contact potential which varied spatially as shown in figure 5.20. The friction measurements were found to be entirely reproducible.

To minimize piezo drift and creep it was critical that the Attocube piezo never be fully retracted after each friction measurement. Instead, upon the completion of a  $\Gamma(d)$  measurement the cantilever was retracted to a point 200nm from the measured surface location. By minimizing the *change* in the DC voltage being applied to Attocube piezo, errors associated with piezo drift were kept to an acceptable level. These errors typically appeared, when these precautions were not observed, as an apparent change in the location of the surface. It was also critical to minimize the noise on the DC voltage applied to piezo. This voltage was supplied directly by the NI DAQ analog output and was low pass filtered at 100Hz to minimize voltage fluctuations on the piezo. During all measurements the Attocube piezo was controlled in an “open-loop” fashion meaning that there was no position feedback employed to maintain tip-sample spacing in a well defined way. This might be employed in the future using a capacitive separation sensor to establish better tip-sample spacing control.

##### 6.2.1 Sample preparation

Noncontact friction was measured at room temperature in high vacuum over polymer thin films that were spin-cast onto epitaxial Au(111) substrates (Molecular Imaging). We measured noncontact friction over poly(methyl methacrylate)

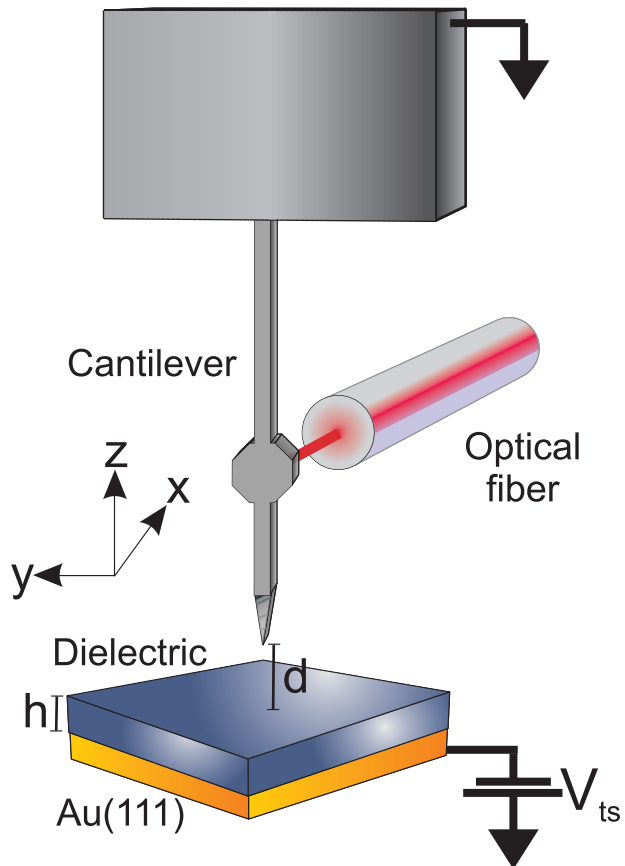


**Figure 6.1:** Our cantilever was brought close to a dielectric layer of thickness  $h$  in the perpendicular geometry. The tip-sample distance, defined as the distance to the surface of the dielectric is given by  $d$ . A voltage  $V_{ts}$  was applied to the epitaxial Au(111) layer beneath the dielectric. The cantilever moved in the  $\pm x$  direction. The motion was detected with  $0.01\text{nm}/\sqrt{\text{Hz}}$  sensitivity by a fiber optic interferometer.

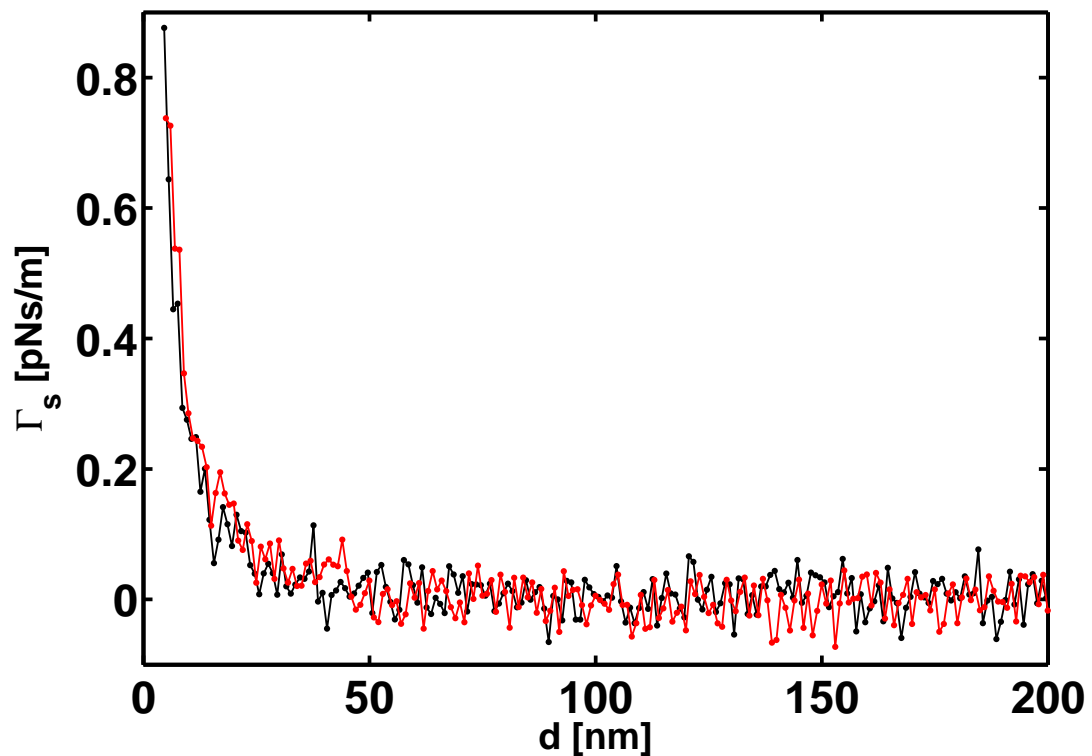


**Figure 6.2:**  $\Gamma_s(d)$  at  $V_{ts} - \phi = \pm 0.5V$ .  $+0.5V$  shown in red,  $-0.5V$  shown in black. Agreement between these measurements was taken as validation of the contact potential measurement and as corroboration that the contact potential was not a function of  $d$  over the measured range. Any significant error in the determination of  $\phi$  would result in the measured friction differing.

**Table 6.1:** Physical properties of polymers studied including molecular weight (MW), polydispersity (PD), glass transition temperature ( $T_g$ ), relative dielectric constant ( $\epsilon_r$ ) and the vendor: Scientific Polymer Products (SPP) or Sigma-Aldrich (A).

Polymer	MW [kDa]	Polydispersity	$T_g$ [K]	$\epsilon_r$	Vendor
PMMA	145	$\leq 1.05$	400	3.9	SPP
PVAc	147	$\leq 3.1$	305	3.4	A
PS	143	$\leq 1.09$	400	2.5	SPP

(PMMA), poly(vinyl acetate) (PVAc), and polystyrene (PS). The important physical properties of these polymers are shown in table 6.2.1.

All polymers were spin-cast on epitaxial Au(111) on mica. The substrates were glued to a piece of silicon wafer to increase rigidity for the spinning process. Polymer solutions were made in toluene in 3mL batches in carefully cleaned 1 dram vials. Toluene was preferred over tetrahydrofuran (THF) as a solvent due to the fact that it retained less water. All thin films were spun at 2000 rpm for 30 seconds. Film thickness was varied by varying the starting concentration of the toluene solution, typical thickness for a range of concentrations are shown in figure 6.3. All polymer films were annealed in a high vacuum environment at  $T = T_g + 10\text{K}$  to drive out water and residual solvent. Identical films were spun on clean pieces of silicon wafer. These films were profiled to determine film thickness and annealed along with the films cast on epitaxial gold. Films were profiled after annealing where it was found that PMMA and PVAc lost approximately 10% of their pre-annealing thickness while PS remained very close to its pre-annealed thickness. Surface roughness of films prepared identically was determined to be 2nm rms or better by conventional AFM. Thinner films tended to be flatter.

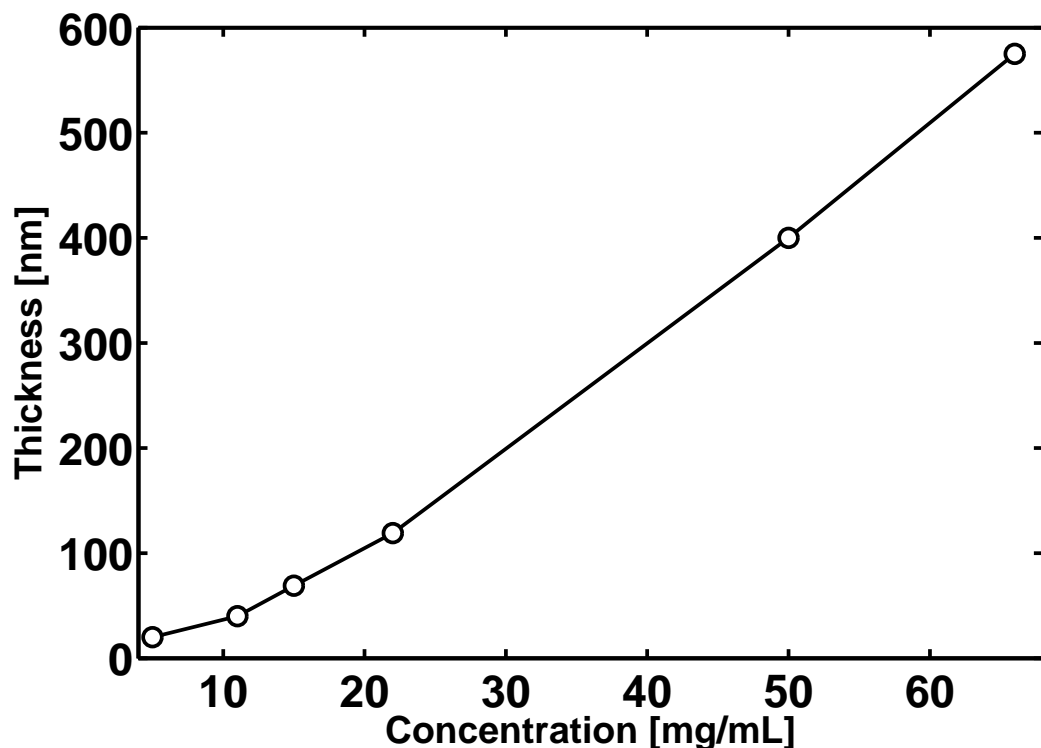
### 6.3 Friction over dielectrics

Figure 6.4 compares friction measured over films of the three polymers as a function of tip-sample separation at  $V_{ts} = \phi + 0.5\text{ V}$ . PMMA clearly produces higher friction than PVAc, and both exhibit dramatically higher friction than PS or Au(111). Since the tip-sample capacitance, and therefore the tip charge, must be larger over the blank Au(111) substrate because the tip is closer to the metal, we conclude from Eq. 6.1 that the fluctuating field is dramatically enhanced by the presence of PMMA and PVAc films, but not by PS. Comparing friction over films of the same thickness and relative dielectric constant makes it clear just how dramatically the friction varies between polymers. We find  $\Gamma_{\text{PMMA}}/\Gamma_{\text{PS}} \sim 75$  for the 450 nm-thick films over the range  $d = 8 - 20\text{nm}$  see figure 6.4. We concluded that the electric field fluctuations are strongly polymer dependent.

#### 6.3.1 Thickness dependence

To prove that the enhanced friction was not purely a surface effect, we varied the thickness  $h$  of the polymer films. We observed a decrease in  $\Gamma_s$  with decreasing  $h$  for both PVAc and PMMA, and a slight increase in friction upon reduction of the PS film thickness (figure 6.6). The change in measured friction due to the reduction in thickness of the film depended on the polymer for PMMA,  $\Gamma_{450\text{ nm}}/\Gamma_{40\text{ nm}} = 1.8 \pm 0.2$ , for PVAc,  $\Gamma_{450\text{ nm}}/\Gamma_{12\text{ nm}} = 1.7 \pm 0.1$ , and for PS,  $\Gamma_{450\text{ nm}}/\Gamma_{30\text{ nm}} = 0.6 \pm 0.4$ . Since  $V_{ts}$  was applied between the tip and the metal layer underlying the polymer film, the tip-sample capacitance (and therefore the tip charge), increased with decreasing film thickness for a fixed tip-sample separation  $d$ . We would therefore expect greater friction at fixed  $d$  and  $V_{ts}$  for the thinner film if  $S_E(\omega_c)$  was constant as would be consistent with a surface effect. Instead, we observe a reduction in  $\Gamma_s$  with decreasing  $h$  for PMMA and PVAc, leading to the conclusion that  $S_E(\omega_c)$  must be smaller over thinner films. The argument is given schematically in figure 6.5. While PS exhibited a slight increase in friction with decreasing  $h$ , we note that the change was not large enough to be explained by increasing tip charge alone, also implying a reduction in  $S_E(\omega_c)$  with decreasing  $h$ . This relation between  $S_E(\omega_c)$  and film thickness provides unambiguous evidence that the fluctuations responsible for the observed noncontact friction originate within the polymer films.

Noncontact friction was measured at some intermediate thicknesses for PMMA, PVAc and PS with no observable reduction in the surface induced dissipation. For PMMA we measured noncontact friction over 350nm thick films and found no reduction in friction as compared to the 450nm thick film (figures 6.4 and 6.10). For PVAc we measured friction over 100nm and 40nm thick films observing friction identical to that measured over the 450nm thick film (data not



**Figure 6.3:** Spin calibration curve for PVAc. Line is a guide for the eye. All films were spun at 2000 rpm for 30s. Very similar behavior was observed for PMMA and PS of similar molecular weight. A third order polynomial least squares fit to the data yielded  $T(C) = -0.0016C^3 + 0.24C^2 - 0.202C + 15$  where  $T(C)$  is the thickness in nanometers as a function of the solution concentration in [mg/mL].

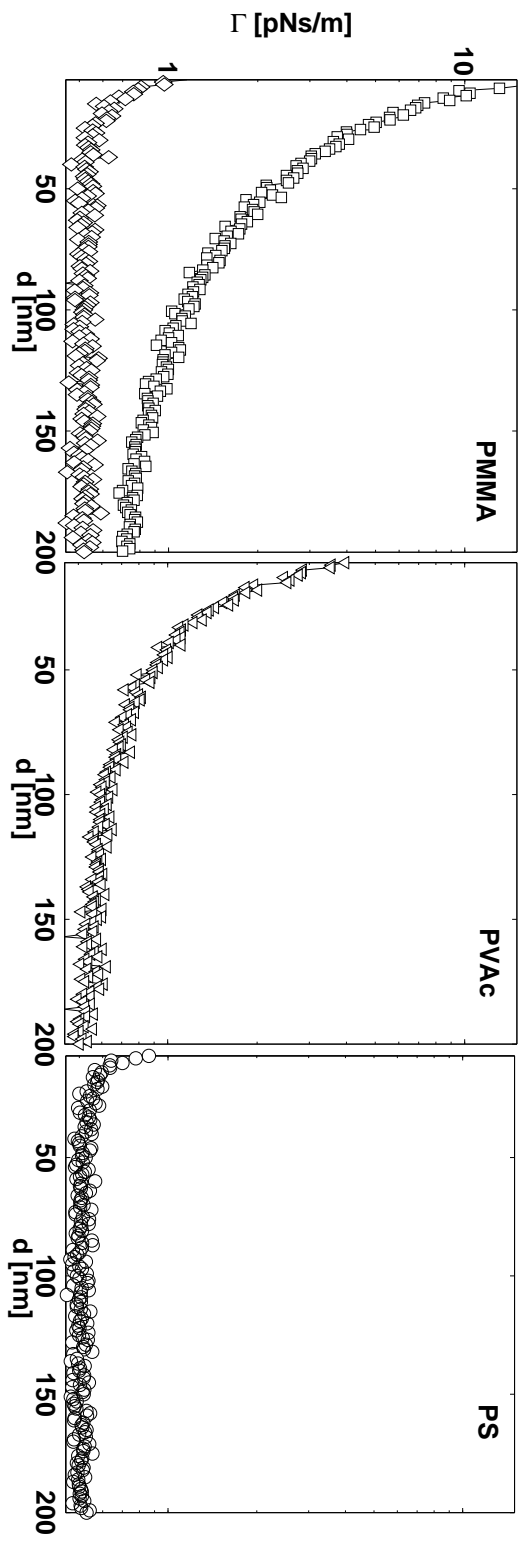


**Figure 6.4:** Total friction  $\Gamma$  over PMMA, PVAC and PS measured at  $V_{ts} - \phi = 0.5\text{V}$ . All films are 450nm thick and prepared as described above. The friction measured over a blank Au(111) substrate is plotted along with the PMMA data (diamonds).

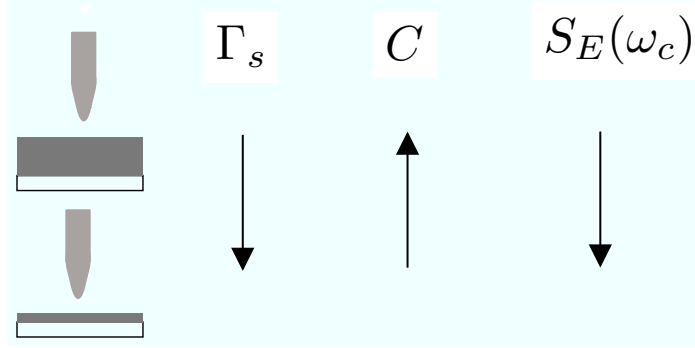


**Figure 6.5:** Schematic of friction measurements over a thick films (above) and thin films (below). Corresponding trends in observed noncontact friction  $\Gamma_s$ , capacitance  $C$  and fluctuating field spectral density  $S_E(\omega_c)$ .

shown). For PS we measured friction over a 100nm thick film observing friction equivalent to that measured over the 30nm film (data not shown).

### 6.3.2 Estimating capacitance

We measured  $\Gamma_s$ , given by equation 6.1, by subtracting  $\Gamma_0$  from the data shown in figures 6.4 and 6.6. To estimate the fluctuating field spectral density we needed an estimate of the tip sample capacitance,  $C$ . While numerical and analytical methods can be used to calculate the capacitance for arbitrarily shaped objects [126] these models are not useful unless we know the tip geometry precisely. In our case the tip morphology on the nanoscale was not well characterized or well controlled, see for example figure 5.12, making complex models of the tip invalid. Instead we simply model the tip of the cantilever as a sphere above an infinite plane covered with a dielectric of thickness  $h$ .

The geometry used for the capacitance calculation is shown in figure 6.7. Following the literature [127] we define the effective distance between the sphere and the metal to be

$$d_{eff} = d + \frac{h}{\epsilon_r}, \quad (6.3)$$

where  $\epsilon_r$  is the relative dielectric constant of the film. Using this effective distance define the following variable

$$\alpha = \log \left( 1 + \sqrt{\left( \frac{d_{eff}}{r} \right)^2 + \left( \frac{2d_{eff}}{r} \right)} + \left( \frac{d_{eff}}{r} \right) \right) \quad (6.4)$$

The capacitance of the sphere and the plane is then given by.

$$C(d_{eff}) = \sum_{n=1}^{\infty} \frac{\sinh(\alpha)}{\sinh(n\alpha)} \quad (6.5)$$

In calculating this sum we found that it converged rapidly. For example, over PMMA films of 450nm thickness with a tip of radius 50nm the contribution of the 5th term was 0.001 that of the first term. In general we have carried the sum out 20 terms and found that this was more than sufficient even in the least convergent cases.

In reality, estimating the capacitance of the tip-sample system as a sphere is unreliable especially since different portions of the tip may dominate the capacitance in different regimes. For example, for very thin films ( $h < r$ ) the capacitance is likely dominated by the very tip of the cantilever, while for thicker films ( $h \gg r$ ) the conical region of cantilever tip may dominate the capacitance. Estimating such effects remains fruitless without a clear experimental measurement of the tip-sample capacitance. As a result, estimating the tip-sample capacitance using a parallel plate approximation is also reasonable and differs only slightly from the sphere estimate outlined above.

A parallel plate estimate treats the tip as a flat circular disc of radius  $r$  and distance  $d$  from the surface of the dielectric. The total capacitance of the tip sample system is then the series capacitance of the gap between the tip and the sample and the parallel plate capacitance, over an area the size of the tip, of the dielectric layer. The total capacitance can be simplified to

$$C_{ts} = A \frac{\epsilon_0 \epsilon_r}{h \epsilon_0 + d \epsilon_r}. \quad (6.6)$$

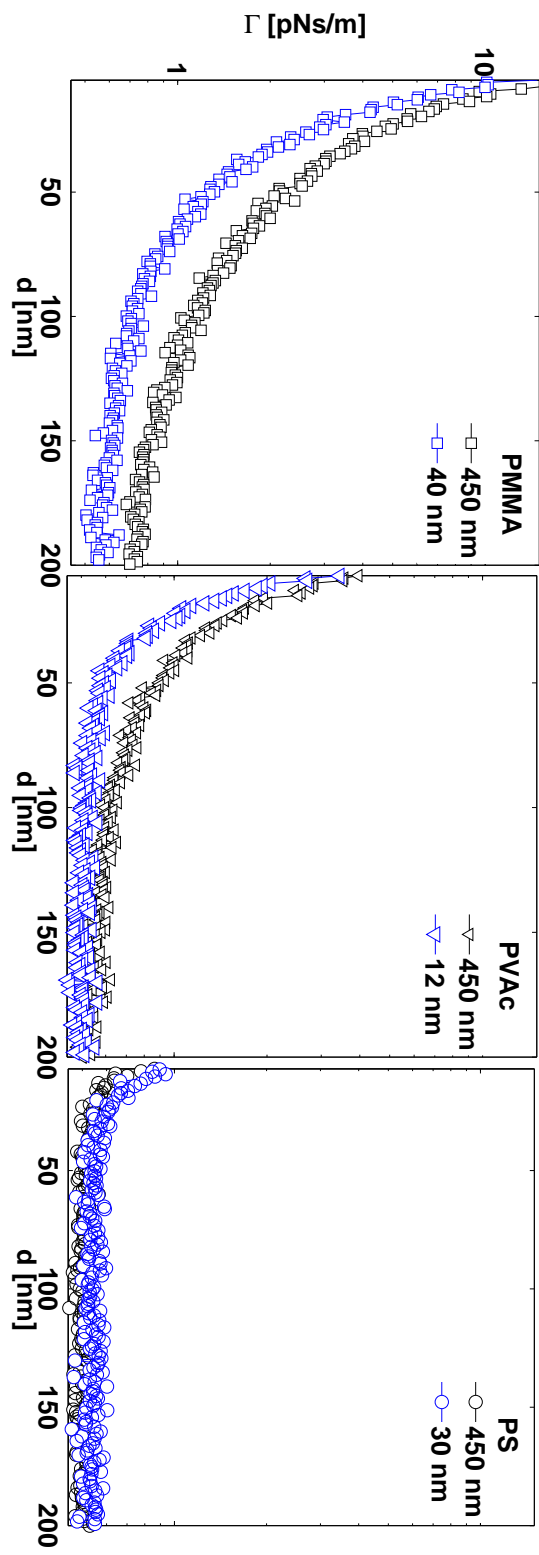


**Figure 6.6:** Thickness dependence of noncontact friction over dielectrics. PMMA films of 450nm (black squares) and 40nm (blue squares), PVAc films of 450nm (black triangles) and 12nm (blue triangles) and PS films of 450nm (black circles) and 30nm (blue circles).

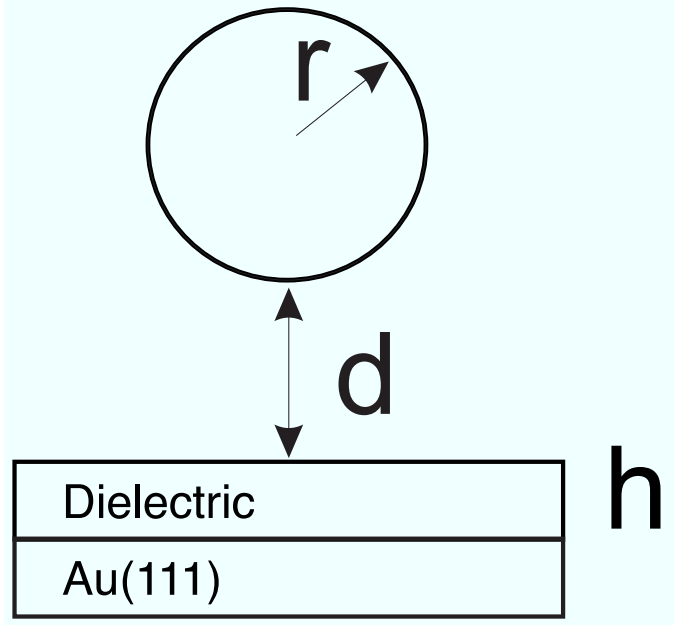


**Figure 6.7:** Diagram of capacitance calculation. A sphere of radius  $r$  is a distance  $d$  from the surface of a dielectric of thickness  $h$  on a conducting surface such as Au(111).

We validated our capacitance estimates and resulting spectral densities through a comparison to previous measurements. Stipe *et. al* [22] estimate, for a tip of radius  $1\mu\text{m}$  located 20nm from a gold surface, a capacitance of  $C \sim 10^{-16}\text{F}$ . Using the formalism presented here we calculated for a sphere of radius  $1\mu\text{m}$  a capacitance of  $3.5 \times 10^{-16}\text{ F}$ . Using this capacitance Stipe *et. al* estimated a fluctuating field spectral density of  $5(\frac{V}{m\sqrt{\text{Hz}}})^2$  resulting in a measured friction of  $3 \times 10^{-12}\text{Ns/m}$ . Figure 6.8 shows the estimated capacitance of the tip-sample system over gold, and the spectral density of electric field fluctuations which result in the measured friction. For our measurements, with  $d = 20\text{nm}$ , and a smaller tip, we computed a field spectral density of  $50(\frac{V}{m\sqrt{\text{Hz}}})^2$  (see figure 6.8 upper plot). The discrepancy is likely due to poor capacitance estimates due to errors in the tip size estimation in both cases and noise in the friction measurement.

### 6.3.3 Estimating $S_E(\omega_c)$

In order to illustrate the chemical dependence of the fluctuating electric field more clearly, we have determined  $S_E(\omega_c)$  from the measured friction using equation 6.1 and our capacitance estimate.. The results are shown in figure 6.9. The tip charge in this calculation is estimated by approximating the tip-sample capacitance as outlined above. The significant variation in  $S_E(\omega_c)$  between polymers clearly indicates that the noncontact friction observed here depends on the chemical composition and, as presented above, the thickness of the film. We are able to conclude that fluctuations *within* the films are responsible for the fluctuating field and associated friction that we observed here. Figure 6.9 is the central finding of this study.

## 6.4 Screening by metals and substrate dependence

We have also shown that polymer electric field fluctuations were shielded by a thin layer of gold. In figure 6.10 we compare the noncontact friction over 350nm PMMA spin cast onto Au(111) to that over a 350 nm PMMA spin cast onto quartz and then capped with 40nm of thermally evaporated gold. The friction observed near uncoated PMMA was significantly larger than that observed over the metal-coated polymer. Since in both measurements  $V_{ts}$  was applied between the tip and the respective gold layer, one might argue that the polymer was not experiencing the tip field in the measurement over gold coated PMMA, making the comparison in figure 6.10(a) ambiguous. However, we have shown that  $S_E(\omega_c)$  is not a function of the applied bias  $V_{ts}$ , which serves only to charge the tip capacitively. The gold-capped PMMA measurement therefore shows that the metal layer screened the electric field fluctuations from the polymer.

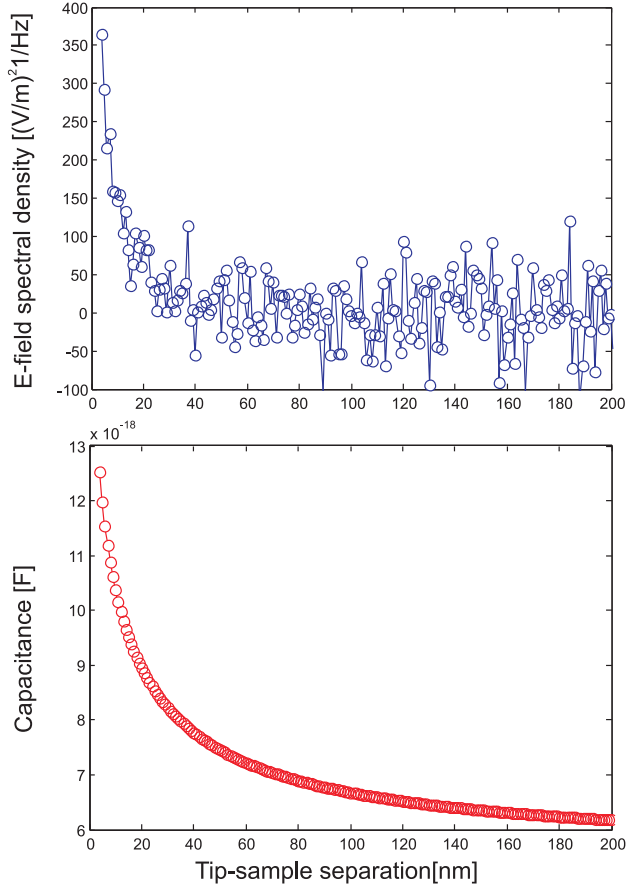


**Figure 6.8:** Top: spectral density of field fluctuations over Au(111) at  $V_{ts} - \phi = +0.5\text{V}$  estimated using the capacitance calculation outlined the text. The capacitance between sphere and a plane, calculated without a dielectric present, for  $r = 50\text{nm}$ .

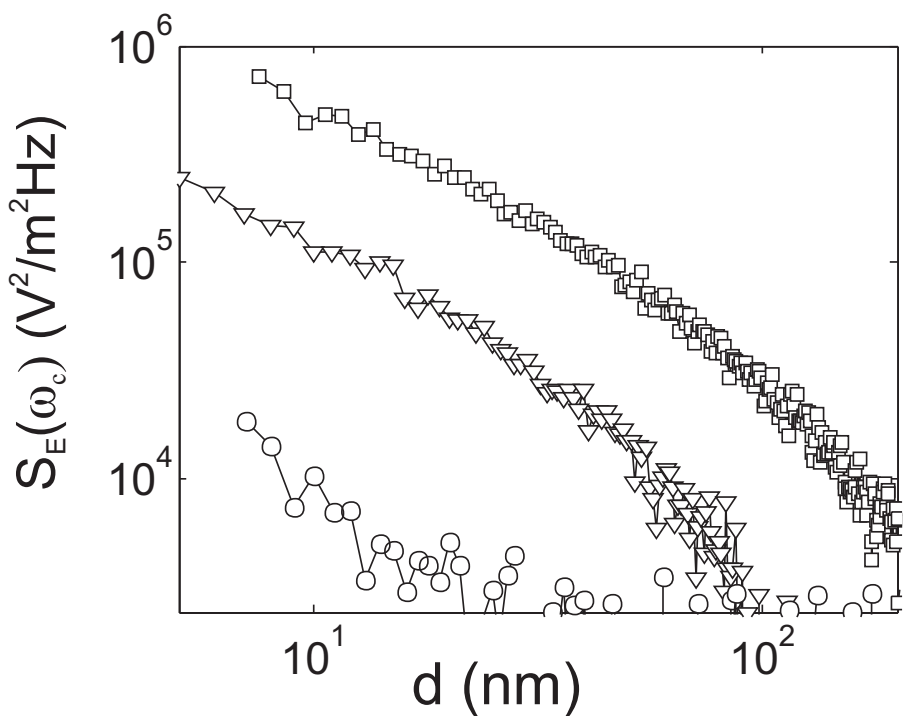


**Figure 6.9:** Spectral density of field fluctuations calculated using an estimate of the tip sample capacitance and the measured noncontact friction. PMMA (squares), PVAc (triangles) and PS(circles).

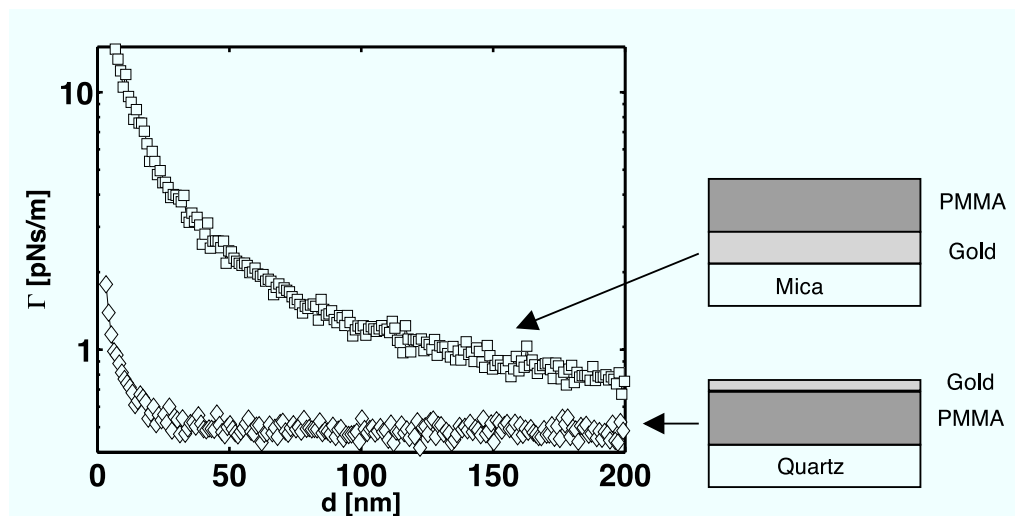


**Figure 6.10:** Friction measured over 350nm thick PMMA film on 150nm thick epitaxial gold on mica shown with friction measured over 350nm PMMA capped by 40nm of thermally evaporated gold on a quartz substrate.

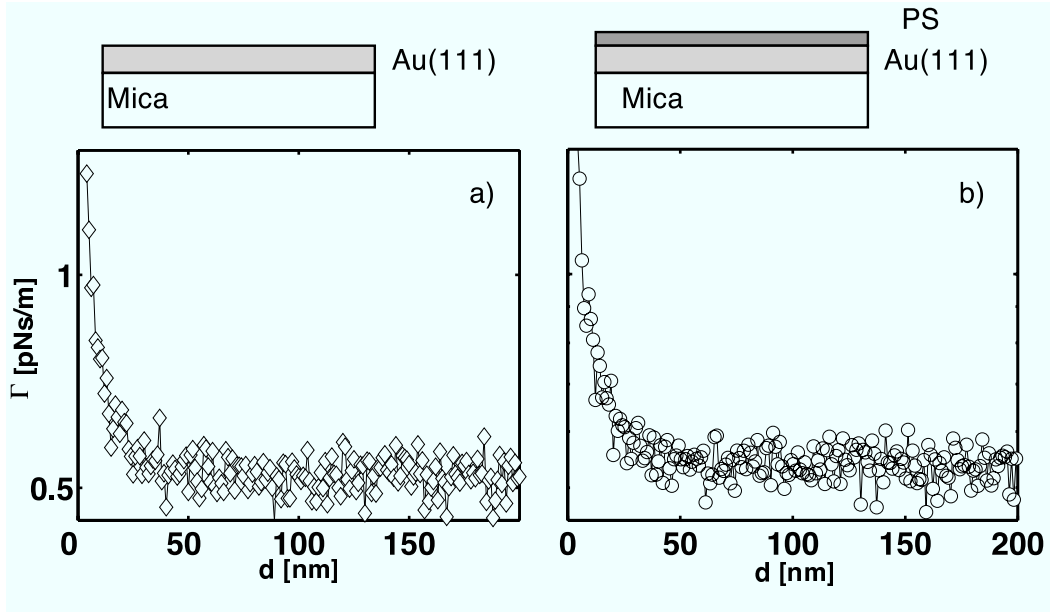


**Figure 6.11:** a) Friction over Au(111) and b) friction over 30nm of polystyrene on Au(111). The level of friction measured in a) is identical to that shown in figure 6.10 for gold capped PMMA, to within the noise of the measurement.

Our data also constrain the possible mechanisms giving rise to the electric field fluctuations seen over bare polycrystalline gold [22]. Figure 6.10 shows noncontact friction over PMMA capped with 40nm of gold on a quartz substrate. The level of friction, measured under identical conditions, was equivalent to the friction measured over 150nm epitaxial Au(111) on a mica substrate (figure 6.6 and 6.11). Therefore, friction did not depend on the nature of the underlying substrate as has been proposed to explain the measurements by Stipe *et. al.* [40] Our data does not constitute a conclusive test with respect to the theory presented by Zurita-Sanchez *et. al* since they considered an uncharged probe moving near a surface while our cantilever tip is known to be charged. Despite this, it was clear in our measurements and those by the IBM group that the mechanism of friction was not dependent on the applied bias, and therefore the tip charge. It is hard to imagine how a fluctuating field at audio frequencies, as is required by equation 6.1 would not be screened by a metal.

## 6.5 Adsorbates

It has been further proposed that acoustic modes in surface adsorbates might dramatically enhance noncontact friction. [39] In the high vacuum measurements presented here, we expect water to be the dominant surface adsorbate. Figure 6.11 compares noncontact friction measured over moderately hydrophilic Au(111) and a 30nm layer of hydrophobic polystyrene. [128, 129] There was no measurable change in the observed friction, leading us to conclude that adsorbed water is not the source of noncontact friction over gold. This measurement did not conclusively determine the role of surface adsorbates on noncontact friction. We believe that such a test would require ultrahigh vacuum conditions.

## 6.6 Friction at $V_{ts} = \phi$

We also measured the noncontact friction for  $V_{ts} = \phi$  where we encountered exceedingly low levels of noncontact friction. As discussed in section 4.4.2, perfectly nulling the tip-sample contact potential was not physically possible when applying a single bias to the entire tip as was the case here. We minimized  $q$  by dialing the tip sample voltage to the measured contact potential and then measured  $\Gamma_s(d)$  as shown in figure 6.12. To within the noise of the measurement we can reasonably say that in this regime, friction over PMMA was larger than over PS, but comparisons with PVAc are unclear from figure 6.12.

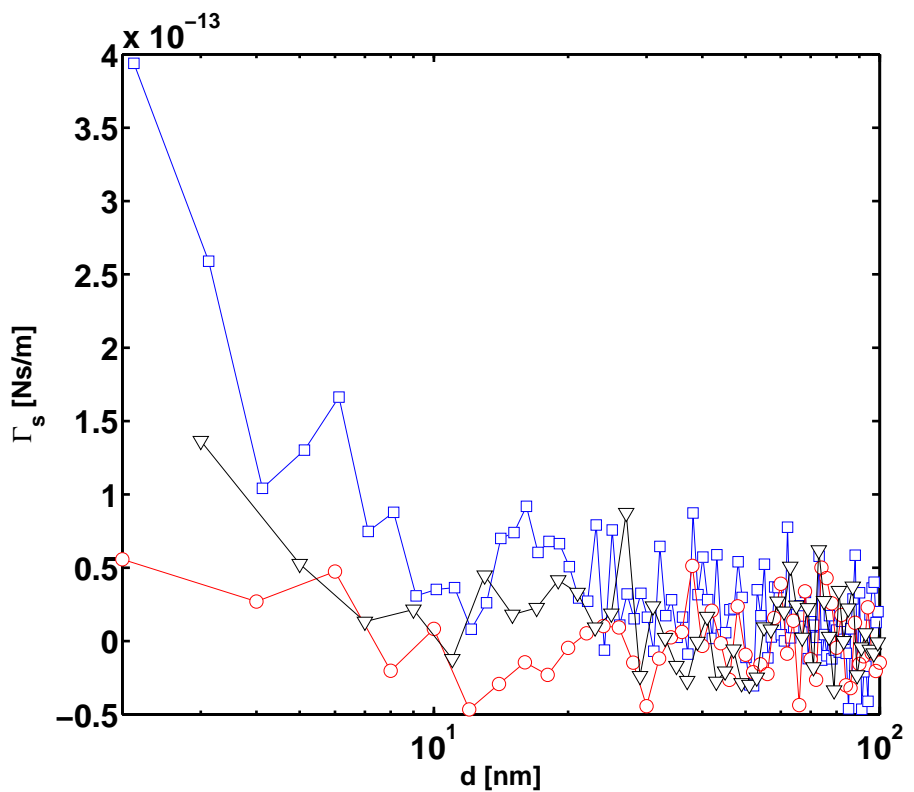


**Figure 6.12:** Friction measured at  $V_{ts} = \phi$  for PMMA (squares), PVAc (triangles) and PS (circles).

## 6.7 Conclusions

From the measurements presented in this chapter we were able to conclude that noncontact friction in our measurements depended strongly on the chemical composition of the sample. We showed that the fluctuating fields responsible for the observed friction originate within the film and were not purely a surface effect. In addition, we showed that our noncontact friction measurements over metals were not sensitive to the underlying substrate, consistent with the hypothesis that the audio frequency fluctuations dominating noncontact friction are screened by metal layers. Finally, we were able to constrain the possibility that noncontact friction originates from surface adsorbates by speculating that water did not play a dominant role in our measurements.

In addition to measuring friction we briefly explored the effects of polymer thin films on cantilever frequency fluctuations.

## 6.8 Cantilever frequency fluctuations

We also made measurements of cantilever frequency fluctuations over dielectrics. While friction is sensitive to electric field fluctuations at the cantilever resonance frequency (equation 6.1), frequency fluctuations are sensitive to electric field, and electric field-gradient, fluctuations around zero frequency. To begin probing these fluctuations we measured the cantilever frequency jitter. Frequency jitter is defined here as the standard deviation of the cantilever frequency fluctuations in the time domain measured in a finite bandwidth. Equivalently, we could take a frequency noise power spectrum and integrate the spectrum to the desired bandwidth calculating the resulting jitter. For the few measurements that we made, the cantilever frequency was measured in a 10Hz bandwidth for a period of 5s and the standard deviation of the resulting data taken in software. The results for PMMA and PVAc films are shown in figure 6.13.

There were a variety of difficulties associated with measuring frequency jitter. First, as can be seen in figure 6.13, cantilever jitter due to interactions with the surface begins at much larger tip-sample separations than noncontact friction (figure 6.4), rendering reliable measurements more difficult due to the piezo drift characteristics discussed in section 6.2. Second, the acquisition of each trace in figure 6.13 required more than 3 hours of measurement due to the slow, low frequency fluctuations responsible for frequency jitter. Finally, because the jitter scales as  $1/x_{rms}$  the cantilever amplitude must be maintained across measurements in order to make measurements comparable between samples.

## 6.9 Future directions

With the sensitivity levels demonstrated here a variety of experiments related to those outlined here are possible. One might study friction over dielectric layers as a function of the sample temperature. Particularly interesting might be to study dynamics at the glass transition. Temperature variability might be added to the current apparatus using piezo electric heating and cooling elements at the sample stage. It would also be very interesting to study the frequency dependence of noncontact friction. These studies might provide insight into the still mysterious mechanism of friction over metals.

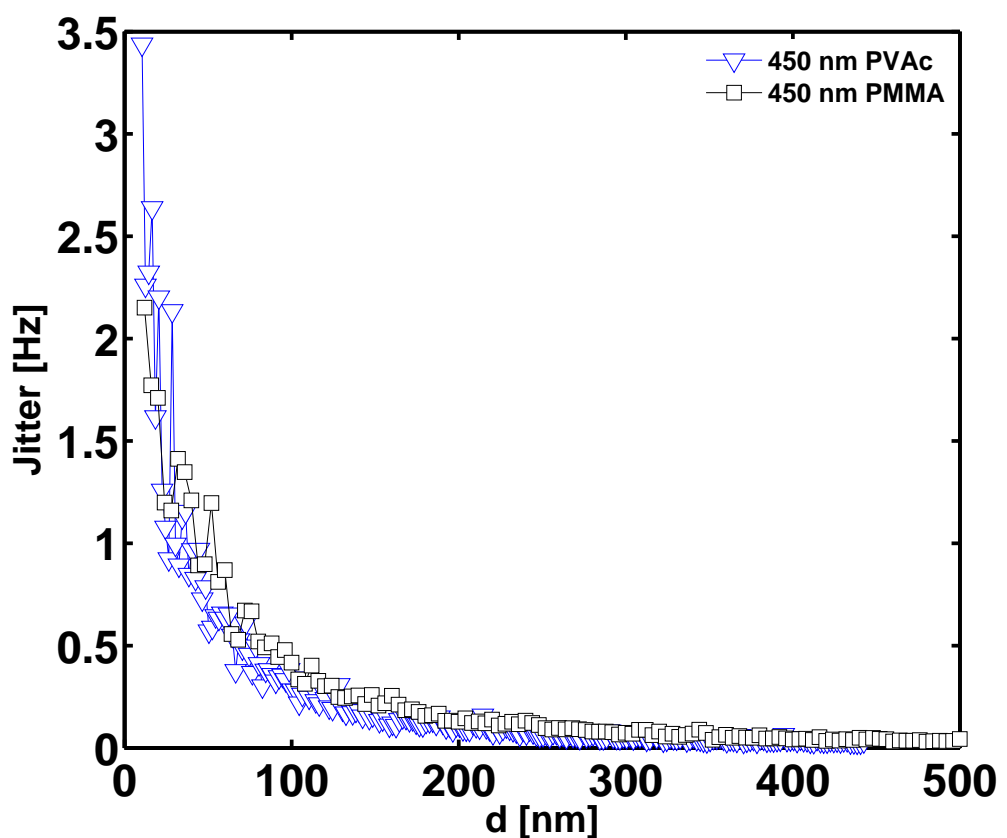


**Figure 6.13:** Cantilever frequency jitter measured in a 10Hz bandwidth over 450nm thick films of PMMA and PVAc. The friction was measured concurrently with the jitter and the surface location was determined by  $Q$  extrapolation.

## CHAPTER 7

### THEORY OF NONCONTACT DIELECTRIC FRICTION

#### 7.1 Introduction and hypothesis

Here we propose that the noncontact friction observed in chapter 6 resulted from dielectric fluctuations within the polymer thin films. We present a theoretical formalism and comparison to measurements presented in [77]. We have proposed that these dielectric fluctuations result in a fluctuating electric field above the dielectric and that this electric field couples to our charged cantilever tip, resulting in noncontact friction as shown schematically in figure 7.1. As discussed in chapter 4, dielectric fluctuations have been shown, by an analogous mechanism, to induce drag on ions moving in polar solvents.

This chapter proceeds by outlining our calculation, including the application of linear response theory and electrostatics, to the problem of a cantilever near a thin dielectric film. Using an adiabatic approximation from the literature we were able to extend this static result to the dynamic case. We then discuss dielectric spectroscopy measurements which facilitated the comparison of our theoretical calculation with the friction measurements presented in the previous chapter. Direct comparisons, requiring an estimate of  $q$ , are made as are comparisons between ratios of measured and predicted friction, allowing us to bypass the poorly defined tip charge estimate.

#### 7.2 Outline of the calculation

The goal of the calculation presented here is to find the correlation function of electric field fluctuations arising from dielectric fluctuations a distance  $d$  above a slab of dielectric backed by a conductor. Using this we can calculate the friction using the formalism presented in chapter 4. Our goal was to calculate

$$\Gamma_s = \frac{q^2}{k_B T} \int_0^\infty dt \cos(\omega_c t) C_E(t), \quad (7.1)$$

$$C_E(t) \equiv \langle \delta E_x(t) \delta E_x(0) \rangle. \quad (7.2)$$

The angular brackets in equation 7.1 represent an equilibrium average for  $q = 0$ . We compute  $\Gamma_s$  by connecting the cosine transform of  $C_E(t)$  in equation 7.1 to  $\hat{\epsilon}(\omega)$ , which may be measured independently.

##### 7.2.1 Linear response

We begin by determining a relation between the static dielectric constant of the polymer  $\epsilon \equiv \hat{\epsilon}(0)$  and the mean-squared electric field fluctuations at the cantilever tip,  $C_E(0) = \langle (\delta E_x)^2 \rangle$ . We consider a fictitious dipole moment of magnitude  $\mu$  oriented along  $x$  at the location of the cantilever tip. A dipole is chosen for this analysis because its energy is linear in the electric field produced by the sample and it is oriented in the direction of the cantilever motion as to be sensitive to the component of the electric field we are interested in calculating. This dipole will polarize the sample, generating a reaction field [130] at the location of the dipole. This reaction field will, in general, depend on the dielectric properties of the film. The average value of this fluctuating reaction field is denoted  $E_x$ . In the regime of linear response,  $E_x$  is linear in the dipole moment and proportional to the mean-squared field fluctuation generated by the sample at the location of the cantilever tip. In the absence of the fictitious dipole,

$$\langle (\delta E_x)^2 \rangle = \frac{k_B T}{\mu} E_x \quad (7.3)$$

where  $\mu$  is dipole moment of the dipole and  $\langle \dots \rangle$  denotes an ensemble average over the configurations of the dielectric in the absence of the polarizing dipole. Linear response theory affords a relationship between the stochastic equilibrium fluctuations of the dielectric and its response to a small perturbation. The reaction field  $E_x$  can also be calculated directly using electrostatics, relating these two calculations explicitly allows us to calculate the friction arising from dielectric fluctuations.

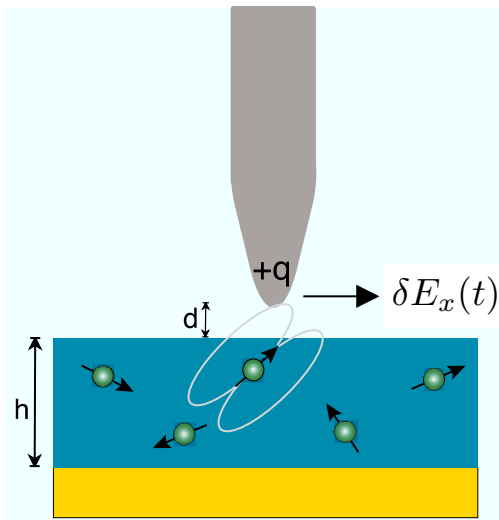


**Figure 7.1:** Schematic of the proposed mechanism of noncontact friction. Dielectric fluctuations couple to the charged cantilever tip resulting in a stochastic force and therefore friction.

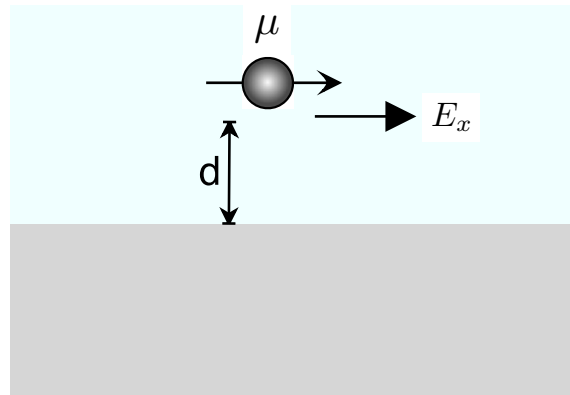


**Figure 7.2:** The reaction field  $E_x$  generated by a test dipole a distance  $d$  from an infinite dielectric. The reaction field results from the polarization of the dielectric by the dipole. A dipole was used because its energy is linear in the reaction field.

### 7.2.2 Electrostatics: infinitely thick film

We begin by considering a dipole a distance  $d$  above an infinite dielectric electric. By slightly modifying a calculation given in [131] we have

$$E_x = \frac{\mu k_B T}{4\pi\epsilon_0} \frac{1}{8d^3} \frac{\epsilon - 1}{\epsilon + 1}. \quad (7.4)$$

We then calculated the field fluctuations directly using equation 7.3,

$$\langle (\delta E_x)^2 \rangle = \frac{\mu k_B T}{4\pi\epsilon_0} \frac{1}{8d^3} \frac{\epsilon - 1}{\epsilon + 1}. \quad (7.5)$$

Equation 7.5 gives us the correlation function in equation 7.2 in the zero time limit. We repeated the calculation for a film of finite thickness backed by a conductor.

### 7.2.3 Electrostatics: films of finite thickness

For a film of finite thickness the problem was solved by the method of images. Using the method of images, the resulting expression became an infinite series which we expressed as an integral. The detailed calculation is given in [132] and also can be found in [133]. The infinite series solution was found to be

$$E_x = \mu\zeta \left\{ \frac{1}{8d^3} - \frac{\zeta}{8(h+d)^3} - (1-\zeta^2) \sum_{j=0}^{\infty} (-\zeta)^j \left( \frac{1}{2d + (4+2j)h} \right)^3 \right\}, \quad (7.6)$$

$$\zeta \equiv \frac{\epsilon - 1}{\epsilon + 1}. \quad (7.7)$$

The first term in equation 7.6 is the reaction field in the limit of an infinitely thick dielectric slab, with  $\zeta$  a dielectric screening function arising in planar geometries, and the infinite series gives corrections for finite slab thickness  $h$ . For a thin dielectric sample, it is convenient to sum the series in equation 7.6 by applying the identity  $b^{-3} = (1/2) \int_0^\infty dy y^2 \exp(-by)$  to each term in the series to yield

$$E_x = \frac{\mu\zeta}{2d^3} \int_0^\infty dx x^2 e^{-2x} \left[ \frac{(1 - e^{-4(h/d)x})}{1 + \zeta e^{-2(h/d)x}} \right]. \quad (7.8)$$

We can calculate the mean-square fluctuation using our linear response argument above

$$\langle (\delta E_x)^2 \rangle = \frac{k_B T \zeta}{2d^3} \int_0^\infty dx x^2 e^{-2x} \left[ \frac{(1 - e^{-4(h/d)x})}{1 + \zeta e^{-2(h/d)x}} \right]. \quad (7.9)$$

Equation 7.9 provides the electric field fluctuations arising from dielectric fluctuations within the dielectric. However, the cantilever friction depends not on these low frequency fluctuations but on the fourier component of the electric field fluctuations at the mechanical resonance frequency of the oscillator. To do this we needed to consider the dynamics of the dielectric fluctuations.

### 7.2.4 Dynamics

Following linear response theory (discussed in detail in appendix B) we related the time derivative correlation function of the field fluctuations to the dielectric response of the film. Following standard linear response arguments we treated the situation where the dipole is turned on at  $t = 0$ , as shown in figure 7.3. We related the response of the film to the Fourier-Laplace transform of the electric field autocorrelation function.

From linear response we know that

$$E_x(t) = \int_0^t \Phi(t-\tau) \mu(\tau) d\tau. \quad (7.10)$$

Where  $\Phi(t-\tau)$  is the response function of the dielectric. We have also seen in appendix B, that the response function in classical mechanics  $\Phi(t)$  is given by

$$\Phi(t) = -\frac{1}{k_B T} \frac{d}{dt} C(t). \quad (7.11)$$

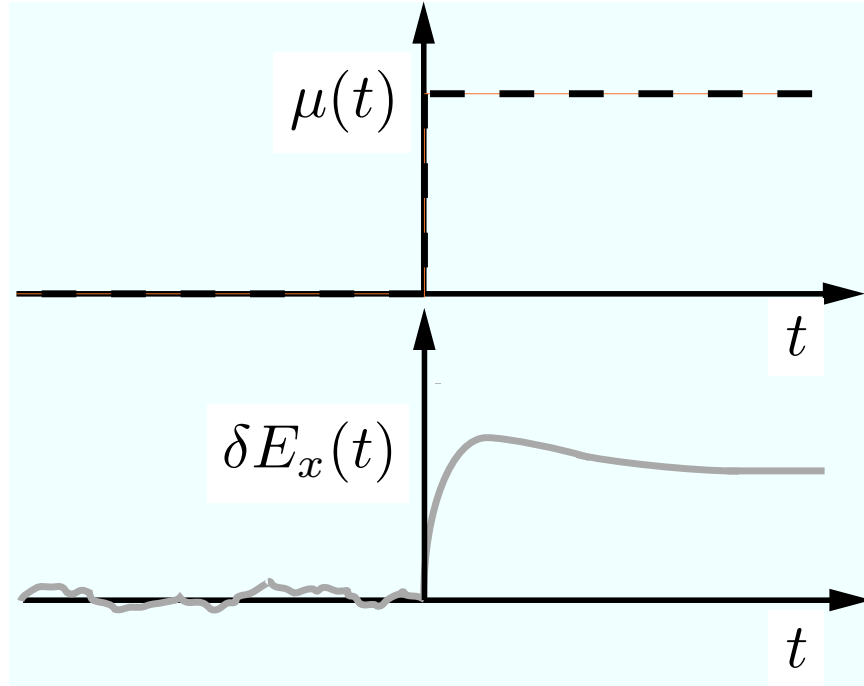


**Figure 7.3:** The time-dependent dipole  $\mu(t)$  is turned on at  $t = 0$  resulting in the reaction field  $E_x(t)$ .  $\Phi(t)$  governs the functional form of the reaction field response as given by equation 7.10 and is equivalent to the time derivative of the autocorrelation function of the fluctuations shown prior to the application of the perturbation.

Putting these together we have

$$E_x(t) = -\frac{1}{k_B T} \int_0^t \dot{C}_E(t-\tau) \mu(\tau) d\tau \quad (7.12)$$

where the dot denotes the time derivative. As discussed in appendix B this integral equation can be solved by the method of Laplace transforms. Here we exploited the method of Fourier-Laplace transforms ( $s = i\omega$ ), essentially a single-sided Fourier transform, defined as  $\hat{F}(\omega) \equiv \int_0^\infty e^{i\omega t} F(t) dt$ . Completing the transform we have

$$\hat{E}_x(\omega) = -\frac{1}{k_B T} \hat{\mu}(\omega) (-i\omega \hat{C}_E(\omega) - C_{xx}(0)). \quad (7.13)$$

In order to continue we require an expression for  $\hat{C}_E(\omega)$  which we could not calculate directly without detailed knowledge of the microscopic dynamics within the dielectric. We next invoke a quasi-static approximation that has been successfully applied to time-dependent solvation phenomena, such as the dynamic Stokes shift, in molecular fluids, [134–137] in which  $\hat{E}_x(\omega)$  is determined by solving a macroscopic electrostatic boundary-value problem for a dielectric with complex dielectric function  $\hat{\epsilon}(\omega)$ . In this approximation, the Maxwell equation  $\epsilon \nabla \cdot \mathbf{E} = 4\pi\rho$  for static electric field  $\mathbf{E}$  and charge distribution  $\rho$  is assumed to hold at finite frequency,  $\hat{\epsilon}(\omega) \nabla \cdot \hat{\mathbf{E}}(\omega) = 4\pi\hat{\rho}(\omega)$ . For the case in which a charge distribution  $\rho(t)$  is switched on at  $t = 0$  and attains an asymptotic limiting value of  $\rho$  as  $t \rightarrow \infty$ , the approximate frequency-dependent Maxwell equation approaches the correct limit as  $\omega \rightarrow 0$ :  $\hat{\mathbf{E}}(\omega) \rightarrow \mathbf{E}/i\omega$ ,  $\hat{\rho}(\omega) \rightarrow \rho/i\omega$ , and  $\hat{\epsilon}(\omega) \rightarrow \epsilon$ . Application of this result at nonzero frequency represents an adiabatic approximation. [134] Using this approximation we substituted our zero frequency linear response expression for the reaction field in equation 7.3 into equation 7.13 assuming that it holds at finite frequency as well. Equation 7.13 became

$$i\omega \hat{C}_{xx}(\omega) = \frac{k_B T}{8d^3} \left( \frac{\hat{\epsilon}(\omega) - 1}{\hat{\epsilon}(\omega) + 1} - \frac{\epsilon - 1}{\epsilon + 1} \right), \quad (7.14)$$

where  $\hat{\epsilon}(\omega) = \hat{\epsilon}'(\omega) + i\hat{\epsilon}''(\omega)$  are the fourier components of the complex valued dielectric response of the *bulk* film.

**Table 7.1:**  $\hat{\epsilon}''(\omega_c)$  for PMMA, PVAc and PS with  $\omega_c/2\pi = 7.8\text{kHz}$ . PMMA and PVAc values were measured as outlined in appendix H and the value for PS was taken from the literature [138].

Polymer	$\hat{\epsilon}'(\omega_c)$	$\hat{\epsilon}''(\omega_c)$
PMMA	2.96	0.137
PVAc	3.23	0.0604
PS	2.5	0.0015

## 7.3 Calculating friction

Combining this adiabatic approximation with our linear response and electrostatic analyses we were able to relate the noncontact friction to the complex dielectric response of the film.

### 7.3.1 Friction over an infinite film

The cosine transform in equation 7.1 is the real part of  $\hat{C}_E(\omega)$  (see also appendix B). Using the real portion of our result combined with equation 7.1 we were able to calculate the friction arising from an infinite dielectric as

$$\Gamma_s(\omega) = \frac{q^2}{4\pi\epsilon_0} \frac{1}{4d^3} \frac{1}{\omega} \frac{\hat{\epsilon}'(\omega)}{(\hat{\epsilon}'(\omega) + 1)^2 + \hat{\epsilon}''(\omega)^2}. \quad (7.15)$$

The simplified form of the equation given here allowed us to develop some intuition. First, while equation 7.15 predicts a  $1/d^3$  dependence of the friction, the charge on the tip  $q$  is dependent on the tip-sample capacitance which will also contain a distance dependent component of an unknown functional form. Least-squares fitting of the  $\Gamma(d)$  data to a power law yielded  $\Gamma(d) \sim 1/d^{1.5}$  consistent with a capacitance contribution to the distance dependence of the friction and with other measurements of noncontact friction. [22] To calculate the friction experienced by a cantilever near an infinite dielectric using this formalism, we set  $\omega = \omega_c$  and used measured values for  $\hat{\epsilon}(\omega_c)$  as discussed below.

### 7.3.2 Friction over a finite film backed by a conductor

For a finite film, backed by a conductor we combine our dynamic approximation with equation 7.8. The surface-induced friction affecting the cantilever tip is then given by

$$\Gamma_s = \frac{q^2 \hat{\zeta}''(\omega_c)}{2\omega_c d^3} \int_0^\infty dx x^2 e^{-2x} \frac{1 - e^{-4(h/d)x}}{\left(1 + \hat{\zeta}'(\omega_c)e^{-2(h/d)x}\right)^2 + \left(\hat{\zeta}''(\omega_c)\right)^2 e^{-4(h/d)x}}, \quad (7.16)$$

with the real and imaginary parts of  $\hat{\zeta}(\omega)$  defined by  $\hat{\zeta}(\omega) = \hat{\zeta}'(\omega) + i\hat{\zeta}''(\omega)$ . To evaluate the friction in this case also required knowledge of  $\hat{\epsilon}(\omega)$  and numerical integration of equation 7.16. It can be shown that the first term in the series expansion of equation 7.16 returns equation 7.15.

### 7.3.3 Dielectric spectroscopy

Dielectric spectroscopy was performed using a Hewlett-Packard 4192A spectrum analyzer on polymer thin films prepared identically to those used in the noncontact friction measurements. Due to instrumentation restrictions dielectric spectroscopy was performed at ambient conditions as opposed to the high vacuum noncontact friction measurements. The sensitivity of the dielectric spectrometer was insufficient to measure the dielectric loss ( $\hat{\epsilon}''(\omega)$ ) in polystyrene due to the very low loss of this material. Therefore, spectroscopy measurements occurred on thin films of PMMA and PVAc only. Details of the sample preparation, apparatus and measurement are given in appendix H. For the friction measurements here we needed only the Fourier component of the complex dielectric response at the cantilever resonance frequency of 7.8kHz. The results are given in table 7.1.

These measured values agreed well with those found in the literature. [139–141] For film thicknesses approximately larger than the radius of gyration of the polymer, the dielectric response will typically follow the bulk dielectric response.

[142] This generalization was supported by our dielectric spectroscopy measurements. The agreement between our dielectric spectroscopy measurements for PMMA and PVAc and published *bulk* values at similar temperatures and frequencies lends support to our use of the published bulk data for analysis of PS thin films.

The measured dielectric response obtained by dielectric spectroscopy is only a first approximation to the dielectric response in the films used for the noncontact friction studies. First, in the dielectric spectroscopy measurements, both surfaces of the dielectrics are confined by metal layers. The dielectric response of thin films has been shown previously to differ greatly between physically confined surfaces and free surfaces. [101–103] In addition, our dielectric spectroscopy measurements were performed under ambient conditions, where water adsorption can change the resulting complex dielectric response.

## 7.4 Comparison with experiment

Combining our dielectric spectroscopy measurements from the previous section and equation 7.16 we were able to independently predict the levels of noncontact friction over dielectrics arising from thermally driven dielectric fluctuations. To do this it was necessary to estimate  $q = C(V_{ts} - \phi)$ . For all measurements outlined above we set  $V_{ts} - \phi = 0.5V$ , therefore the tip charge estimate required an estimate of the tip sample capacitance as discussed in section 6.3.2. The integral in equation 7.16 was evaluated numerically in Matlab and was found to converge rapidly for all film thicknesses and tip sample separations. To check the numerical integration the series expansion of equation 7.16 was also evaluated explicitly and found to converge rapidly to the same value as the integral. The first term in the expansion dominated typically taking on a value ten times larger than the third term. The predicted friction due to dielectric fluctuations is shown in figure 7.4. All plots of equation 7.16 were generated with the tip radius as the sole free parameter, taken to be 10nm.

The qualitative agreement in figure 7.4 is striking given the simplicity of the theory and the crude estimation of the tip charge. Our theory correctly predicted two trends in the data. First, it predicted the dependence of noncontact friction on the chemistry of the sample for the three samples measured. In addition, our theory correctly predicted the trend of decreasing friction with film thickness. It should be noted that the theoretical formalism predicts only  $\Gamma_s$  and makes no claim to predicting the cantilever's intrinsic friction. The data plotted in figure 7.4 is the total friction  $\Gamma$ , therefore the *measured* value of  $\Gamma_0$  has been added to the predicted levels of  $\Gamma_s$  to facilitate the comparison to the measured  $\Gamma$ . Plotting  $\Gamma$  is preferable to  $\Gamma_s$  so that a log scale can be used on the friction axis.

Our theoretical formalism correctly predicts the measured levels of noncontact friction over dielectrics. We conclude from the qualitative agreement between theory and experiment that the noncontact friction in our measurements was dominated by electric field fluctuations arising from thermally driven dielectric fluctuations within the sample.

### 7.4.1 Ratios

Here we make a comparison between measurement and calculation that does not require the determination of the tip charge  $q$ , by examining the ratio of  $\Gamma_s$  values for two different polymers at constant tip-sample separation  $d$ , and film thickness,  $h = 450\text{nm}$ . Tip charge  $q$  is approximately constant at fixed  $d$  and  $h$ . This is true because the tip-sample capacitance  $C$  is approximately constant for fixed  $d$  since the zero frequency dielectric constants are nearly equal for all polymer films. Then according to equation 7.16, this friction ratio is independent of  $q$ , depending only on  $h/d$  and the dielectric functions of the two materials.

The three friction ratios for each pair of polymer samples are plotted in figure 7.5 for  $7\text{nm} \leq d \leq 20\text{nm}$ . Measured ratios are shown by symbols, connected by line segments to guide the eye. The circles show  $\Gamma_s^{\text{PMMA}}/\Gamma_s^{\text{PS}}$ , the squares show  $\Gamma_s^{\text{PVAc}}/\Gamma_s^{\text{PS}}$ , and the triangles show  $\Gamma_s^{\text{PMMA}}/\Gamma_s^{\text{PVAc}}$ . Over this range of  $d$  and for a relatively thick film of  $h = 450\text{nm}$ , these ratios do not depend significantly on  $d$ , and hence the variation displayed in figure 7.5 is noise, arising from errors in the friction measurement, that provided an estimate for error bars on the mean values of these ratios. The resulting mean values of these friction ratios are  $\Gamma_s^{\text{PMMA}}/\Gamma_s^{\text{PS}} = 75 \pm 21$ ,  $\Gamma_s^{\text{PVAc}}/\Gamma_s^{\text{PS}} = 18 \pm 5$ , and  $\Gamma_s^{\text{PMMA}}/\Gamma_s^{\text{PVAc}} = 4.4 \pm 0.4$ . The prediction of equation 7.16 for each ratio is shown by the continuous curves in figure 7.5, which do not vary significantly with  $d$  for  $h \gg d$ . Dashed lines show error bars for the calculated friction ratio, which arise from uncertainties in the measured dielectric functions. The calculated friction ratios are  $\Gamma_s^{\text{PMMA}}/\Gamma_s^{\text{PS}} = 71 \pm 7$ ,  $\Gamma_s^{\text{PVAc}}/\Gamma_s^{\text{PS}} = 27 \pm 3$ , and  $\Gamma_s^{\text{PMMA}}/\Gamma_s^{\text{PVAc}} = 2.6 \pm 0.3$ , within 50 % of the measured results in the worst case.

Friction measurements for PMMA and PVAc could be carried out for larger  $d$  than for PS due to higher levels of noncontact friction. The ratio  $\Gamma_s^{\text{PMMA}}/\Gamma_s^{\text{PVAc}}$  is shown up to  $d = 60\text{nm}$  in figure 7.6, in which the ordinate shows a linear scale in contrast to figure 7.5. The greater range of  $d$  in figure 7.6 reveals that the ratio  $\Gamma_s^{\text{PMMA}}/\Gamma_s^{\text{PVAc}}$  increased

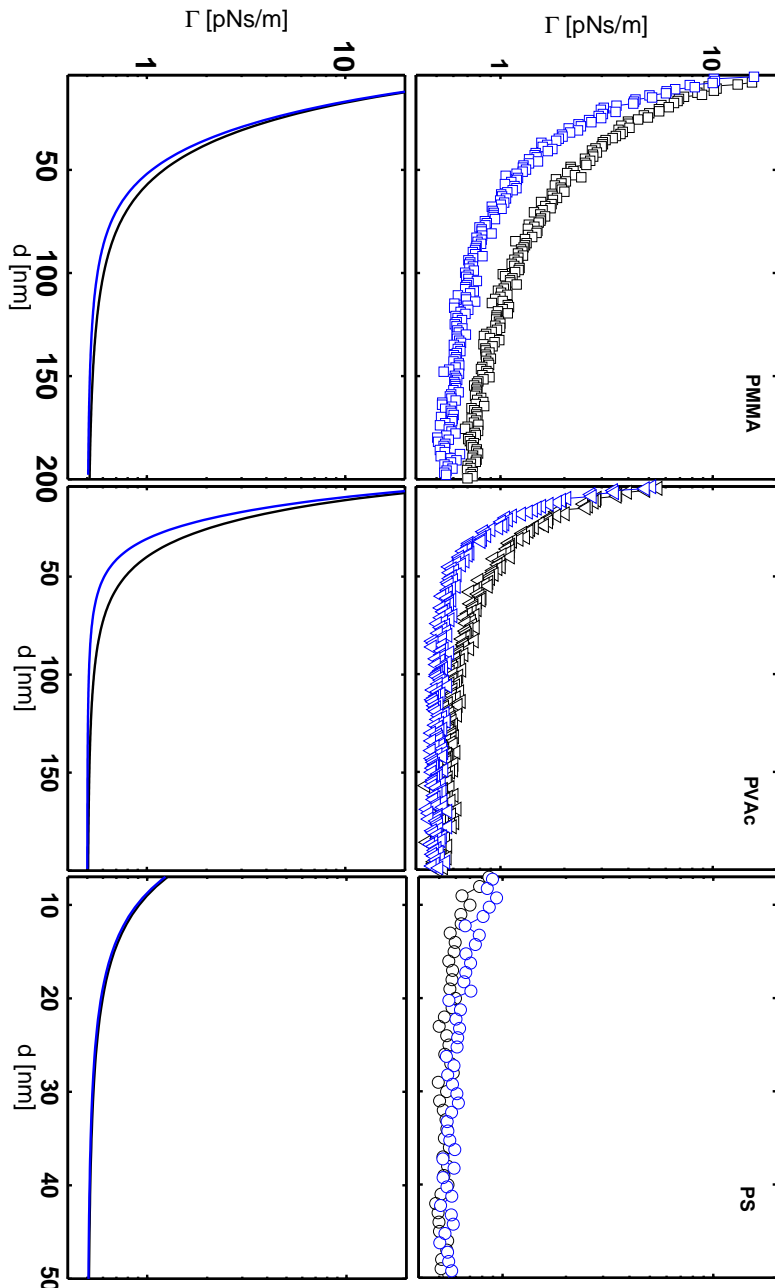


**Figure 7.4:** Upper plots: total measured friction  $\Gamma$  plotted for the six films measured. Black symbols are 450 nm thick films, blue symbols are 40 nm thick PVAc and 30 nm thick PS. Lower plots: predicted friction using capacitance estimate, dielectric spectroscopy and equation 7.16 for the measured film thicknesses.

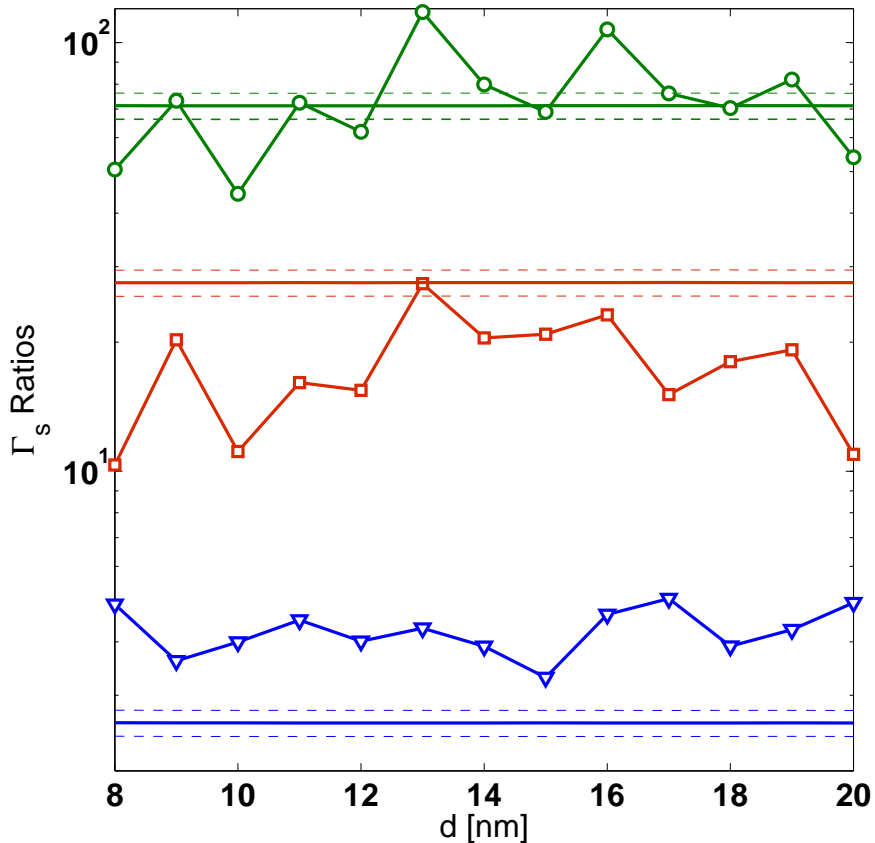


**Figure 7.5:** The ratio of friction coefficients for pairs of polymers is shown for  $7\text{nm} \leq d \leq 20\text{nm}$  at fixed film thickness  $h = 450\text{nm}$ . Symbols show the measured friction ratios  $\Gamma_s^{\text{PMMA}}/\Gamma_s^{\text{PS}}$  (circles),  $\Gamma_s^{\text{PVAc}}/\Gamma_s^{\text{PS}}$  (squares), and  $\Gamma_s^{\text{PMMA}}/\Gamma_s^{\text{PVAc}}$  (triangles). The predictions of equation 7.16 together with dielectric relaxation measurements are shown by the solid curves with  $\Gamma_s^{\text{PMMA}}/\Gamma_s^{\text{PS}}$  having the highest value and  $\Gamma_s^{\text{PMMA}}/\Gamma_s^{\text{PVAc}}$  having the lowest value, in agreement with the measurement. Dashed lines indicate the error bars on the calculated friction ratios, which are associated with the dielectric spectroscopy measurements.

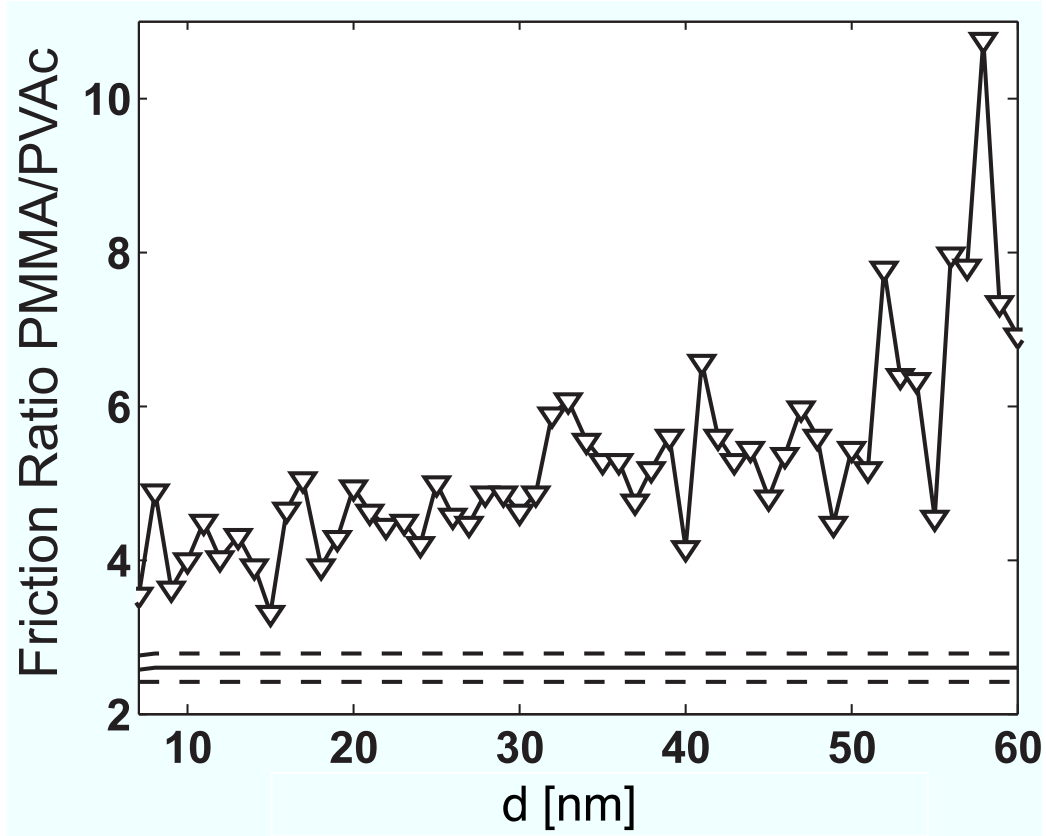


**Figure 7.6:** The ratio of friction coefficients  $\Gamma_s^{\text{PMMA}}/\Gamma_s^{\text{PVAc}}$  is shown for  $7\text{ nm} \leq d \leq 60\text{ nm}$  at fixed film thickness  $h = 450\text{ nm}$ , a larger range of tip-sample separation than covered in figure 7.5. Note the linear scale of the ordinate, in contrast to figure 7.5. As in figure 7.5, the solid curve shows the prediction of equation 7.16, with error bars indicated by dashed lines.

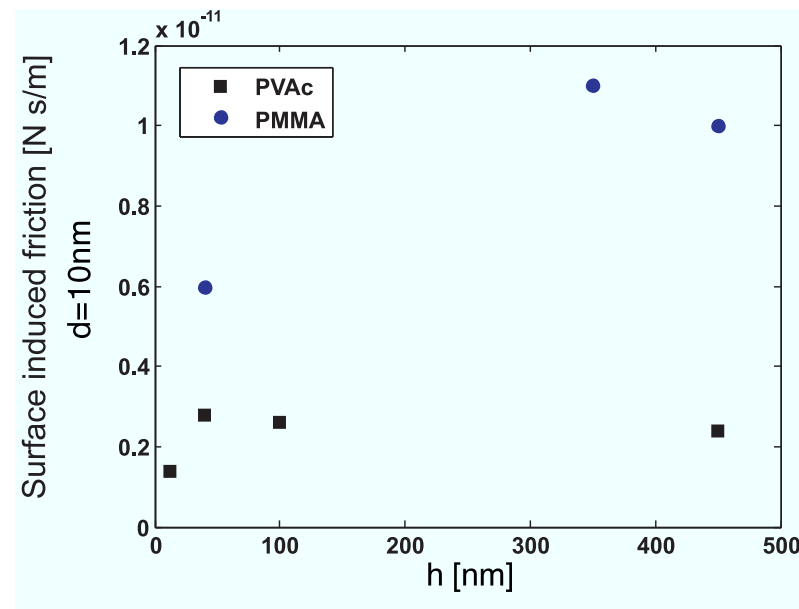


**Figure 7.7:** The measured dependence of noncontact friction  $\Gamma_s$  on film thickness  $h$  for PMMA and PVAc.

with increasing  $d$  in a way that was not reproduced by the calculation. Note also that the signal-to-noise ratio was seen to decrease with increasing  $d$  as  $\Gamma_s \rightarrow \Gamma_0$ . The present analysis treats the polymer film as dynamically homogeneous, so that any variation in polymer dynamics with depth in the film [143] that was dependent on molecular identity could result in additional  $d$  dependence in the friction ratio not included in equation 7.16. The calculation of the friction from equation 7.16, together with measured dielectric spectra, reproduces the trends shown by the measured friction, that  $\Gamma_s^{\text{PMMA}} > \Gamma_s^{\text{PVAc}} > \Gamma_s^{\text{PS}}$ .

The comparison of between our calculation and measurement in figure 7.5 is performed without any adjustable parameters. The agreement between theory and experiment strongly supports the picture that the noncontact friction in these experiments is dominated by dielectric fluctuations in the polymer samples.

#### 7.4.2 Further considerations

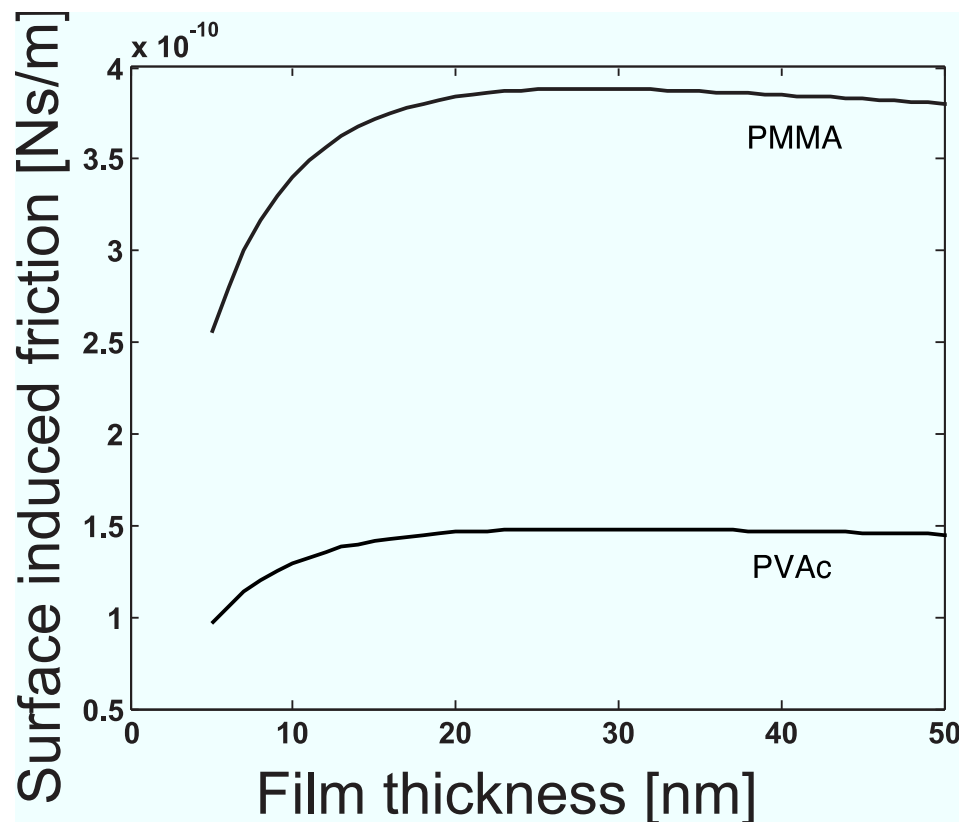
##### Chemical composition and thickness dependence

Figure 6.6 shows that the dependence of noncontact friction on thickness was stronger for PMMA than PVAc. Namely, thinner films of PVAc than PMMA are required for equivalent reduction in friction. The measured trend is shown in figure 7.7. Note that a reduction in friction over PVAc requires that we go from  $h = 450 \rightarrow 12\text{nm}$  while for PMMA a comparable reduction requires only  $h = 450 \rightarrow 40\text{nm}$ .

Our theory qualitatively explains this trend. Figure 7.8 shows noncontact friction calculated using equation 7.16 as a function of  $h$  for a fixed  $d$  of 5nm. The observed behavior is consistent with the greater overall levels of friction observed over PMMA. For PMMA greater fluctuations are present therefore fluctuating dipoles deeper in the dielectric layer are able to make a significant contribution to the fluctuating field resulting in increased friction. Since dipoles deeper in the dielectric are contributing to the friction it is intuitive that the thickness dependence will arise for *thicker* films of PMMA than PVAc. Figure 7.9 illustrates both the distance and thickness dependence of noncontact friction over PMMA displaying the nearly constant noncontact friction down to thicknesses on the order of the tip size.

##### Better capacitance estimates?

The qualitative agreement in figure 7.4 may in large part have been due to the crude nature of the tip-sample capacitance estimate. Far more complicated estimates of the tip sample capacitance are possible by including contributions from other parts of the cantilever tip. [127] While we believe that the agreement between theory and experiment in



**Figure 7.8:** The calculated dependence of noncontact friction  $\Gamma_s$  on film thickness  $h$  for PMMA and PVAc using equation 7.16.  $d = 5\text{nm}$  was chosen to highlight the effect.

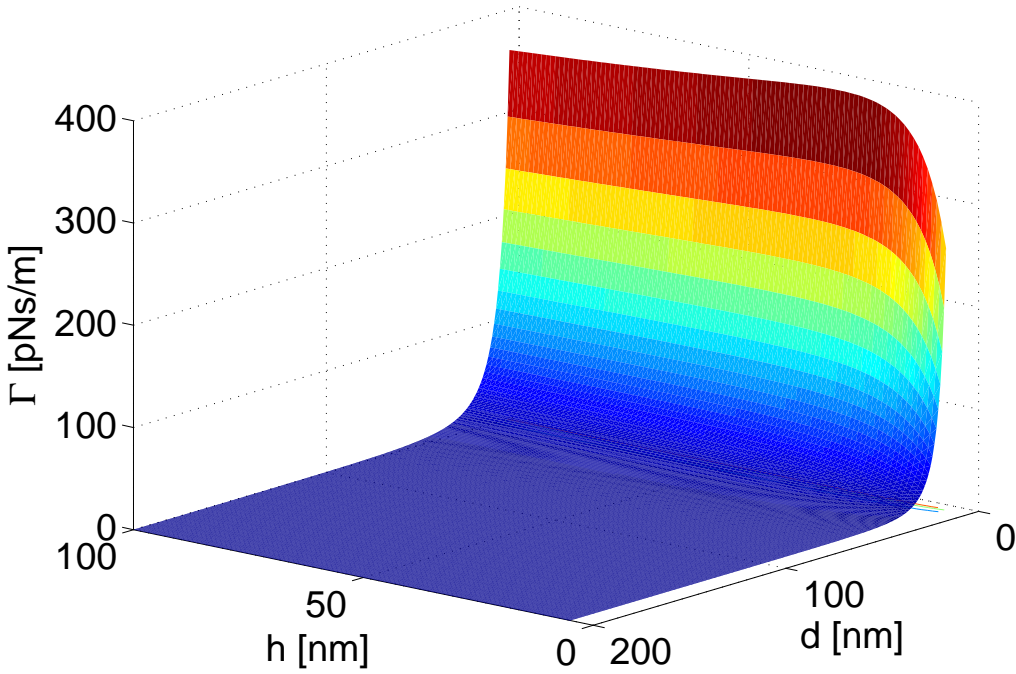


**Figure 7.9:**  $\Gamma_s$  as a function of  $d$  and  $h$  over PMMA calculated using equation 7.16 and the spherical estimate for the tip sample capacitance.

figures 7.4 and 7.5 is sufficient to justify our conclusion that dielectric fluctuations result in noncontact friction, it is reasonable to ask if improved tip-sample capacitance estimates are capable of improving the agreement between theory and experiment. To do this we modeled the tip as a sphere and a cone following work in the literature. [127] These estimates served only to increase the capacitance estimate and therefore the tip charge estimate. While this improved agreement at large  $d$ , it degraded agreement at small  $d$  as shown in figure 7.10. Since the validity of such models are not based in any *measurable* quantity we believed that they could not strengthen our conclusion.

### Dynamic heterogeneity

As mentioned above, our theory treats the entire film as dynamically homogenous. The dielectric response of the film is assumed to follow the bulk response even near the surface. This assumption may well be a significant source of disagreement between theory and experiment. As an exercise we re-fit the data to the theory and assumed that a small layer of the dielectric near the surface was “dead” exhibiting no dielectric fluctuations at the cantilever frequency. We left the thickness of this assumed dead layer to be a free parameter for each polymer the results are shown in figure 7.11. While we found that this additional free parameter in the model dramatically improved the fit of the theory to the data, we have no experimental assay of its validity. While it is intuitive to expect dynamic heterogeneity within the film, we did not find that the addition of free parameters to the model strengthened our conclusion, and therefore they were therefore omitted from the published results. [76]

## 7.5 Discussion

Although the noncontact friction observed here resulted from a coupling between dielectric fluctuations in the sample and charge on the cantilever, in the linear response regime, the fluctuating polarization induced by the cantilever’s electric field is proportional to the fluctuations present in the absence of a perturbing field. The theory employed here could be generalized to include interactions with inhomogeneous tip electric fields likely to be present even at  $V_{ts} = \phi$ . [22] In

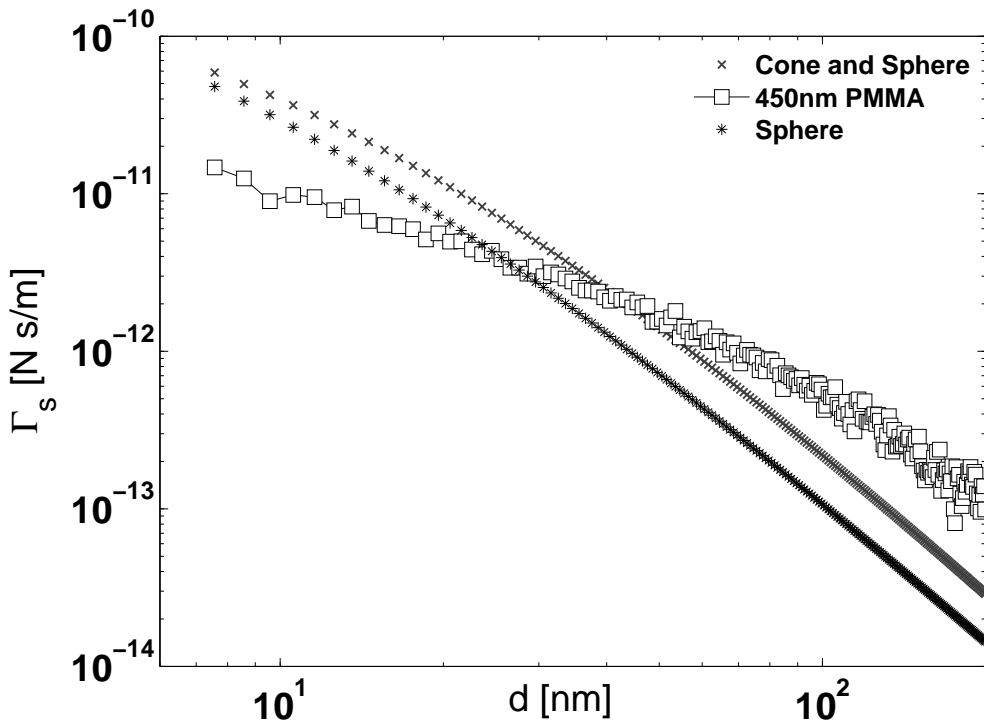


**Figure 7.10:** Friction calculated over PMMA using two tip-sample capacitance estimates: treating the tip as a sphere and a sphere+cone.

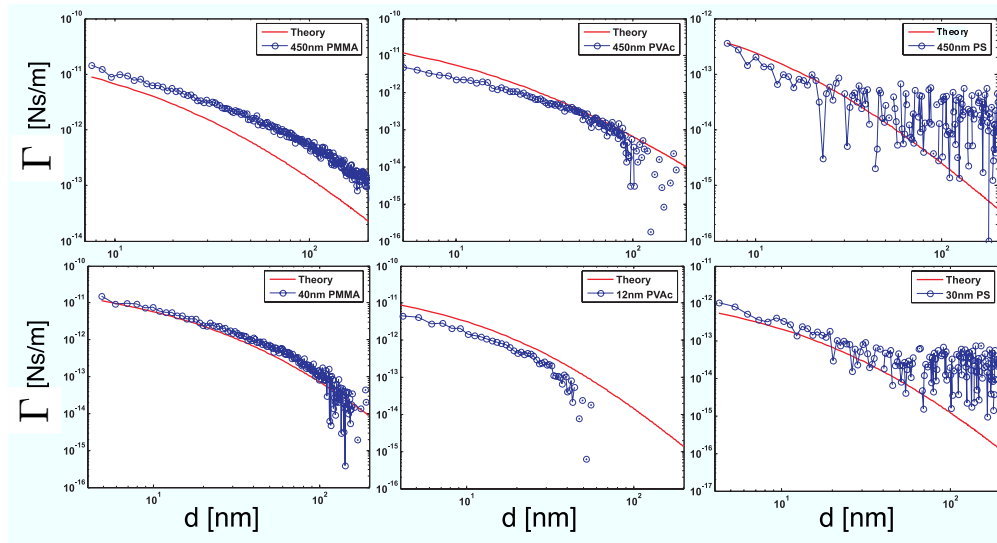


**Figure 7.11:** Plots comparing the integral in equation 7.16 with the effective dielectric thickness and distance ( $d_{\text{effective}}$ ) modified as described above. This effectively amounted to moving the tip further away from the active region of the polymer. All traces use a tip radius of 15nm. The dead layer thicknesses are taken to be 20nm for PMMA, 10nm for PVAc, and 8 nm for PS.

this case, the tip will couple to the same dielectric fluctuations observed here, although other mechanisms may become important. [39, 40, 120]

While very low frequency dielectric fluctuations have been detected as a slowly varying force-gradient by scanned probe methods before [144], we believe our measurements constitute the first, direct, mechanical detection of non-contact friction due to dielectric fluctuations. This technique, generally applicable to any system exhibiting dielectric fluctuations with appreciable spectral density at  $\omega_c$ , will enable exploration of dielectric fluctuations at the nanoscale. Equation 7.16 suggests that one route to minimizing noncontact friction due to dielectric fluctuations is to work with radio-frequency cantilevers. Changing the cantilever frequency requires that the dimensions of the cantilever be changed significantly. It would be fascinating to construct cantilevers across several decades in frequency with comparable tip geometries to measure noncontact friction under conditions of equivalent tip charge.

In addition, we anticipate that numerous applications, including the direct detection of polymer fluctuations at or around the glass transition, should result from the new view of non-contact friction presented here. One difficulty with studying the glass transition using this technique might be spatial resolution. The spatial resolution of our measurements were of the order of 100nm. Most experimental measurements of dynamic heterogeneity around the glass transition predict heterogeneous regions of  $\sim 5\text{nm}$ . [111, 144] The spatial resolution of our measurement could be improved to a few tens of nanometers by making much smaller tips, perhaps using carbon nanotubes, and measuring friction without self oscillating the cantilever.

### 7.5.1 Relevance to MRFM

Our measurements over dielectrics occurred at room temperature, while MRFM measurements are typically undertaken at 4K and below. From the present data we cannot say if dielectric fluctuations will dominate the low temperature contribution to surface induced dissipation. Despite this, it has been reported that PMMA is a potent source of noncontact friction even at cryogenic temperatures. [17]

Our data does point to several routes to minimizing noncontact friction in MRFM measurements. First, thin films backed by metals produce the lowest levels of fluctuating fields and therefore the lowest levels of noncontact friction. Better yet would be to coat organic layers with metals, since metals appear to produce the lowest levels of noncontact friction. Two issues are associated with this, first coating samples moves the tip further from the target spin and second, the effects of conduction electrons in metals on nearby spin relaxation times is unknown.

## APPENDIX A SOLUTION TO BLOCH EQUATIONS FOR $T_1 = T_2$

### A.1 Solution to the Vector Equation of Motion

For some electron spin resonance ESR experiments it is safe to assume that  $T_1 = T_2$ . This is the case, for example, in the ESR experiments presented in [47, 49]. Experiments of this nature were carried out early in the work discussed in this thesis. Here we present only the derivation of the saturation behavior discussed in greater length elsewhere.

If we make the assumption that  $T_1 = T_2$  we can write the equation of motion given in equation 2.13 to include relaxation as

$$\dot{\boldsymbol{\mu}} = \gamma(\boldsymbol{\mu} \times \mathbf{H}_{\text{eff}}). \quad (\text{A.1})$$

There are several important things to notice about equation A.1. First, the components of this equation are the familiar Bloch equations if we take the static field to be along the  $\hat{z}$  direction and  $T_1 = T_2$ . Second, notice that  $\boldsymbol{\mu}$  is included in vector cross products; thus any standard solution to this differential equation requires breaking equation A.1 into vector components and solving those components individually. Using this as a motivator we embark on the following manipulation. Begin by finding the steady state solution to this equation, such that

$$\dot{\boldsymbol{\mu}} = 0. \quad (\text{A.2})$$

From which we see that

$$\boldsymbol{\mu} \times T_1 \gamma \mathbf{H}_{\text{eff}} = (\boldsymbol{\mu} - \boldsymbol{\mu}_0). \quad (\text{A.3})$$

Now, define the unitless vector which points along the effective field as

$$\boldsymbol{\Omega} = T_1 \gamma \mathbf{H}_{\text{eff}}. \quad (\text{A.4})$$

Leaving us with

$$\boldsymbol{\mu} \times \boldsymbol{\Omega} = (\boldsymbol{\mu} - \boldsymbol{\mu}_0). \quad (\text{A.5})$$

By vector identities we know that,

$$\boldsymbol{\mu} \cdot \boldsymbol{\mu} \times \boldsymbol{\Omega} = 0 \quad (\text{A.6})$$

and,

$$\boldsymbol{\Omega} \cdot \boldsymbol{\mu} \times \boldsymbol{\Omega} = 0. \quad (\text{A.7})$$

Plugging both equation A.6 and equation A.7 into equation A.5 we can deduce that

$$\boldsymbol{\Omega} \cdot \boldsymbol{\mu} - \boldsymbol{\Omega} \cdot \boldsymbol{\mu}_0 = 0 \quad (\text{A.8})$$

$$\boldsymbol{\mu} \cdot \boldsymbol{\mu} - \boldsymbol{\mu} \cdot \boldsymbol{\mu}_0 = 0. \quad (\text{A.9})$$

Also, take the cross product of equation A.5 with  $\boldsymbol{\Omega}$

$$\boldsymbol{\mu} \times \boldsymbol{\Omega} \times \boldsymbol{\Omega} = \boldsymbol{\mu} \times \boldsymbol{\Omega} \cdot \boldsymbol{\mu}_0 \times \boldsymbol{\Omega}. \quad (\text{A.10})$$

Recall the following vector identity:

$$\mathbf{A} \times \mathbf{B} \times \mathbf{C} = \mathbf{B}(\mathbf{A} \cdot \mathbf{C}) - \mathbf{C}(\mathbf{A} \cdot \mathbf{B}). \quad (\text{A.11})$$

So, the left hand side of equation A.10 can be simplified to

$$\boldsymbol{\Omega}(\boldsymbol{\mu} \cdot \boldsymbol{\Omega}) - \boldsymbol{\Omega}^2 \boldsymbol{\mu} = \boldsymbol{\mu} \times \boldsymbol{\Omega} \cdot \boldsymbol{\mu}_0 \times \boldsymbol{\Omega}. \quad (\text{A.12})$$

Substituting both equation A.3 and A.8 into equation A.12 we arrive at the following expression

$$\boldsymbol{\Omega}(\boldsymbol{\mu}_0 \cdot \boldsymbol{\Omega}) - \boldsymbol{\Omega}^2 \boldsymbol{\mu} = \boldsymbol{\mu} - \boldsymbol{\mu}_0 - \boldsymbol{\mu}_0 \times \boldsymbol{\Omega}. \quad (\text{A.13})$$

Isolating  $\boldsymbol{\mu}$  in equation A.13 we arrive at the following expression for the dipole moment

$$\boldsymbol{\mu} = \frac{1}{1 + \boldsymbol{\Omega}^2} (\boldsymbol{\mu}_0 + (\boldsymbol{\mu}_0 \cdot \boldsymbol{\Omega}) \boldsymbol{\Omega} + \boldsymbol{\mu}_0 \times \boldsymbol{\Omega}). \quad (\text{A.14})$$

The terms of equation A.14 yield a simple physical picture. In the rotating frame, the direction of the effective field is dictated by the magnitude and direction of the radio frequency field and by the proximity of the frequency of the rf to the resonance frequency of the spins. We can now easily isolate the individual components of the magnetic moment. Recalling equation A.4 we see that

$$\boldsymbol{\Omega} = T_1 \gamma \left( H_0 - \frac{\omega}{\gamma} \right) \hat{z} + T_1 \gamma H_1 \hat{x}. \quad (\text{A.15})$$

Define two new unitless quantities

$$\omega_0 = \gamma B_0, \quad (\text{A.16})$$

$$\omega_1 = \gamma B_1. \quad (\text{A.17})$$

Further, define

$$\Delta\Omega = T_1(\omega_0 - \omega). \quad (\text{A.18})$$

and,

$$\Omega_1 = T_1 \omega_1. \quad (\text{A.19})$$

Finally we have, for equation A.15

$$\boldsymbol{\Omega} = \Delta\Omega \hat{z} + \Omega_1 \hat{x}. \quad (\text{A.20})$$

The value of  $\Delta\Omega$  is typically varied during the experiment. In our case by varying the static field, which is equivalent to varying the frequency of the applied field. Also, since the static field has been taken to be in the  $\hat{z}$  direction we know that the equilibrium magnetic moment,  $\boldsymbol{\mu}_0$ , also points in the  $\hat{z}$  direction. Using this notation we may write down the following

$$\boldsymbol{\mu} = \frac{(\mu_0 \hat{z} + \mu_0 \Delta\Omega (\Delta\Omega \hat{z} + \Omega_1 \hat{x}) + \mu_0 \Omega_1 \hat{y})}{1 + \Delta\Omega^2 + \Omega_1^2}. \quad (\text{A.21})$$

Note: I used the fact that

$$\boldsymbol{\mu}_0 \times \boldsymbol{\Omega} = \mu_0 \Omega_1 \hat{y}. \quad (\text{A.22})$$

From the expression in equation A.21 we can pick out the components of the vector describing the magnetic moment as follows.

$$\mu_x = \mu_0 \left( \frac{\Delta\Omega \Omega_1}{1 + \Delta\Omega^2 + \Omega_1^2} \right), \quad (\text{A.23a})$$

$$\mu_y = \mu_0 \left( \frac{\Omega_1}{1 + \Delta\Omega^2 + \Omega_1^2} \right), \quad (\text{A.23b})$$

$$\mu_z = \mu_0 \left( \frac{1 + \Delta\Omega^2}{1 + \Delta\Omega^2 + \Omega_1^2} \right). \quad (\text{A.23c})$$

Thus, we have completed the solution the an equivalent to the familiar Bloch equations using only vector identities. The above solutions are valid only for the regime where  $T_1 = T_2$ .

## APPENDIX B LANGEVIN RELAXATION OF A CLASSICAL OSCILLATOR

### B.1 Introduction

What is presented here is a re-working of Chapter 8 in David Chandler's [Introduction to Modern Statistical Mechanics](#). Some mathematical manipulations, left to the reader by Chandler, have been completed. We have put the essential concepts in our own words and made them relevant to the work in this laboratory. We begin with an intuitive explanation of Onsager's regression hypothesis and how this seemingly simple idea leads to the fluctuation-dissipation theorem. The fluctuation-dissipation theorem leads us to discuss response functions in general and finally the generalized Langevin equation. We then apply the generalized Langevin equation to the simplest interesting case: the harmonic oscillator.

### B.2 Onsager's regression

Lars Onsager's regression hypothesis as stated in 1930 reads: "The relaxation of macroscopic non-equilibrium disturbances are governed by the same laws as the regression of spontaneous microscopic fluctuations in an equilibrium system." Simply said - if we prepare a system in a non-equilibrium state and let it relax back to thermodynamic equilibrium that relaxation is identical to the relaxation a system experiences after a *spontaneous fluctuation* from equilibrium. Figure B.1 gives a schematic illustration of Onsager's hypothesis. This concept, which clearly capitalizes on Einstein's 1905 insight into Brownian motion, earned Onsager the Nobel Prize in Chemistry in 1968.

To talk about this relationship in mathematical terms we need to define some quantities.  $\langle A \rangle$  is the ensemble average of the quantity of interest. This quantity is *time-independent*, this would be the value predicted by thermodynamics for the observable  $A$ . In the cantilever example this would be the position of the cantilever averaged over a long period of time. On some time scale, to be discussed in more detail later, there are fluctuations in the quantity  $A$ . So, if we look on a short enough time scale  $A = A(t)$ . To discuss time dependence we define:

$$\delta A(t) = A(t) - \langle A \rangle. \quad (\text{B.1})$$

In general,

$$\delta A(t) = \delta A[t; r^N, p^N] = \delta A[r^N(t), p^N(t)]. \quad (\text{B.2})$$

for a general system with  $N$  particles described fully by the generalized coordinates  $r$  and  $p$ . We note that at equilibrium

$$\langle \delta A(t) \rangle = \langle A(t) - \langle A \rangle \rangle = 0. \quad (\text{B.3})$$

#### B.2.1 Correlation functions

A common method for discussing the properties of fluctuating quantities with zero mean is the correlation function, defined as,

$$C(t) = \langle \delta A(0) \delta A(t) \rangle = \langle A(0) A(t) \rangle - \langle A \rangle^2 \quad (\text{B.4})$$

where we have obtained the second equality by substituting in equation B.1 and exploiting equation B.3. The function in equation B.4 is a specific example of a time-autocorrelation function. This tells us about the time over which the system has a memory of its previous state. Systems that fluctuate rapidly have short correlation times or a short memory of their previous state. Systems which fluctuate slowly have long correlation times and retain a memory of their previous state for a longer period (figure B.2). An understanding of correlation functions like equation B.4 is essential to all relaxation phenomena, both quantum and classical. We now discuss some common properties of correlation functions which we will exploit in what follows.

Fluctuations around equilibrium are a stationary process. A stationary processes arises from fluctuations whose probability distribution is time-independent. That is, the probability that any given fluctuation will happen is constant at all times. This means that relative time is the only relevant quantity for a correlation function of a stationary process,

$$C(t) = \langle \delta A(t') \delta A(t'') \rangle. \quad (\text{B.5})$$

Where  $t = t' - t''$ . Essentially, the exact value of  $t'$  and  $t''$  don't matter, only the absolute difference between them. Using this fact we can show that the correlation function above (equation B.4) is symmetric in time

$$C(t) = \langle \delta A(0) \delta A(t) \rangle = \langle \delta A(-t) \delta A(0) \rangle. \quad (\text{B.6})$$

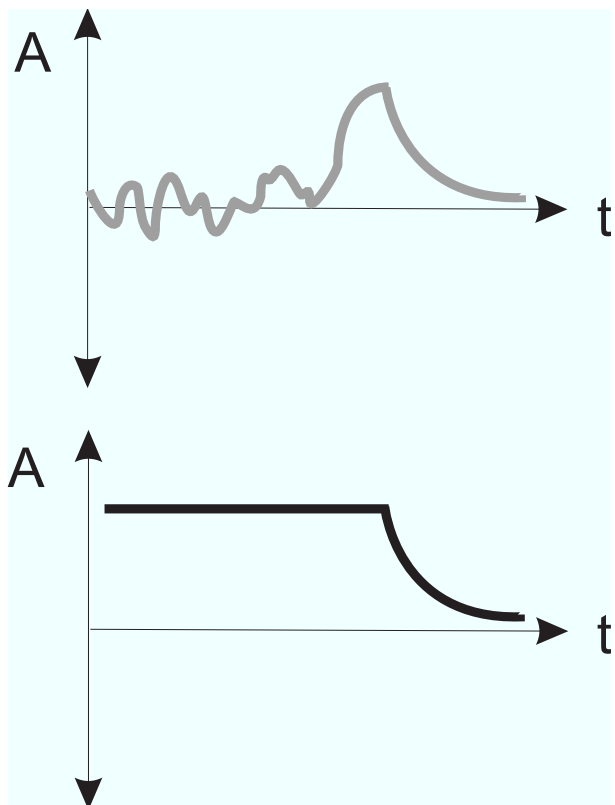


**Figure B.1:** The time evolution of a system's observable 'A'; this could be the cantilever position but not a constant of the motion, which does not evolve in time, like the total energy of a closed system. Top: the system evolves randomly for some time and then experiences a large fluctuation far from equilibrium, it then decays back to equilibrium. Bottom: a system is prepared and held in a non-equilibrium state, it is then released and allowed to relax. The relaxation of both the fluctuation (top) and the prepared system are governed by the same time constant, which is the correlation time of the random fluctuations in the top trace.

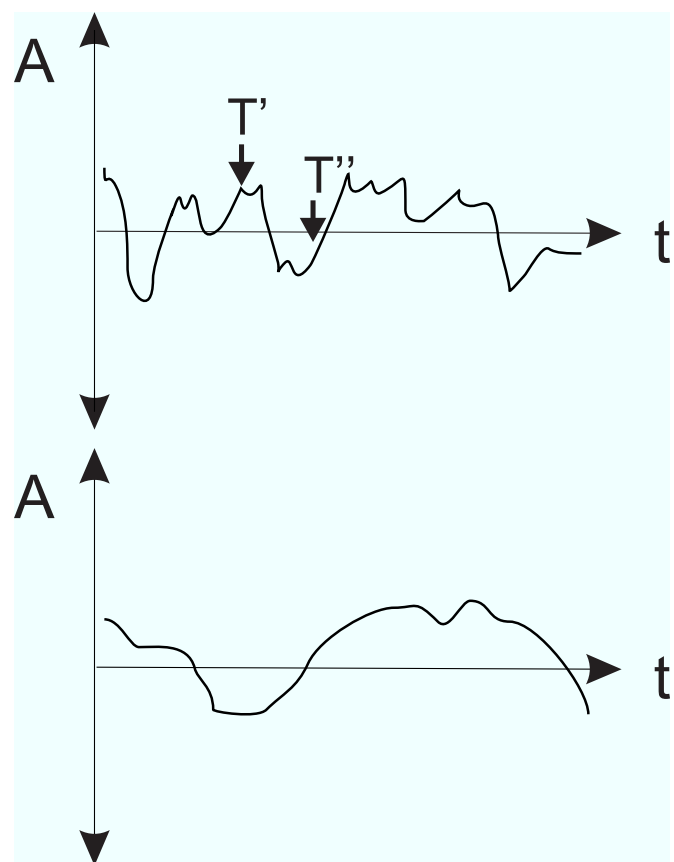


**Figure B.2:** Two examples of fluctuating quantities. The top trace (black) fluctuates quickly and has a short correlation time. The bottom trace (red) fluctuates slowly and has a long correlation time.

Since the order of multiplication inside  $\langle \dots \rangle$  does not matter we can switch the terms. Note, this is NOT true in Quantum Mechanics! Therefore,

$$\langle \delta A(-t) \delta A(0) \rangle = \langle \delta A(0) \delta A(-t) \rangle = C(-t), \quad (\text{B.7})$$

$$C(t) = C(-t). \quad (\text{B.8})$$

Two other obvious properties of correlation functions are

$$C(0) = \langle \delta A(0)^2 \rangle = \sigma_A^2, \quad (\text{B.9})$$

and

$$\lim_{t \rightarrow \infty} C(t) = 0 \quad (\text{B.10})$$

where  $\sigma_A^2$  is the variance of  $A$ .

Correlation functions can be written, and evaluated, in a variety of ways. In order to elucidate another way in which a correlation function like equation B.4 may be evaluated consider the precise meaning of the  $\langle \dots \rangle$  brackets in equation B.4. Consider the top trace in figure B.2. Notice the interval labeled  $T'$  and  $T''$  in the upper trace. The  $\langle \dots \rangle$  brackets denote the average over the infinity of intervals like this one. The ergodic hypothesis states that an average over many short intervals is identical to one long average. In other words, one could observe many identical systems, each for a short period of time, or one such system for a long period of time. So long as the observation time is long enough in the second example the two observations will result in the same value of the observable. Therefore, we may write:

$$\langle A(0) A(t) \rangle = \lim_{\tau \rightarrow \infty} \int_0^\tau \delta A(\bar{t} + t') \delta A(\bar{t} + t'') d\bar{t}. \quad (\text{B.11})$$

Having understood correlation functions we are now armed with the necessary formalism to make a more precise statement of Onsager's regression hypothesis.

### B.2.2 Regression hypothesis formalized

We begin with a definition of *non-equilibrium* ensemble averages, which deserves some explanation. In statistical mechanics we do not know the complete state of the system, that is the position and momentum of each particle. However, Newton's laws or the Schrodinger equation tells us how these evolve in time. In general

$$A(t) = A[r^N(t), p^N(t)]. \quad (\text{B.12})$$

First, we specify some initial conditions. Specify some initial conditions for the system:  $[r^N(0), p^N(0)] = (r^N, p^N)$ . Then we denote the integration of these initial conditions forward in time by

$$A(t) = A(t; r^N, p^N). \quad (\text{B.13})$$

As stated above, we cannot observe  $A(t)$  directly, but instead we measure an average (ensemble average) of all experimental possibilities. We denote a distribution of initial conditions as  $F(r^N, p^N)$ . We then evolve this distribution of initial conditions forward in time to find the state of the system at time  $t > 0$ . After evolving the distribution to some time  $t$  we then can calculate the state of the system at that time as follows

$$\delta \bar{A}(t) = \int dr^N dp^N F(r^N, p^N) \delta A(t; r^N, p^N). \quad (\text{B.14})$$

This is the formal definition of a non-equilibrium ensemble average, which we utilize below. For simplicity you can think of it as the time evolution of the systems' expectation value, which is really what we're plotting in figure B.1.

The regression hypothesis says that the decay to equilibrium is the same for a system prepared in a non-equilibrium state and a system which randomly fluctuates from equilibrium. In the language of correlations this means that the *correlations* in a fluctuating equilibrium system exhibit the same behavior in time as *relaxation* from a non-equilibrium state. Here we state the regression hypothesis without proof

$$\frac{\delta \bar{A}(t)}{\delta \bar{A}(0)} = \frac{C(t)}{C(0)}. \quad (\text{B.15})$$

What follows is a careful derivation of the fluctuation-dissipation theorem which formalizes this statement of the regression hypothesis and supplies an intuitive interpretation.

### B.3 Fluctuation-dissipation theorem

Here we assume some knowledge of classical statistical mechanics. The ensemble average of  $A$  is given by,

$$\langle A \rangle = \frac{\int dr^N dp^N e^{-\beta H} A(r^N, p^N)}{\int dr^N dp^N e^{-\beta H}}. \quad (\text{B.16})$$

Where  $\beta = 1/k_B T$  and  $H$  is the Hamiltonian governing the system. This is the classical analog to summing over states in the partition function. Integrals take the place of sums due to the continuous classical variables. The denominator serves only to normalize the probability distribution. In the spirit of quantum mechanics we write this in a more compact form to facilitate manipulation

$$\langle A \rangle = \frac{\text{Tr} e^{-\beta H} A}{\text{Tr} e^{-\beta H}}. \quad (\text{B.17})$$

where the trace denotes the integration is equation B.16. We are using the trace merely for ease of algebraic manipulations in what follows; in general it should be treated as an integral. Now, we prepare the system away from equilibrium. What we're interested in is how  $\bar{A}(t)$  decays to  $\langle A \rangle$ . In general this is very hard to solve, but if we assume that we begin reasonably close to equilibrium then the analysis is accomplished by perturbation theory. This assumption is the basic assumption of all of Linear Response Theory. In that sense the fluctuation-dissipation theorem is nothing more than first order perturbation theory applied with the formalism of statistical mechanics. Imagine the system is prepared in a non-equilibrium state by the perturbing Hamiltonian  $\Delta H = -fA$ .  $f$  could be an applied electric field to many dipoles, or a small force to an oscillator. We then prepare the system under the influence of the total Hamiltonian  $H + \Delta H$ . At time  $t = 0$  we will turn off  $\Delta H$  and let the system relax. The initial probability distribution, which we evolve forward in time after  $t = 0$  is governed by :  $F(r^N, p^N) \propto e^{-\beta(H+\Delta H)}$ . In other words, we begin in the state

$$\bar{A}(0) = \frac{\text{Tr} e^{-\beta(H+\Delta H)} A}{\text{Tr} e^{-\beta(H+\Delta H)}}. \quad (\text{B.18})$$

Now, the evolution of  $A$  in time is just the evolution of this probability distribution in time under the unperturbed Hamiltonian  $H$ , which is written as

$$\bar{A}(t) = \frac{\text{Tr} e^{-\beta(H+\Delta H)} A(t; r^N, p^N)}{\text{Tr} e^{-\beta(H+\Delta H)}}, \quad (\text{B.19})$$

where it is very important to note that  $A(t; r^N, p^N)$  is the time evolution of  $A$  under only  $H$ , not  $H + \Delta H$ . The  $\Delta H$  remains in the exponentials because we are evolving a probability distribution  $F$  which was initiated by  $\Delta H$ . Since we observe that  $\Delta H$  is very small we can approximate the exponentials as the first two terms of their power series expansion

$$\bar{A}(t) = \frac{\text{Tr}[e^{-\beta H} A(t)(1 - \beta\Delta H)]}{\text{Tr}[e^{-\beta H}(1 - \beta\Delta H)]}, \quad (\text{B.20})$$

$$\bar{A}(t) = \frac{\text{Tr}[e^{-\beta H} A(t)(1 - \beta\Delta H)]}{\text{Tr}[e^{-\beta H}](1 - \frac{\text{Tr}[e^{-\beta H}\beta\Delta H]}{\text{Tr}[e^{-\beta H}]})}. \quad (\text{B.21})$$

Using the fact that  $1 + x \sim 1/(1 - x)$  for small  $x$  we can write this as,

$$\bar{A}(t) = \frac{\text{Tr}[e^{-\beta H} A(t)(1 - \beta\Delta H)](1 + \frac{\text{Tr}[e^{-\beta H}\beta\Delta H]}{\text{Tr}[e^{-\beta H}]})}{\text{Tr}[e^{-\beta H}]} \quad (\text{B.22})$$

Expand this, keeping only terms linear in  $\Delta H$

$$\bar{A}(t) = \frac{\text{Tr}[e^{-\beta H}(A(t) - A(t)\beta\Delta H + A(t)\frac{\text{Tr}[e^{-\beta H}\beta\Delta H]}{\text{Tr}[e^{-\beta H}]})]}{\text{Tr}[e^{-\beta H}]} \quad (\text{B.23})$$

Using equation B.17 and assuming that the processes we are discussing is stationary, where a stationary processes has an ensemble average which is time independent. Meaning that  $\langle A(t) \rangle = \langle A \rangle$ . We can write this as follows

$$\bar{A}(t) = \langle A \rangle - \beta[\langle \Delta H A(t) \rangle - \langle A \rangle \langle \Delta H \rangle]. \quad (\text{B.24})$$

Reordering things a little and plugging in  $\Delta H = -fA$  and taking care with the “-” signs we get,

$$\bar{A}(t) - \langle A \rangle = \beta f [\langle A(0)A(t) \rangle - \langle A \rangle^2]. \quad (\text{B.25})$$

Recalling the definition of  $\delta A = A - \langle A \rangle$  from above and defining  $\Delta \bar{A}(t) = \bar{A}(t) - \langle A \rangle$  we have

$$\boxed{\Delta \bar{A}(t) = \beta f \langle \delta A(0) \delta A(t) \rangle}. \quad (\text{B.26})$$

This result has profound physical implications. It is a statement of the regression hypothesis above, and is sometimes called the fluctuation-dissipation theorem. The left hand side is the time dependent behavior of a system after a linear perturbation has been applied. The right hand side is the correlation function for the *random* fluctuation in an *equilibrium* system. Therefore, the time dependent relaxation and the equilibrium correlations have the same physical origins! We haven't shown its relationship to dissipation, or friction, in a physical system as yet. Before moving forward we'll cover one other topic necessary for the Langevin treatment of the harmonic oscillator: response functions.

## B.4 Response functions

Another convenient way to present the fluctuation-dissipation theorem is through response functions. A familiar example of a response function might be the electric or magnetic susceptibility which dictates the response of a system to an applied perturbation, say an electric or magnetic field. Consider a time dependent, linear perturbation  $f$  coupling to a dynamical variable  $A(t)$ . Meaning,

$$\bar{A}(t, \lambda f) = \lambda \bar{A}(t, f). \quad (\text{B.27})$$

Take it as an axiom that the most general form of this type is given by,

$$\bar{A}(t) = \int_{-\infty}^{\infty} \chi(t, t') f(t') dt'. \quad (\text{B.28})$$

Think of  $\chi(t, t')$  as an intrinsic property of the system, like the polarizability say and  $f(t')$  as the perturbation which defines  $\bar{A}(t)$  as a functional. Essentially,  $f$  is a different variable at all times  $t'$  which defines  $\bar{A}(t)$ . Write  $\bar{A}(t)$  as a Taylor Series in  $f$

$$\Delta \bar{A}(t) = \sum_i \left( \frac{\partial \Delta \bar{A}(t)}{\partial f(t_i)} \right)_0 f(t_i). \quad (\text{B.29})$$

Notice that the first term is zero because if  $f = 0$  then  $\Delta \bar{A}(t) = 0$ . Consider a delta function perturbation which occurs at time  $t = t_0$ , so  $f(t) = f_0 \delta(t - t_0)$ . So the Taylor Series from equation B.29 becomes,

$$\Delta \bar{A}(t) \approx f_0 \chi(t, t_0). \quad (\text{B.30})$$

From some physical consideration we can place some constraints on the above relation. First,  $\chi$  depends only on the time relative to the applied perturbation, not absolute time. So  $\chi(t, t') = \chi(t - t')$ . Also, causality sets another obvious constraint, the response cannot happen before the perturbation so,  $\chi(t - t') = 0$  for  $t - t' \leq 0$ . We now use the same physical scenario that was discussed previously. The perturbation is turned on in the distant past, and turned off at  $t = 0$  where the system is allowed to relax. Therefore,

$$f(t) = \begin{cases} f & \text{if } t < 0, \\ 0 & \text{if } t > 0. \end{cases} \quad (\text{B.31})$$

We know from the previous section that the behavior of the system after the perturbation is turned off obeys,

$$\Delta \bar{A}(t) = \beta f \langle \delta A(0) \delta A(t) \rangle. \quad (\text{B.32})$$

Also, from the definition of the response function we know that after the perturbation is turned off,

$$\Delta \bar{A}(t) = f \int_{-\infty}^0 dt' \chi(t - t'). \quad (\text{B.33})$$

Because for  $t > 0$  the integral on the right hand side is zero by definition. Change the variables of integration to  $t - t'$  and the integral becomes.

$$\Delta \bar{A}(t) = f \int_t^\infty dt' \chi(t'). \quad (\text{B.34})$$

Combine this result with the fluctuation-dissipation theorem and we have

$$\boxed{\chi(t) = \begin{cases} -\beta \frac{d}{dt} \langle \delta A(0) \delta A(t) \rangle & \text{if } t > 0, \\ 0 & \text{if } t < 0. \end{cases}} \quad (\text{B.35})$$

This relates the response from a system to a linear applied perturbation to the correlation of the random fluctuations of that system in equilibrium. This formalism can be applied to a variety of physical systems including the coherent driving of a system and the resulting absorption of energy. We skip this treatment (see Chandler's book) and move on to the Langevin formulation.

For an example of a calculation exploiting the relationship between a linear perturbation and a system's equilibrium fluctuations see our discussion of dielectric fluctuations in chapter 7. In that calculation we situated a test electric dipole near a dielectric and related the reaction field from the dielectric on the dipole, due to the dipole, to the fluctuations in the dielectric. Therefore, the assumptions of linear response stated here apply directly to our previous calculation.

## B.5 Langevin formalism

The Langevin formalism essentially combines Newton's laws with statistical mechanics, resulting in a stochastic (random) differential equation. One of the most readily addressed problems with the Langevin formalism is friction of an object in contact with a bath. In general, objects experience a drag linearly proportional to the velocity with which they travel through a medium,  $f_{\text{drag}} = -\gamma v$ . Our goal of this section is to use Newton's laws and what we've learned about random processes to derive this relationship a priori.

Consider an oscillator in contact with a bath (figure B.3). We write the Hamiltonian for this system as follows,

$$H = H_0(x) - xf + H_b(y_1 \dots y_N). \quad (\text{B.36})$$

Where  $H_0 = m\dot{x}/2 + V(x)$  is the oscillator Hamiltonian. We assume only that this Hamiltonian is time-independent and that the oscillator itself conserves energy ( $F = -dV(x)/dx$ ).  $f$  is the force on the oscillator by the bath, and depends linearly on the bath coordinates ( $y_i$ 's) as  $f = \sum_i c_i y_i$ . It is important to note that this implies that the correlation function of the fluctuations in the  $y_i$ 's is linearly proportional to the force fluctuations the oscillator feels from the bath. So,

$$C_b(t) = \sum_{i,j} c_i c_j \langle \delta y_i(0) \delta y_j(t) \rangle = \langle \delta f(0) \delta f(t) \rangle_b. \quad (\text{B.37})$$

$H_b$  is the hamiltonian describing the bath. We need to make some specific statements about the bath. We assume that  $H_b$  is of the form of a collection of harmonic oscillators. This assumption is essential because it means that the response of the bath is exactly linear in the coordinate. Meaning that for a harmonic oscillator  $f = -kx$ . This must be true for the bath for the analysis that follows to be valid. This seems like quite a restriction, but it turns out that many physical systems adhere to this requirement, making this model a popular one for a wide variety of dissipative systems.

What we're calculating here is  $m\ddot{x}$  = force, where the right hand side is all of the forces acting on the oscillator, and  $x$  is the coordinate of the oscillator. There are two basic forces to consider. 1) the force of the spring which binds our particle to the wall ( $f_0(t)$ ), and 2) the force that the bath exerts on the particle ( $f_b(t)$ ). We know that the force the spring exerts is  $f_0 = -dV(x)/dx = -kx$ . The force that the bath exerts is slightly more complicated: it has two terms. One is due to the bath interacting with the particle, and second includes the "back action" of the particles motion on the bath itself

$$f(t) = f_b(t) + \int_{-\infty}^{\infty} dt' \chi_b(t - t') x(t'). \quad (\text{B.38})$$

The first term is described by the force the bath would exert on the particle if the particle had no effect on the bath. The second term compensates for the fact that when the particle responds to the bath it changes the bath (the  $y_i$ 's). The first term is said to be local in time, the second term is said to be non-local in time. The non-locality of the second term is a result of the persistence (in time) of the effect of the particles motion on the bath. If the particle moves and

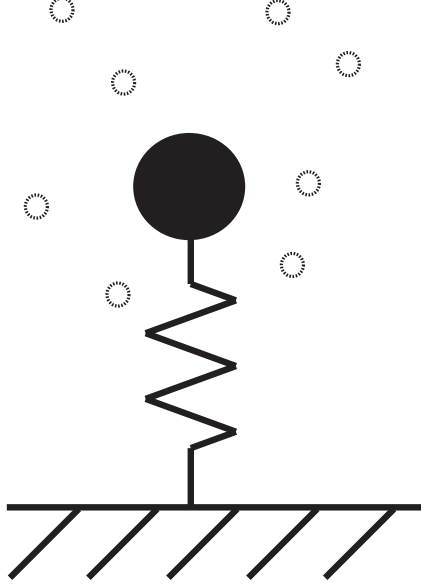


**Figure B.3:** A schematic of a harmonic oscillator in contact with a bath. The small dashed circles indicate the bath degrees of freedom, these might be gas molecules. The large black mass, bound to the wall by a spring, could be a cantilever or any system bound by a harmonic potential.

interacts with the bath then the baths' response to this interaction will persist for some time - this time is the correlation time of the bath. This gives us our first glimpse of how correlations in the bath can be important to the dynamics of a dissipative system. In what follows we will illustrate this relationship explicitly. The total force on the particle is,

$$m\ddot{x} = -\frac{dV(x)}{dx} + f_b(t) + \int_{-\infty}^{\infty} dt' \chi_b(t-t')x(t'). \quad (\text{B.39})$$

What follows is a slightly messy simplification of the above equation. The result, which you can skip ahead to if you'd rather not wade through this analysis, sheds significant light on the physical origins of each term and their effects on the dynamics of the oscillator. From equation B.35 we know that,

$$\chi_b(t-t') = \begin{cases} -\beta \frac{dC_b(t-t')}{d(t-t')} & t > t', \\ 0 & t < t'. \end{cases} \quad (\text{B.40})$$

Using this we can rewrite equation B.39 as follows,

$$m\ddot{x} = -\frac{dV(x)}{dx} + f_b(t) - \beta \int_t^0 dt' \dot{C}_b(t-t')x(t'). \quad (\text{B.41})$$

Where the limits of integration have changed in the conversion to the correlation function. This is a tricky change of variables. Use  $t'' = t - t'$  and keep careful track of the constraints on the response function to arrive at the equation above. A mistake here results in a sign error in the following step. Evaluate the integral in the last term by parts, and group some of the terms in strategic ways as follows,

$$m\ddot{x} = -\frac{dV(x)}{dx} + f_b(t) + \beta \left[ C_b(0)x(t) - C_b(t)x(0) - \int_0^t dt' C_b(t-t')\dot{x}(t') \right], \quad (\text{B.42})$$

$$m\ddot{x} = -\frac{d}{dx} \left[ V(x) - \beta C_b(0) \frac{x(t)^2}{2} \right] + f_b(t) - \beta C_b(t)x(0) - \beta \int_0^t dt' C_b(t-t')\dot{x}(t'). \quad (\text{B.43})$$

We can simplify this equation by compacting our notation a bit,

$$\boxed{m\ddot{x} = -\frac{d\bar{V}(x)}{dx} + \delta f(t) - \beta \int_0^t dt' C_b(t-t') \dot{x}(t')} \quad (\text{B.44})$$

Where

$$\bar{V}(x) = \left( V(x) - \beta C_b(0) \frac{x(t)^2}{2} \right) \quad \text{and} \quad (\text{B.45})$$

$$\delta f(t) = f_b(t) - \beta C_b(t)x(0). \quad (\text{B.46})$$

Equation B.44 is called the *Generalized Langevin Equation*, it was first derived by Robert Zwanzig. Each term has an intuitive physical interpretation.  $\bar{V}(x)$  is the intrinsic oscillator potential modulated by the zero frequency correlations of the bath. This term corresponds to the frequency jitter that we observe when measuring a cantilever frequency in a finite bandwidth. The second term,  $\delta f(t)$  corresponds to time dependent force exerted on the oscillator by the bath. If we measure this for a time longer than the correlation time of the bath it will have zero mean and be a random force with a Gaussian probability distribution (because of the assumed harmonic nature of the bath). The third term  $\int_0^t C_b(t-t') \dot{x}(t) dt'$  is exactly what we set out to discover, a velocity dependent force!

This approach is extremely general, we have not included anything specific about the oscillators potential at this point. We have only relied on the linear response of the *bath*. We now apply this equation to the harmonic oscillator.

## B.6 Harmonic oscillator

Here we set  $V(x) = \frac{m\omega_0 x^2}{2}$  in equation B.44 and integrate this equation of motion. What follows is given as the final exercise of Chandler's book; we have filled in the gaps and learned some new techniques along the way. The result will allow us to demonstrate how the relaxation of the harmonic oscillator depends on the properties of the bath

$$\ddot{x} = -\frac{d}{dx} \left[ \frac{\omega_0 x^2}{2} - \beta C_b(0) \frac{x(t)^2}{2m} \right] + \frac{\delta f_b(t)}{m} - \frac{\beta}{m} \int_0^t dt' C_b(t-t') x(t'). \quad (\text{B.47})$$

In order to move forward we need to integrate over the probability distribution for  $x$ , specifically, we need to take the non-equilibrium ensemble average of  $x$ . This step will allow us to invoke the fluctuation-dissipation theorem as we derived above and it allows us to throw out the  $\delta f$  term which will average to zero as per the argument stated previously. Therefore,

$$\frac{d^2 \bar{x}}{dt^2} = -\left(\omega_0^2 - \frac{\beta}{m} C_b(0)\right) \bar{x} - \frac{\beta}{m} \int_0^t dt' C_b(t-t') \frac{d\bar{x}(t')}{dt'}. \quad (\text{B.48})$$

We make two substitutions in order to simplify things. First, as mentioned above, the first term on the right hand side is the fundamental frequency of the oscillator shifted by the low frequency ( $C_b(0)$ ) fluctuations of the bath. Rewrite this as,

$$\bar{\omega}^2 = \omega_0^2 - \frac{\beta}{m} C_b(0). \quad (\text{B.49})$$

Also, recall that the fluctuation-dissipation theorem allows us to equate  $\bar{x}(t) = \langle x(0)x(t) \rangle$ . Finally, we have,

$$\boxed{\frac{d^2 \langle x(0)x(t) \rangle}{dt^2} = -\bar{\omega} \langle x(0)x(t) \rangle - \frac{\beta}{m} \int_0^t dt' C_b(t-t') \frac{d\langle x(0)x(t) \rangle}{dt'}} \quad (\text{B.50})$$

Linear differential-integral equations like equation B.50 are readily solved by the method of Laplace transforms. This requires that we recall some of the properties of Laplace transforms. Armed with this knowledge we break the equation into two parts and present a final solution, in the form of a Laplace transformed correlation function.

### B.6.1 Laplace transforms

A Laplace transform is an integral transform like the Fourier transform. The Laplace transform of a function  $y(t)$  is given by,

$$y(0) = L\{y(t)\} = \int_0^\infty y(t)e^{-st} dt. \quad (\text{B.51})$$

If we integrate this equation by parts, it is easy to show that,

$$L\{\dot{y}(t)\} = sL\{y(t)\} - y(0), \quad (\text{B.52})$$

$$L\{\ddot{y}(t)\} = sL\{\dot{y}(t)\} - \dot{y}(0). \quad (\text{B.53})$$

Also, the Laplace transform of a correlation function looks like

$$L\left\{\int_0^t f_1(\tau)f_2(t-\tau)d\tau\right\} = F_1(s)F_2(s). \quad (\text{B.54})$$

Where  $F_1(s)$  and  $F_2(s)$  are the Laplace transforms of  $f_1$  and  $f_2$ . Also, the Laplace transform with a complex argument, that is  $s = i\omega$ , becomes a Fourier-Laplace Transform,

$$y(i\omega) = \int_0^\infty y(t)e^{-i\omega t}dt. \quad (\text{B.55})$$

We will exploit all of these properties extensively in what follows.

### B.6.2 Solution to equation of motion

Take the Laplace transform of equation B.50. Write  $\tilde{C}(s) = L\{\langle x(0)x(t) \rangle\}$ , and begin by considering the left hand side (LHS) of equation B.50. Invoke equation B.53 which yields,

$$L\left\{\frac{d^2\langle x(0)x(t) \rangle}{dt^2}\right\} = sL\left\{\frac{d\langle x(0)x(t) \rangle}{dx}\right\} - \frac{d}{dt}\langle x^2 \rangle. \quad (\text{B.56})$$

Noting that the second term vanishes by the stationary assumption made previously, that is that the expectation value of  $x$  is time independent, and applying equation B.52, we get,

$$= s[sL\{\langle x(0)x(t) \rangle\} - \langle x^2 \rangle]. \quad (\text{B.57})$$

Finally,

$$\text{LHS} = s^2\tilde{C}(s) - s\langle x^2 \rangle. \quad (\text{B.58})$$

Now, take the Laplace transform of the right hand side of equation B.50

$$\text{RHS} = -\bar{\omega}\tilde{C}(s) - \frac{\beta}{m} \int_0^t dt' C_b(t-t') \frac{d\langle x(0)x(t) \rangle}{dt'}. \quad (\text{B.59})$$

On the second term we apply equation B.54 to the integral followed by equation B.52 to the resulting Laplace transform of the time derivative of  $\langle x(0)x(t) \rangle$ . Denoting the Laplace transform of the bath correlation function as  $C_b(s)$  we get,

$$\text{RHS} = -\bar{\omega}\tilde{C}(s) - \frac{\beta}{m}C_b(s)s\tilde{C}(s) + \frac{\beta}{m}C_b(s)\langle x^2 \rangle. \quad (\text{B.60})$$

Equating LHS = RHS and grouping like terms we have

$$\boxed{\tilde{C}(s) = \frac{s + \frac{\beta}{m}C_b(s)}{s^2 + \bar{\omega}^2 + s\frac{\beta}{m}C_b(s)}\langle x^2 \rangle}. \quad (\text{B.61})$$

This is a powerful result. What it says is that given the correlation function of the bath we can compute the correlation function of the oscillator which is in contact with that bath. We can make this even more intuitive by utilizing equation B.55 above. The correlation function and the power spectral density are Fourier transform pairs. Meaning that the FT of the autocorrelation function of  $x$  yields the power spectral density of position fluctuations. This is exactly the thermal noise that we measure in the lab when observing a cantilever interferometrically! Remembering that  $C_b$  is the correlations of the force fluctuations by the bath on the system (equation B.37) and setting  $s = i\omega$  we get,

$$\boxed{S_x(\omega) = \frac{i\omega + \frac{\beta}{m}S_f^b(\omega)}{\bar{\omega}^2 - \omega^2 + i\omega\frac{\beta}{m}S_f^b(\omega)}\langle x^2 \rangle}. \quad (\text{B.62})$$

This result says that given the spectral density of the bath's fluctuations we can calculate the spectral density of the resulting position fluctuations in our cantilever. To move forward we need to specify something about the spectral density, or equivalently, the correlation function, of the bath's fluctuations. We consider two common cases here, a white noise spectrum and a Lorentzian noise spectrum.

### B.6.3 White noise

A white noise spectrum has the same spectral density at all frequencies up to some very high frequency. We assume that this high frequency cut-off is so high that it has no impact on the dynamics of our system. We can then consider equation B.62 where the  $S_f^b(\omega) = S_f^b = \text{constant}$  and solve the resulting equation. Simplify the resulting equation by multiplying the numerator and denominator by the complex conjugate of the denominator. The absorption spectrum of the oscillator is equal to the real component of this Fourier transform (See Chandler's section 8.7 for a proof of this). The result is the familiar Lorentzian lineshape for harmonic oscillator

$$S_x(\omega) = \text{Re}\{C(i\omega)\} = \frac{(\bar{\omega}^2 + \omega^2) \frac{\beta S_f^b}{m}}{(\bar{\omega}^2 - \omega^2)^2 + \omega^2 \left(\frac{\beta S_f^b}{m}\right)^2} \langle x^2 \rangle. \quad (\text{B.63})$$

The units here work without considering the bandwidth of the spectral density. Our goal here is to better understand the relationship between the bath fluctuations at the relaxation of the oscillator.

### B.6.4 Exponential Bath Correlations

A more physically realistic model of the bath correlation function is an exponential correlation. An exponential correlation function yields a lorentzian spectral density with zero mean. This is commonly observed in many noise processes. Therefore, we write,

$$C_b(t) = C_0^b e^{-\frac{t}{\tau}}. \quad (\text{B.64})$$

The Laplace transform is,

$$C_b(s) = \frac{C_0^b}{s + \tau^{-1}}. \quad (\text{B.65})$$

Plug this into equation B.61, and substitute  $s = i\omega$  as before

$$\tilde{C}(i\omega) = \frac{i\omega + \frac{\beta}{m} \frac{C_0^b}{i\omega + \tau^{-1}}}{\bar{\omega}^2 - \omega^2 + i\omega \frac{\beta}{m} \frac{C_0^b}{i\omega + \tau^{-1}}} \langle x^2 \rangle. \quad (\text{B.66})$$

Again, the real part of this equation is the absorption spectrum of the oscillator. We need to separate this into its real and imaginary components. To do this, multiply the numerator and the denominator by the complex conjugate of the denominator. The result is,

$$\tilde{C}(i\omega) = \frac{i\omega \left(1 - \frac{\beta C_0^b}{m(\omega^2 + \tau^{-2})}\right) + \frac{\beta}{m} \frac{C_0^b}{\tau(\omega^2 + \tau^{-2})}}{(\bar{\omega}^2 - \omega^2)^2 + \omega^2 \frac{\beta C_0^b}{m}}. \quad (\text{B.67})$$

As before, the real component of this is the absorption spectrum of the oscillator

$$\text{Re}\{\tilde{C}(i\omega)\} = \frac{\frac{\beta}{m} \frac{C_0^b}{\tau(\omega^2 + \tau^{-2})}}{(\bar{\omega}^2 - \omega^2)^2 + \omega^2 \frac{\beta C_0^b}{m}}.$$

(B.68)

This result is a useful one, it allows us to compute the shape of the absorption spectrum given the details of the correlation function (equivalently spectral density) of the bath. This is the result we set out to compute. Plotting this function shows allows an intuitive interpretation, the larger the bath fluctuation at the resonance of the oscillator the greater the relaxation of the oscillator (the wider the absorption line). Figure B.4 shows some plots of equation B.68. Notice that a larger fluctuation in the bath gives a wider line and therefore higher friction experienced by the oscillator.

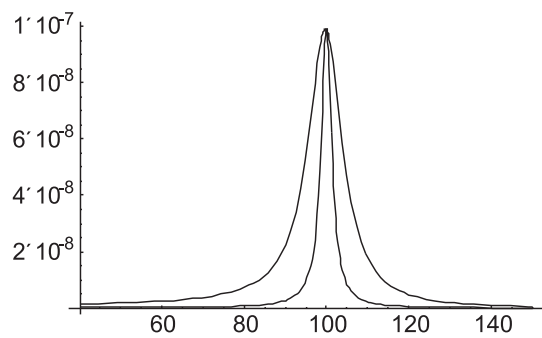


**Figure B.4:** Two plots of equation B.68. For the wider line the quantity  $\frac{\beta C_0^b}{m}$  is 10 times larger than the narrow line. Both are plotted with the same bath correlation time which is  $1/\tau = 10 \times \bar{\omega}$ .

## APPENDIX C SECOND GENERATION MRFM PROBE

### C.1 Filling liquid helium

The probe design outlined here works in conjunction with our American Magnetics 9T swept field magnet. The magnet dewar was filled with helium prior to each experiment. Here we outline some properties of the magnet and the cryogen filling process.

#### C.1.1 Swept field magnet

The American Magnetics swept field magnet was run using an American Magnetics model 4Q05100PS four-quadrant power supply controlled by an American Magnetics model 420 programmer. The four-quadrant supply allows for more rapid field ramp downs. The properties of the magnet and controller are listed below. The dewar is super-insulated and does not contain the typical liquid nitrogen jacket. It is important to keep the vacuum jacket of the magnet dewar evacuated. The dewar will appear “soft” when condensation appears around the center of the cooled dewar. Pump on the jacket overnight using a turbo pump. Pump on the dewar only when it is warm. The capacity of the magnet dewar is 90L.

- Magnet model #9040 – 3
- Max/Min output voltage =  $\pm 2V$
- Max/Min output current =  $\pm 81.6A$
- Coil constant =  $1.103kG/A$
- Installed persistent heater switch current = 70 mA
- Quench detection enabled
- GPIB address 22
- Typical ramp rate =  $0.04kG/A$
- Do not run the magnet with less than 19 inches of liquid helium in the dewar

#### C.1.2 Cryogen filling protocol

The cryogen filling process taken the dewar from room temperature to 4K. Typically, prior to an MRFM experiment the probe is placed in the dewar and all subsystems tested prior to beginning the fill. Pump on the probe during the fill. It is also generally a good idea to test all subsystems when the probe is cooled to 77K. With the probe secured to the dewar follow the filling process as outlined below. During the fill do not float the vibration isolation platform.

##### Nitrogen fill

- Place the vent line in the vent port of the dewar top plate so that it vents down toward the floor
- Purge the dewar with room temperature high purity nitrogen gas for  $\sim 10$  minutes
- Using the 180L liquid nitrogen dewar begin filling the magnet dewar with liquid nitrogen using red flexible hose connection with hose clamps and the uninsulated nitrogen filling line. If the pressure on the nitrogen dewar drops too low pressurize it using  $\sim 5$ psi from the nitrogen cylinder. Fill the dewar completely( $\sim 1.5$  hours)
- Check all of the microscope subsystems - thermometers, Attocube motion, cantilever self oscillation, cantilever fiber, Attocube fiber, radio frequency electronics

## Helium fill

Filling with helium requires a 100L dewar of liquid helium. Typically a the magnet dewar will contain 25 – 30 inches of liquid helium after a fill with a 100L dewar if the cooling of the line is done efficiently. This is sufficient helium to remain cold for 2-3 days depending on how much the magnet is run during that time.

- With liquid nitrogen still in the dewar pass some cold nitrogen gas through the vapor cooled magnet leads to purge the small amount of air present. This can also be done during the initial nitrogen fill
- Thump the helium transfer dewar and mark the helium level on the helium transfer line
- Close the safety valve on the transfer dewar
- Purge the liquid nitrogen into unpressurized dewars by pressurizing the magnet dewar through the vent line using room temperature nitrogen gas. The nitrogen will emerge from the fill line. Be absolutely certain that the fill line is going to the bottom of the magnet dewar. Removing all of the liquid nitrogen is crucial as it will form ice during the helium fill. Finish the purge with room temperature helium gas to be sure that the magnet dewar is pressurized slightly with helium gas. Vent the vapor cooled leads.(1.5 hours)
- Place the helium transfer line in the magnet dewar and the transfer dewar. Do not lower the transfer line into the liquid in the transfer dewar. Monitor the output of the vent line on the magnet dewar keeping a moderate flow. The flow can be increased by lowering the transfer line into the liquid in the transfer dewar. When the transfer line reaches the bottom of the transfer dewar - begin pressurizing that dewar with 1 – 2psi of helium gas
- Observe the probe thermometers. Connect a multimeter to the magnet leads and observe the resistance of the magnet. Observe the level sensor readings on both the transfer and magnet dewars. The resistance of the magnet will drop to near zero when liquid is beginning to collect in the magnet dewar. Turn the pressure on the transfer dewar up to 10 psi. The flow on the vent line in the magnet dewar should not increase, but should remain quiet. The helium transfer will be complete in a few minutes
- Remove the fill line
- Open the safety valve on the transfer dewar
- Close both the fill and vent to the magnet dewar
- Purge the vapor cooled leads on the magnet
- Connect the magnet leads
- Connect the magnet controller to the magnet and run the persistent switch prior to running the magnet

## Helium refill

In some cases the magnet dewar will be refilled after too much helium has burned off to continue to run the magnet. When this is the case a different filling protocol is required because the magnet dewar is already cooled to 4K. In this case it is necessary to cool the transfer line entirely *before* placing it in the magnet dewar. Helium refills are often done with 60L helium dewars as follows.

- Close the safety valve on the transfer dewar
- Thump the dewar and mark the helium liquid level on the transfer line
- Lower the evacuated end of the transfer line (as with a regular fill) into the transfer dewar but not into the liquid. Hang the other end of the line, which will later be inserted into the magnet dewar from a hook in the ceiling so that the line is not under significant stress
- Again, maintain a constant but low pressure flowing through the transfer line by lowering into the liquid in the transfer dewar and pressurizing the transfer dewar with room temperature helium gas

- The line is sufficiently cooled when the plume emerging from the free end of the transfer line begins to look more like a flame than a plume of smoke, this point is subjective and someone with expertise should be consulted
- When the line is cool rapidly place the transfer line into the magnet dewar and pressurize the transfer dewar to initiate the transfer of liquid. Watch the liquid helium level sensors to know when the transfer dewar is empty
- Open the transfer dewar safety valve when transfer is complete

## C.2 Probe design

This appendix contains details of the second generation MRFM probe design and construction as discussed in section 3.4. All dimensions are in inches; all machine screws are English as written. Note that it is critical to use vented screws (UC Components) in blind holes to avoid virtual vacuum leaks which have been observed to diminish cantilever  $Q$ 's dramatically.

The probe can be changed between two geometries corresponding to the two microscope stages shown here. In the first geometry the applied field is along the cantilever length and the tip magnet will interact with the applied field resulting in a field dependent contribution to the spring constant. The second stage stage is used in experiments where the tip magnetization must lie along the cantilever width as is the case for larger ( $> 1\mu\text{m}$ ) magnetic tips.

The probe superstructure (figure C.1) was designed and constructed at CryoIndustries with our specifications for the helium dewar and microscope mounting plate provided. Several problems arose with respect to this design. First, right angles were installed at the feedthroughs making installation of semi-rigid coaxial cable very challenging. Second, feedthroughs provided no extra space for connectors (such as the BNC to SMA adaptor needed on the rf) so custom expansion plates were constructed. In addition wire heat sinking proved difficult since the microscope mounting plate could not be removed making the job of wrapping wires around the copper post challenging.

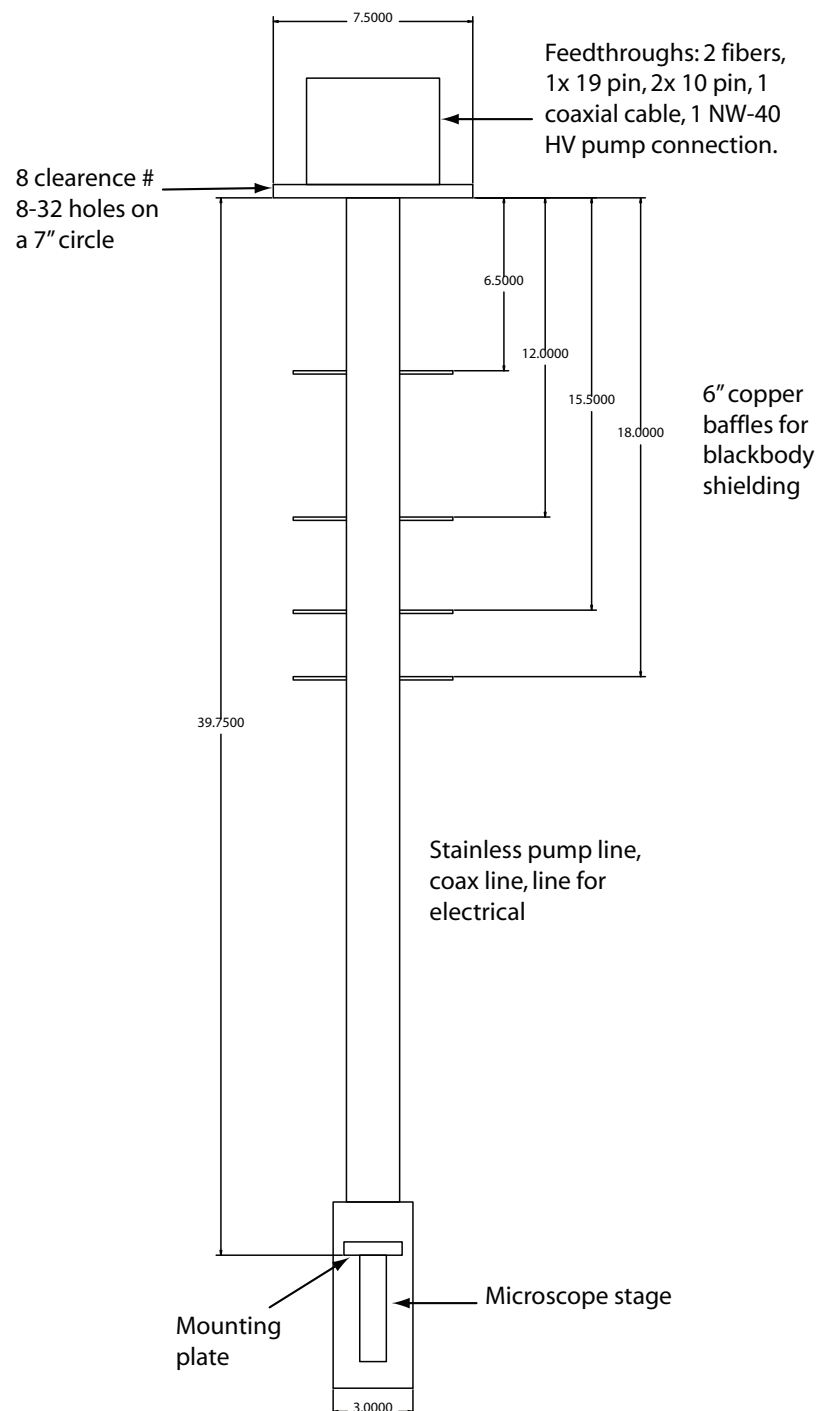


**Figure C.1:** Super structure of second generation probe designed and constructed by George Svenconis at CryoIndustries.

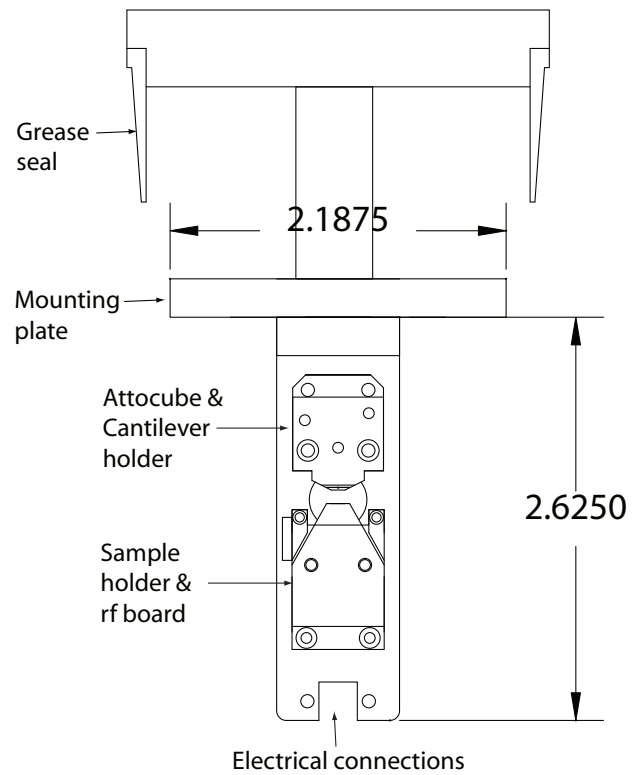


**Figure C.2:** A 2D projection of the MRFM probe. This view corresponds to the picture shown in figure 3.14 (b).

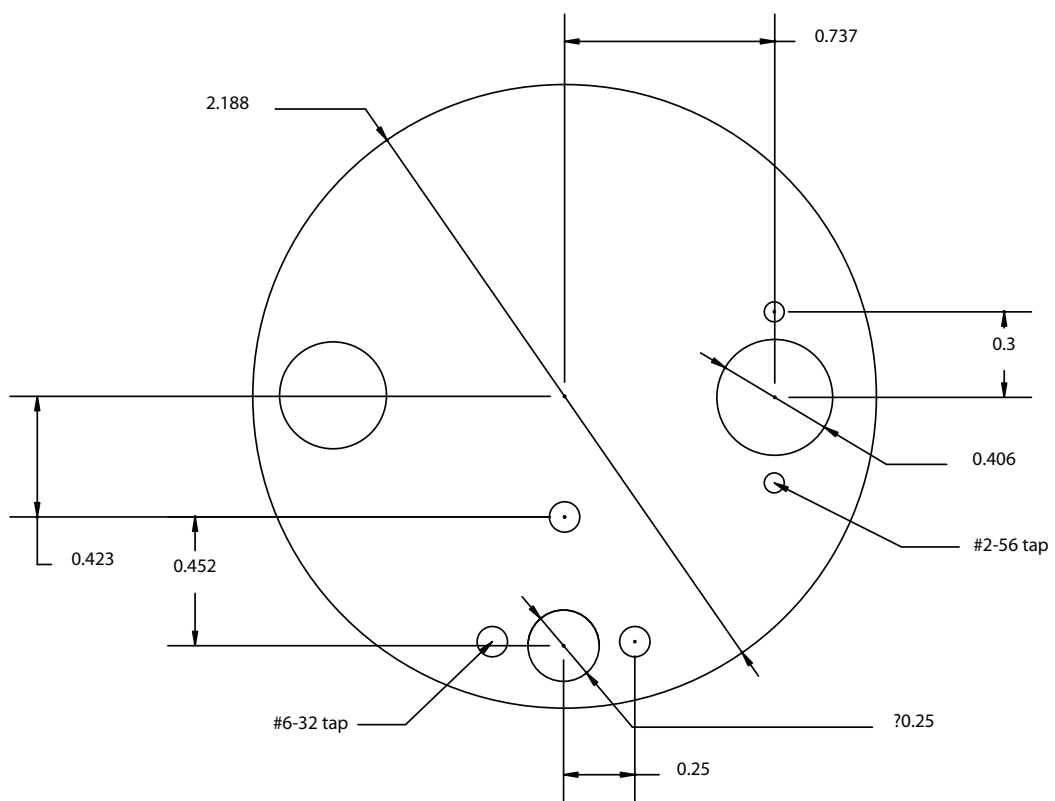


**Figure C.3:** Detailed CAD of the mounting plate.

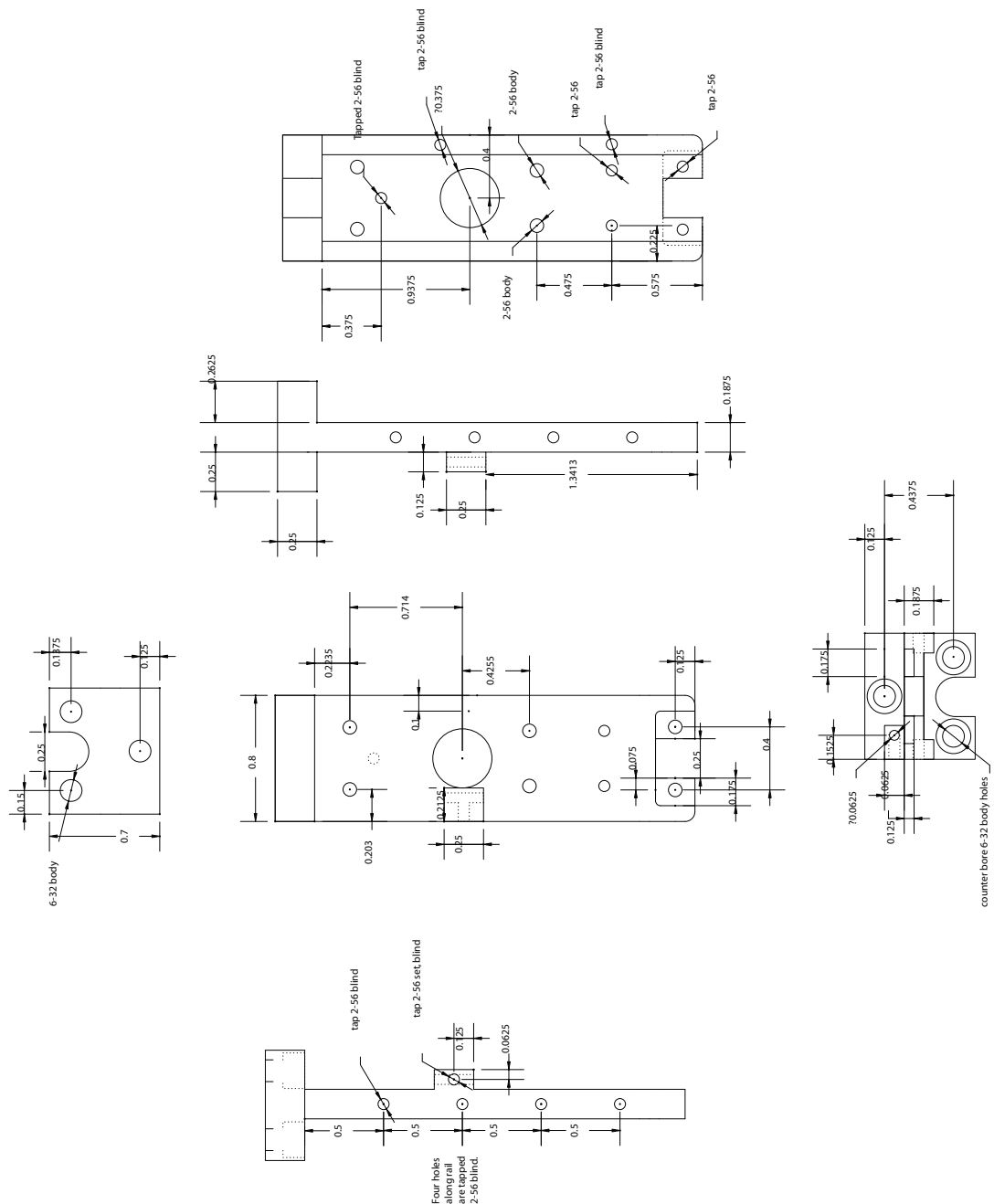


**Figure C.4:** Detailed CAD of the microscope stage. When using this stage the applied field  $H_0$  is along the cantilever length, appropriate for small tip magnets.

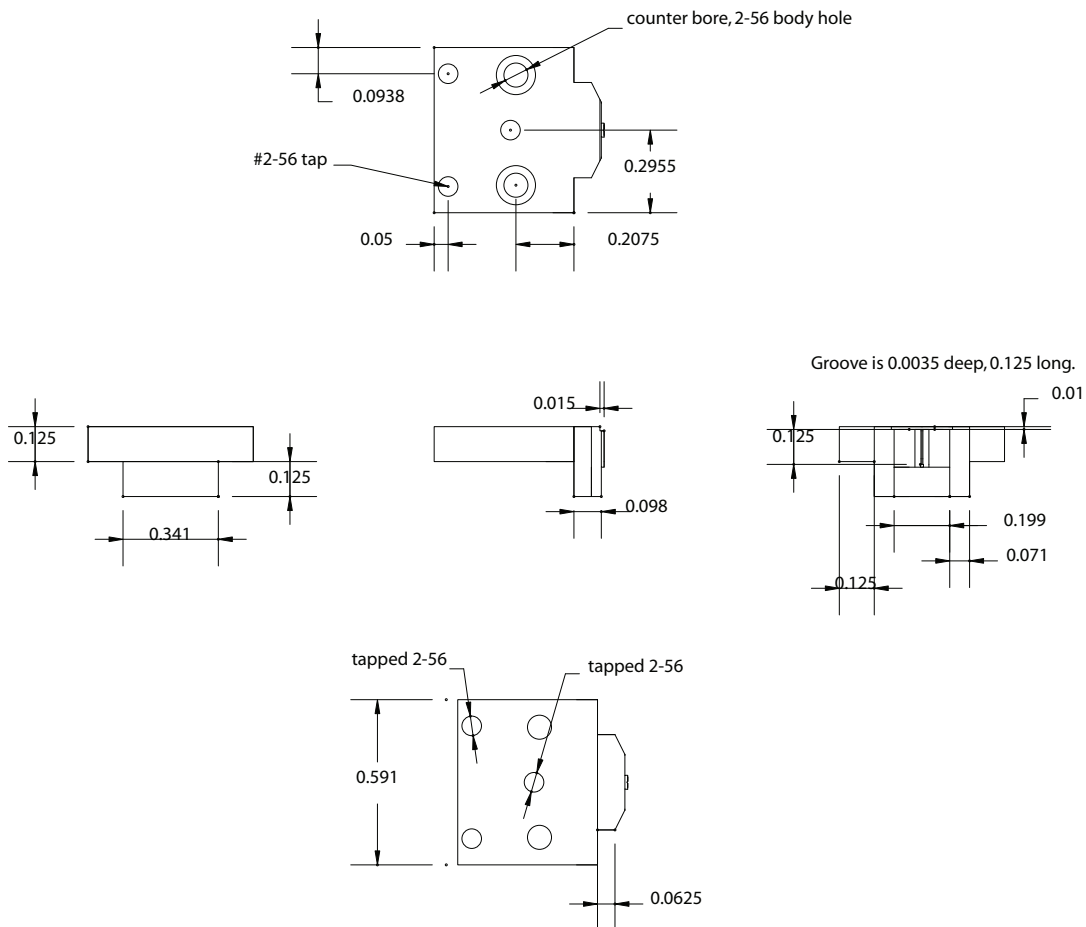


**Figure C.5:** Detailed CAD of the cantilever holder. The groove in the right most view of the sample holder is where the fiber is glued. The groove was machined by EDM.

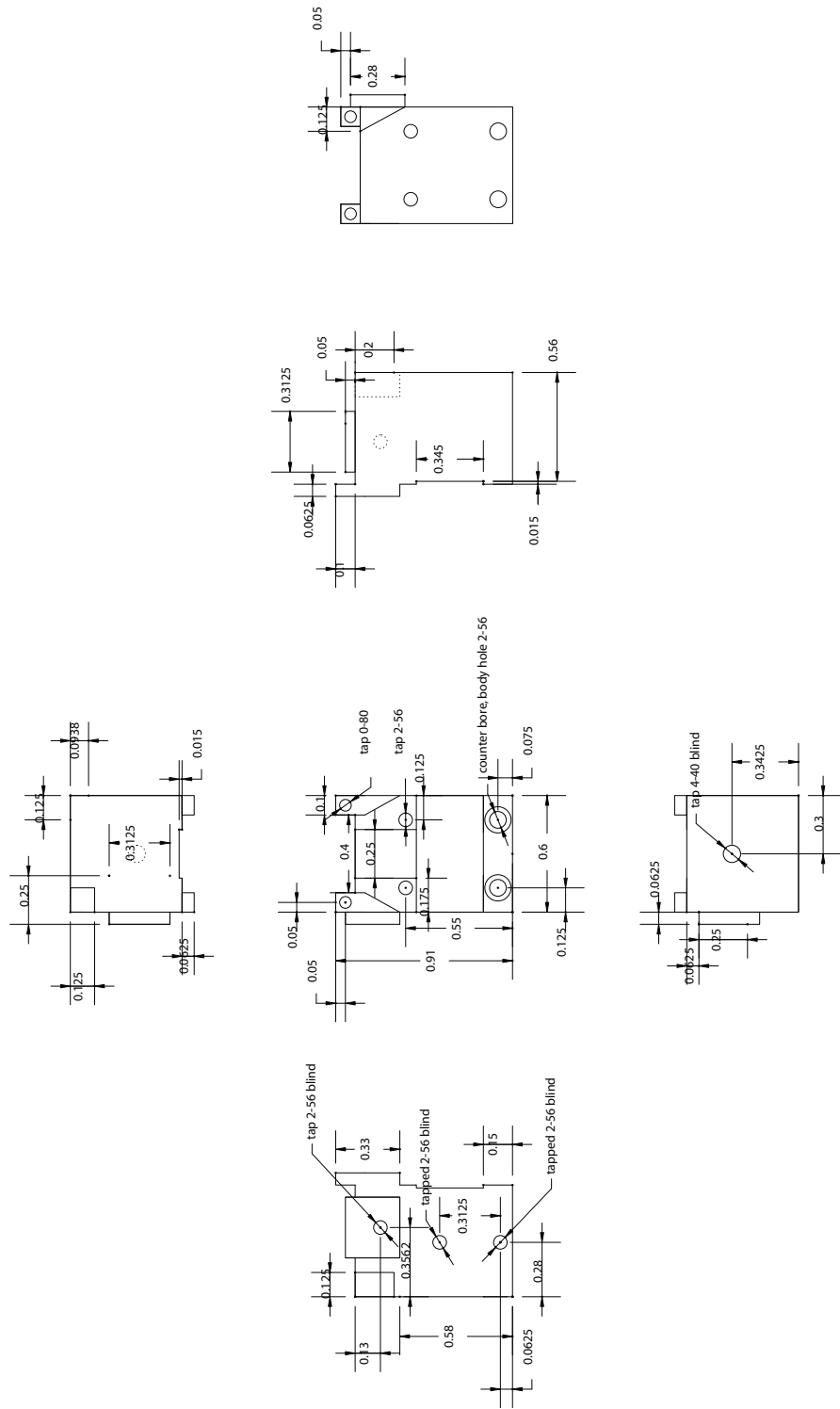


**Figure C.6:** Detailed CAD of the sample holder.

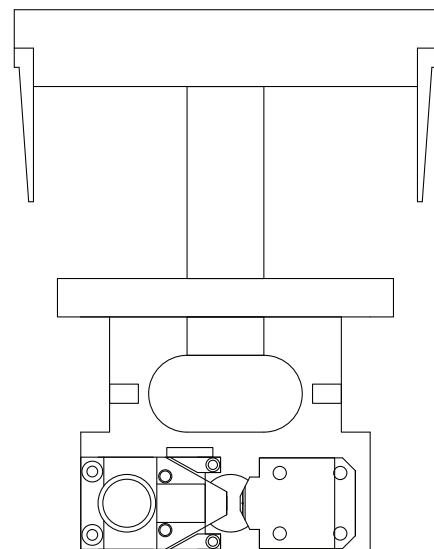


**Figure C.7:** View of the microscope stage used in experiments, where the magnetic particle magnetization lies along the cantilever width as discussed in section 3.2.

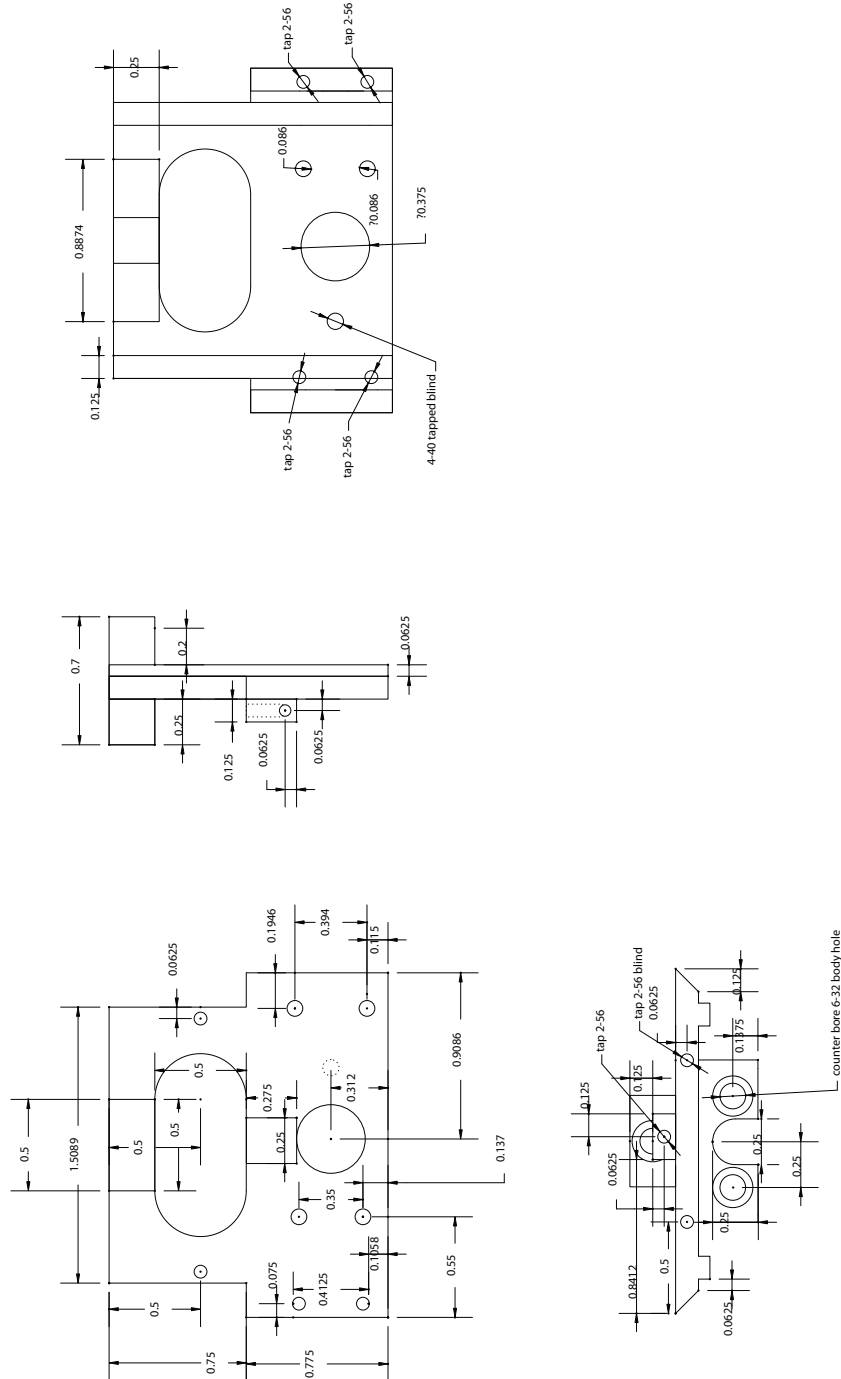


**Figure C.8:** Detailed CAD of the microscope stage used for experiments with the magnetic moment of the tip magnet parallel to the width of the cantilever as discussed in section 3.2 and illustrated in figure 3.4.

## APPENDIX D MAGNETOMETRY CALCULATIONS

Here we estimate the signal-to-noise ratio for frequency shift magnetometry measurements. These measurements are especially important for magnetic tips which have been nanofabricated. The fabrication process may effect the magnetic tips in undetermined ways, magnetometry provides an unambiguous route to determining the magnetic properties of the tip magnet *in situ*. For a detailed discussion of what is shown here see [145].

### D.1 Calculation of frequency shift

Cantilever magnetometry has been used previously to characterize the magnetic particle used in MRFM. [146] We measure the cantilever frequency as a function of the applied field, where the field is applied along the length of the cantilever, and from the resulting data are able to back out the magnetization of the magnetic tip. It is also possible to study the magnetic field fluctuations by measuring the cantilever quality factor a function of the applied magnetic field. These fluctuations are important as they can contribute to the magnetic field fluctuations spectral density which governs spin relaxation times. [23] Here we are primarily concerned with using cantilever magnetometry to prove that the magnetic particle located at the tip of the cantilever has the desired magnetic properties. Measuring the magnetic moment of the tip magnet enables more rigorous data analysis in MRFM measurements.

For the calculations presented here it is assumed that the applied field lies along the cantilever *length* and not the width as shown in figure 3.4. In this geometry the cross product  $m \times H_0 \neq 0$  and the cantilever experiences a frequency shift that is proportional to the applied field. Analysis and data of the type discussed here is given in [51].

The minimum detectable magnetic moment is set by the minimum detectable frequency shift and the geometric parameters of the magnet by

$$\mu_{min} = \left(\frac{l}{\alpha}\right)^2 \frac{\sqrt{2}F_{min}}{B_s \Delta N x_{pk}}. \quad (\text{D.1})$$

where  $l$  is the cantilever length,  $\alpha$  is a geometrical factor for the lever,  $F_{min}$  is the minimum detectable force of the cantilever,  $\Delta N = N_{\text{thickness}} - N_{\text{length}}$  is the difference in the demagnetization factors along the thickness and the length of the magnet (a function of the magnets geometry),  $x_{pk}$  is the amplitude of the cantilever drive. Since  $F_{min}$  scales with the cantilever parameters it can be shown that  $\mu_{min} \propto w^{1/2}l^{3/2}t$  with  $l, w, t$  the cantilever length, width, and thickness respectively. The saturated magnetic moment of the magnet is calculated using,

$$\mu_s = \frac{l_m w_m t_m B_s}{\mu_0}. \quad (\text{D.2})$$

with  $l_m, w_m, t_m$  the magnet length, width, and thickness respectively,  $B_s$  is the bulk saturation magnetization of the material used (1T for Cobalt, 0.6T for Nickel), and  $\mu_0 = 4\pi \times 10^{-7} \text{Tm/A}$ . The SNR is then the ratio  $\mu_s/\mu_{min}$ .

#### D.1.1 Checks

The above calculation was implemented in Matlab. To check the calculation we compared the results to known values. The calculation of  $\Delta N$  was checked against published numbers for demagnetization factors of known magnet geometries. For a cube we calculated  $N = 1/3$  as expected. This was especially important as  $\Delta N$  is unitless. We have calculated  $\mu_{min}$  for cantilever C3 listed in [51] and these numbers were found to agree.

#### D.1.2 Results

Figure D.1 shows the predicted signal-to-noise ratio for magnets of two different lengths as a function of the width of the magnet. The following parameters were used in the calculation:  $T = 4\text{K}$ ,  $Q = 10^4$ ,  $l = 400\mu\text{m}$ ,  $w = 5\mu\text{m}$ ,  $t = 0.34\mu\text{m}$ ,  $x_{pk} = 100\text{nm}$ . The magnet thickness,  $t_m$  is taken to be 50nm because this was the thickness in the most recent cantilever fabrication process.

#### D.1.3 Comments

Ng *et. al* estimate that with their most sensitive cantilever they could detect a Nickel magnet  $360\text{nm} \times 10\text{nm} \times 10\text{nm}$ . The cantilevers discussed here have been optimized for force sensitivity, not magnetic moment sensitivity. Despite this

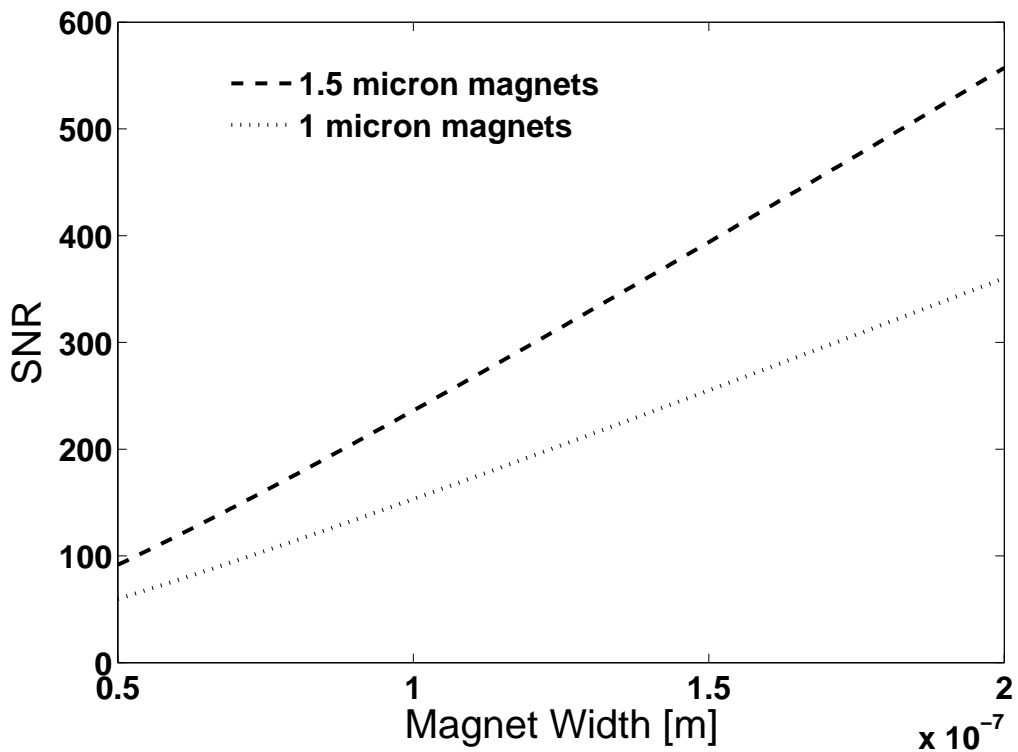


**Figure D.1:** Frequency shift magnetometry SNR estimates for magnets between 50nm and 200nm wide. The black trace is for magnets 1.5 microns long, the blue traces is for magnets 1.0 microns long. The magnet thickness is taken to be 50 nm. The cantilever has dimensions  $400\mu\text{m} \times 5\mu\text{m} \times 0.34\mu\text{m}$ . The narrowest magnets may be at the detection limit due to background noise resulting from frequency shifts present even with a blank cantilever. The mechanism for frequency shifts of cantilevers without magnetic tips in an applied field remains unknown.

we predict comparable magnetic moment sensitivity given a similar Q near 30 000. The sensitivity is attained by using narrower cantilevers and magnetic tips comprised of cobalt ( $\mu_0 M = 1.0\text{T}$ ) instead of nickel ( $\mu_0 M = 0.6\text{T}$ ).

These SNR estimates do not include a correction for the frequency shift experienced by a blank cantilever without a magnetic tip which has been observed experimentally. The mechanism of frequency shift for a blank cantilever has not yet been elucidated. The frequency shift experienced by blank cantilevers in an applied field has been observed to change from wafer to wafer and is speculated to result from contamination during the fabrication process of unknown origin.

Finally, consider magnet C1 in chapter 2 of [145]. We predict an SNR for that magnet-cantilever combination of  $10^3$ , while the observed SNR was  $10^2$ . It appears that under these conditions we should have enough SNR for the widest magnets (see Fig. D.1), while the 50nm wide magnets appear to approach the detection limit.

#### D.1.4 Frequency shifts

Here we predict that fractional frequency shift due to a magnet present at the tip of the cantilever. The minimum detectable frequency shift is not included in this calculation but is typically on the order  $10^{-6}$ . The results are shown in figure D.2.

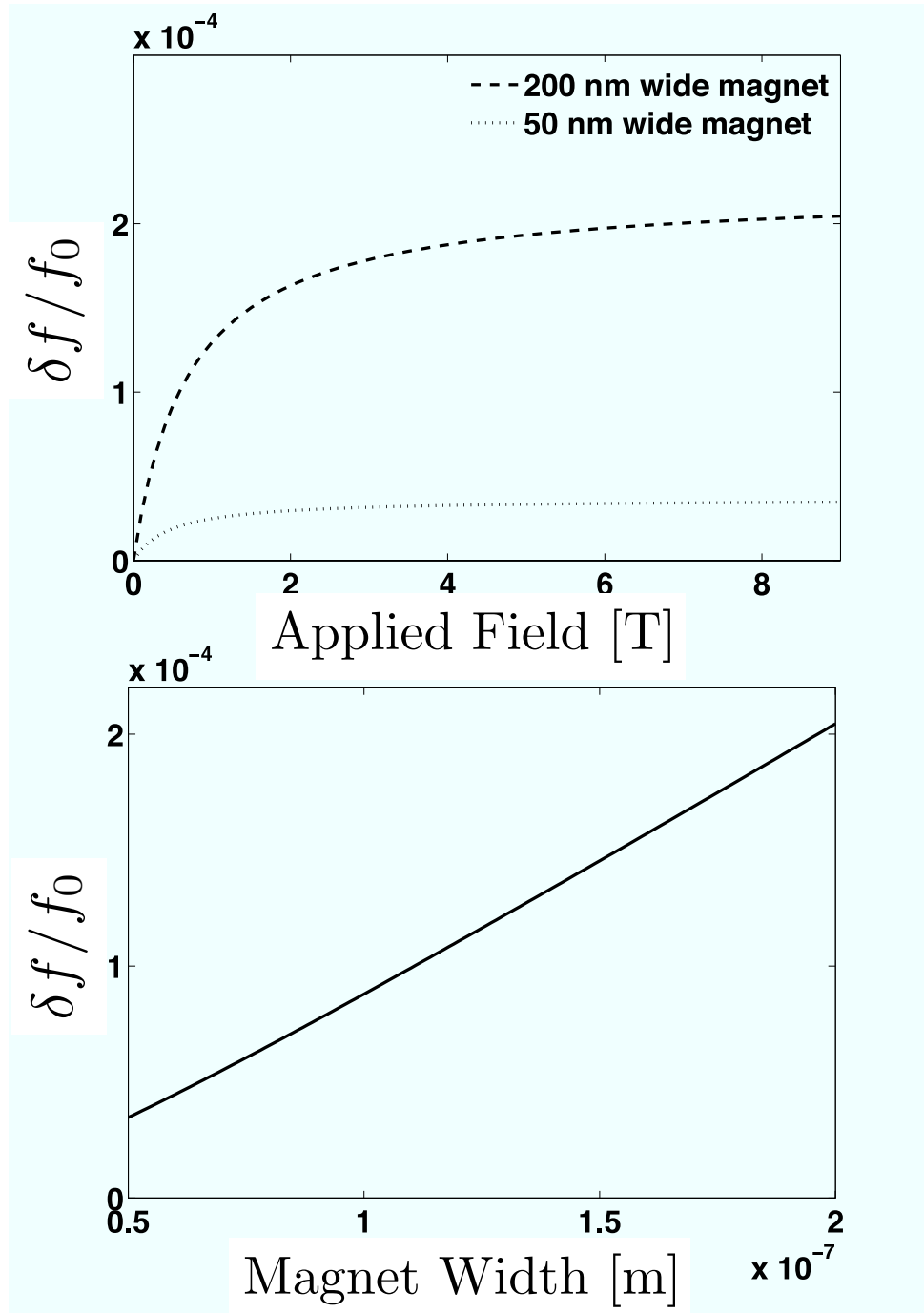


**Figure D.2:** Magnetometry frequency shift predicted for various magnet geometries. The cantilever is  $400\mu\text{m} \times 5\mu\text{m} \times 0.34\mu\text{m}$ . For both plots the magnet length is  $1\mu\text{m}$ , and the thickness is  $50\text{nm}$ . In the lower plot the applied field is  $9\text{T}$ .

## APPENDIX E SPECTRAL THEOREMS AND SPECTRAL CONVENTIONS

Here we outline important spectral theorems and conventions and notation used for spectral densities and correlation functions throughout this thesis. We also illustrate the equivalence between the spectral density conventions used in [22] and [77].

### E.1 Exact form of equation 4.11

Stipe *et. al* give the friction experienced by a cantilever due to a fluctuating electric field as

$$\Gamma = \frac{(V_{ts} - \phi)^2}{4k_B T} S_F(\omega_c). \quad (\text{E.1})$$

### E.2 Conventions

The spectral density and correlation function conventions in this thesis are presented here. The correlation functions used here are those followed in [147]. First, we define a correlation function as

$$G(\tau) = \langle F(t + \tau)F(t) \rangle = \lim_{T \rightarrow \infty} \frac{1}{2T} \int_{-T}^T F(t)F(t + \tau)dt \sim [N^2]. \quad (\text{E.2})$$

Note that for stationary processes  $\langle F(t + \tau)F(t) \rangle = \langle F(\tau)F(0) \rangle$  because time is relative. The correlation function written above is a force autocorrelation function resulting in the units of  $N^2$ . Taking the FT of this we get

$$\lim_{T \rightarrow \infty} \int_{-\infty}^{\infty} G_T(\tau) e^{i\omega\tau} d\tau = \lim_{T \rightarrow \infty} \frac{1}{2T} |\hat{F}(\omega)|^2 \sim [\frac{N^2}{Hz}]. \quad (\text{E.3})$$

Note that these units are 'physically relevant' in that they are per Hz. This reflects the fact that all measurements in the lab occur in a finite bandwidth. We define the spectral density as

$$J(\omega) = \lim_{T \rightarrow \infty} \frac{1}{2T} |\hat{F}(\omega)|^2 \sim [\frac{N^2}{Hz}]. \quad (\text{E.4})$$

and the one sided power spectral density as

$$S_F(\omega) = \lim_{T \rightarrow \infty} \frac{1}{2T} |\hat{F}(\omega)|^2 + |\hat{F}(-\omega)|^2 \sim [\frac{N^2}{Hz}], \quad (\text{E.5})$$

with

$$S_F(\omega) = J(\omega) + J(-\omega) = 2J(\omega). \quad (\text{E.6})$$

where the last equality follows from the assumption that the noise is an even function of frequency. Note that  $F$  denotes force  $\sim [N]$ , and  $f$  denotes frequency  $\sim [Hz]$ . The latter is an important difference and will contribute a factor of  $2\pi$ . This single sided power spectrum is what we typically measure in the lab. Using this definition of spectral density equation E.1 is correct.

Due to our collaboration with Professor Roger Loring a hybrid of this notation and notation typically used by Professor Loring was often employed. This slight difference in notation is reflected by the factor of 4 difference between equations E.1 and 4.11. Here we show that these notations are equivalent.

Reflecting the fact that the correlation function and the spectral density are fourier transform pairs, Professor Loring typically expresses the spectral density as

$$\hat{C}' \equiv \int_0^\infty dt \cos(\omega t) \langle \delta F_x(t) \delta F_x(0) \rangle. \quad (\text{E.7})$$

Therefore  $J(\omega) = 2\hat{C}'$ . We have then

$$S_F(\omega) = 2J(\omega) = 4\hat{C}'. \quad (\text{E.8})$$

Plugging this into equation E.1 yields equation 4.11.

### E.3 The Wiener-Khinchin Theorem

Here we examine the Wiener-Khinchin Theorem. Parseval's Theorem results as a limiting case of the Wiener-Khinchin Theorem. The theorem is stated here without proof. For a complete derivation see [46]. Using the conventions outlined above the theorem states

$$\langle x(t)x(t-\tau) \rangle = \int_0^\infty d\omega S_x(\omega) e^{-i\omega\tau}. \quad (\text{E.9})$$

In the limit of  $\tau \rightarrow 0$  we have

$$\langle |x|^2(t) \rangle = \int_0^\infty d\omega S_x(\omega). \quad (\text{E.10})$$

Meaning that the mean squared deviation is the area under the power spectrum. This relationship is referred to as Parseval's Theorem.

## APPENDIX F DISSIPATION MICROSCOPE DESIGN

Here we present a detailed view of the dissipation microscope design. All discs, parts (b)-(f), (j) and (l) were machined from brass using a protocol similar to that described in [53]. Parts (g) and (h) were machined from aluminum to a tolerance of 0.002 inches. Parts (i) and (k) were machined from Macor as discussed in the text. All dimensions are in inches.

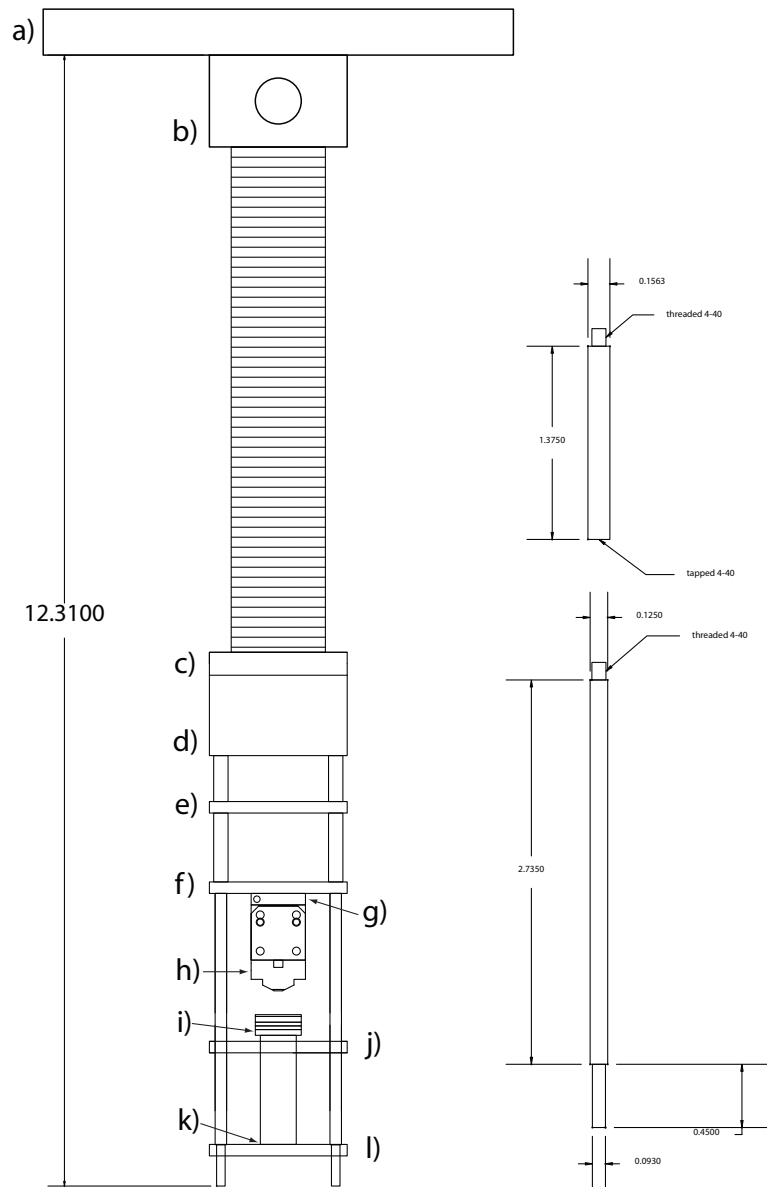


**Figure F.1:** An overview of the dissipation microscope CAD. The individual parts are labeled and detailed views are presented below.

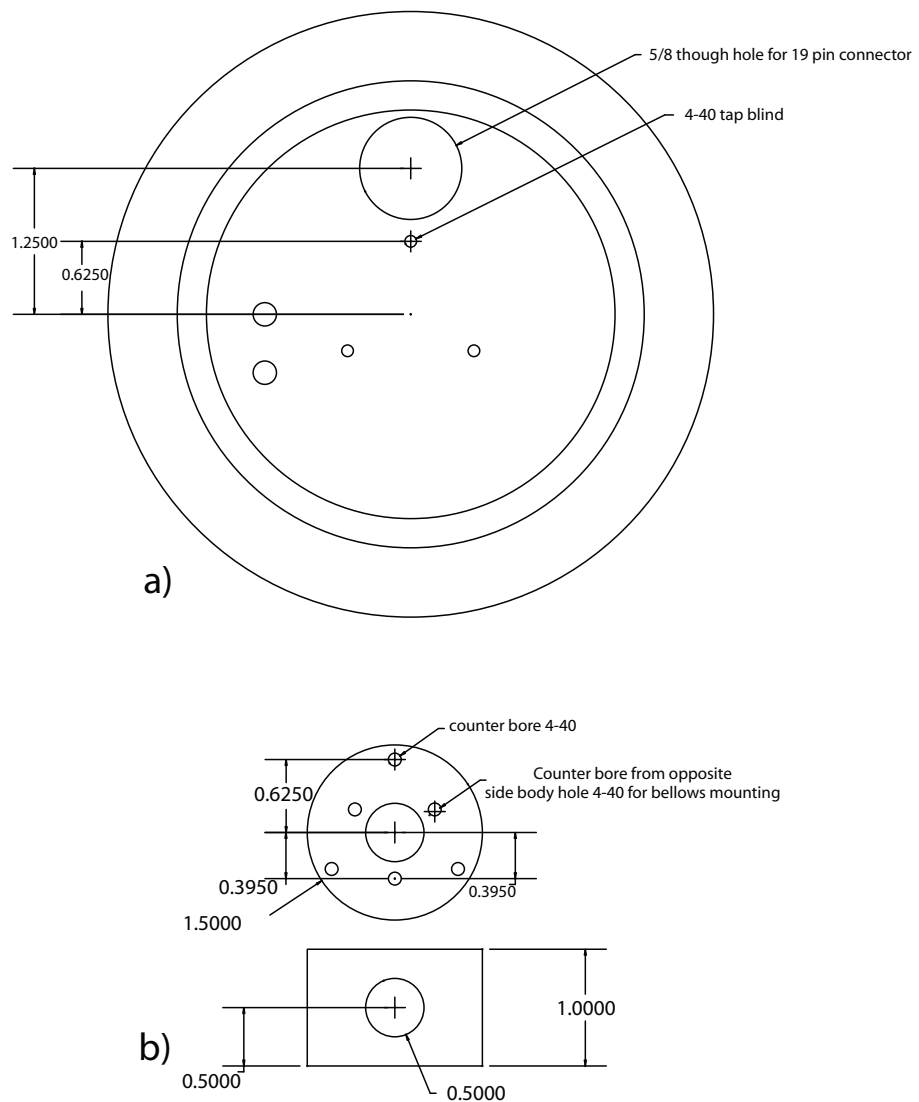


**Figure F.2:** Parts (a) and (b). Part (a) is the 5.118 OD ISO flange. The two holes on the left are through holes where the swage-lock fiber feed throughs were welded. (b) is the adaptor plate which attached the bellows to the flange and includes a hole allowing wires from the 19 pin to be fed through the center of the bellows.

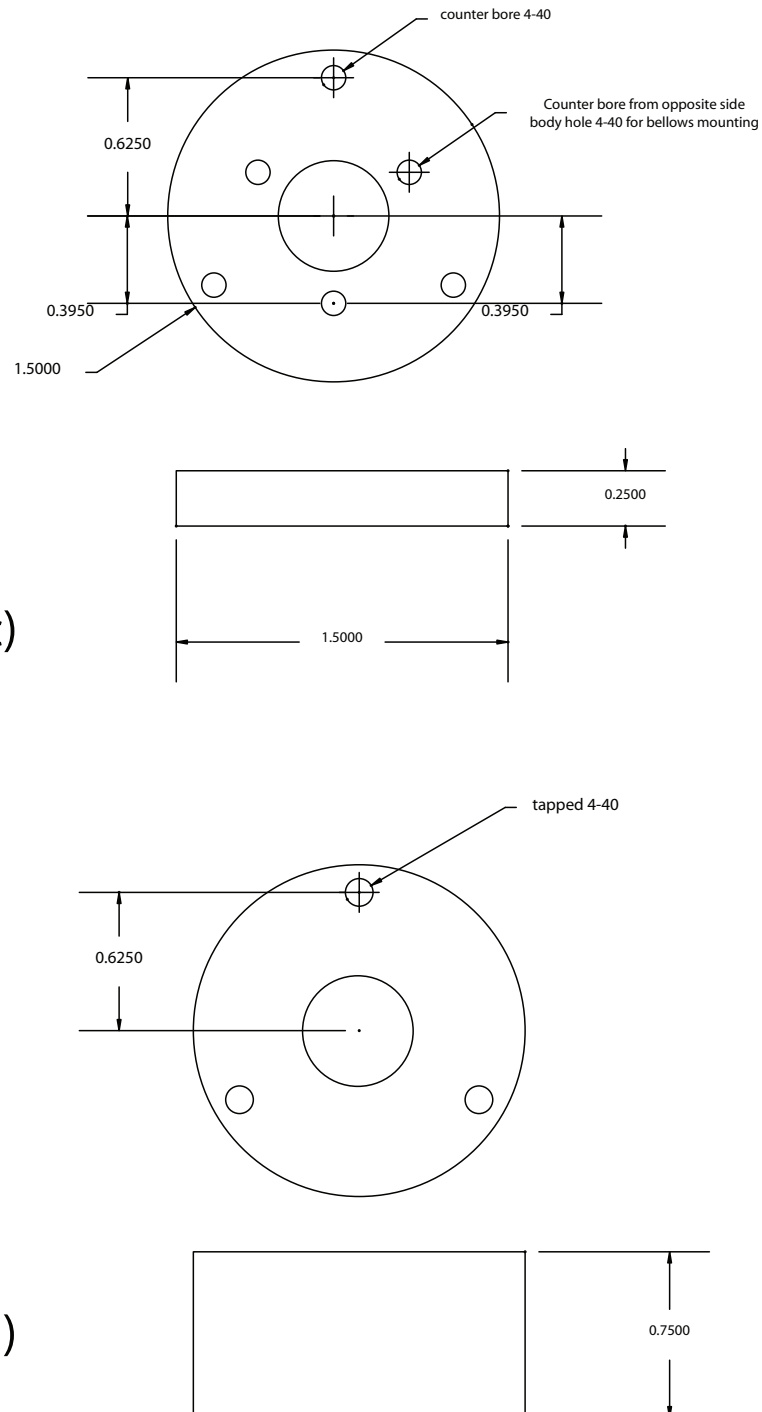


**Figure F.3:** Parts (c) and (d). Part (c) is an adaptor plate between the bellows and part (d) the cylinder of brass which is drilled and tapped appropriately for the rods. The upper portion of the stainless steel rods attach to part (d).

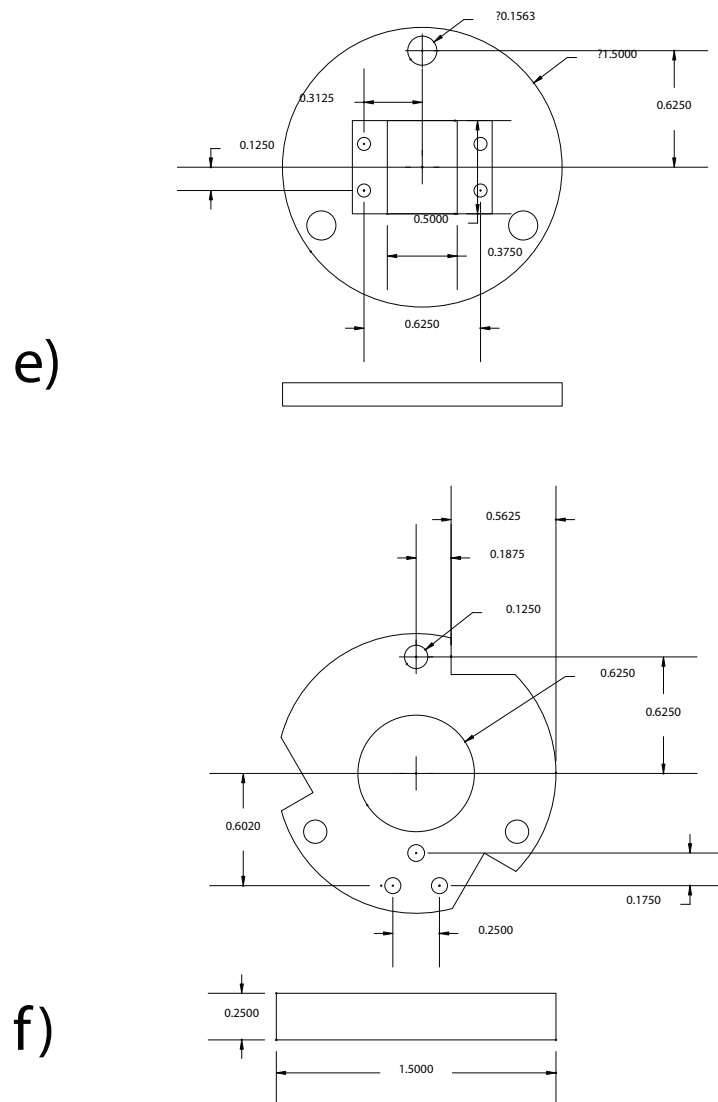


**Figure F.4:** Parts (e) and (f). Part (e) supports the electrical connections for the wires which emerge from the bottom of the flexible bellows. Printed circuit boards containing Samtec connectors are bolted into the center of this part. Part (f) supports the Attocube and cantilever holder.

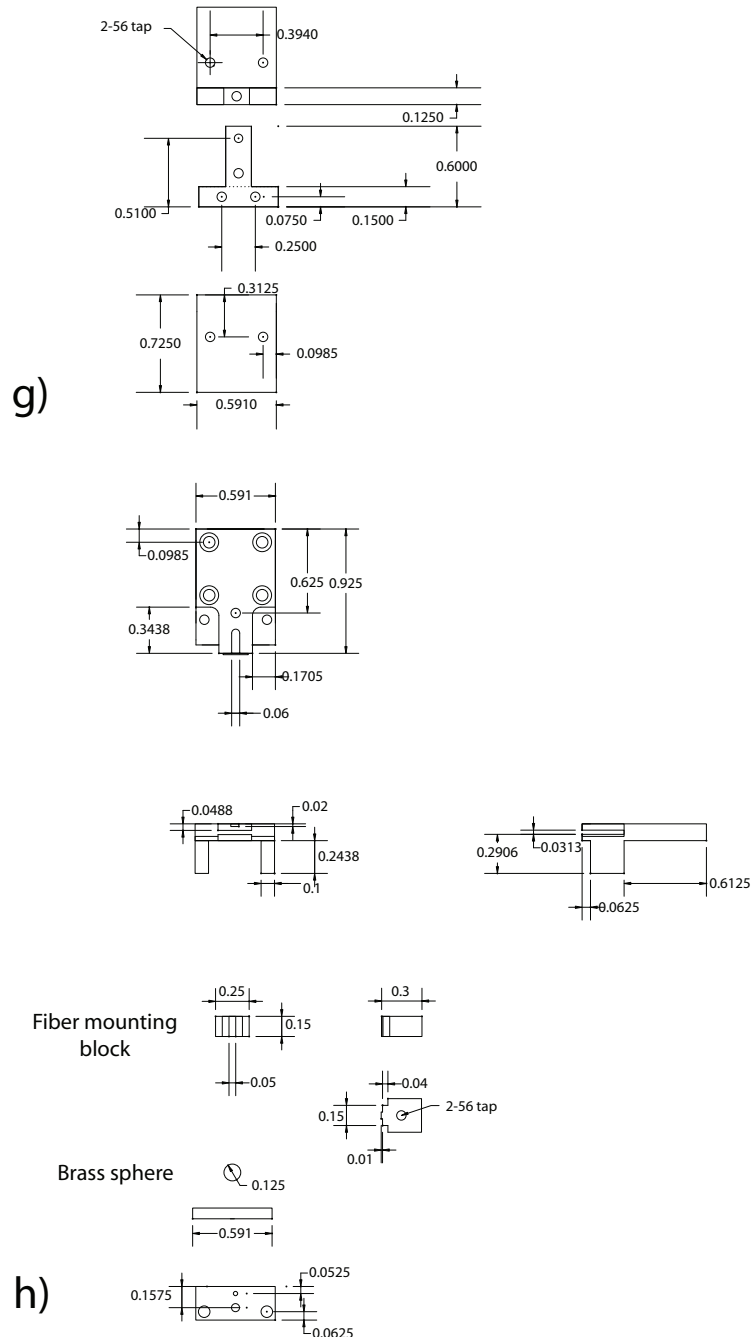


**Figure F.5:** Parts (g) and (h). Part (g) bolts to the three holes in part (f) and provides a platform for the Attocube ANPx50 positioner. Part (h) is the cantilever and fiber holder which is discussed in detail in the text.

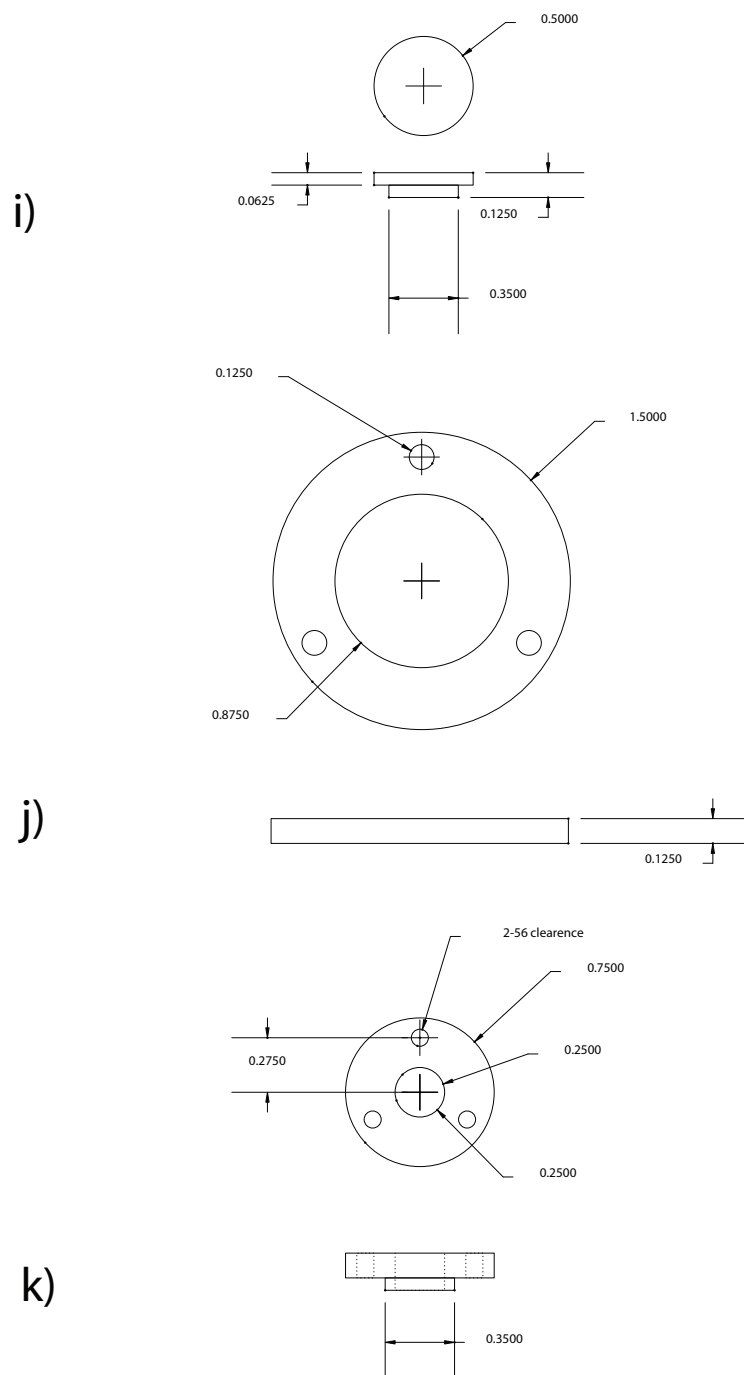


**Figure F.6:** Parts (i),(j) and (k). Part (i) is the Macor part capping the piezo tube. Part (j) is the stabilizing ring serving only to make the structure more rigid. Part (k) is the Macor part attaching to the bottom of the piezo tube scanner.

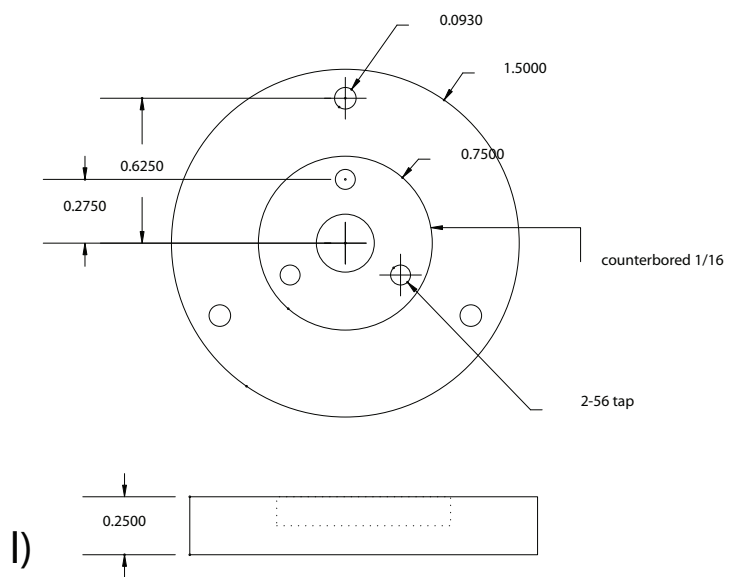


**Figure F.7:** Part (l) provides the mounting plate for the scanner.

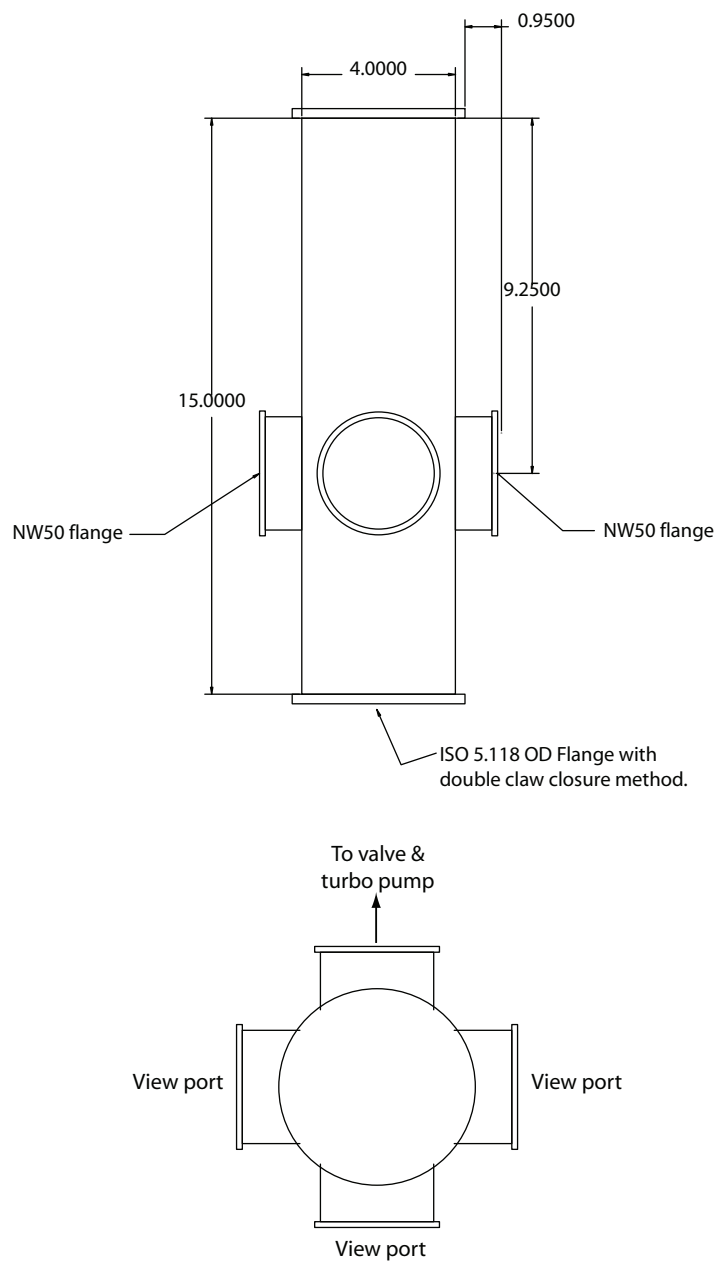


**Figure F.8:** High vacuum chamber containing the microscope. The flexible bellows attach to the ISO 5.118OD flange on top. The microscope hangs such that the sample and cantilever holder are visible through the three NW50 viewports.

## APPENDIX G CANTILEVER FABRICATION RECIPE

Here we outline the cantilever fabrication process. SOI  $\langle 100 \rangle$  wafers were obtained from Soitech with a device layer 340nm thick and a 400nm thick buried oxide layer. During the fabrication process two wafers were run in parallel; one SOI and one standard silicon used to calibrate etch times and inspect optical lithography dosages prior to etching into the more expensive SOI wafer. The process outlined here was used on the wafer labeled SOI dissipation 2 which had an unprecedented yield of 97%. ‘Topside’ denotes the side of the wafer comprised of the device layer and ‘backside’ denotes the much less precisely controlled side of the wafer comprised of the handle silicon.

### G.1 Topside processing

#### G.1.1 Tip thinning

- Acetone followed by isopropanol clean on spinner
- 20s P20 primer - spin clean
- SPR 955 CM 2.1 resist, spin at 3000 rpm for 30s resulting in 2 $\mu\text{m}$  thickness
- soft bake 90°C for 90s
- Expose, 0.6s on 5 $\times$  GCA Autostep
- 2min 300 MIF developer, DI H<sub>2</sub>O and N<sub>2</sub>(g) clean
- Calibrate PT72 RIE etch process 5 (SF<sub>6</sub>) etch rates on silicon wafer, determine rate by profilometry on P10 profiler - 45nm/min taking care to profile both the resist thickness and the etch depth to determine the etch rate
- Etch tip holes for 6min, process 5 PT72
- Strip resist in hot resist strip solvent baths: bath #1 for 15min bath #2 for 25min
- Profile tip hole depth - in this case 220  $\pm$  20nm

#### G.1.2 Definition of cantilevers

- Acetone followed by isopropanol clean on spinner
- SPR 955 CM 2.1 resist, spin at 3000 rpm for 30s resulting in 2 $\mu\text{m}$  thickness
- Expose, 0.6s on 5 $\times$  GCA Autostep, key offset  $x = -0.252$  units are millimeters
- Post exposure bake (PEB) 120°C 90s
- 2.5min 300 MIF developer, DI H<sub>2</sub>O and N<sub>2</sub>(g) clean
- PT72 process 5, 12.5min etch, confirm etch is all the way through device layer by profilometry
- Strip resist in hot resist strip solvent baths: bath #1 for 15min bath #2 for 25min
- Acetone followed by isopropanol clean on spinner
- SPR 955 CM 2.1 resist, spin at 3000 rpm for 30s resulting in 2 $\mu\text{m}$  thickness
- Expose, 0.6s on 5 $\times$  GCA Autostep, key offset  $x = -0.250$  - this 2 $\mu\text{m}$  offset supplies the tip definition as described in [124]
- Post exposure bake (PEB) 120°C 90s
- 2.5min 300 MIF developer, DI H<sub>2</sub>O and N<sub>2</sub>(g) clean
- Inspect optically prior to etch to confirm alignment

- PT72 process 5, 12.5min etch, confirm etch is all the way through device layer by profilometry
- Strip resist in hot resist strip solvent baths: bath #1 for 15min bath #2 for 25min
- 3 hours in 1165 resist strip to provide additional cleaning - **do not** use O<sub>2</sub> plasma clean such as Branson Barrell Etcher or Aura. It is critical to thoroughly clean the topside prior to depositing oxide as any contamination may effect cantilever yield or performance
- Thorough DI H<sub>2</sub>O rinse and N<sub>2</sub>(g) clean
- 1.5μm oxide deposition, 4min GSI low stress TEOS

## G.2 Backside processing

- Backside resist - spin Shipley 1075 ramp from 500 – 2500 rpm over 30s
- 90°C 120s bake
- EV620 contact aligner backside alignment procedure. Expose 12s at 12.8mW/cm<sup>2</sup> too long an exposure results in excessive resist bubbling PEB skipped for this reason as well
- 5min 300MIF, DI H<sub>2</sub>O rinse and N<sub>2</sub>(g) clean
- Measure resist thickness by profilometry - 11.5μm or greater is OK
- Backside DRIE etch using Unaxis ICP 770 etcher. Etch rate decreases as etch pits get deeper. After 580 loops ~ 450μm have been etched as determined by profilometry. Do not profile the wafer when backside silicon is less than ~ 100μm thick to avoid oxide membrane breakage. 100 or so more loops complete the backside etch. The backside etch is most rapid in the center of the wafer resulting in the formation of a ledge at the base of the cantilevers. Continue etching until the entire wafer is free of silicon below the cantilevers as observed with an optical microscope through the topside silicon dioxide. Handle wafer with care at this point!
- 30min PT72 Bosch descum process 3. Elevate the wafer in the etcher chamber by placing it on some scraps, be sure that the backside of the wafer is facing up
- HF etch - 13min in 6 : 1 BOE using teflon wafer boat which allows wafer to remain submerged during transfer between HF and DI H<sub>2</sub>O
- 3× 4min DI H<sub>2</sub>O rinse in teflon boat
- 3× 4min methanol rinse in teflon boat
- Careful, rapid transfer of wafer from teflon boat in methanol to critical point dryer (CPD)
- Remove from CPD and inspect checking for curling under high magnification optical microscope

## APPENDIX H

### DIELECTRIC SPECTROSCOPY MEASUREMENTS

#### H.1 Custom capacitors

Dielectric spectroscopy measurements were made on 450nm thick PMMA and PVAc films. Dielectric spectroscopy measurements necessitated construction of capacitors of known area using these thin films. To do this standard quartz wafers were diced into 1 inch squares on a wafer dicing saw. These wafers were then cleaned by repeated ultrasonication in methanol. The squares were then loaded into an electron gun evaporator with an evaporation jig as shown in figure H.1. 50nm of aluminum was then evaporated at a rate of 0.5nm/s constituting the bottom electrode of the capacitor. The thin films were then spin cast using the polymers discussed in the text (see table 6.2.1). Thin films were annealed in high vacuum at  $T_g + 10\text{K}$  as with the friction measurement sample preparation. The films were removed from the annealing oven and placed in the high vacuum chamber of the electron gun evaporator within 30 minutes to minimize contamination and water absorption. On the second evaporation, again in the jig shown in figure H.1, the substrates were rotated 180° with respect to their orientation during the first evaporation. Also, to minimize substrate heating the evaporation rate was kept below 0.1nm/s as not to melt the polymer thin film. The substrate thermometer reading never exceeded 17°C. This was especially important for the low  $T_g$  PVAc samples. The result was a capacitor formed by the overlapping region and pads where electrical contact could be made with clips as shown in figure H.2. The result was a capacitor with a total area of 0.5in × 0.75in and an electrode separation set by the spin case film thickness. Several devices were sacrificed to check that evaporation of the second electrode did not alter the film thickness and to check the overall thickness of the devices by profilometry.

Attempts were made to construct capacitor electrodes by sputtering gold. The advantage being that sputtering required only a few minutes while the aluminum evaporation of electrodes took 2 hours. Gold electrodes shorted without exception. This was presumably due to the mobility of gold within the polymer films or during the sputtering process. Aluminum electrodes were not shorted 90% of the time.

#### H.2 Results

The HP spectrum analyzer measured the real portion of the capacitance and the loss tangent. The loss tangent is defined as

$$\tan \delta = \frac{C''}{C'} = \frac{\hat{\epsilon}''(\omega)}{\hat{\epsilon}'(\omega)}. \quad (\text{H.1})$$

Using the known area of the capacitor of  $2.4 \times 10^{-4}\text{m}^2$  and the parallel plate approximation we converted the observed  $C'(\omega)$  to  $\hat{\epsilon}'(\omega)$ . We constructed 3 copies of PMMA and PVAc capacitors and measured each using the HP spectrum analyzer. There was approximately a 10% variation in the measured values across the three capacitors for both PMMA and PVAc. This variation is likely due to variation in the film thickness and possibly the metal roughness. These measurements were averaged and are shown in figure H.4. The rising portion of the curve in the  $\tan \delta$  plot is an artifact from the leads which could be compensated for by measuring that capacitance independently. The contribution of this artifact to the Fourier component of interest near 8kHz was within the error due to averaging of several data sets. Some details of the HP spectrum analyzer used for dielectric spectroscopy can be found in [148].

Capacitors with dielectric layers of PS were also constructed. The sensitivity of the HP spectrum analyzer was not sufficient to measure the very low losses in PS dielectrics ( $\tan \delta \sim 0.001$ ) requiring that we use literature values, see the text.

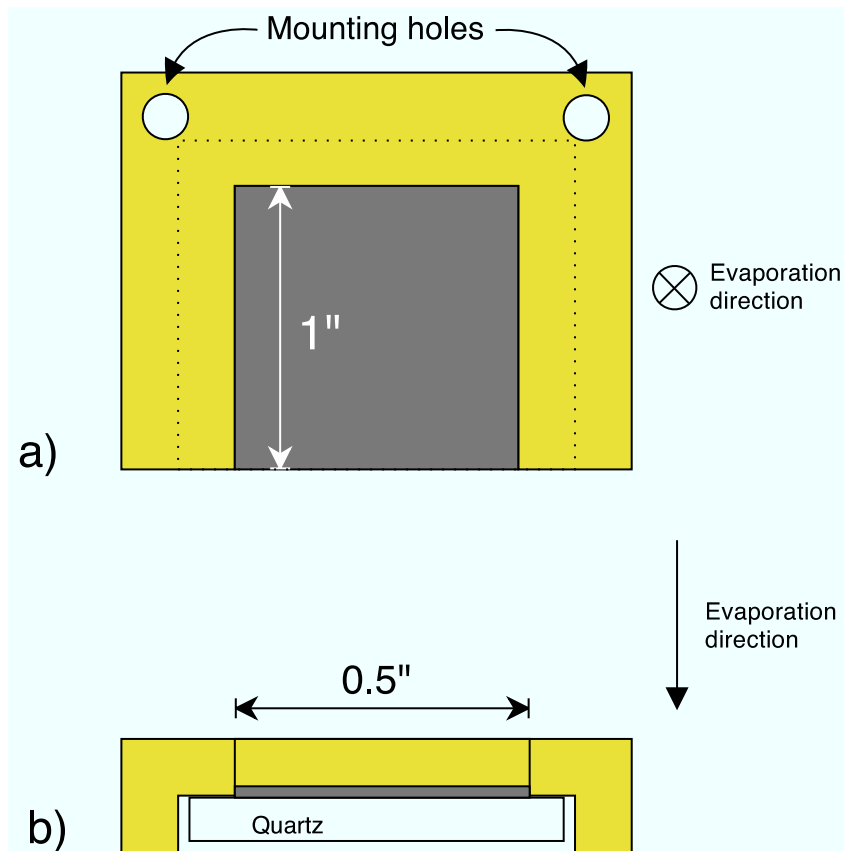


**Figure H.1:** A custom brass evaporation jig for making capacitors from polymer thin films on quartz substrates. The actual jig evaporates four substrates simultaneously. a) Tip down view, the exposed portion of the quartz substrate is evaporated with a 50nm aluminum thin film by electron gun evaporation. The mounting holes allow mounting in the evaporator using machine screws. b) Profile view showing the quartz substrate the aluminum electrode. See figure H.2 for completed capacitor geometry.

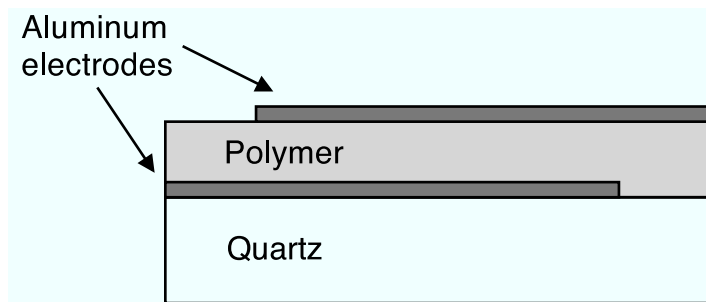


**Figure H.2:** Custom capacitors constructed as outlined in the text. Several capacitors were sacrificed for profiling where it was shown that the film thickness was not altered by evaporation of the topside electrodes.

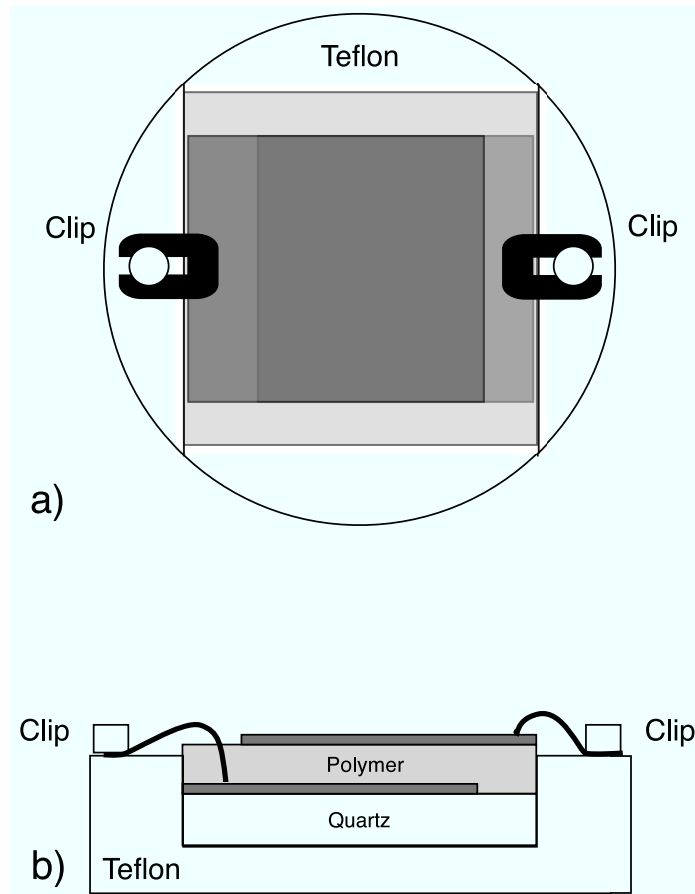


**Figure H.3:** Custom dielectric spectroscopy jig for capacitors constructed from thin films. Electrical contacts to electrodes are made with clips which are connected to the leads of the spectrum analyzer. For the low frequency measurements presented here coaxial cables were not necessary.

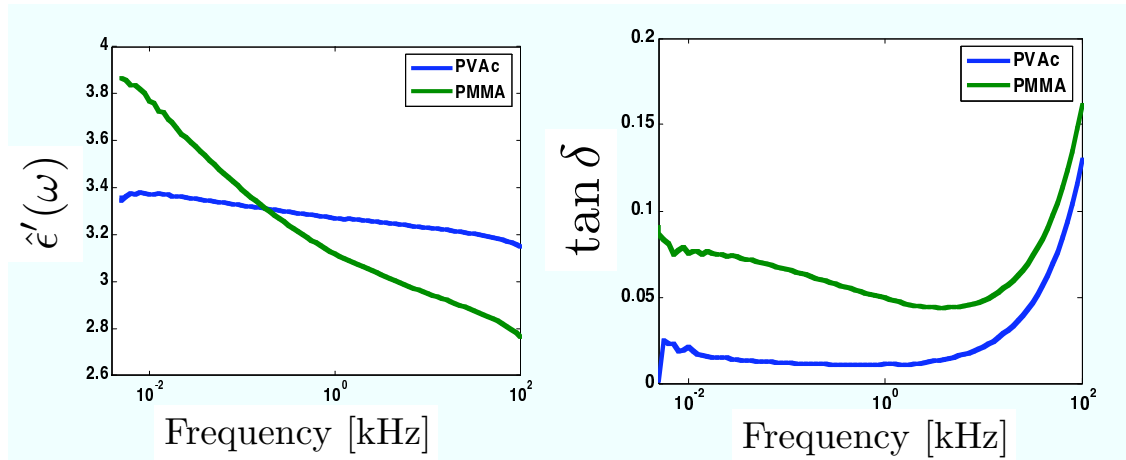


**Figure H.4:** Measured  $\hat{\epsilon}'(\omega)$  and  $\tan \delta$  for PMMA and PVAc at room temperature.

## REFERENCES

- [1] J. A. Sidles, *Appl. Phys. Lett.* **58**, 2854 (1991).
- [2] J. C. Kendrew et al., *Nature* **181(4610)**, 662 (1958).
- [3] <http://www.pdb.org>.
- [4] <http://blanco.biomol.uci.edu>.
- [5] S. G. Zech, A. J. Wand, and A. E. McDermott, *J. Am. Chem. Soc.* **127**, 8618 (2005).
- [6] N. A. Oyler and R. Tycko, *J. Am. Chem. Soc.* **126**, 4478 (2004).
- [7] N.R.C., *Beyond the Molecular Frontier: Challenges for Chemistry and Chemical Engineering*, 2003.
- [8] P. Lauterbur, *Nature* **242**, 190 (1973).
- [9] G. Binnig, C. Quate, and C. Gerber, *Phys. Rev. Lett.* **56**, 930 (1986).
- [10] J. Marohn, Unpublished (2002).
- [11] S. R. Garner, S. Kuehn, J. M. Dawlaty, N. E. Jenkins, and J. A. Marohn, *Appl. Phys. Lett.* **84**, 5091 (2004).
- [12] H. J. Mamin and D. Rugar, *Appl. Phys. Lett.* **79**, 3358 (2001).
- [13] V. Sazonova et al., *Nature* **431**, 284 (2004).
- [14] K. R. Thurber, L. E. Harrell, R. Fainchtein, and D. D. Smith, *Appl. Phys. Lett.* **80**, 1794 (2002).
- [15] R. Budakian, H. Mamin, B. Chui, and D. Rugar, *Science* **307**, 408 (2005).
- [16] F. Bloch, *Physical Review* **70**, 460 (1946).
- [17] H. Mamin, R. Budakian, B. Chui, and D. Rugar, *Physical Review B (Condensed Matter and Materials Physics)* **72**, 24413 (2005).
- [18] D. Rugar, R. Budakian, H. Mamin, and B. Chui, *Nature* **430**, 329 (2004).
- [19] Y. Wang, J. A. Henry, A. T. Zehnder, and M. A. Hines, *J. Phys. Chem. B* **107**, 14270 (2003).
- [20] Y. Wang, J. A. Henry, D. Sengupta, and M. A. Hines, *Appl. Phys. Lett.* **85**, 5736 (2004).
- [21] J. A. Henry, Y. Wang, and M. A. Hines, *Appl. Phys. lett.* **84**, 1765 (2004).
- [22] B. C. Stipe, H. J. Mamin, T. D. Stowe, T. W. Kenny, and D. Rugar, *Phys. Rev. Lett.* **87**, 96801 (2001).
- [23] B. Stipe et al., *Phys. Rev. Lett.* **87**, 277602 (2001).
- [24] J. A. Sidles and D. Rugar, *Phys. Rev. Lett.* **70**, 3506 (1993).
- [25] D. L. Olson, M. E. Lacey, and J. V. Sweedler, *Anal. Chem.* **70**, 645 (1998).
- [26] D. Rugar, C. S. Yannoni, and J. A. Sidles, *Nature* **360**, 563 (1992).
- [27] D. Rugar et al., *Science* **264**, 1560 (1994).
- [28] O. Züger and D. Rugar, *J. Appl. Phys.* **75**, 6211 (1994).
- [29] K. Wago, O. Züger, R. Kendrick, C. S. Yannoni, and D. Rugar, *J. Vac. Sci. Tech. B* **14**, 1197 (1996).
- [30] T. D. Stowe et al., *Appl. Phys. Lett.* **71**, 288 (1997).
- [31] N. Jenkins et al., *J. Vac. Sci. Tech. B* **22**, 909 (2004).

- [32] H. Mamin, R. Budakian, B. Chui, and D. Rugar, Phys. Rev. Lett. **91**, 207604 (2003).
- [33] B. C. Stipe et al., Phys. Rev. Lett. **87**, A267602+ (2001).
- [34] R. Budakian, H. Mamin, and D. Rugar, Appl. Phys. Lett. **89**, 113113 (2006).
- [35] C. L. Degen et al., Phys. Rev. Lett. **94**, 207601 (2005).
- [36] Q. Lin et al., Phys. Rev. Lett. **96**, 137604 (2006).
- [37] L. A. Madsen, G. M. Leskowitz, and D. P. Weitekamp, Proc. Nat. Acad. Sci. **101**, 12804 (2004).
- [38] M. C. Butler, V. A. Norton, and D. P. Weitekamp, Am. Chem. Soc. Abstracts **229**, U735 (2005).
- [39] A. I. Volokitin and B. J. Persson, Phys. Rev. Lett. **94**, 086104 (2005).
- [40] J. R. Zurita-Sanchez, J. J. Greffet, and L. Novotny, Phys. Rev. A **69**, 022902 (2003).
- [41] H. Mamin, R. Budakian, and D. Rugar, Rev. Sci. Inst. **74**, 2749 (2003).
- [42] A. Abragam, *Principles of Nuclear Magnetism*, Oxford, 1961.
- [43] C. Slichter, *Principles of Magnetic Resonance*, Springer, 1978.
- [44] M. Goldman, *Quantum Description of High-Resolution NMR in Liquids*, Oxford, 1988.
- [45] M. Levitt, *Spin Dynamics*, Wiley, 2001.
- [46] N. Gershenfeld, *The Physics of Information Technology*, Cambridge, 2000.
- [47] S. Garner, *Force-gradient detected nuclear magnetic resonance*, PhD thesis, Cornell University, 2005.
- [48] T. R. Albrecht, P. Grütter, D. Horne, and D. Rugar, J. Appl. Phys. **69**, 668 (1991).
- [49] N. Jenkins, *Expanding the limits of magnetic resonance force microscopy*, PhD thesis, Cornell University, 2007.
- [50] J. A. Marohn, R. Fainchtein, and D. D. Smith, Appl. Phys. Lett. **73**, 3778 (1998).
- [51] T. Ng, N. Jenkins, and J. Marohn, IEEE Trans. Magn. **42(3)**, 378 (2006).
- [52] W. R. Silveira and J. A. Marohn, Rev. Sci. Instrum. **74**, 267 (2003).
- [53] W. Silveira, *A microscopic view of charge injection in an organic semiconductor*, PhD thesis, Cornell University, 2005.
- [54] E. Muller, *Electric force microscopy of charge trapping in thin-film pentacene transistors*, PhD thesis, Cornell University, 2005.
- [55] R. Subramanian et al., Anal. Chem. **71**, 5335 (1999).
- [56] A. M. Wolters, D. A. Jayawickrama, and J. V. Sweedler, Curr. Opin. Chem. Bio. **6**, 711 (2002).
- [57] A. G. Webb, J. Pharma. Biomed. Anal. **38**, 892 (2005).
- [58] K. Yamauchi, J. W. G. Janssen, and A. P. M. Kentgens, J. Mag. Res. **167**, 87 (2004).
- [59] D. A. Seeber, J. H. Hoftiezer, W. B. Daniel, M. A. Rutgers, and C. H. Pennington, Rev. Sci. Instr. **71**, 4263 (2000).
- [60] D. A. Seeber, J. H. Hoftiezer, and C. H. Pennington, Rev. Sci. Instr. **71**, 2908 (2000).
- [61] D. A. Seeber, R. L. Cooper, L. Ciobanu, and C. H. Pennington, Rev. Sci. Instr. **72**, 2171 (2001).
- [62] T. L. Peck, R. L. Magin, and P. C. Lauterbur, J. Magn. Res. B **108**, 114 (1995).
- [63] Z. Zhang, P. C. Hammel, and G. J. Moore, Rev. Sci. Instrum. **67**, 3307 (1996).

- [64] T. D. Stowe, *Extending the lower limits of force sensitivity using micromachined silicon cantilevers*, PhD thesis, Stanford University, 2000.
- [65] D. Rugar, H. J. Mamin, and P. Guethner, Appl. Phys. Lett. **55**, 2588 (1989).
- [66] O. Züger, S. T. Hoen, C. S. Yannoni, and D. Rugar, J. Appl. Phys. **79**, 1881 (1996).
- [67] J. A. Marohn and J. G. Kempf, Phys. Rev. Lett. **90**, 087601 (2003).
- [68] A. Suter, D. V. Pelekhov, M. L. Roukes, and P. C. Hammel, J. Mag. Res. **154**, 210 (2002).
- [69] R. Richardson and E. Smith, editors, *Experimental techniques in condensed matter physics at low temperatures*, Addison-Wesley, 1988.
- [70] H. Hug et al., Rev. Sci. Instru. **70**(9), 3625 (1999).
- [71] M. Roseman and P. Grutter, Rev. Sci. Instr. **71**(10), 3782 (2000).
- [72] M. Liebmann, A. Schwarz, S. Langkat, and R. Wiesendanger, Rev. Sci. Instr. **73**(10), 3508 (2002).
- [73] D. Rugar, Personal Communication, 2006.
- [74] S. A. Hickman, Cornell university, Ph.d. Thesis, 2006.
- [75] H. Mamin, M. Poggio, C. Degen, and D. Rugar, Nature Nanotech. **Adv. Online Pub.**, 1 (2007).
- [76] S. Kuehn, R. Loring, and J. Marohn, Phys. Rev. Lett. **96**, 156103 (2006).
- [77] S. Kuehn, J. Marohn, and R. Loring, J. Phys. Chem. B **110**, 14525 (2006).
- [78] H. B. Chan, Science **293**, 1766 (2001).
- [79] A. A. Chumak, P. W. Milonni, and G. P. Berman, Phys. Rev. B **70**, 085407 (2004).
- [80] N. Arkani-Hamed, S. Dimopoulos, and G. Dvali, Sci. Am. **283**, 62 (2000).
- [81] C. Henkel and M. Wilkens, Europhys. Lett. **47**, 414 (1999).
- [82] D. J. Wineland et al., J. Res. Natl. Inst. Stand. Technol. **103**, 259 (1998).
- [83] T. Gramila, J. Eisenstein, A. Macdonald, L. Pfeiffer, and K. West, Phys. Rev. Lett. **66**, 1216 (1991).
- [84] M. S. Tomassone and A. Widom, Phys. Rev. B. **56**, 4938 (1997).
- [85] S. Garrett-Roe et al., J. Phys. Chem. B **109**(43), 20370 (2005).
- [86] P. C. Nelson, *Biological Physics: Energy, Information, Life*, W.H. Freeman, 2004.
- [87] P. G. Wolynes, Annu. Rev. Phys. Chem. **31**, 345 (1980).
- [88] B. Bagchi, J. Chem. Phys. **95**, 467 (1991).
- [89] J. Hubbard and L. Onsager, J. Chem. Phys. **67**, 4850 (1977).
- [90] L. Onsager, Science **166**, 1359 (1969).
- [91] T. Nee and R. Zwanzig, J. Chem. Phys. **52**, 6353 (1970).
- [92] J. Hubbard and R. Kayser, J. Chem. Phys. **74**(6), 3535 (1981).
- [93] P. W. Fenimore, H. Frauenfelder, B. H. McMahon, and F. G. Parak, Proc. Natl. Acad. Sci **99**, 14408 (2002).
- [94] P. W. Fenimore, H. Frauenfelder, B. H. McMahon, and R. D. Young, Proc. Natl. Acad. Sci. **101**, 14408 (2004).
- [95] J. M. Martinis et al., Phys. Rev. Lett. **95**, 210503 (2005).

- [96] P. Debye, *Polar Molecules*, Dover, 1929.
- [97] H. Frohlich, *Theory of Dielectrics*, Oxford, 1949.
- [98] A. K. Jonscher, J. Phys. D - Appl. Phys. **32**, R57 (1999).
- [99] U. Schneider, P. Lunkenheimer, R. Brand, and A. Loidl, Phys. Rev. E **59**, 6924 (1998).
- [100] M. Arndt, R. Stannarius, H. Groothues, E. Hempel, and F. Kremer, Phys. Rev. Lett. **79**(11), 2077 (1997).
- [101] F. He, L. M. Wang, and R. Richert, Phys. Rev. B **71**, 144205 (2005).
- [102] J. Forrest, K. Dalnoki-Veress, J. Stevens, and J. Dutcher, Phys. Rev. Lett. **77**(10), 2002 (1996).
- [103] G. DeMaggio, W. Frieze, and D. Gidley, Phys. Rev. Lett **78**(8), 1524 (1997).
- [104] N. Israeloff, Phys. Rev. B **53**, 11913 (1996).
- [105] N. Israeloff and T. Grigera, Europhysics Letters **43**, 308 (1998).
- [106] E. Vidal-Russell, N. Israeloff, L. Walther, and H. A. Gomariz, Phys. Rev. Lett. **81**(7), 1461 (1998).
- [107] E. Vidal-Russell and N. Israeloff, Nature **408**, 695 (2000).
- [108] K. S. Sinnathamby, H. Oukris, and N. E. Israeloff, Phys. Rev. Lett. **95**, 067205 (2005).
- [109] N. Israeloff, H. Oukris, and P. Crider, J. Non-Cryst. Sol. **352**, 4915 (2006).
- [110] K. Schmidt-Rohn et al., Macromolecules **27**, 4733 (1994).
- [111] U. Tracht et al., Phys. Rev. Lett. **81**, 2727 (1998).
- [112] U. Tracht, H. Wilhelm, A. Heuer, and H. W. Spiess, J. Magn. Res. **140**, 460 (1999).
- [113] A. Einstein, Ann. Phys. **17**, 549 (1905).
- [114] W. Denk and D. Pohl, Appl. Phys. Lett. **59**(17), 2171 (1991).
- [115] T. D. Stowe, T. W. Kenny, D. J. Thomson, and D. Rugar, Appl. Phys. Lett. **75**, 2785 (1999).
- [116] B. J. Persson and Z. Zhang, Phys. Rev. B **57**, 7327 (1998).
- [117] I. Dorofeyev, H. Fuchs, G. Wenning, and B. Gotsmann, Phys. Rev. Lett. **83**(12), 2402 (1999).
- [118] A. I. Volokitin and N. J. Persson, Phys. Rev. B **65**, 115419 (2002).
- [119] A. I. Volokitin and B. J. Persson, Phys. Rev. B **68**, 155420 (2003).
- [120] A. I. Volokitin and B. J. Persson, Phys. Rev. Lett. **91**, 106101 (2003).
- [121] V. Mkrtchian, V. A. Parsegian, R. Podgornik, and W. M. Saslow, Phys. Rev. Lett. **91**, 220801 (2003).
- [122] A. Volokitin, B. Persson, and H. Ueba, J. Exp. and Theor. Phys. **104**(1), 107 (2007).
- [123] A. Volokitin and B. Persson, Phys. Rev. B **74**, 205413 (2007).
- [124] T. Stowe et al., Appl. Phys. Lett. **71**(2), 288 (1997).
- [125] D. Rugar et al., Applied Physics A: Materials Science & Processing **72**, S3 (2001).
- [126] S. Hudlet, M. Saint Jean, C. Guthmann, and J. Berger, Euro. Phys. J. B **2**, 5 (1998).
- [127] O. Cherniavskaya, L. W. Chen, V. Weng, L. Yuditsky, and L. E. Brus, J. Phys. Chem. B **107**, 1525 (2003).
- [128] A. Augsburg, K. Grundke, K. Poschel, H. J. Jacobasch, and A. W. Neumann, Act. Poly. **49**, 417 (1998).

- [129] K. Bewig and W. Zisman, J. Phys. Chem. **69**, 4238 (1965).
- [130] L. Onsager, J. Am. Chem. Soc. **58**, 1486 (1936).
- [131] J. Jackson, *Classical Electrodynamics*, Academic Press, 1998.
- [132] J. Marohn, S. Kuehn, and R. Loring, Dissipation of a cantilever above a metal/dielectric film, Group Document, 2005.
- [133] S. F. Lyuksyutov, P. B. Paramonov, R. A. Sharipov, and G. Sigalov, Phys. Rev. B **70**, 174110 (2004).
- [134] B. Bagchi, D. Oxtoby, and G. Fleming, Chem. Phys. **86**, 257 (1984).
- [135] P. Wolynes, J. Chem. Phys. **86**, 5133 (1987).
- [136] I. Rips, J. Klafter, and J. Jortner, J. Chem. Phys. **88**, 3246 (1988).
- [137] H. Zhou, B. Bagchi, A. Papazyan, and M. Maroncelli, J. Chem. Phys. **97**, 9311 (1992).
- [138] J. Bandrup and E. Immergut, *Polymer Handbook*, Wiley, 1965.
- [139] D. J. Mead and R. M. Fuoss, J. Am. Chem. Soc **63**, 2832 (1941).
- [140] D. J. Mead and R. M. Fuoss, J. Am. Chem. Soc. **64**, 2389 (1942).
- [141] N. G. McCrum, B. Read, and G. Williams, *Anelastic and Dielectric Effects in Polymeric Solids*, Wiley, 1967.
- [142] K. Fukao, S. Uno, Y. Miyamoto, A. Hoshino, and H. Miyaji, Phys. Rev. E **64**, 051807 (2001).
- [143] R. D. Priestley, C. J. Ellison, L. J. Broadbelt, and J. M. Torkelson, Science **309**, 456 (2005).
- [144] E. Vidal Russel and N. E. Israeloff, Nature **408**, 695 (2000).
- [145] T. N. Ng, *High sensitivity cantilever magnetometry and the temperature dependence of charge injection in an organic conductor*, PhD thesis, Cornell University, 2006.
- [146] B. C. Stipe, H. J. Mamin, T. D. Stowe, T. W. Kenny, and D. Rugar, Phys. Rev. Lett. **86**, 2874 (2001).
- [147] M. Weissbluth, *Photon-Atom Interactions*, Elsevier, 1997.
- [148] W. Scaife and G. McMullin, Meas. Sci. Technol. **5**, 1576 (1994).